Physically Consistent Indoor Wireless Channel Modelling and Optimisation with Ray Tracing

Gang Yu

School of Electrical and Electronic Engineering

The University of Sheffield

Supervisors: Prof. Jie Zhang & Prof. Mohammed Benaissa

This thesis is submitted for the approval of the

Doctor of Philosophy

August 2026

March winds and April showers bring forth May flowers.

Acknowledgements

It is with sincere gratitude that I acknowledge the many individuals and institutions who have supported and inspired me throughout my doctoral research.

First and foremost, I wish to express my deepest appreciation to my supervisor, Prof. Jie Zhang, for his constant encouragement and wise guidance, especially during times of frustration and self-doubt. His support has greatly influenced not only my perseverance in research but also my outlook on life. I am equally grateful to Prof. Jiliang Zhang, Prof. Gabriele Gradoni and Prof. Yihan Xu, whose profound knowledge and insightful guidance in various aspects of communication technologies have greatly deepened my understanding of the field and inspired me to explore it further.

I would also like to extend my thanks to my colleagues and friends in the Communication Group within the School of Electrical and Electronic Engineering at the University of Sheffield and in 6G Innovation Centre (5GIC & 6GIC) within the Institute for Communication Systems (ICS) at the University of Surrey. Their collaboration, assistance, and conversations have made this journey both productive and enjoyable.

I gratefully acknowledge the financial support provided by EPSRC Telecom Hub HASC under Grant Ref: EP/Y037197/1, which made the research work presented in Chapter 5 of this thesis possible.

Part of the work presented in Chapter 5 was conducted using resources provided by 6G Innovation Centre (5GIC & 6GIC) within the Institute for Communication Systems (ICS) at the University of Surrey, and I acknowledge the use of reconfigurable intelligent surface (RIS), Anritsu MG3692A signal generator and A-INFOMW LB-229-20-C-SF standard-gain horn antenna for simulation, computation, and validation.

Finally, and most importantly, I must pay tribute to my family for their unconditional love, patience, and understanding. Their constant encouragement has been my greatest source of strength.

Abstract

Polarisation is important in modelling wireless propagation, particularly indoors, where signals undergo multiple reflections and transmissions through complex building materials. Conventional ray tracing predicts propagation paths effectively, but often represents polarisation with insufficient accuracy. To address this limitation, this thesis proposes a physically consistent three-dimensional ray-tracing framework that tracks polarisation through a rotation transfer matrix. The framework follows each polarisation component through successive interactions, enabling estimation of polarisation-dependent received power and cross-polarisation ratio while preserving electromagnetic transformations.

Using this framework, the thesis investigates how indoor depolarisation affects wireless channels and polarisation shift keying. The results show that assigning a constant cross-polarisation ratio to multipath components cannot represent the variation caused by propagation conditions and may yield inaccurate average bit error-probability predictions. The framework supports an optimisation procedure that jointly adjusts the complex permittivity and thickness of multilayer materials. Within the cases studied, the optimised material configurations reduce the average bit error probability of the polarisation shift keying system at high signal-to-noise ratios and lower the resulting error floor.

The framework is then extended to reconfigurable intelligent surfaces under indoor multipath illumination. A circuit-based macromodel is incorporated into the ray-tracing formulation, while physical optics and diffraction grating theory describe multimode reradiation, finite-aperture diffraction, and parasitic scattering. The extended framework relates the electromagnetic behaviour of the surface to site-specific channel prediction. Comparisons with full-wave simulations and indoor measurements show agreement in the evaluated cases and demonstrate its ability to predict changes in received-power coverage and spatial received-power dispersion.

Overall, the framework provides a physically grounded, coherent, and computationally efficient basis for analysing and optimising polarised indoor wireless systems assisted by reconfigurable intelligent surfaces.

List of Publications

Published

[1] **G. Yu**, Y. Zhang, X. Dong, W. Xi, L. Zhou, Y. Zheng, J. Zhang, and J. Zhang, "Eliminating the bit error floor of polarization modulation by using wireless friendly building materials," *IEEE Trans. Commun.*, vol. 74, pp. 8701–8717, May. 2026.

[2] **G. Yu**, L. Zhou, J. Zhang, and J. Zhang, "A ray-launching algorithm for polarized wireless channel prediction," in *Proc. 2023 IEEE Globecom Workshops (GC Wkshps)*, Dec. 2023, pp. 1928–1933.

[3] **G. Yu**, W. Xi, A. T. Joy, J. Chen, A. Tishchenko, D. Serghiou, H. Taghvaee, M. Khalily, J. Zhang, G. Gradoni and R. Tafazolli, "Self-consistent modeling of RIS operating in real-life propagation environments via ray-tracing simulations," in *Proc. IEEE Conf. Comput. Commun. Workshops (INFOCOM WKSHPS)*, May. 2025, pp. 1–6.

[4] **G. Yu**, A. T. Joy, W. Xi, J. Zhang, M. Khalily, G. Gradoni and R. Tafazolli, "Physically consistent modelling and analysis of RIS under multipath incidence," in *Proc. 20th Eur. Conf. Antennas Propag. (EuCAP)*, Apr. 2026, pp. 1–5.

[5] **G. Yu** and G. Gradoni, "Physically consistent modelling and analysis of RIS under multipath incidence," in *Proc. 12th Int. Conf. Antennas Electromagn. Syst. (AES)*, Jun. 2026. (Accepted)

[6] **G. Yu** and G. Gradoni, "Physically consistent modeling of RIS scattering under multipath incidence," in *Proc. 2026 IEEE Int. Symp. Antennas Propag. and USNC-URSI Radio Sci. Meeting (AP-S/URSI)*, Jul. 2026. (Accepted)

[7] **G. Yu** and G. Gradoni, "Self-consistent electromagnetics modeling of reconfigurable intelligent surfaces under multipath propagation," in *Proc. XXXVIth URSI Gen. Assem. Sci. Symp. (URSI GASS)*, Aug. 2026. (Accepted)

[8] **G. Yu** and G. Gradoni, "Physics consistent machine learning aided ray tracing for efficient and generalizable radio propagation modeling," in *Proc. XXXVIth URSI Gen. Assem. Sci. Symp. (URSI GASS)*, Aug. 2026. (Accepted)

[9] **G. Yu**, M. Kamoun, M. Amara, and G. Gradoni, "Geometric algebra Schrödinger bridge for electromagnetic inverse scattering," in *Proc. 2026 Int. Conf. Electromagn. Adv. Appl. (ICEAA)*, Sep. 2026. (Accepted)

Submitted

[10] **G. Yu**, A. T. Joy, W. Xi, J. Zhang, M. Khalily, G. Gradoni and R. Tafazolli, "Physically consistent RIS modeling and verification using impedance-matrix-based methods in multipath EM environments," under review in *IEEE Trans. Antennas Propag.*.

Manuscripts in preparation

[11] **G. Yu**, M. Nerini, G. Gradoni, and B. Clerckx, "Multipath-aware physically consistent beyond-diagonal RIS," manuscript in preparation for submission to *IEEE Trans. Wireless Commun.*.

Relationship Between Publications and Thesis Chapters

The relationship between the publications arising from this research and the relevant thesis chapters is summarised as follows:

- **Chapter 3:** Publication [2] presents the polarisation-aware ray tracing framework that forms the basis of the polarised indoor channel modelling and prediction methods developed in this chapter.
- **Chapter 4:** Publication [1] supports the analysis of polarisation shift keying performance, the identification of the average bit error probability floor at high signal-to-noise ratios, and the optimisation of the multilayer building-material parameters presented in this chapter.
- **Chapter 5:** Publications [3]–[7] support the development of the physically consistent reconfigurable intelligent surface modelling framework under realistic indoor multipath illumination conditions. Publication [10] is most directly related to the impedance-matrix-based reconfigurable intelligent surface macromodel and its validation using full-wave simulations and room-level measurements. Publication [11] supports the theoretical extension from a local diagonal reconfigurable intelligent surface response to a multipath-aware beyond-diagonal reconfigurable intelligent surface formulation.

Table of contents

List of Publications **ix**

List of figures **xvii**

List of tables **xxiii**

Abbreviations **xxv**

1 Introduction **1**

1.1 Background and Motivation 2

1.2 Definition and Scope of Physically Consistent Modelling 6

1.3 Objectives of the Thesis 8

1.4 Contributions 9

1.5 Structure of the Thesis 11

2 State of the Art and Research Challenges **13**

2.1 Indoor Propagation Modelling 14

2.1.1 Stochastic models 14

2.1.2 Deterministic Models 20

2.2 Indoor Ray-Based Polarisation Propagation Models 25

2.3 Depolarisation Effects Modelling of Polarised Wireless Channel 27

2.4 Propagation Modelling for RIS 29

2.5 Commercial and Publicly Available Indoor Ray-Based Simulators 31

2.5.1 Sionna RT 32

2.5.2 CloudRT 34
2.5.3 Altair WinProp 36
2.5.4 Ranplan Professional 38
2.5.5 EDX Advanced Propagation 40
2.5.6 Siradel Web Services 42
2.5.7 Wireless InSite 45
2.5.8 CrossWave 47
2.6 Critical Comparison and Research Challenges 63

3 An RT Algorithm for Polarised Wireless Channel Prediction 67
3.1 Introduction 68
3.2 RT Algorithm 69
3.2.1 Geometry of Rays and Polarisation Components 73
3.2.2 Reflection and Transmission Coefficients 74
3.2.3 Physical Angle of Refraction in Double-Positive Materials 75
3.2.4 Rotation Transfer Matrix Method for RT 80
3.3 RT Simulation 82
3.3.1 System Description and Modelling Assumptions 83
3.3.2 Effective Channel Representation for Polarised Components 83
3.4 Polarised Channel Simulation and Performance Evaluation 86
3.4.1 Simulation Scenario and Parameter Configuration 86
3.4.2 Simulation Results and Discussion 89
3.5 Summary 91

4 Performance Analysis and Optimisation of Indoor Polarisation Modulation via Polarisation-Aware RT 93
4.1 Introduction 94
4.2 PolarSK Transmission Scheme 103
4.3 Channel Modelling of the PolarSK System Using RT 106
4.4 ABEP Analysis 108

4.4.1 Modelling of SC and i.i.d. Rayleigh Fading Channels 110
4.4.2 Simulation Results under Three Channel Conditions 113
4.5 Reduction of the ABEP Floor in PolarSK Systems 116
4.5.1 Problem Formulation 116
4.5.2 Iterative Solution Method 119
4.5.3 Simulation Results 120
4.5.4 Physical Interpretation of Simulation Results 124
4.6 Discussion 128
4.7 Summary 136

5 Physically Consistent RIS Macromodelling for Indoor Wireless Channel Prediction via RT 139

5.1 Introduction 140
5.2 Plane-Wave Expansion of EM Waves Reflected by RIS under Multipath Incidence 150
5.3 Macromodelling of RIS 154
5.3.1 Derivation of the Reflection Coefficient Using a Multiport Unit-Cell Model 155
5.3.2 Validation of the Multiport Reflection Coefficient 159
5.3.3 Far-Field Radiation Pattern of the RIS 161
5.3.4 Small Meeting Room RT and Measurement Validation 162
5.4 Simulation Framework and Settings 168
5.4.1 Scenario I: Single-Path-Based Design 168
5.4.2 Scenario II: Multipath-Based Design 182
5.4.3 Multipath Illumination of a Nonlocal Beyond-Diagonal RIS 191
5.5 Performance Evaluation of Single-Path and Multipath RIS Designs 198
5.5.1 CST Full-Wave Validation 198
5.5.2 Application to the PEC T-Shaped Room 204
5.6 Summary 213

6 Conclusion and Future Work **215**

6.1 Conclusion 215

6.2 Future Work 217

References **221**

List of figures

2.1 Classification of stochastic channel models. 15
2.2 Classification of deterministic channel models. 21
2.3 Illustration of image-based ray tracing for LOS and reflected NLOS paths. . 22
2.4 Illustration of the ray-launching method for LOS and reflected NLOS paths. 23

3.1 Planes of constant phase and amplitude for the refracted wave. 79
3.2 Visualisation of reference frame transformations via rotation matrices in sequential reflections and transmissions. 82
3.3 Spherical coordinate systems for Tx and Rx. 83
3.4 Block diagram of a crossed dipole antenna system with co-polarisation and cross-polarisation propagation gains α and β. 85
3.5 Layout of the indoor scenario used for simulation. 86
3.6 Received power (dBW) corresponding to LOS (OLOS) path for horizontal and vertical polarisation components. 88
3.7 Received power (dBW) corresponding to RNLOS path for horizontal and vertical polarisation components. 88
3.8 Received power (dBW) corresponding to the superposition of LOS (OLOS) and RNLOS paths for horizontal and vertical polarisation components. . . . 89
3.9 XPR (dB) corresponding to LOS (OLOS) path for horizontal and vertical polarisation components. 90
3.10 XPR (dB) corresponding to RNLOS path for horizontal and vertical polarisation components. 90

3.11 XPR (dB) corresponding to the superposition of LOS (OLOS) and RNLOS paths for horizontal and vertical polarisation components. 91

4.1 The ABEP performance of PolarSK for unnormalised 1×1, 1×2 and 1×4 MIMO systems employing $K = 2$, $M = 2$ signal constellation under 55dB, 65dB and 75dB SNR. 109
4.2 ABEP performance of the PolarSK scheme for a normalised 1×4 MIMO system with $K = 2$ and $M = 2$ under three channel conditions: a ray-based channel, an i.i.d. Rayleigh fading channel, and an SC channel. 113
4.3 ABEP performance of the PolarSK scheme for normalised 1×1, 1×2, and 1×4 MIMO systems with $K = 2$ and $M = 2$. 114
4.4 ABEP performance of the PolarSK scheme for a normalised 1×4 MIMO system with $K = 2$ and modulation orders $M \in \{2,4,16\}$. 115
4.5 $ABEP_{\mathrm{avg}}(50\,\mathrm{dB})$ improvement of the PolarSK scheme versus the number of iterations for normalised 1×1, 1×2, and 1×4 MIMO systems with $K = 2$ and $M = 2$ under NLOS conditions. 121
4.6 $ABEP_{\mathrm{avg}}(50\,\mathrm{dB})$ improvement of the PolarSK scheme versus the number of iterations for a normalised 1×1 MIMO system with $K = 2$ and $M = 2$ under NLOS conditions, evaluated at Rx locations with different heights. 122
4.7 ABEP performance under optimised and baseline wall parameters for normalised 1×1, 1×2, and 1×4 MIMO systems with $K = 2$ and $M \in \{2,4,16\}$. 124
4.8 Mean and maximum absolute logarithmic power ratio deviations for normalised 1×1, 1×2, and 1×4 MIMO systems under optimised and baseline wall parameters. 125
4.9 Empirical cumulative distribution functions (CDFs) of $|D_{\mathrm{ln}}|$ for normalised 1×1, 1×2, and 1×4 MIMO systems under optimised and baseline wall parameters. 126
4.10 ABEP performance of the PolarSK scheme for normalised 1×1 MIMO systems with $K = 2$ and $M = 2$ at $50\,\mathrm{dB}$ SNR under unoptimised building material conditions. 126

4.11 Variation of the electric-field vector orientation upon reflection of a plane wave at different incidence angles. 127
4.12 Uniform plane-wave propagation. 129
4.13 Standing-wave patterns as functions of spatial distance for a uniform plane wave under different reflection coefficient values. 130
4.14 The ABEP performance of the PolarSK scheme for normalised 1×1, 1×2, and 1×4 MIMO systems with $K=2$ and $M=2$, under Channel A and Channel B, respectively. 135
4.15 The ABEP performance of the PolarSK scheme for normalised 1×1, 1×2, and 1×4 MIMO systems with $K=2$ and $M=2$, under Channel A and Channel B, respectively. 136

5.1 Geometry of a rectangular conducting plate with an aperture illuminated by three uniform plane waves. 155
5.2 Equivalent multiport network representation of the RIS unit cell. 156
5.3 Floquet modal circles (left) and modal amplitudes (right) for a rectangular periodic array. 158
5.4 Reflection coefficient obtained from full-wave simulation and the multiport model for capacitances from 0.22 to 0.33 pF. 159
5.5 Reflection coefficient obtained from full-wave simulation and the multiport model for capacitances from 0.38 to 0.71 pF. 160
5.6 Reflection coefficient obtained from full-wave simulation and the multiport model for capacitances from 0.82 to 2.1 pF. 160
5.7 Calculated far-field electric-field distribution $E(\theta,\phi)$ of the complete RIS aperture. 162
5.8 Small meeting room and its RT reconstruction at 5G/6GIC. 163
5.9 Measured and RT-predicted received power versus distance from the RIS at Rx azimuths of (a) 60°, (b) 70°, and (c) 80°. The RIS is configured for 60° reradiation. 164

5.10 Agreement between measured and RT-predicted received power at the ten accessible Rx positions: (a) proposed RIS model, configured state; (b) simplified RIS model, configured state; and (c) RIS inactive state. 165
5.11 Spatial dispersion of received power across the ten accessible Rx positions in the RIS inactive and configured states: (a) measurements, (b) proposed RIS model RT results, and (c) simplified RIS model RT results. 166
5.12 Comparison of the designed RIS phase distributions under single-path and multipath illumination. 200
5.13 Radiation-pattern cuts obtained using the proposed analytical method. . . . 202
5.14 Radiation-pattern cuts obtained from full-wave simulations. 203
5.15 RIS phase distributions synthesised from the incident fields predicted by the RT algorithm developed in this thesis. 205
5.16 Polarisation-resolved background field distributions predicted by the RT algorithm developed in this thesis for the PEC T-shaped room at $P_{\mathrm{tx}} = -15$ dBW. 205
5.17 ϕ-polarised RIS-only field distributions predicted by the RT algorithm developed in this thesis under multipath illumination at $P_{\mathrm{tx}} = -15$ dBW. 206
5.18 θ-polarised RIS-only field distributions predicted by the RT algorithm developed in this thesis under multipath illumination at $P_{\mathrm{tx}} = -15$ dBW. 206
5.19 Normalised polarisation-resolved RIS reradiation patterns predicted by the RT algorithm developed in this thesis. 207
5.20 RIS phase distributions synthesised from the Sionna-derived incident fields. 209
5.21 Polarisation-resolved background field distributions predicted using Sionna for the PEC T-shaped room at $P_{\mathrm{tx}} = -15$ dBW. 209
5.22 Sionna-based ϕ-polarised RIS-only field distributions under multipath illumination at $P_{\mathrm{tx}} = -15$ dBW. 210
5.23 Sionna-based θ-polarised RIS-only field distributions under multipath illumination at $P_{\mathrm{tx}} = -15$ dBW. 210

5.24 Normalised polarisation-resolved RIS reradiation patterns obtained using Sionna-derived incident fields. 211

List of tables

2.1 Critical comparison of representative modelling approaches with respect to the EM requirements of this thesis. 50

3.1 Notation of Chapter 3 69
3.2 Three-layer wall properties and frequency-dependent parameters. 87

4.1 Notation of Chapter 4 98
4.2 Optimisation search ranges and algorithm parameters. 119

5.1 Notation of Chapter 5 142
5.2 Three incident paths used in the CST full-wave benchmark. 198
5.3 Target-direction asymptotic far-field amplitudes referenced to 1 m for the CST three-path benchmark. 201
5.4 Incident paths generated by the RT algorithm developed in this thesis for the first evaluation in the PEC T-shaped room. 205
5.5 Normalised RIS-only target-direction reradiation gain comparison obtained using the RT algorithm developed in this thesis. 208
5.6 Incident paths generated in the Sionna-based evaluation of the PEC T-shaped room. 208
5.7 Normalised Sionna-based RIS-only target-direction reradiation gain comparison. 212

Abbreviations

3GPP Third Generation Partnership Project

4G Fourth Generation

5G Fifth Generation

5G/6GIC 5G/6G Innovation Centre

6G Sixth Generation

ABEP Average Bit Error Probability

AoA Angle of Arrival

AoD Angle of Departure

API Application Programming Interface

BIM Building Information Modelling

BWP Building Wireless Performance

CAD Computer-Aided Design

CDF Cumulative Distribution Function

COST European Cooperation in Science and Technology

CPR Co-Polarisation Ratio

CST CST Studio Suite

CPU Central Processing Unit

DC Direct Current

DoF Degrees of Freedom

DPM Dominant Path Model

DPS Double-Positive

DPSK Differential Phase-Shift Keying

ER Effective Roughness

EM Electromagnetic

FDTD Finite-Difference Time Domain

FEM Finite-Element Method

FFT Fast Fourier Transform

GCS Global Coordinate System

GHz Gigahertz

GO Geometrical Optics

GPU Graphics Processing Unit

GSM Global System for Mobile Communications

IFC Industry Foundation Classes

i.i.d. independent and identically distributed

IoT Internet of Things

IRL Intelligent Ray Launching

IRT Intelligent Ray Tracing

ITU International Telecommunication Union

LAM Linear Attenuation Model

LCS Local Coordinate System

LiDAR Light Detection and Ranging

LOS Line-of-Sight

LTE Long-Term Evolution

MAD Mean Absolute Deviation

MIMO Multiple Input Multiple Output

MISO Multiple Input Single Output

MHz Megahertz

ML Maximum Likelihood

MLFMM Multilevel Fast Multipole Method

MoM Method of Moments

MPSK M-ary Phase-Shift Keying

MWM Multiwall Model

NLOS Non-Line-of-Sight

NR New Radio

NRSRP New Radio Reference Signal Received Power

OLOS Obstructed Line-of-Sight

OpenCL Open Computing Language

OSM One Slope Model

P25 Project 25

PDL Polarisation-Dependent Loss

PDM Polarisation Division Multiplexing

PEC Perfect Electric Conductor

PEP Pairwise Error Probability

PMC Perfect Magnetic Conductor

PSK Phase-Shift Keying

PMD Polarisation Mode Dispersion

PO Physical Optics

PolarSK Polarisation Shift Keying

RAN Radio Access Network

RCS Radar Cross Section

REST Representational State Transfer

RIS Reconfigurable Intelligent Surface

RNLOS Reflected Non-Line-of-Sight

RSS Received Signal Strength

RT Ray Tracing

Rx Receiver

RMSE Root-Mean-Square Error

SBR Shooting and Bouncing Ray

SC Spatial Correlation

SINR Signal-to-Interference-plus-Noise Ratio

SISO Single Input Single Output

SNR Signal-to-Noise Ratio

SOP State of Polarisation

TE Transverse Electric

TETRA Terrestrial Trunked Radio

TM Transverse Magnetic

Tx Transmitter

UAV Unmanned Aerial Vehicle

UMTS Universal Mobile Telecommunications System

UTD Uniform Theory of Diffraction

V2X Vehicle-to-Everything

VHF Very High Frequency

Wi-Fi Wireless Fidelity

WINNER Wireless World Initiative New Radio

XML Extensible Markup Language

XPD Cross-Polarisation Discrimination

XPI Cross-Polarisation Isolation

XPR Cross-Polarisation Ratio

Chapter 1

Introduction

Overview

This chapter establishes the background and motivation for the thesis by outlining the transition from fifth generation (5G) to sixth generation (6G) wireless systems and the resulting need for accurate indoor channel prediction. Indoor radio propagation is governed by multipath interactions and by the electromagnetic response of building materials, which varies with frequency, angle of incidence, and polarisation. This chapter therefore motivates a vector ray-tracing framework that preserves these interactions while remaining computationally tractable. It also introduces building wireless performance (BWP) as a link between material properties and metrics at the system-level, and reconfigurable intelligent surfaces (RISs) as programmable components for modifying an otherwise passive propagation environment. Once the geometry and material composition of a building have been fixed, substantial alterations are generally costly and impractical. RISs can therefore provide a programmable means of improving coverage or signal quality in selected indoor regions without requiring major changes to the building fabric. However, idealised RIS models based on single plane-wave illumination and an infinite aperture do not represent the multipath excitation and finite dimensions encountered in realistic indoor environments, which motivates the site-specific, multipath-aware RIS formulation developed later in this thesis.

1.1 Background and Motivation

Although 5G deployment is continuing, research has shifted towards the capabilities and propagation requirements anticipated for 6G systems. Demand for higher data rates and network capacity continues to drive the introduction of new frequency bands, deployment scenarios, and transmission methods [1–4]. Each change modifies the relevant propagation mechanisms and can therefore alter link and system performance [5]. Wireless channels also vary with interference, terminal position, and the surrounding environment [6]. Channel models must represent these variations at the level of fidelity required by the intended design task [7].

Indoor environments are central to contemporary network design. Recent studies estimate that approximately 80%–96% of wireless data traffic will be carried indoors in the coming years, further highlighting the importance of indoor wireless communication research [8, 9]. Indoor channels are strongly site-dependent: walls, doors, ceilings, floors, and furniture generate reflected, transmitted, diffracted, and scattered components [7]. Their different electromagnetic properties produce spatially varying received power, delay, phase, and polarisation. Consequently, an indoor model must be selected according to both the physical environment and the performance metric being evaluated.

Statistical fading models, including Rayleigh and Rician models, and empirical expressions for path loss are widely used because they provide tractable descriptions of average or distributional channel behaviour [10–12]. In their standard forms, however, they do not resolve the geometry of individual propagation paths or the electromagnetic response of a specific multilayer material. They are therefore unsuitable when the required output depends explicitly on receiver position, the polarisation transformation along each propagation path, or the construction of a particular building.

Deterministic methods complement statistical models by deriving the propagation behaviour of a specific site from the geometry of the environment and the electromagnetic properties of its materials [7]. Among these methods, ray-based models describe indoor propagation by tracing individual paths and evaluating their interactions with surrounding objects. For each path, they can retain the propagation distance, interaction sequence, accumulated phase, and vector field while accounting for reflection, transmission, diffraction, and, where included, diffuse scattering. Compared with a full-wave simulation of an entire room, ray-based models usually require much less computation and are therefore more suitable for repeated channel evaluations. Their reliability, however, depends on the accuracy of the geometric description and material parameters, the number of interactions retained, and the validity of the underlying high-frequency approximations.

Geometrical optics (GO) alone cannot represent every propagation mechanism encountered in indoor environments. Ray-based models are therefore often supplemented with electromagnetic or statistical methods that describe effects beyond specular propagation. Physical optics (PO) can describe radiation from finite apertures, effective roughness (ER) models can represent diffuse scattering, and full-wave solvers such as finite-difference time domain (FDTD) methods can resolve local interactions that require greater electromagnetic detail. These hybrid approaches extend the physical scope of ray-based modelling without requiring a full-wave simulation of the entire environment [7, 13].

Indoor propagation is governed by both the geometry of a building and the electromagnetic response of its materials. For each reflection or transmission, the corresponding complex coefficient depends on the angle of incidence, polarisation, frequency, layer thickness, permittivity, permeability, and conductivity. These quantities determine how the amplitude and phase of each propagation path are modified. Even small changes in the response of an individual path can therefore produce noticeable spatial variations after coherent multipath combination.

This dependence becomes particularly important when channel polarisation is considered. At each reflection, transmission, diffraction, or scattering event, the orthogonal field components may undergo different changes in amplitude and phase. Successive interactions can therefore alter the polarisation state of each path and produce depolarisation and coupling between orthogonal polarisations. When the paths are superposed coherently at the receiver, the resulting polarisation depends on the receiver position and on the propagation paths that contribute to the received field. A channel model that explicitly represents polarisation must therefore track the vector field and the material response as a function of frequency along every propagation path, rather than assign a single constant cross-polarisation ratio (XPR) to an otherwise scalar channel [13]. This path-level electromagnetic description provides the physical basis for relating material properties to communication performance.

The BWP framework formalises this connection by relating the electromagnetic properties of building materials to system-level communication metrics, such as spatially averaged channel capacity [8]. In this thesis, the same principle is extended to polarisation-dependent propagation and average bit error probability (ABEP). Material modifications are therefore evaluated through their influence on the resulting polarised channel and communication performance, rather than through an isolated reflection or transmission coefficient.

The BWP framework provides a passive means of evaluating and improving indoor propagation through material design. However, once the geometry and material composition of a building have been fixed, substantial modifications are usually costly and impractical. Local coverage deficiencies may therefore remain, particularly in non-line-of-sight (NLOS) regions where blockage and destructive interference reduce the received power. These limitations motivate the introduction of programmable electromagnetic structures that can adapt the propagation environment after deployment.

An RIS provides a programmable means of modifying the effective response of a surface and redirecting part of an incident field towards regions with weak coverage. The resulting reradiated field depends not only on the selected surface state, but also on the angular spectrum, amplitude, phase, and polarisation of the illuminating field. In indoor environments, an RIS may be mounted on, integrated into, or embedded within a multilayer building structure [14]. The surrounding materials can therefore modify both the field that illuminates the RIS and the field reradiated into the room. A realistic site-specific model must consequently account for the incident multipath field, the electromagnetic response of the RIS, and the local material environment [15].

To evaluate RIS-assisted propagation within a material-aware indoor channel model, the mapping from the incident field to the reradiated field must preserve the propagation phase while accounting for finite-aperture effects, material and load losses, parasitic scattering, and polarisation conversion [16]. Many existing studies simplify this mapping by assuming perfect redirection into a single prescribed beam, an infinite planar aperture, or illumination by one plane wave at a fixed angle [15, 17–20]. Although these assumptions are useful for canonical analysis, they do not represent finite-aperture diffraction, the angular response away from the design condition, or coherent multipath illumination. Full-wave electromagnetic simulation can resolve these effects, but repeated evaluation at room-scale is generally too costly for channel analysis and design [21]. An RIS macromodel is therefore required to retain the dominant electromagnetic behaviour while remaining suitable for deterministic indoor channel simulation.

These modelling requirements also clarify the complementary roles of BWP and RIS. The BWP framework provides a passive means of relating the electromagnetic properties of building materials to system-level performance and can guide material design before or during construction. Once the geometry and material composition of a building have been fixed, however, substantial modifications are usually costly and impractical. RIS then provides a programmable means of adapting selected regions of the propagation environment after deployment, although it also introduces hardware, control, calibration, and installation complexity. A physically consistent treatment of both approaches can therefore support the design of wireless friendly buildings while enabling local and adaptive improvements in indoor communication performance.

Against this background, the thesis makes three closely connected contributions. First, it develops a physically consistent three-dimensional ray-tracing framework for polarised indoor propagation. The framework tracks the vector field through successive interactions with multilayer materials and predicts path-dependent quantities such as received power and XPR. Building on this framework, the second contribution extends the BWP principle to polarisation-dependent propagation and system-level performance. Polarisation shift keying (PolarSK) is used as a representative case because its information symbols are encoded directly in the polarisation state and are therefore sensitive to depolarisation, polarisation imbalance, and phase distortion. The resulting model is used to evaluate ABEP and to optimise the electromagnetic parameters and thicknesses of multilayer materials. Third, the same physically consistent modelling approach is extended to RIS-assisted indoor propagation through an RIS macromodel that represents a finite surface under multipath illumination and can be incorporated into the site-specific ray-tracing framework. Across all three contributions, the electromagnetic assumptions, computational approximations, and practical limitations are stated explicitly.

1.2 Definition and Scope of Physically Consistent Modelling

In this thesis, the term “physically consistent” has a precise and limited meaning. It means that the electromagnetic quantities and physical relations used at different stages of the model are defined and applied in a mutually compatible manner. When electromagnetic quantities are passed from one modelling stage to the next, their physical definitions and associated conventions are preserved, while any required change of coordinate or polarisation basis is explicitly represented. Accordingly, the electric field, polarisation bases, material and load responses, the chosen time-harmonic convention and the associated propagation and interaction phase definitions, and the boundary or circuit relations form one coherent modelling chain. The term does not imply that the complete indoor environment is solved using a full-wave method, that every propagation mechanism is included, or that the model provides the same prediction accuracy for every building.

Within this general definition, physical consistency in the polarisation-aware ray-tracing framework is achieved by preserving the vector nature of the electric field along each retained propagation path. At every reflection or transmission, the field is resolved into consistently oriented local transverse electric (TE) and transverse magnetic (TM) components. The interaction is then evaluated using complex coefficients for finite-thickness multilayer materials whose electromagnetic properties vary with frequency. For the passive, lossy materials considered in this thesis, the physically admissible solutions for the complex propagation quantities are selected so that the transmitted field propagates into the material and attenuates with distance, rather than remaining constant or increasing, either of which would be unphysical. In lossy double-positive media, the physical direction of phase propagation is obtained from the real phase vector rather than by treating the complex refraction angle as a geometrical angle. Ordered rotation matrices connect the local polarisation bases at successive interactions, while propagation and interaction phases are retained so that all included path contributions can be combined coherently at the receiver. Material loss is represented through the complex propagation, reflection, and transmission coefficients. The reflected, transmitted, and dissipated powers may also be examined through an energy balance check, although this thesis does not perform a separate power audit for every simulated path.

Building on this path-level electromagnetic framework, physical consistency in the BWP application is maintained through a traceable connection from material properties to propagation behaviour and, subsequently, to system-level performance. The permittivity, conductivity, and thickness of the multilayer materials are selected from experimentally characterised or documented ranges and are evaluated at the operating frequency using the adopted material models. For each candidate material configuration, these parameters are used to recalculate the multilayer reflection and transmission coefficients, the polarisation transformation along each propagation path, the coherent channel response, and finally the relevant communication metric. The BWP objective is therefore evaluated through the physical effect of the material configuration on the complete communication link, rather than through a direct empirical association between material parameters and ABEP.

This physical grounding does not, however, guarantee that every optimised continuous parameter combination corresponds to a commercially available or directly manufacturable wall. The practical implementation of such optimised designs remains subject to material tolerances, construction constraints, and experimental validation.

The RIS macromodel provides a separate but complementary application of the same general definition. Whereas the BWP analysis traces the influence of material properties through the propagation channel to system-level performance, the RIS formulation traces the coherent multipath incident field through the surface response to the resulting reradiated field. Physical consistency in the RIS formulation requires the incident field obtained from ray tracing to be coupled to an electromagnetic or circuit response that depends on the incidence conditions and varactor diode bias state. The reradiated field is then constructed from the corresponding surface currents, finite-aperture radiation, and retained modal components rather than from independently assigned ideal phase shifts. Within the adopted approximation, the formulation retains the relevant Floquet–Bloch modes, parasitic scattering, polarisation, propagation phase, and finite-aperture effects. Passivity, power balance, reciprocity, stability, and hardware-realisability are imposed or examined where they form part of the corresponding RIS formulation.

Taken together, these definitions show that physical consistency is specific to each formulation and applies to the electromagnetic mechanisms and modelling levels explicitly represented in each part of the thesis. The mechanisms considered therefore differ among the polarisation-aware ray-tracing framework, the BWP application, and the RIS macromodel. Diffraction, diffuse and rough-surface scattering, detailed furniture scattering, human blockage, higher-order interactions, anisotropic media, and complete mutual coupling are not common to all three formulations and are represented only in those parts of the thesis where they are explicitly modelled. Their omission limits the scope of the corresponding results, but does not make the electromagnetic relations used within the relevant formulation mutually inconsistent.

1.3 Objectives of the Thesis

As established in Section 1.1, there is a need for a computationally tractable framework that can analyse polarised and RIS-assisted indoor wireless propagation within the scope of physical consistency defined in Section 1.2. The overarching aim of this thesis is therefore to establish such a framework by connecting electromagnetic interactions with path, channel, and system-level performance. Achieving this aim requires the consistent modelling of polarised propagation through multilayer materials, the establishment of a traceable relationship between building material properties and communication performance, and the representation of finite RIS surfaces under coherent multipath illumination.

To achieve this overarching aim, the thesis pursues the following three objectives:

1. **To develop a three-dimensional polarisation-aware ray-tracing formulation** for propagation through finite-thickness, frequency-dependent multilayer materials, while

consistently representing the vector electric field, local TE and TM basis transformations, propagation phase, and material loss.

2. **To establish and evaluate a BWP optimisation framework** that connects the permittivity, conductivity, and thickness of multilayer materials to the coherent polarised channel response and the ABEP of the considered communication system.

3. **To develop an RIS macromodel for finite surfaces under coherent multipath illumination** that couples the incident field obtained from ray tracing to an incidence- and load-dependent electromagnetic or circuit response, while representing polarisation, propagation phase, finite-aperture effects, and the relevant modal components.

1.4 Contributions

This thesis makes three core contributions. First, it develops a physically consistent polarisation-aware ray-tracing framework to address limitations in tracking the amplitude, phase, and polarisation of the electric field along each propagation path, in transforming the field components between successive local polarisation bases, and in modelling propagation through multilayer building materials. Second, building on this framework, this thesis establishes a PolarSK performance analysis and BWP material optimisation framework that links multilayer wall parameters to the coherent polarisation-resolved channel response and ABEP. Third, as a complementary extension of the indoor ray-tracing framework, this thesis develops a multipath-aware RIS macromodelling framework that couples incident fields obtained from ray tracing to a surface response dependent on the incidence conditions and varactor diode bias state, enabling finite-aperture RIS reradiation to be represented within indoor ray tracing. These contributions are detailed as follows:

1. **A physically consistent polarisation-aware ray-tracing framework for indoor propagation through multilayer building materials is developed.** The framework preserves the complex vector nature of the electric field, consistently represents transformations between local TE and TM bases, and retains propagation and interaction

phases along each path included in the model. The polarisation-aware ray-tracing framework incorporates complex reflection and transmission coefficients for finite-thickness, frequency-dependent multilayer building materials and determines the physical direction of phase propagation in lossy double-positive media separately from the associated complex refraction angle. The resulting path contributions are combined coherently to provide polarisation-resolved predictions of received power and XPR for paths.

2. **A PolarSK performance analysis and BWP material optimisation framework based on polarisation-aware ray tracing is established and evaluated.** Building on the ray-tracing framework, this contribution traces the effects of the permittivity, conductivity, and thickness of multilayer wall materials through the coherent channel response for different polarisation components to the resulting PolarSK ABEP. The analysis identifies ABEP floors at a high signal-to-noise ratio (SNR) in the evaluated reflected NLOS scenarios and relates them to polarisation-power imbalance, coherent small-scale fading, and Brewster angle behaviour. A BWP optimisation method is then developed to jointly optimise the permittivity, conductivity, and thickness of the multilayer wall materials by minimising $ABEP_{\mathrm{avg}}$. Within the investigated scenarios and optimisation constraints, the optimised material configurations reduce ABEP by several orders of magnitude and suppress the ABEP floors observed in the simulations. These findings provide scenario-specific evidence that PolarSK performance is sensitive to the electromagnetic properties and thicknesses of multilayer wall materials.

3. **A multipath-aware RIS macromodelling framework is developed and integrated with indoor ray tracing.** As a complementary extension of the indoor ray-tracing framework, the RIS macromodel couples the coherent multipath incident field obtained from ray tracing to a response that depends on the incidence conditions and varactor diode bias state. The incidence- and bias-dependent RIS unit-cell response is represented using a unit-cell multiport impedance matrix and Floquet–Bloch reflection matrices. PO and diffraction grating relations are used to represent finite-aperture

reradiation, polarisation, propagation phase, retained modal components, and parasitic scattering. The macromodel is implemented in the Ranplan platform and compared with measurements in one small meeting room under inactive and configured RIS states, with the limitations of the available measurement data stated explicitly. A multipath-aware phase-synthesis method is also developed and evaluated under simultaneous multipath illumination.

1.5 Structure of the Thesis

This thesis is organised as follows.

Chapter 2 establishes the theoretical background and identifies the research gaps addressed in the subsequent chapters. It first reviews stochastic and deterministic approaches to indoor propagation modelling, with particular emphasis on the suitability of ray-based methods for site-specific analysis. It then examines ray-based polarisation modelling, including the principal depolarisation mechanisms and the limitations of existing frameworks. Finally, this chapter reviews electromagnetic modelling approaches for RISs, compares ray-based and wave optics perspectives, and evaluates representative academic and commercial ray-based simulators.

Building on the research gaps identified in Chapter 2, Chapter 3 develops the proposed physically consistent ray-based model for polarised indoor channels. The formulation represents multilayer material interactions, transformations between successive local polarisation bases, and the coherent combination of path contributions. It is then used to evaluate path-resolved received power and XPR in a controlled indoor geometry. The resulting polarisation-resolved propagation model provides the foundation for the system-level analysis presented in Chapter 4.

Using the propagation model developed in Chapter 3, Chapter 4 investigates PolarSK performance and introduces the BWP material optimisation framework. The analysis traces the effects of multilayer wall permittivity, conductivity, and thickness through the polarised channel response to ABEP. A coordinatewise optimisation procedure is then applied to minimise ABEP by adjusting the material parameters. This chapter presents analytical and numerical evidence for the investigated scenarios, while recognising that the material optimisation results are not directly validated through measurements.

As a complementary extension of the indoor ray-tracing framework, Chapter 5 develops a circuit-based RIS macromodel for integration with deterministic ray tracing. This chapter first evaluates the unit-cell response through comparison with full-wave simulation and then assesses room-level channel predictions against indoor measurements, thereby distinguishing the evidence available at the two validation levels. The circuit-based RIS formulation is subsequently extended to account for coherent multipath illumination, the dependence of the unit-cell response on the incidence conditions, reradiation from a finite RIS aperture, and phase synthesis subject to hardware constraints. The circuit-based RIS formulation also distinguishes local diagonal control from beyond-diagonal control with nonlocal coupling and specifies the passivity, stability, and hardware-feasibility conditions required by the beyond-diagonal RIS architecture.

Finally, Chapter 6 summarises the principal findings and conclusions of the thesis, discusses the limitations of the developed methods, and outlines directions for future research.

Chapter 2

State of the Art and Research Challenges

Overview

This chapter provides a critical review of indoor propagation modelling and identifies the research gaps that motivate the subsequent chapters. It first distinguishes stochastic models from deterministic models and evaluates the suitability of ray-based methods for site-specific analysis. It then examines ray-based polarisation modelling, focusing on the principal depolarisation mechanisms, the metrics used to quantify polarisation coupling, and the limitations of existing methods in consistently tracking vector electric fields through multilayer building materials. The discussion subsequently turns to the electromagnetic modelling of RISs, comparing ray optical and wave optical descriptions with respect to physical consistency, passivity, and power balance. Representative academic and commercial ray-based simulators are then assessed in terms of geometry handling, frequency-dependent material modelling, supported propagation mechanisms, and computational acceleration strategies. Finally, this chapter brings these strands together and identifies two connected challenges: physically consistent polarisation tracking through multilayer building materials and scalable multipath-aware modelling of finite-aperture RIS reradiation. These challenges provide the motivation for the modelling methods developed in the subsequent chapters.

2.1 Indoor Propagation Modelling

Indoor wireless channels are typically described by two main classes of models: deterministic models and stochastic models [10].

Stochastic models infer distributions or parametric relationships from channel measurements. They describe quantities such as angle of arrival (AoA), delay spread, received signal strength (RSS), phase, and cross-polarisation discrimination (XPD) statistically rather than deterministically reconstructing the exact physical propagation paths for a particular link [11, 12, 22, 23]. Their validity therefore depends on how closely the target deployment resembles the environments, frequency bands, antenna configurations, and sampling procedures represented by the calibration data [7, 10].

Deterministic models, by contrast, calculate the field or channel response for a specified transmitter–receiver link from an explicit representation of the propagation environment. Depending on the adopted approximation and the propagation mechanisms included in the model, they may account for reflection, transmission, diffraction, and scattering from objects and surfaces in the environment [24, 25]. Their prediction accuracy depends jointly on the electromagnetic formulation and on the fidelity of the input geometry, material parameters, antenna radiation patterns, selected interaction mechanisms, and numerical settings. Increasing the level of geometric detail alone does not therefore guarantee a more accurate prediction [7, 24–26].

Thus, stochastic models characterise an ensemble of channels within their domain of validity, whereas deterministic models predict a specified scenario subject to the assumptions and resolution of the selected electromagnetic approximation.

2.1.1 Stochastic models

The applicability of an indoor stochastic model depends on the structural and material characteristics captured in the measurement data used for its calibration. Environments classified as residential or office settings can differ substantially across geographical regions because of variations in building materials, wall construction, and layout practices [27–29].

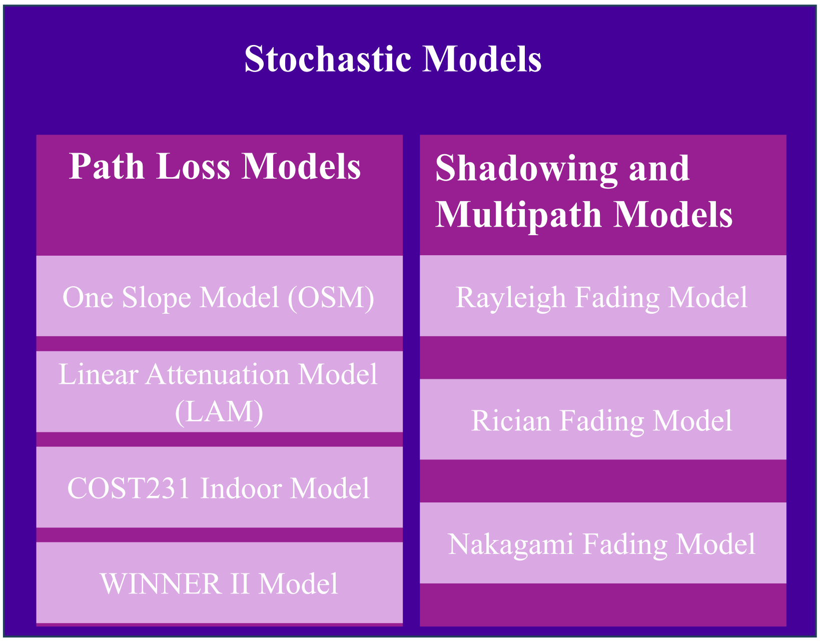

Fig. 2.1 Classification of stochastic channel models.

For example, residential partitions may be constructed from concrete, brick, or plasterboard with different thicknesses and material compositions [8], whereas office environments may range from open plan areas with movable partitions to enclosed office layouts with fixed walls [8, 30, 31]. These characteristics should be reported explicitly because they affect both model calibration and the interpretation of comparisons across studies. Fig. 2.1 classifies the stochastic models considered in this chapter into path loss models and models of shadowing and multipath fading.

Path loss models

In this subsection, several representative path loss models are discussed to illustrate their applicability under different propagation conditions.

1. **One Slope Model (OSM):** The OSM, also referred to as the simplified log distance path loss model, represents the large-scale average received power as a logarithmic function of the transmitter–receiver separation [7]:

$$P_r(d) = P_0 - 10n\log_{10}\left(\frac{d}{d_0}\right), \qquad d \geq d_0, \tag{2.1}$$

where $P_r(d)$ is the average received power at distance d, $P_0 = P_r(d_0)$ is the corresponding received power at the reference distance, and both quantities are expressed in dBm. In this thesis, $d_0 = 1$ m, while n is the dimensionless path loss exponent. The ratio d/d_0 is dimensionless, as required for the logarithmic term. The fitted value of n depends on the propagation environment, operating frequency, antenna configuration, and line-of-sight (LOS) or NLOS condition [7]. This basic form represents the distance-dependent mean trend and does not explicitly include random shadowing or small-scale fading.

2. **Linear Attenuation Model (LAM):** The LAM represents the total path loss as the sum of the free-space path loss and an additional attenuation term that increases linearly with propagation distance [7, 32]:

$$L(d) = L_{\mathrm{FS}}(d) + \alpha d, \tag{2.2}$$

where $L(d)$ is the total path loss in dB, $L_{\mathrm{FS}}(d)$ is the free-space path loss at distance d, d is expressed in metres, and α is the linear attenuation coefficient in dB/m. The coefficient α is generally obtained by fitting the model to measurement or simulation data and depends on the operating frequency and the characteristics of the propagation environment.

3. **European Cooperation in Science and Technology (COST) 231 Multiwall Model (MWM):** The MWM represents the total path loss as the sum of free-space loss, a constant correction term, wall penetration losses, and a nonlinear floor penetration loss [7, 33]:

$$L = L_{\mathrm{FS}} + L_{\mathrm{C}} + \sum_{i=1}^{I} N_{w_i} L_{w_i} + n_f^{\left[\frac{n_f+2}{n_f+1} - b\right]} L_f. \tag{2.3}$$

Here, L, L_{FS}, L_{C}, L_{w_i}, and L_f are expressed in dB. The term L_{FS} denotes the free-space path loss between the transmitter and receiver, while L_{C} is an empirical constant correction term estimated by fitting the model to measured path loss data. The parameter N_{w_i} denotes the number of walls of type i intersected by the direct geometrical path between the transmitter and receiver. L_{w_i} is the corresponding wall penetration loss coefficient, and I is the number of wall types considered. The parameter n_f denotes the number of penetrated floors, while L_f is the loss coefficient between adjacent floors. The parameters L_{w_i} and L_f are empirical coefficients fitted to measured path loss data and therefore represent effective wall and floor losses within the calibrated environment, rather than isolated physical penetration losses of individual structures. The dimensionless empirical parameter b controls the nonlinear dependence of the total floor attenuation on n_f. For fixed wall loss coefficients, the wall attenuation increases linearly with the number of penetrated walls of each type, whereas the total floor attenuation varies nonlinearly with the number of penetrated floors [7, 33].

4. **Wireless World Initiative New Radio (WINNER) II Path Loss Model for the A1 Indoor Office Scenario:** For the A1 indoor office scenario, the WINNER II channel model represents the mean path loss using a logarithmic function of the transmitter–receiver separation and carrier frequency, with coefficients selected according to the propagation condition [34]:

$$PL(d, f_c) = A \log_{10}\left(\frac{d}{1\ \text{m}}\right) + B + C \log_{10}\left(\frac{f_c}{5\ \text{GHz}}\right) + X. \tag{2.4}$$

Here, $PL(d, f_c)$ denotes the path loss in dB predicted by the WINNER II model, d is the transmitter–receiver separation in metres, and f_c is the carrier frequency in GHz. The coefficient A determines the slope of the path loss with respect to the logarithm of the transmitter–receiver separation, B is the intercept, and C describes the frequency dependence. The term X is an optional environment specific correction term. Under the A1 NLOS conditions, it represents additional wall attenuation, whose value depends on the number and type of walls between the transmitter and receiver. The specific values of A, B, C, and X depend on the relevant LOS or NLOS condition.

The WINNER II path loss models are based mainly on measurements at 2 and 5 GHz and are extended to the frequency range from 2 to 6 GHz [34]. When the transmitter and receiver are located on different floors, the total path loss is obtained by adding a floor loss:

$$PL_{\text{total}} = PL(d, f_c) + L_{\text{floor}}, \tag{2.5}$$

where

$$L_{\text{floor}} = 17 + 4(n_f - 1), \qquad n_f > 0. \tag{2.6}$$

The quantity L_{floor} is expressed in dB, and n_f denotes the floor separation between the transmitter and receiver, with $n_f = 1$ corresponding to adjacent floors. The coefficients and correction terms should be selected using the parameter set and validity range specified for the relevant WINNER II propagation condition [34].

Shadowing and Multipath Models

Indoor channel variations are commonly separated into large-scale shadowing and small-scale multipath fading. Shadowing describes relatively slow variations in the local mean received power caused by obstruction from walls, furniture, and other large structures. Multipath fading arises from the coherent superposition of propagation components that arrive through different paths with different amplitudes, delays, phases, and angles.

Early investigations of indoor propagation developed statistical models to characterise these effects [35]. The received signal was represented as the superposition of multiple delayed and attenuated components produced by reflection, transmission, diffraction, and scattering within the environment. Because the number and characteristics of these components vary with position and surrounding structures, the resulting channel response was treated as a random process whose statistical properties depend on the propagation environment [36]. These studies established the basis for the stochastic representation of indoor shadowing and multipath propagation.

Building on this foundation, small-scale fading models were introduced to describe the rapid fluctuations in received signal amplitude and phase caused by constructive and destructive interference among multipath components. The statistical distribution of the signal envelope depends particularly on whether a dominant propagation component is present and on the relative strengths and distributions of the remaining multipath components.

These considerations motivate the Rayleigh, Rician, and other statistical fading models discussed below.

- **Rayleigh Fading Model:** The Rayleigh fading model is commonly used when the received signal contains no dominant deterministic propagation component and is formed by the superposition of many weak multipath components with approximately independent random phases. Such conditions are often associated with rich scattering NLOS environments, although the absence of LOS alone does not guarantee Rayleigh fading. Under the usual central limit conditions, the in phase and quadrature components of the complex baseband fading coefficient can be approximated as independent Gaussian random variables with equal variance and zero mean. Consequently, the magnitude of the fading coefficient follows a Rayleigh distribution, while its phase is uniformly distributed over 0 to 2π radians [11].

- **Rician Fading Model:** The Rician fading model is commonly used when the received signal contains a dominant deterministic propagation component, such as a LOS path or a strong specular reflection, together with multiple weaker diffuse multipath components. The complex baseband fading coefficient can therefore be represented as the sum of a deterministic component and a complex Gaussian component with zero mean associated with diffuse multipath propagation. The Rician K-factor is defined as the ratio of the average power in the dominant deterministic component to the aggregate average power in the diffuse multipath components. A larger K-factor therefore indicates that the dominant component contributes a greater proportion of the received signal power. In contrast to Rayleigh fading, which assumes that no deterministic propagation component has significant power, Rician fading accounts explicitly for the presence of a dominant component with appreciable power. Consequently, the magnitude of the complex baseband fading coefficient follows a Rician distribution [37].

- **Nakagami-*m* Fading Model:** The Nakagami-*m* fading model is a flexible statistical model used to characterise the envelope fluctuations caused by small-scale multipath fading. The model is parameterised by the shape parameter m and the average envelope power Ω, where $\Omega = \mathbb{E}[R^2]$ and R denotes the fading envelope. The parameter m controls the severity of fading. When $m = 1$, the Nakagami-m distribution reduces to the Rayleigh distribution. Values satisfying $1/2 \leq m < 1$ represent fading more severe than Rayleigh fading, whereas $m > 1$ represents less severe fading. For suitable parameter values, the Nakagami-m distribution can also approximate certain Rician fading conditions, although the two distributions are not identical. Owing to its flexibility and analytical tractability, the Nakagami-m model has been used to characterise a broad range of multipath fading conditions and to analyse the performance of wireless communication systems [38].

2.1.2 Deterministic Models

Deterministic channel models calculate site-specific electromagnetic fields or channel responses for a prescribed propagation environment. In principle, a full-wave solution of Maxwell's equations provides the reference electromagnetic description once the geometry, source excitation, material constitutive properties, and boundary conditions have been specified. For electrically large indoor environments, however, the fine spatial discretisation required by full-wave methods, together with temporal discretisation in time domain formulations, can make direct simulation computationally prohibitive, particularly when large simulation domains, dense receiver grids, or repeated parameter sweeps are considered [39]. The deterministic methods considered in Fig. 2.2 therefore include both full-wave techniques and high frequency ray-based approximations, which offer different tradeoffs among electromagnetic fidelity, computational tractability, and modelling complexity.

Full-Wave Methods

Full-wave methods require a geometrical representation of the environment, source excitation, material constitutive parameters, boundary conditions, and an appropriate numerical discretisation capable of resolving the shortest relevant wavelength, material variation, and geometrical features. Representative full-wave methods include the method of moments

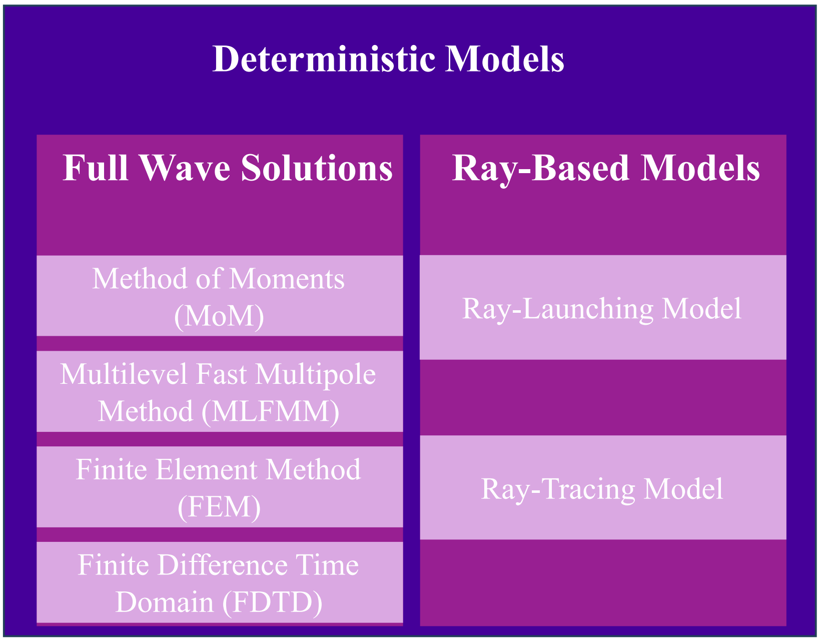

Fig. 2.2 Classification of deterministic channel models.

(MoM) [40], often accelerated using the multilevel fast multipole method (MLFMM) [41], the finite-element method (FEM) [42], and the FDTD method [43].

Full-wave techniques can provide high electromagnetic fidelity when the geometry, material properties, boundary conditions, and numerical discretisation are represented with sufficient accuracy. Their computational cost, however, increases substantially when they are applied to electrically large indoor environments. High frequency asymptotic methods provide an alternative by approximating electromagnetic propagation under the assumption that the wavelength is small relative to the characteristic dimensions of the environment. When their underlying assumptions are satisfied, these methods can retain the dominant propagation mechanisms while substantially reducing the computational cost.

Ray-Based Models

Ray-based propagation modelling provides a computationally tractable framework for predicting site-specific wireless channel behaviour in electrically large indoor and outdoor environments [44]. These methods are commonly based on GO and the uniform theory of diffraction (UTD), under which electromagnetic propagation is represented by rays according

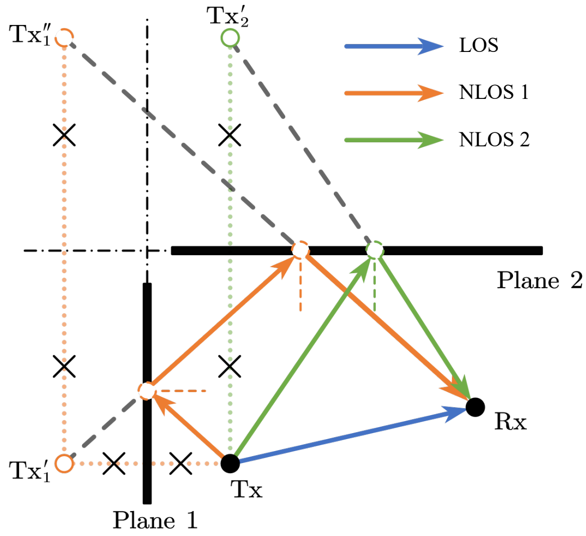

Fig. 2.3 Illustration of image-based ray tracing for LOS and reflected NLOS paths.

to high-frequency asymptotic assumptions. Depending on the propagation mechanisms included in the model, the rays may undergo reflection, transmission, and diffraction at environmental interfaces and edges, while diffuse scattering can be incorporated through additional scattering models. In coherent ray-based models, the complex field at the receiver is obtained by superposing the contributions from the identified multipath components, including their amplitudes, phases, delays, and polarisation states [45].

Ray-based models are commonly implemented using image-based ray tracing or ray-launching techniques.

1. **Image-based ray tracing:** The image-based ray-tracing method constructs virtual images of the transmitter through successive specular reflections across the corresponding reflecting planes. Candidate propagation paths are then traced back from the receiver towards the associated transmitter images. A candidate path is retained only if the reconstructed reflection points lie on the corresponding finite surfaces and all physical path segments are unobstructed [7, 44–47].

   As illustrated in Fig. 2.3, the coloured solid arrows represent the physical LOS and reflected NLOS propagation paths. The dashed and dotted lines extending towards the virtual transmitter images are auxiliary geometrical construction lines used to

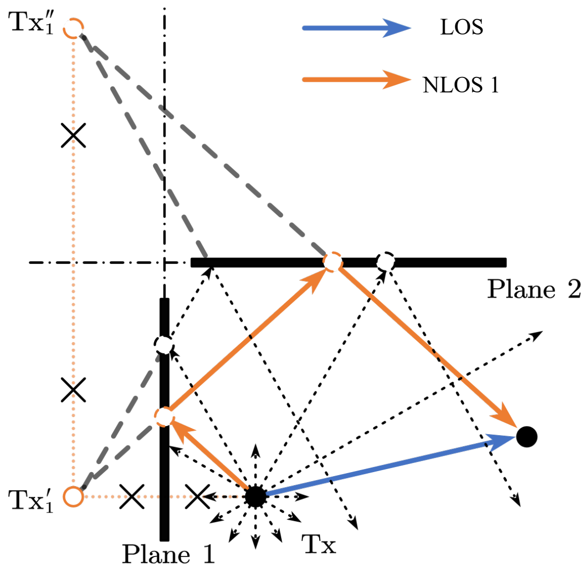

Fig. 2.4 Illustration of the ray-launching method for LOS and reflected NLOS paths.

determine the specular reflection points. The black crosses mark portions of this auxiliary geometrical construction that do not correspond to physical ray propagation.

2. **Ray launching:** In contrast to image-based ray tracing, the ray-launching method, also referred to as the shooting and bouncing ray (SBR) method, launches a discrete set of rays from the transmitter over the required angular domain and traces their trajectories through successive interactions with the environment. In three-dimensional implementations, approximately uniform angular sampling can be achieved using a tessellated geodesic sphere. Each ray is traced until a prescribed termination condition, such as a maximum interaction order, propagation distance, or power threshold, is satisfied. A ray entering a reception region centred on the receiver is identified as a received ray. The angular sampling interval therefore determines a tradeoff between spatial resolution and computational cost [7, 44, 45, 48].

   As illustrated in Fig. 2.4, the black dotted arrows represent rays launched from the transmitter in discrete directions, while the coloured solid arrows represent the LOS and reflected NLOS propagation paths that reach the receiver. The virtual transmitter images and their associated dashed and dotted construction lines are included only to illustrate the geometrical correspondence between the received reflected path and the equivalent image source construction. They do not form part of the ray-launching search procedure. The black crosses mark portions of this auxiliary geometrical construction that do not correspond to physical ray propagation.

Although ray-based models can provide useful site-specific predictions at substantially lower computational cost than direct full-wave simulation, their computational burden can still increase rapidly in electrically large or geometrically complex environments. As the maximum interaction order increases, the number of candidate interaction sequences in image-based methods can grow combinatorially, often resulting in exponential growth in computational complexity. The resulting computational cost is particularly significant for large propagation domains, dense receiver grids, and models that include multiple reflections, transmissions, diffractions, or diffuse scattering interactions.

A range of acceleration techniques has therefore been developed to reduce redundant path searches and intersection checks between rays and environmental objects. For example, intelligent ray tracing (IRT) [49] and intelligent ray launching (IRL) [50, 51] use environment specific visibility and spatial information to restrict the search to propagation paths that are more likely to contribute to the received field. Other acceleration techniques employ visibility graphs, spatial partitioning, bounding volumes, or parallel processing to reduce the computational effort without changing the underlying propagation formulation.

Separate from computational acceleration, electromagnetic extensions have been introduced to broaden the range of propagation phenomena represented by ray-based models. Diffraction is commonly incorporated into high-frequency ray formulations using UTD [52]. Hybrid approaches can additionally couple ray tracing with PO to model scattering from apertures or finite surfaces, or with numerical methods such as the FDTD method to obtain a more detailed field description within selected regions [45, 53].

Algorithmic extensions have also been developed to improve the spatial resolution and geometrical accuracy of ray-launching methods. Ray jumping with resolution awareness maintains a more nearly uniform spatial resolution as the rays propagate away from the transmitter. By contrast, SBR image methods use ray launching to identify likely interaction sequences and subsequently apply the image method to refine the corresponding interaction points [45, 54].

Overall, these acceleration techniques, electromagnetic extensions, and algorithmic refinements enable ray-based models to offer a practical tradeoff between electromagnetic fidelity and computational tractability for site-specific channel analysis, coverage prediction, and system-level performance evaluation. Their predictive accuracy, however, depends on the fidelity of the environmental geometry and material parameters, the propagation mechanisms included in the model, the angular and spatial resolution, the retained interaction order, and the selected path termination criteria.

2.2 Indoor Ray-Based Polarisation Propagation Models

Polarisation is one of the fundamental characteristics of an electromagnetic wave, alongside its amplitude, frequency, and phase [13]. It has been exploited in optical fibre, radar, satellite, and indoor wireless communication systems. In wireless links, the use of multiple polarisation states can provide additional signalling degrees of freedom (DoF) and, when the resulting polarisation channels are sufficiently distinct, can improve spectral efficiency and channel capacity [13].

Although the ray-based models discussed in Section 2.1.2 are widely used for site-specific indoor channel analysis, purely scalar implementations cannot fully represent the evolution of polarisation along a propagation path. Representing each path solely by scalar quantities such as loss, delay, or received power does not capture the rotation of the electric-field vector, transformations between successive local TE and TM bases, co-polarised and cross-polarised coupling, or polarisation-dependent amplitude and phase changes caused by multilayer material interactions. Consequently, the analysis of dual-polarised antennas and polarisation-based signalling requires a vector formulation that tracks the complex electric field, the transmit and receive antenna responses, and the ordered basis transformations introduced by successive propagation interactions.

To represent these effects in indoor wireless channels, polarisation-aware channel models have been developed using both physical and analytical approaches. Physical models describe polarisation by relating the antenna responses and field components to specific propagation mechanisms and environmental interactions, whereas analytical models represent the polarisation channel through parameterised mathematical or statistical relationships. Within the physical category, ray-based models explicitly track the changes in the complex electric field introduced by reflections, transmissions, diffractions, and changes in the local polarisation basis.

An early example is a three-dimensional indoor ray-tracing model that incorporates polarisation into the propagation simulation [55]. The model permits arbitrary three-dimensional antenna orientations and combines the antenna polarisation responses with vector descriptions of reflected and diffracted fields. The three-dimensional polarisation-aware indoor ray-tracing model in [55] can therefore be used to examine how antenna orientation and propagation interactions affect the polarisation characteristics of the predicted indoor channel response.

While the three-dimensional polarisation-aware ray-tracing model in [55] accounts for the polarisation effects associated with reflection and diffraction, additional modelling is required to represent nonspecular scattering from rough or irregular surfaces. Other studies therefore extended polarisation-aware ray-based modelling to include diffuse scattering. In particular, a polarimetric version of the ER diffuse scattering model was calibrated using measurements conducted in office and laboratory environments [56]. Within the calibrated scenarios, the model characterises nonspecular scattering in both co-polarised and cross-polarised-field components.

In addition to diffuse scattering, transmission through building partitions can introduce further polarisation changes when the transmitter and receiver are separated by one or more walls. Two heuristic depolarisation models for fields transmitted through partitions were implemented in a ray-tracing tool in [57]. Including depolarisation induced by transmission improved agreement with the reported measurements. However, residual errors in the predicted cross-polarisation levels suggested that additional depolarising mechanisms or modelling uncertainties were not fully represented.

To represent multiple depolarising mechanisms within a unified framework that uses ray methods, an enhanced ray-tracing tool based on UTD was developed by incorporating both transmission through partitions and diffuse scattering models [58]. The tool was evaluated against data from two indoor measurement campaigns and showed improved agreement with measurements for wideband and polarimetric channel metrics, including delay spread and XPR.

Overall, these studies demonstrate the importance of incorporating reflection, partition transmission, and diffuse scattering into polarimetric ray-based models for indoor propagation analysis. Accounting for these mechanisms is particularly important for links within indoor environments and from outdoor to indoor environments, where the received field may undergo multiple interactions with walls and other environmental surfaces before reaching the receiver. However, the accuracy of such models depends on how consistently the vector electric field, local polarisation bases, and material interactions are represented along each propagation path.

2.3 Depolarisation Effects Modelling of Polarised Wireless Channel

With the growing demand for indoor wireless connectivity, modulation based on polarisation has attracted attention as a means of using the polarisation domain for information transmission. Unlike conventional schemes based on phase and quadrature, which represent symbols as points in a two-dimensional plane defined by the in phase and quadrature components, polarisation modulation uses the carrier polarisation state as an additional domain for carrying information. This approach can provide additional signalling DoF, provided that the polarisation states remain sufficiently distinguishable after propagation.

Studies in [59, 60] reported that, under the evaluated system assumptions, polarisation modulation reduced the energy required to transmit each bit by up to approximately 25%

relative to M-ary phase-shift keying (MPSK) at a target symbol error rate of 10^{-6}. This potential reduction in transmission energy is attractive for wireless devices with limited energy resources and large-scale indoor networks.

Accurate recovery of the transmitted polarisation state requires a channel model that resolves the polarisation transformations and coupling introduced by propagation and by the transmit and receive antenna responses. Modelling these effects is therefore necessary for the reliable evaluation of modulation based on polarisation in indoor wireless channels.

The polarisation characteristics of a dual-polarised channel can be quantified using metrics that describe power imbalance, correlation, cross-polarisation coupling, differential attenuation, and differential delay. Two important aspects are the power imbalance between the polarisation channels and the correlation between their complex responses. The co-polarisation ratio (CPR) compares the powers of the two co-polarised branches of the channel, whereas XPR compares the co-polarised and cross-polarised received powers for a specified transmitted polarisation. XPD characterises the discrimination between the desired polarisation component and its orthogonal component, although the precise distinction between XPD and XPR varies across the literature. Their definitions should therefore be stated explicitly for the channel and antenna configuration under consideration. Polarisation-dependent loss (PDL) describes the difference in attenuation experienced by different polarisation states, whereas polarisation mode dispersion (PMD) describes the difference in propagation delay or group delay between the principal polarisation states. These quantities describe related but distinct properties and should not be used interchangeably. Moreover, a single constant XPR value may not capture the variations caused by path geometry, interaction angle, material properties, and antenna orientation, which are relevant to site-specific PolarSK and depolarisation analysis [13].

Measurement-based studies have reported XPD, polarisation correlation, and related channel characteristics in a range of indoor and outdoor environments [61]. Empirical models incorporating depolarisation parameters were subsequently developed from measured channel statistics [62, 63]. Other studies introduced analytical and geometry-based formulations that relate polarisation metrics to the angular and spatial characteristics of the propagation environment [64, 65]. For example, [65] used the von Mises–Fisher distribution to derive expressions for XPD and polarisation correlation, while [66] proposed and validated an analytical expression for XPD that accounts for channel and receiver conditions. Correlation in three-dimensional dual-polarised channels was examined in [67]. Analytical relationships for electromagnetic vector sensors and environments with uniform angular spread were presented in [68] and [69], respectively. An extended analytical channel model for evaluating correlation and XPD in closed-form was presented in [70]. These studies provide useful statistical and analytical descriptions of polarisation behaviour, but they do not necessarily resolve the ordered evolution of the complex vector electric field along individual propagation paths.

Overall, prior work has established physical, empirical, and analytical descriptions of several polarisation effects. The reviewed literature places greater emphasis on polarisation-power imbalance and correlation than on PMD and PDL in indoor ray-based models. A remaining gap is the lack of a unified treatment that tracks the complex TE and TM field components through successive material interfaces while also accounting for transformations between the local polarisation bases associated with successive propagation interactions. Because each material layer may have distinct permittivity, conductivity, permeability, and thickness, the reflected and transmitted field components can undergo different changes in amplitude and phase at each interface. The framework developed in Chapter 3 addresses this specific gap for the propagation mechanisms and material configurations included in the formulation. Diffuse scattering, surface roughness, and dynamic environmental interactions remain outside the scope of the current model and its validation.

2.4 Propagation Modelling for RIS

Sections 2.2 and 2.3 establish the need for accurate prediction of polarised indoor channels. A channel model characterises the propagation link but does not itself modify the electromagnetic environment. When the direct path is attenuated or obstructed, an RIS may be introduced to redirect part of the incident field towards a target region. The channel model predicts the multipath field incident on the RIS, whereas the RIS surface model determines the field scattered by the configured surface.

RISs have emerged as a candidate technology for controlling wireless propagation using electrically reconfigurable, nominally passive, and low profile surfaces. Their performance should be evaluated using a model that relates the relevant incident-field components to the desired and parasitic scattered fields, together with any transmitted or dissipated power permitted by the surface architecture and its operating state [16].

RIS models can be broadly described using formulations based on ray optics or wave optics. A model based on ray optics represents the incident field using geometrical propagation paths and assigns each path a propagation phase and an interaction coefficient. This representation is computationally tractable for room-scale simulations and can predict a desired anomalous-reflection direction when the RIS aperture is electrically large and the assumptions of high-frequency propagation are satisfied. However, a ray optics model based only on a prescribed phase response does not by itself determine the local normal power flow, diffraction from a finite-aperture, coupling between amplitude and phase, or the excitation of parasitic modes. Consequently, prescribing a phase gradient alone does not generally guarantee local power balance or passivity for an arbitrary field transformation [71–73].

In contrast, a formulation based on wave optics retains the electric and magnetic-field distributions over the surface and applies electromagnetic boundary conditions or field equivalence relations. The time average of the Poynting vector can then be used to evaluate power balance, while an aperture integral can be used to predict the field reradiated by the finite-aperture. Depending on the adopted formulation, this description can represent coupling between amplitude and phase, polarisation conversion, dissipation, parasitic scattering, and power transport across the surface [17, 71, 73]. In this thesis, ray tracing provides the coherent multipath field incident on the RIS, whereas the RIS macromodel uses an aperture formulation expressed in terms of the field to combine the incident path contributions and predict the resulting reradiated field.

Within the scope defined in Chapter 5, physical consistency in RIS modelling requires the surface response to relate the incident electromagnetic field to the reradiated field and dissipated power while satisfying passive power balance within the adopted approximation. Depending on the surface architecture and the adopted formulation, the model may also need to represent finite-aperture effects, polarisation conversion, parasitic scattering, and the supported reradiation modes.

Evaluating links assisted by an RIS therefore requires a macroscopic surface model whose computational complexity is compatible with room-scale ray tracing while retaining the field quantities and power constraints required for coherent reradiation under multipath illumination. Simplified ray models are computationally attractive, but they may omit finite-aperture diffraction, modal reradiation, parasitic scattering, and polarisation conversion. By contrast, simulation-based on a direct full-wave formulation can represent these effects with greater electromagnetic detail, but is often too costly for repeated room-scale channel studies. This gap motivates the RIS macromodel developed and evaluated in Chapter 5, which provides an intermediate representation suitable for integration with indoor ray tracing.

2.5 Commercial and Publicly Available Indoor Ray-Based Simulators

Advances in ray-based models, together with the growing demand for computationally efficient indoor channel prediction, have led to the development of numerous academic and commercial simulation platforms for radio propagation analysis and wireless network planning. These tools represent the interaction of radio waves with three-dimensional environments through reflection, transmission, and diffraction. Some implementations also include diffuse scattering. Depending on their implementation, they can predict channel quantities such as received power, path loss, propagation delay, and delay spread [7, 74].

The predictive accuracy of these platforms depends on the fidelity of the environmental geometry and material parameters, the antenna descriptions, the propagation mechanisms included in the model, and the selected spatial, angular, and numerical settings. Academic simulators are commonly used to investigate and evaluate new modelling methods, whereas commercial platforms generally provide integrated workflows for practical coverage analysis and network planning. The following discussion compares selected representative tools in terms of their modelling approaches, supported propagation mechanisms, material and antenna treatment, computational features, validation, and typical applications.

2.5.1 Sionna RT

Sionna is an open source Python library developed by NVIDIA for research on communication systems. Sionna RT is the standalone radio propagation package within the Sionna ecosystem. It is built on Mitsuba 3 and Dr.Jit, which provide scene handling, hardware acceleration, and automatic differentiation. This differentiable formulation enables gradients of channel responses, radio maps, and derived objective functions to be evaluated with respect to supported scene and system parameters. These parameters include radio material properties, antenna and scattering patterns, array geometries, and the positions and orientations of radio devices and scene objects [75–77].

The propagation mechanisms available in Sionna RT depend on the software version and solver configuration. Current releases support LOS propagation, specular reflection, diffuse reflection, refraction through material slabs, and diffraction. For the computation of channel impulse responses, the path solver combines the SBR method with the image method. The SBR stage identifies candidate interaction sequences, while the image method refines the corresponding interaction points. By contrast, radio maps are generated using an SBR procedure. The resulting propagation paths can be represented as channel impulse responses and transformed into channel frequency responses or discrete channel taps. Radio maps can provide quantities such as path gain, RSS, and signal-to-interference-plus-noise ratio (SINR) over a specified measurement surface in the three-dimensional scene [76, 77].

Scene geometry can be loaded using the Mitsuba Extensible Markup Language (XML) format or prepared using Blender and related scene creation tools. Each scene object can be assigned a radio material defined by properties such as relative permittivity, conductivity, thickness, and diffuse scattering parameters. The reflection and refraction coefficients account for the finite-thickness of the material slab, while frequency-dependent material properties can be implemented through predefined models or user-defined functions. Sionna

RT also supports configurable antenna and scattering patterns and permits data exchange with NumPy, JAX, TensorFlow, and PyTorch. These capabilities facilitate its integration with communication system simulation, optimisation, and machine learning workflows [77].

Several studies have extended the evaluation of Sionna RT beyond software demonstrations. A method for learning radio environments used its differentiable formulation to estimate material, scattering, and antenna parameters from synthetic data and real indoor measurements obtained with a distributed multiple input multiple output (MIMO) channel sounder [78]. In a separate industrial study, a three-dimensional model derived from laser scanning data was simulated at 187.5 GHz and compared with double directional channel measurements under dynamic blockage caused by a moving forklift [79]. These studies demonstrate the use of Sionna RT for measurement-based calibration and comparison, while also showing that prediction errors can arise from simplified geometry, omitted objects, uncertain material properties, and differences between the simulated and measured antenna responses.

Sionna RT has also been used for channel data generation and system integration. The WiSegRT dataset contains site-specific indoor channel impulse responses generated in semantically segmented three-dimensional scenes and is intended for applications including channel prediction, localisation, sensing, and wireless digital twins [80]. Its integration with Ray-Mobtime has enabled the generation of channel datasets for dynamic vehicular environments in which the positions of vehicles and other scene objects vary over time [81]. However, that study also reported substantial differences between some channels generated by Sionna RT and Wireless InSite, and therefore emphasised the need for systematic comparison with measured channels.

Further extensions have connected Sionna RT to network simulation and digital twin applications. Ns3Sionna integrates scene specific RT channels with the ns-3 network simulator to provide spatially and temporally correlated channel information for indoor and outdoor network studies [82]. The DT-RaDaR framework uses radio maps generated with Blender and Sionna RT for robot navigation in digital twin environments [83]. Sionna RT has also been used to evaluate RIS optimisation algorithms and coverage maps in urban digital twin scenarios, together with experimental comparisons [84].

Overall, Sionna RT provides an extensible platform for site-specific channel generation, radio coverage analysis, parameter estimation, data generation, and integration with higher layer simulation tools. Its open source implementation and automatic differentiation support reproducible and optimisation oriented research. Nevertheless, these features do not by themselves guarantee predictive accuracy. The results remain dependent on the fidelity of the scene geometry, the calibration and valid frequency range of the material and scattering models, the antenna descriptions, the propagation mechanisms included, the solver configuration, and the software version. The version and principal numerical settings should therefore be stated explicitly when reporting results obtained using Sionna RT.

2.5.2 CloudRT

CloudRT was introduced as an open access cloud native platform for high-performance RT of radio propagation channels. It was developed by a research team led by Beijing Jiaotong University and uses parallel and distributed computing to support computationally intensive propagation simulations. Its architecture separates the user interface and data management functions from the RT engine executed on the computing cluster. Users can provide three-dimensional environment models, antenna descriptions, and radio material parameters for the required propagation scenario [74, 85].

Depending on the adopted configuration and propagation models, CloudRT can represent direct, reflected, transmitted, diffracted, and scattered propagation components. It can generate channel information such as path loss, channel impulse response, propagation delay, direction of departure, direction of arrival, and the contributions of individual multipath components. Published surveys report that CloudRT has been calibrated or validated for railway, urban, indoor, and outdoor environments over frequencies ranging from approximately 450 MHz to 325 GHz [74, 86]. This frequency range should be interpreted as the span covered by published simulation and validation studies, rather than as a guarantee of uniform prediction accuracy for every frequency, environment, and model configuration.

CloudRT has been applied in several studies involving railway and other transport environments. For railway tunnels, CloudRT generated channel data that were used to derive tapped-delay-line models for high-speed railway and metro tunnel scenarios. The resulting models characterised tap delay, power, fading, and Doppler properties for radio technology emulation [87]. In a separate study, a three-dimensional high speed railway environment was reconstructed and imported into CloudRT to characterise terrestrial and satellite to terrestrial links at 22.6 GHz under different weather conditions [88]. These studies demonstrate the use of the platform for generating site-specific channels in railway environments with complex geometries and mobility conditions.

The platform has also been applied to enclosed environments with strong reflection. In an intra-ship study at 3.5 GHz, CloudRT was used to generate channel impulse responses and analyse propagation within metal corridors and rooms under different hatch configurations [89]. Separate path loss models were developed for LOS, light NLOS, and deep NLOS regions. The fitted models were evaluated using additional CloudRT simulation data. This study illustrates the application of CloudRT to metal rich environments, but it should not be interpreted as measurement validation unless an independent measurement campaign is also provided.

CloudRT has further been extended for the investigation of RIS-assisted railway communications. In [90], an additional RIS representation was integrated into CloudRT and evaluated in railway tunnel scenarios. The RIS formulation was an extension introduced by the authors rather than a propagation mechanism originally provided by the CloudRT platform. CloudRT supplied the surrounding multipath propagation environment, while the prediction of the RIS response depended on the additional surface model and its assumptions. This distinction is important when assessing the physical accuracy of RIS-assisted channel predictions.

Overall, CloudRT provides a high-performance environment for site-specific channel generation and large simulation campaigns. Its main strengths include parallel and distributed computation, support for shared environment and material resources, and demonstrated applications over a wide range of frequencies and propagation scenarios. Its predictive accuracy nevertheless depends on the fidelity of the environment geometry, the calibration and valid frequency range of the material and scattering models, the antenna descriptions, the propagation mechanisms included, and the numerical settings used in the simulation. Specialised components such as RISs also require additional models whose physical assumptions and validation should be stated explicitly.

2.5.3 Altair WinProp

Altair WinProp is a commercial software suite for radio propagation prediction and wireless network planning. It provides empirical, semi empirical, and deterministic propagation models for indoor, urban, rural, tunnel, and combined scenarios. The available models include the dominant-path model (DPM), standard three-dimensional RT, IRT, and the SBR method. WinProp can also be coupled with Feko, allowing antenna patterns calculated using full-wave or asymptotic electromagnetic methods to be included in propagation and network simulations [91, 92].

The supported frequency range depends on the selected propagation model and the software version. Current documentation specifies frequency ranges extending from approximately 30 MHz to 100 GHz for several deterministic models, although individual empirical models and material databases may have narrower ranges. Depending on the selected formulation, WinProp can account for direct propagation, reflection, transmission, diffraction, and diffuse scattering. The software can predict quantities including path loss, received power, LOS conditions, propagation paths, directional channel impulse responses, delay spread, and angular spread. Measurement data can also be used to calibrate many of the available propagation models [91].

WinProp includes several tools for preparing propagation scenarios. WallMan is used to construct or import three-dimensional building geometry, TuMan supports tunnel modelling, AMan prepares antenna patterns, and ProMan performs propagation prediction and network planning. Static and time-varying scenarios can be considered, and trajectories may be assigned to transmitters, receivers, or other moving objects. However, the physical detail and computational cost vary considerably among the available models. For example, the DPM reduces computation by retaining the principal propagation path, whereas the RT methods retain a larger set of multipath components and are more suitable when channel impulse responses or delay and angular spreads are required [91].

Several studies have evaluated WinProp in indoor environments. In [93], three-dimensional RT results at 2.4 GHz were compared with RSS measurements in an indoor environment. The study examined the effects of material parameters, furniture representation, antenna patterns, and time-varying objects. The results showed that many simulated values were within the reported measurement uncertainty, but also demonstrated that uncertainty in material parameters and geometrical detail can produce significant errors, particularly under NLOS conditions. WinProp has also been used to investigate the placement of wireless access points at 2.4 and 5 GHz for indoor coverage optimisation [94].

Automotive communication is another established application. A virtual drive test study combined antenna patterns calculated using Feko with the IRT model in WinProp to evaluate the received power of an antenna installed on a vehicle in an urban environment [95]. WinProp has also been used to generate millimetre wave vehicular channels and to study the effects of vehicle geometry and mobility on propagation [96]. These applications illustrate how installed antenna characteristics and site-specific propagation can be evaluated within a common workflow.

WinProp has further been applied to transport and aerial communication scenarios. A parametric railway study used RT simulations to characterise propagation for a wireless train backbone and a wireless consist network under different train geometries and antenna configurations [97]. In an outdoor millimetre wave study, WinProp was used at 30 and 60 GHz to evaluate coverage provided by unmanned aerial vehicles (UAVs) acting as relays in an integrated access and backhaul network [98]. These examples demonstrate the use of the platform beyond conventional static indoor network planning.

WinProp has also been used as a reference simulator when evaluating new propagation algorithms. In [99], RT indoor scenes generated using WinProp were compared with a new model that incorporated diffraction from smooth curved surfaces. Such comparisons are useful for evaluating computation time and differences between the propagation mechanisms represented by alternative simulators, but they do not by themselves establish measurement accuracy.

Overall, WinProp provides a broad set of propagation and network planning tools for indoor, urban, transport, and vehicular scenarios. Its integration with Feko is particularly useful when installed antenna patterns must be included in a site-specific propagation model. Nevertheless, its predictive accuracy depends on the selected propagation model, the fidelity of the geometry, the calibration and frequency range of the material parameters, the antenna descriptions, the retained interactions, and the numerical settings. The software version and principal simulation parameters should therefore be reported when presenting results generated using WinProp.

2.5.4 Ranplan Professional

Ranplan Professional is a commercial platform for the coordinated design, simulation, and optimisation of indoor and outdoor wireless networks. It combines three-dimensional environment modelling with radio propagation prediction and network performance analysis. Building models can be created from floor plans or imported from building information modelling (BIM) data, Industry Foundation Classes (IFC) files, light detection and ranging (LiDAR) data, computer-aided design (CAD) data, mesh data, and geographic information sources. Materials can be assigned to walls, doors, windows, terrain, foliage, and interior objects to represent their frequency-dependent radio properties [74, 100, 101].

The stated frequency capability depends on the software version and the selected propagation model. A published description of an earlier release reported support from 100 MHz to 70 GHz, whereas the current version 7.2 data sheet additionally lists support for research on technologies operating between 70 and 120 GHz. These values should be interpreted as version specific software capabilities rather than as evidence of uniform prediction accuracy or measurement validation across the entire frequency range [101, 102].

The propagation engine combines RT and ray-launching methods and can represent direct propagation, reflection, transmission, diffraction, and scattering, depending on the selected model and configuration. The reviewed implementation employs acceleration methods including dimension reduction, space partitioning, and the combined use of ray launching and RT. Simulation outputs can be used to evaluate quantities such as path loss, RSS, coverage, capacity, latency, reliability, and interference. The platform also provides network planning functions for distributed antenna systems, small cells, Wi-Fi, cellular networks, MIMO, massive MIMO, and beamforming [74, 100, 101].

The indoor propagation engine has been assessed through comparison with channel measurements. In [103], three-dimensional models of a classroom, an office, and a corridor were constructed in Ranplan Professional for simulations in the Ka band. The simulated and measured results were compared in terms of power delay profiles, path loss, and root-mean-square delay spread. The study found similar overall propagation trends, while also showing that simplified geometry and incomplete representation of small environmental objects can produce differences between simulation and measurement.

Ranplan Professional has also been used to generate channels for system and antenna studies. In [104], RT channels were generated for nine combinations of indoor environment and massive MIMO array topology to investigate spatial channel hardening. Empty, furnished, and room to room scenarios were considered together with colocated, split, and distributed antenna arrays. This application demonstrates the use of the simulator for relating site-specific multipath structure to system-level MIMO behaviour.

The platform has further been used to generate training and reference data for models based on machine learning. The electromagnetic (EM) DeepRay model was trained using indoor propagation data generated with Ranplan Professional to predict path loss distributions over different building geometries and material configurations [105]. In [106], Ranplan Professional was used to generate 10,000 indoor path loss maps at 2.4 GHz for the development of a diffusion model for radio map interpolation. Related work used RT results and models trained from them to evaluate indoor network coverage and capacity while accounting for uncertainty in material properties [107].

Beyond indoor radio maps, Ranplan Professional has been used for the evaluation of propagation models. In [108], simulated path loss data were used to evaluate an environment-adaptive path loss model and to compare it with the Third Generation Partnership Project (3GPP) and alpha beta gamma models. This illustrates the use of the platform as a reference generator for the development of computationally simpler propagation models, rather than only as a network planning tool.

Commercial case studies also report the use of Ranplan Professional for practical network design. One case study describes the modelling and simulation of a six floor hospital wing for a two operator indoor network operating at 900 MHz and 2.1 GHz [109]. Another reports the design and measurement-based calibration of a private 5G network for a 20,000 m^2 smart factory containing metal machinery and different operating configurations [110]. These examples demonstrate commercial planning workflows, although they should be distinguished from independent peer reviewed validation studies.

Overall, Ranplan Professional provides a broad workflow for three-dimensional environment construction, site-specific propagation prediction, network design, optimisation, and data generation. Its predictive accuracy nevertheless depends on the selected propagation model, the fidelity of the geometry, the material and antenna parameters, the retained propagation mechanisms, the numerical settings, and the calibration data. The software version and the main simulation parameters should therefore be reported explicitly when presenting results generated using Ranplan Professional.

2.5.5 EDX Advanced Propagation

EDX Advanced Propagation is a propagation modelling capability available within the EDX SignalPro wireless network planning platform. Current product information states that SignalPro supports radio network planning from approximately 30 MHz to 100 GHz and provides more than thirty published propagation models. This frequency range describes the overall model library and should not be interpreted as a uniform validity or validation range for every model and scenario [74, 111].

The Advanced Propagation capability includes two-dimensional RT, three-dimensional indoor RT, and three-dimensional outdoor RT. Depending on the selected model and simulation configuration, the propagation calculation can represent direct propagation, reflection, transmission, diffraction, and scattering. Other models within SignalPro account for effects associated with terrain, clutter, foliage, buildings, and atmospheric attenuation. The available formulations therefore range from empirical coverage models to site-specific RT methods [74, 112].

SignalPro supports coverage studies, route studies, point to point and point to multipoint link analysis, interference analysis, and network planning. Measurement data can be imported to compare predictions with field observations and to adjust selected propagation model parameters. In particular, its model tuning procedure uses measured drive test data to estimate corrections to clutter attenuation values. This capability can improve agreement within the calibrated environment, although the fitted parameters should not be assumed to remain valid for different frequencies, environments, or antenna configurations [111, 113].

An early measurement-based study used EDX SignalPro to analyse very high frequency (VHF) propagation around three base stations in the eastern region of Saudi Arabia [114]. Field measurements were collected in coastal and desert environments under different atmospheric conditions. SignalPro was used to predict signal strength using selected propagation models, and the predictions were compared with the measured values. The study subsequently developed correction terms to reduce the differences between the empirical predictions and the measurements. This work demonstrates the use of SignalPro for measurement comparison and model adjustment, but it does not constitute a validation of the three-dimensional indoor RT capability.

EDX SignalPro has also been used as a simulation platform for network planning and optimisation. In [115], version 7.4.0 B was used to evaluate a binary-search-based method for determining the number and positions of base stations in indoor and outdoor microcell networks. The study considered different antenna configurations, including single input single output (SISO), multiple input single output (MISO), and MIMO, and evaluated the resulting coverage and received power. This application illustrates the use of SignalPro for testing network optimisation algorithms, but the results were based on simulated coverage rather than an independent channel measurement campaign.

The wider SignalPro platform provides additional planning functions for Wi-Fi, cellular, public safety, mesh, and Internet of Things (IoT) networks. Vendor documentation describes applications involving traffic and security cameras, communication links for UAVs, irrigation control, smart street lighting, and advanced metering infrastructure. It also includes automatic frequency planning and network dimensioning functions for applications such as Project 25 (P25), Terrestrial Trunked Radio (TETRA), and large mesh networks [116, 117]. These examples document the intended engineering workflows of the commercial platform and should be distinguished from independently published measurement validation.

The broader EDX product suite also provides planning functions for satellite communication, including link budget evaluation and atmospheric loss models. These capabilities belong to the wider SignalPro planning environment and should not be conflated with the site-specific terrestrial RT formulations of the Advanced Propagation capability [118].

Overall, EDX SignalPro provides an integrated environment for propagation prediction, measurement-based model tuning, interference analysis, frequency planning, and network optimisation. The Advanced Propagation capability extends this workflow with two-dimensional and three-dimensional RT for environments in which detailed building or terrain geometry is available. Its predictive accuracy nevertheless depends on the selected propagation model, the fidelity of the environmental geometry, the material and clutter parameters, the antenna descriptions, the retained propagation mechanisms, and the numerical settings. The software version, propagation model, and calibration procedure should therefore be stated explicitly when reporting results obtained using EDX SignalPro.

2.5.6 Siradel Web Services

Siradel Web Services, formerly known as Volcano 5G, is a cloud native simulation and network planning platform developed around the Volcano radio propagation engine. The platform provides access to propagation simulation functions and high resolution three-dimensional geographic data through a web interface and a representational state transfer (REST) application programming interface (API). It can be integrated into external applications and scripting environments and is available through both hosted and on premises deployments [119–121].

The frequency capability depends on the software version, propagation model, and calibration data. An earlier review reported support for sub 6 GHz and millimetre wave simulations up to 73 GHz for the implementation considered in that study [74]. This value should be interpreted as a version specific capability rather than as a uniform validation range for every environment and model configuration.

The Volcano engine uses ray-based propagation methods to represent interactions between radio waves and three-dimensional environments. Depending on the selected configuration, the calculation can account for direct propagation, reflection, transmission, diffraction, and diffuse scattering. Published research implementations have included separate diffuse scattering descriptions for buildings, vehicles, and foliage. Siradel Web Services also includes detailed vegetation representation for modelling propagation below, through, and above tree canopies [121, 122].

Siradel Web Services supports indoor and outdoor planning for technologies including fourth generation (4G), 5G, IoT, and Wi-Fi 6. Its REST API enables on demand and large-scale simulation generation, automatic coverage map production, and integration with external network planning workflows. The platform has also been used to automate simulations covering extensive geographic regions, including nationwide 4G and 5G coverage studies. These capabilities primarily concern simulation automation and scalability and do not by themselves establish the accuracy of the underlying propagation model [119, 120].

The Volcano propagation engine has been evaluated through comparison with channel measurements. In an urban study at 28 GHz, the ray-based model was calibrated against directional channel measurements by matching predicted and measured multipath components in terms of path gain, delay, and AoA in three dimensions. The study also calibrated separate diffuse scattering models for buildings, vehicles, and foliage. The results demonstrated the importance of representing non specular propagation when predicting directional millimetre wave channels [122].

A separate study investigated street level backhaul propagation at 60 GHz using channel measurements and simulations based on detailed LiDAR environment data. The Volcano engine was used to analyse multipath propagation in residential and urban canyon scenarios.

The comparison illustrated the value of accurate three-dimensional representations of buildings, vegetation, and street objects, while also showing that the predicted channel remains sensitive to the completeness of the environmental model [123].

Volcano has also been applied to indoor industrial channel modelling. One study investigated the effects of the digital representation of a factory and the permitted number of ray interactions at 2 and 28 GHz [124]. Further work tuned the model against published industrial channel measurements at 3.7 and 28 GHz, including both specular and diffuse contributions, and compared power delay profiles and delay spread statistics under LOS and NLOS conditions [125]. More direct measurement-based calibration was subsequently performed in a metal rich machine room at millimetre wave frequencies, where the predicted received power, delay spread, and angular spread were compared with channel sounding results [126].

The engine has further been extended for RIS-assisted industrial propagation studies. In [127], an additional RIS model was integrated with Volcano to investigate coverage enhancement in a factory at sub 6 GHz and millimetre wave frequencies. The RIS response in that study was supplied by the model introduced by the authors and should therefore be distinguished from the native propagation functions of Siradel Web Services. Volcano represented the surrounding multipath environment, while the predicted RIS contribution depended on the additional surface model and its assumptions.

Overall, Siradel Web Services provides a scalable environment for site-specific propagation prediction, coverage analysis, and automated network planning. Its REST API and cloud computing architecture are useful for large simulation campaigns and integration with external workflows. Its predictive accuracy, however, depends on the fidelity of the geographic and building data, the material and vegetation parameters, the antenna descriptions, the propagation mechanisms included, and the calibration of the selected model. The software version, simulation settings, and any externally integrated propagation components should therefore be stated explicitly when reporting results obtained using the platform.

2.5.7 Wireless InSite

Wireless InSite is a commercial propagation simulation suite developed by Remcom for the analysis of site-specific wireless channels in indoor, urban, and rural environments. The platform provides three-dimensional RT, faster ray-based propagation models, and empirical models for coverage and communication system analysis. The frequency range depends on the selected propagation model and software version. For the X3D model considered in the official indoor workflow, the stated operating range extends from 100 MHz to 100 GHz. This range should be interpreted as a software capability rather than as evidence of uniform prediction accuracy or measurement validation across all frequencies and environments [74, 128, 129].

The X3D propagation model uses an SBR procedure to identify propagation paths and applies an exact path calculation to direct the reconstructed paths towards the receiver. Depending on the selected configuration, the model can account for direct propagation, reflection, transmission, diffraction, atmospheric absorption, and diffuse scattering. In the reviewed configuration, the user can specify up to 30 reflections, eight transmissions, and three diffractions. These values are separate limits for the individual interaction mechanisms and should not be described as a single limit of 30 ray interactions [128, 129].

Wireless InSite can provide detailed path and channel information, including received power, propagation paths, complex channel impulse responses, delay spread, directions of arrival and departure, and the amplitude and phase contributions of individual multipath components. Antenna polarisation and orientation can be included in the field calculation, while measured or numerically calculated antenna patterns can be imported. The platform also supports MIMO and massive MIMO analysis, including beamforming, spatial multiplexing, capacity, and throughput evaluation. Current versions additionally support frequency sweeps and dynamic scenarios containing moving radio devices, vehicles, pedestrians, and other scene objects [128].

Indoor environments can be constructed from floor plans or imported three-dimensional geometry. Walls, floors, windows, doors, furniture, and other objects can be assigned material properties such as relative permittivity, conductivity, and thickness. The installed material library includes common construction materials over a range of frequencies, while measured reflection and transmission coefficients can also be introduced. These capabilities allow the effects of geometry, material selection, antenna orientation, and the retained propagation mechanisms to be examined within a common simulation workflow [129].

Several studies have compared Wireless InSite predictions with indoor measurements. In [130], received power predictions at 2.4 and 5 GHz were compared with measurements collected on one floor of a university building. The study investigated the effects of the selected propagation model, ray generation method, number of interactions, and concrete material parameters. The reported average root-mean-square errors were approximately 4.97 dB at 2.4 GHz and 5.09 dB at 5 GHz. The results also showed that the simulation accuracy and computation time varied substantially with the selected interaction limits and material parameters.

Wireless InSite has also been evaluated in indoor millimetre wave environments. In [131], a detailed three-dimensional model of an office environment was constructed at 60 GHz and compared with measurements obtained using commercial 60 GHz communication equipment. Received power, delay spread, and coherence bandwidth were evaluated at different receiver positions, and the reported results showed agreement between the predicted and measured propagation behaviour. This study demonstrates the importance of representing the building geometry and EM material properties when modelling indoor millimetre wave channels.

Diffuse scattering has been investigated in a separate 73 GHz office example provided by Remcom. In this example, the simulation included rough-surface scattering and was compared with published office measurements. The inclusion of diffuse scattering affected both the received multipath structure and the cross-polarised-field components [132]. Because this example is a vendor demonstration, it should be distinguished from an independent measurement validation study.

The platform has further been used for indoor simulations at frequencies beyond conventional millimetre wave bands. In [133], Wireless InSite was used to generate directional and omnidirectional channel data at 245 GHz in LOS and NLOS indoor scenarios. The study derived quantities including path loss, delay spread, multipath cluster statistics, and angular characteristics. Received power and path loss results were compared with those generated using WinProp. This comparison provides evidence of consistency between two simulation approaches, but it does not replace validation against measured channels.

Beyond direct propagation analysis, Wireless InSite has been used to generate communication channel data for combined sensing and communication research. The M^3SC dataset used Wireless InSite to generate channel impulse responses and combined these data with images, depth maps, LiDAR point clouds, and radar information obtained from other simulation platforms [134]. This application illustrates the use of RT for channel data generation and digital environment research, rather than measurement validation of the propagation model itself.

Overall, Wireless InSite provides a broad workflow for scene construction, material and antenna modelling, multipath channel generation, coverage analysis, MIMO evaluation, and communication system analysis. Its predictive accuracy nevertheless depends on the fidelity of the environment geometry, the calibration and valid frequency range of the material and scattering parameters, the antenna descriptions, the propagation mechanisms included, and the numerical settings of the selected solver. The software version, propagation model, interaction limits, ray spacing, material parameters, and antenna configuration should therefore be reported when presenting results obtained using Wireless InSite.

2.5.8 CrossWave

CrossWave is a commercial propagation model developed by Orange Labs and distributed and supported by Forsk as an optional component of the Atoll radio network planning platform. According to the current product description, the model supports frequencies from 200 MHz to 40 GHz, macro, micro, and small cells, and propagation environments ranging from rural to dense urban areas. It also supports outdoor to indoor and indoor to indoor propagation [74, 135].

The stated frequency range should be interpreted as the operating scope of the model rather than as evidence of uniform measurement validation across every frequency and propagation environment. CrossWave can use raster data and three-dimensional building vector data to represent terrain, clutter, and buildings. Its propagation formulation includes vertical diffraction, horizontally guided propagation, and reflection from mountainous terrain. CrossWave is therefore more appropriately described as a universal propagation model that combines geometrical and empirically calibrated mechanisms than as a general purpose full three-dimensional RT solver [135].

CrossWave is supplied with coefficients that have been calibrated using propagation measurements collected under a range of geographical and environmental conditions. The model can also be tuned to a specific deployment using continuous wave measurements. Within Atoll, predicted and measured signal levels can be compared and the model parameters can be adjusted through an automatic calibration procedure. Multi threaded and distributed computation are supported to reduce the processing time required for extensive coverage calculations [135, 136].

It is important to distinguish the propagation functions of CrossWave from the wider network planning capabilities of Atoll. CrossWave provides propagation loss and coverage predictions, whereas Atoll provides the surrounding workflow for multi technology radio access network design and optimisation. The wider platform supports functions such as coverage and interference analysis, massive MIMO and three-dimensional beamforming studies, automatic frequency and cell planning, measurement data processing, and combined indoor and outdoor network planning [136].

CrossWave has been used in a live 5G New Radio (NR) trial conducted in a suburban area of Sydney at 3.5 GHz. In this study, coverage predictions were generated using Atoll and CrossWave with terrain and clutter data at a spatial resolution of 2 m, together with three-dimensional building and vegetation data. The predictions were compared with NR reference signal received power (NRSRP) measurements collected over a drive test route exceeding 30 km and with stationary throughput measurements [137]. The study reported that the locally averaged measurements and coverage predictions showed similar behaviour. However, the work considered a single deployment environment, so its findings should not be interpreted as general validation of the model across all supported frequencies and scenarios.

CrossWave has also been used for coverage modelling at a national regulatory scale. The Commission for Communications Regulation in Ireland uses Atoll together with CrossWave to generate coverage predictions for mobile networks. The model is tuned to the local geography using separate configurations for urban, suburban, and rural areas, while terrain, clutter, and building height data are included in the prediction process [138, 139]. Drive surveys are used to compare field measurements with the resulting coverage predictions. This application demonstrates the operational use of CrossWave for large-scale coverage reporting, although it does not provide public path-level validation of the underlying propagation mechanisms.

Overall, CrossWave provides a computationally efficient model for coverage prediction and radio network planning across indoor, outdoor, and combined propagation environments. Its main strengths include support for several cell types and radio technologies, automatic calibration using measurements, and integration with the wider Atoll planning workflow. Its predictive accuracy nevertheless depends on the resolution and fidelity of the terrain, clutter, and building data, the calibration measurements, the selected model parameters, the antenna descriptions, and the frequency and environment for which the model is applied. The CrossWave and Atoll versions, input data resolution, calibration procedure, and principal prediction settings should therefore be reported when presenting results obtained using the model.

Table 2.1 Critical comparison of representative modelling approaches with respect to the EM requirements of this thesis.

Assessment criterion	**Current capability**	**Relation to the requirements of this thesis**
Empirical and statistical channel models [61–63]		
Polarisation treatment	Polarisation is represented through average parameters or statistical distributions.	The path-dependent evolution of the complex vector electric field is not reconstructed.
Multilayer material treatment	Individual material layers and interfaces are generally not resolved. Wall and floor effects are instead represented through aggregate loss parameters.	There is no direct EM connection between individual layer properties and the resulting polarisation channel.
XPR and system-level link	XPR or XPD is commonly assigned through average values, fitted parameters, or probability distributions.	A direct relationship from material properties through path-dependent XPR to PolarSK ABEP is not normally available.
RIS capability	RISs are usually absent or represented through an abstract channel coefficient or an additional statistical link.	Incidence-dependent unit-cell behaviour, coherent multipath illumination, and finite-aperture reradiation are not explicitly resolved.
Validation evidence and scope	Model parameters are generally estimated from measurement campaigns, standardisation data, or fitted simulation data.	The evidence is limited to the environments, frequencies, antenna configurations, and sampling procedures represented by the calibration data.

Continued on the next page

Table 2.1 continued from the previous page

Assessment criterion	Current capability	Relation to the requirements of this thesis
Computational cost and scalability	The models have low computational cost and are well suited to extensive system-level simulations and Monte Carlo evaluation.	Their efficiency is obtained by replacing path-level EM interactions with aggregate or statistical descriptions.
Role in the modelling workflow	They act mainly as system-level reference models, ensemble channel generators, or low-complexity performance benchmarks.	They provide useful comparison cases but do not supply the site-specific geometry, path records, or vector fields required by the framework developed in this thesis.
Conventional scalar ray models [7, 45, 74]		
Polarisation treatment	Each path is represented mainly through scalar loss, delay, and phase. Polarisation is omitted or simplified.	Vector-field rotation, local TE and TM basis transformations, and cross-polarisation coupling cannot be reconstructed consistently.
Multilayer material treatment	Walls are commonly represented using effective penetration loss or a scalar reflection or transmission coefficient.	The separate amplitude and phase transformations introduced by successive material layers and interfaces are not explicitly retained.
XPR and system-level link	Path-dependent co- and cross-polarised components are not normally predicted.	An aggregate XPR value cannot describe the spatial variation caused by path geometry, incidence angle, material response, and coherent multipath interference.

Continued on the next page

Table 2.1 continued from the previous page

Assessment criterion	Current capability	Relation to the requirements of this thesis
RIS capability	A RIS may be represented using a prescribed phase profile, radiation pattern, or scalar interaction coefficient.	Such representations may omit coherent multipath illumination, finite-aperture effects, parasitic scattering, and passive power balance [71–73].
Validation evidence and scope	Validation may use analytical checks, comparison with other propagation models, or measurements in specified scenarios.	Agreement in received power or path loss does not establish that the omitted vector-field transformations are physically represented.
Computational cost and scalability	Scalar ray models provide relatively efficient geometry processing and path search. Their cost nevertheless increases with scene complexity, receiver density, and interaction order.	They are more scalable than full-wave methods but provide less EM information than a vector polarisation-aware formulation.
Role in the modelling workflow	They can act as geometry and path generation layers that return path lengths, interaction points, directions, and material identities.	They are suitable host engines for an additional EM processing layer, provided that the required path information is accessible.
Existing polarimetric ray models closest to Chapter 3 [55–58]		

Continued on the next page

Table 2.1 continued from the previous page

Assessment criterion	**Current capability**	**Relation to the requirements of this thesis**
Polarisation treatment	Vector or dual-polarised fields are supported in selected implementations.	Existing studies establish the importance of representing polarisation changes introduced by reflection, transmission, diffraction, and diffuse scattering.
Multilayer material treatment	Many formulations use single interfaces, single material layers, or heuristic penetration and scattering models.	A unified treatment of finite-thickness, frequency-dependent multilayer partitions remains limited.
XPR and system-level link	Selected studies predict XPR, XPD, polarisation correlation, or related polarisation quantities.	These quantities are not commonly connected directly to multilayer material parameters and PolarSK ABEP within one modelling chain.
RIS capability	RIS modelling is generally treated separately from polarimetric indoor propagation.	The same vector-field description is not normally carried from the building channel into a finite RIS surface model.
Validation evidence and scope	Selected formulations have been compared with indoor polarimetric measurements, including co- and cross-polarised channel quantities.	The resulting evidence remains specific to the propagation mechanisms, material descriptions, frequencies, and measurement scenarios included in each implementation.

Continued on the next page

Table 2.1 continued from the previous page

Assessment criterion	**Current capability**	**Relation to the requirements of this thesis**
Computational cost and scalability	Vector-field tracking and additional depolarisation mechanisms incur greater computational cost than scalar path processing, while remaining substantially more tractable than room-scale full-wave simulation.	The additional cost is justified when path-dependent polarisation is required, but it depends on the number of paths and field interaction models retained.
Role in the modelling workflow	These models act as vector EM propagation layers applied to geometrically identified ray paths.	They are the closest existing approaches to Chapter 3, but the reviewed formulations do not simultaneously provide ordered local basis transformations, multilayer coefficients, coherent channel construction, and a system-level ABEP connection.
Commercial and publicly available ray platforms [74, 77, 91, 100, 111, 119, 128, 135]		
Polarisation treatment	The available treatment depends on the software version and selected propagation model. Some platforms include antenna polarisation, complex path quantities, and polarisation-dependent field outputs.	The internal sequence of local polarisation basis transformations is not always publicly documented, inspectable, or accessible through the user interface.

Continued on the next page

Table 2.1 continued from the previous page

Assessment criterion	**Current capability**	**Relation to the requirements of this thesis**
Multilayer material treatment	Material databases, frequency-dependent properties, thickness parameters, and finite slab models are available in selected tools.	The complete complex TE and TM interaction chain through successive layers is not consistently exposed through publicly documented interfaces.
XPR and system-level link	Received power, channel impulse response, delay spread, angular information, and other channel quantities are widely available. Polarisation related outputs are available in selected tools.	Path-resolved polarisation transformations and a direct connection from material properties through XPR to PolarSK ABEP are not commonly provided as one integrated chain.
RIS capability	Depending on the platform and software version, RIS support may be native, simplified, externally implemented, or unavailable.	No single reviewed platform publicly provides all the polarisation-dependent RIS response, coherent multipath RIS, and system metric capabilities required in this thesis.
Validation evidence and scope	Evidence includes vendor documentation, measurement-based calibration, independent measurement comparisons, inter simulator comparisons, and application studies.	Published validation remains specific to the software version, propagation model, frequency, environment, antenna configuration, output quantity, calibration procedure, and numerical settings.

Continued on the next page

Table 2.1 continued from the previous page

Assessment criterion	**Current capability**	**Relation to the requirements of this thesis**
Computational cost and scalability	These platforms provide accelerated geometry handling and path generation using multi threaded processing, graphics processing unit (GPU) computation, distributed computation, spatial partitioning, or related techniques, depending on the tool.	Their computational performance is solver- and configuration-dependent. Faster coverage models may retain less multipath detail than more complete RT configurations.
Role in the modelling workflow	Selected platforms provide path export, scripting, application programming interfaces, or external model integration. They can therefore act as host scene, geometry, path, and network planning environments.	They can potentially supply the paths required by the EM extensions developed in this thesis, provided that path lengths, ordered interaction points, surface normals, material identities, antenna responses, amplitudes, and phases are accessible.
External RIS models coupled to ray platforms closest to Chapter 5 [84, 90, 127]		
Polarisation treatment	The treatment of polarisation depends on the field quantities supplied by the host ray engine and on the formulation of the external surface model.	Some implementations use a scalar or co-polarised surface response and therefore do not retain the complete incident and reradiated vector fields.

Continued on the next page

Table 2.1 continued from the previous page

Assessment criterion	Current capability	Relation to the requirements of this thesis
Multilayer material treatment	The host platform generally represents the surrounding building materials, while the external model separately represents the RIS.	The building material response and RIS response are not necessarily connected through one inspectable EM field formulation.
XPR and system-level link	Most studies focus on received power, coverage, path loss, or signal-to-interference quantities.	A complete connection from path-dependent polarisation and RIS reradiation to XPR and PolarSK ABEP is generally not provided.
RIS capability	The RIS is introduced through an external surface, circuit, radiation pattern, phase profile, or element response model.	Many implementations do not simultaneously retain incidence and load dependent response, coherent multipath illumination, polarisation, finite-aperture effects, parasitic scattering, and passive power balance.
Validation evidence and scope	Validation ranges from inter simulator comparison to comparison with full-wave simulation or measurements in selected scenarios.	The experimentally validated parts of the complete propagation chain must be distinguished from parts supported only by analytical or numerical evidence.

Continued on the next page

Table 2.1 continued from the previous page

Assessment criterion	**Current capability**	**Relation to the requirements of this thesis**
Computational cost and scalability	These models occupy an intermediate computational position between an ideal scalar RIS coefficient and direct full-wave simulation of the complete RIS-assisted environment.	Their cost depends on the number of incident paths, RIS cells, retained modes, observation points, and the complexity of the adopted surface response.
Role in the modelling workflow	They act as additional surface response layers coupled to a host ray engine. The host engine supplies the surrounding propagation paths, while the external model calculates the RIS reradiated field.	They provide the closest existing software architecture to the modular integration proposed in Chapter 5, without replacing the host platform's geometry handling and path-search functions.
Full-wave EM simulation [39, 40, 42, 43]		
Polarisation treatment	Complex electric and magnetic vector fields are solved directly within the numerical formulation.	Polarisation conversion, coupling, differential attenuation, and phase changes can be obtained from the solved field distribution.
Multilayer material treatment	Material layers, constitutive parameters, finite geometry, and detailed interfaces can be represented explicitly.	The method provides a reference EM description when the geometry, material data, boundary conditions, and numerical discretisation are sufficiently accurate.

Continued on the next page

Table 2.1 continued from the previous page

Assessment criterion	Current capability	Relation to the requirements of this thesis
XPR and system-level link	Co- and cross-polarised fields can be obtained directly, and XPR or XPD can subsequently be calculated.	A separate communication and receiver model is still required to connect the EM fields to ABEP or another system-level performance metric.
RIS capability	Finite geometry, tunable loading, detailed unit cells, mutual coupling, modal scattering, and parasitic effects can be represented.	Applying this level of detail repeatedly to complete indoor rooms, dense receiver grids, and many RIS states is generally computationally expensive.
Validation evidence and scope	Accuracy is assessed through mesh or basis convergence studies, canonical analytical benchmarks, comparison between numerical methods, and measurements where available.	Numerical convergence establishes consistency of the discretised solution but does not remove uncertainty in material parameters, geometry, or measurement conditions.
Computational cost and scalability	Full-wave methods have the highest EM detail among the approaches compared here, but their memory and runtime requirements increase rapidly with electrical size and geometrical complexity.	Large rooms, dense receiver grids, extensive parameter sweeps, and repeated optimisation may become computationally prohibitive.

Continued on the next page

Table 2.1 continued from the previous page

Assessment criterion	Current capability	Relation to the requirements of this thesis
Role in the modelling workflow	Full-wave solvers commonly act as local high fidelity solvers, unit-cell characterisation tools, or reference methods for validating lower complexity models.	They complement rather than replace room-scale RT when the intended workflow requires repeated site-specific channel evaluation.
Framework developed in this thesis		
Polarisation treatment	The complex electric field is resolved into consistently oriented local TE and TM components. Ordered rotation matrices connect the local bases associated with successive interactions.	This preserves path-dependent amplitude, phase, and polarisation transformations through the complete retained interaction sequence in Chapter 3.
Multilayer material treatment	Finite-thickness, frequency-dependent multilayer materials are evaluated recursively using complex reflection and transmission coefficients and physically admissible propagation branches for passive lossy materials.	The formulation creates a traceable connection from layer permittivity, conductivity, permeability, and thickness to the polarised channel.

Continued on the next page

Table 2.1 continued from the previous page

Assessment criterion	**Current capability**	**Relation to the requirements of this thesis**
XPR and system-level link	The coherently combined path contributions form a site-specific dual-polarised channel matrix. XPR is subsequently connected to PolarSK ABEP and BWP material optimisation.	This provides the EM to channel to system-level modelling chain developed across Chapters 3 and 4.
RIS capability	The RIS macromodel uses the coherent multipath incident field together with an incidence- and load-dependent unit-cell response, finite-aperture radiation, retained modal components, and parasitic contributions.	The formulation occupies an intermediate position between an ideal ray optics abstraction and direct full-wave simulation, as developed in Chapter 5.
Validation evidence and scope	Chapters 3 and 4 provide analytical and numerical evidence. Chapter 5 includes comparison with full-wave unit cell simulations and indoor measurements.	Direct polarimetric measurement validation of the Chapter 3 and Chapter 4 formulations remains future work. The available RIS measurements provide scenario-specific rather than building-independent validation.

Continued on the next page

Table 2.1 continued from the previous page

Assessment criterion	**Current capability**	**Relation to the requirements of this thesis**
Computational cost and scalability	The path-level formulation adds complex TE and TM transformations and multilayer coefficient calculations to each retained ray. The RIS macromodel avoids repeated full-wave simulation of the complete room and surface for every load configuration.	The framework is more computationally demanding than scalar ray processing but more tractable than repeated room-scale full-wave simulation. A complete end-to-end runtime comparison with representative commercial solvers remains future work.
Role in the modelling workflow	The framework can reuse paths generated by a host ray engine and apply an additional EM processing layer. Integration of the RIS macromodel with the Ranplan propagation environment is demonstrated in Chapter 5.	The framework is positioned as a modular extension, external module, post processing layer, or potential plugin, rather than as a replacement for the geometry management, path search, acceleration, and network planning capabilities of commercial software.

Note: In this table, *Validation evidence and scope* denotes the type and scope of evidence used to assess a modelling approach, including analytical benchmarks, numerical comparison, calibration, and measurement comparison. *Computational cost and scalability* denotes the relative computational burden, scalability, and suitability for repeated room-scale evaluation. *Role in the modelling workflow* denotes the functional role of an approach within an end-to-end simulation chain and its relationship to other modelling components.

2.6 Critical Comparison and Research Challenges

The reviewed commercial and publicly available simulators provide strong capabilities in environment construction, path generation, propagation analysis, computational acceleration, calibration, and network planning. Most of the reviewed platforms represent direct propagation, reflection, transmission, and diffraction, while selected implementations also include diffuse scattering, moving objects, frequency-dependent materials, and detailed antenna patterns. However, these capabilities depend on the software version, selected propagation model, available material data, and numerical configuration. Published validation is similarly specific to the frequency, environment, antenna configuration, and output quantities considered in each study. It should therefore not be interpreted as evidence of uniform accuracy across all operating conditions.

Table 2.1 compares the principal modelling approaches considered in this chapter. The comparison distinguishes the ability to generate propagation paths from the ability to preserve the EM state carried by each path. This distinction is important because a simulator may predict received power and delay accurately for a calibrated scenario without exposing the complete sequence of vector-field transformations required for polarisation-resolved material analysis or RIS reradiation.

The existing methods closest to the polarisation formulation developed in Chapter 3 are the polarimetric ray models reviewed in Sections 2.2 and 2.3. These studies demonstrate that reflection, diffraction, transmission, and diffuse scattering can produce measurable polarisation changes. However, the present review did not identify a single publicly inspectable formulation that simultaneously retains the ordered transformations between successive local TE and TM bases, the complex reflection and transmission coefficients of finite-thickness frequency-dependent multilayer partitions, the propagation and interaction phases, and the coherent construction of a site-specific dual-polarised channel matrix.

The main advantage of the framework developed in this thesis should therefore not be interpreted as universally more accurate path generation or faster geometrical search than commercial software. Instead, its contribution is a transparent EM processing chain applied to each retained path. The path geometry determines the successive propagation directions, surface normals, incidence angles, and interaction sequence. These quantities are then used to construct the local TE and TM bases, evaluate the complex multilayer interaction coefficients, determine the physical phase propagation direction in lossy materials, and apply the ordered rotation matrices. The resulting path contributions are combined coherently to form the polarisation-resolved channel matrix. This provides a direct and traceable connection from material properties and path geometry to received co- and cross-polarised fields, XPR, and, through the framework of Chapter 4, PolarSK ABEP.

This formulation is consequently positioned as an extension to, rather than a replacement for, an established RT platform. A host simulator can remain responsible for importing building geometry, identifying visible paths, performing intersection checks, supporting diffraction or diffuse scattering where available, and accelerating large receiver grid calculations. The proposed EM layer can then process the resulting path records, provided that the interface supplies, or permits reconstruction of, the path lengths, ordered interaction points, surface normals, incidence directions, material identities, antenna responses, and complex path amplitudes and phases. It can return path-resolved Jones or channel matrices, polarisation-resolved received fields, XPR, and system-level quantities to the host simulation workflow.

Under this architecture, the proposed method could be implemented as a software extension, post processing module, or plugin when the host platform provides a suitable API or path export facility. This portability is conditional on access to the required path-level information and should not be claimed for every commercial tool. Chapter 5 nevertheless demonstrates the practical feasibility of this extension layer by integrating the RIS macromodel with the Ranplan propagation environment. Ranplan supplies the site-specific multipath illumination, while the added EM model maps that illumination to the field reradiated by the configured finite RIS.

A similar distinction applies to the RIS studies reviewed in this chapter. The research gap is not the complete absence of RIS representations in ray-based simulators. Several platforms have been extended using prescribed radiation patterns, phase profiles, element responses, or external RIS models. The unresolved issue is the simultaneous treatment of coherent multipath illumination, incidence and load-dependent unit-cell behaviour, polarisation, finite-aperture reradiation, retained modal content, parasitic scattering, and passive power balance within a model suitable for repeated room-scale simulation. The field-based RIS macromodel developed in Chapter 5 addresses this gap within the assumptions of the adopted circuit, modal, and aperture formulations.

The progression of the thesis follows directly from the two research challenges identified above: physically consistent polarisation tracking through multilayer building materials, and scalable multipath-aware modelling of finite-aperture RIS reradiation. Chapter 3 establishes the path-level vector-field formulation required to obtain a coherent polarisation-resolved indoor channel. Chapter 4 then demonstrates why this additional EM information matters at the system-level by connecting multilayer material properties to PolarSK ABEP. These two chapters provide the propagation and system-level foundation for Chapter 5, where the coherent multipath field becomes the excitation of the RIS macromodel. The resulting framework links path geometry, material response, polarisation, system performance, and RIS reradiation within a common modelling chain.

The scope of these contributions must nevertheless be stated explicitly. The polarisation-aware results in Chapters 3 and 4 are supported by analytical derivations and numerical simulations but have not been directly validated using a full indoor polarimetric measurement campaign. The RIS unit-cell model is compared with full-wave simulations, and the integrated RIS and RT framework is compared with measurements in indoor environment. Furthermore, diffraction, diffuse scattering, measured rough surface statistics, furniture scattering, human blockage, dynamic objects, anisotropic media, higher-order interactions, and complete mutual coupling are not included consistently across all parts of the framework. These mechanisms remain subjects for further validation and extension.

Chapter 3

An RT Algorithm for Polarised Wireless Channel Prediction

Overview

Polarisation plays an important role in describing wireless propagation channels, especially in indoor environments. In such settings, the signal is strongly affected by reflections and transmissions from walls and other building materials. Although conventional RT models are widely used to predict channel behaviour, they are not well suited to modelling polarisation with high accuracy or detail. To address these limitations, this chapter presents a physically consistent RT method that explicitly takes polarisation into account. The key idea is the use of a rotation transfer matrix to handle the changes in polarisation during propagation. This framework makes it possible to trace how each polarisation component changes in strength after reflections and transmissions along the path. I also use this framework to examine the received power of each polarisation component and the XPR. The chapter provides analytical and simulation-based verification; direct polarimetric measurement validation remains future work.

3.1 Introduction

Ray-based models are regarded as key methods for indoor radio propagation prediction [140]. Compared with full-wave methods, which suffer from high computational complexity, and stochastic models, which often lack universality, ray-based approaches provide a balanced solution [74, 140–142]. Among the various characteristics of indoor wireless channels, polarisation is of particular importance since it enables channel capacity enhancement through the multiplexing of data streams. Orthogonally polarised antennas can exhibit nearly zero correlation in LOS scenarios even when colocated, thereby providing additional DoF for communication systems [13, 143]. However, polarisation characteristics are inherently complex, and channel prediction becomes challenging due to depolarisation effects caused by reflections, transmissions, diffractions, and scattering [144]. These processes exhibit considerable intricacy, highlighting the necessity for a simple yet effective method for polarised wireless channel prediction.

Despite the significant progress of ray-based algorithms, only limited attention has been devoted to polarisation in channel prediction. Early attempts [55] incorporated polarisation into RT models and accelerated the study of polarised channel prediction in indoor scenarios. Nevertheless, those works primarily focused on delay spread and received power for reflections and transmissions through single-layer walls, without addressing XPD. Since XPD plays a crucial role in assessing the performance of systems that exploit polarisation domain resources [145–148], its omission leaves a gap in the modelling framework. Moreover, the single-layer wall scenario considered in [55] is too simplified to represent realistic indoor environments. In modern buildings, multilayer walls are common, and their diverse EM properties strongly affect propagation [8, 149, 150]. High-frequency waves are particularly sensitive to wall thickness, and even coatings of a few millimetres cannot be ignored [151]. Although subsequent ray-based studies [13, 144] refined the earlier models, they did not systematically address the reflection and transmission through multilayer walls, nor did they explore XPD in depth.

Considering these limitations, the ray-launching model, which has been validated through experimental measurements [103], emerges as a promising candidate for polarised channel prediction. Building on this foundation, this chapter introduces a novel RT algorithm based on the rotation transfer matrix method, a simple and efficient technique for handling polarisation. The proposed approach explicitly accounts for the diattenuation of polarisation due to reflections and transmissions in multilayer indoor structures, thereby achieving high accuracy in channel prediction. In addition, theoretical analyses of the received power for different polarisation components and the XPR are presented.

The remainder of this chapter is structured as follows. Section 3.2 introduces the RT algorithm and the rotation transfer matrix method, including the formulation of the proposed polarised channel model. Section 3.3 presents RT simulations for indoor propagation scenarios. Section 3.4 provides polarised channel simulation and performance evaluation. Section 3.5 concludes the chapter. The notation used throughout this chapter is summarised in Table 3.1.

3.2 RT Algorithm

In this section, the fundamentals of the RT algorithm adopted in this work are presented in a structured manner. The exposition begins with the geometric relationship between rays and their associated electric-field components. This is followed by the derivation of general expressions for the reflection and transmission coefficients of multislab layers. Finally, the procedure for tracking the polarisation state of a ray by means of rotation matrices is detailed.

Table 3.1 Notation of Chapter 3

Notation	**Definition**
j	Imaginary unit, $j^2 = -1$.
R_{TE}	Complex reflection coefficient of the TE field component.
R_{TM}	Complex reflection coefficient of the TM field component.

Continued on next page

Table 3.1: Notation of Chapter 3 (Continued)

Notation	**Definition**
T_{TE}	Complex transmission coefficient of the TE field component.
T_{TM}	Complex transmission coefficient of the TM field component.
$\hat{\mathbf{a}}_{\mathrm{TE}}$	Unit vector of the local TE polarisation basis.
$\hat{\mathbf{a}}_{\mathrm{TM}}$	Unit vector of the local TM polarisation basis.
$\hat{\mathbf{k}}$	Unit vector in the ray propagation direction.
$\hat{\mathbf{n}}$	Unit surface normal at the current interaction point.
$\mathbf{E}$	Complex electric-field vector.
E	Complex scalar electric-field component.
$E^{\mathrm{inc}}_{\mathrm{TE},0}$	Incident TE electric-field amplitude at the interface reference point.
$E^{\mathrm{inc}}_{\mathrm{TM},0}$	Incident TM electric-field amplitude at the interface reference point.
s	Material layer index.
N	Number of material layers.
A_s	Forward TE recursion coefficient in layer s.
B_s	Backward TE recursion coefficient in layer s.
C_s	Forward TM recursion coefficient in layer s.
D_s	Backward TM recursion coefficient in layer s.
Q_s	TE interface factor used by the multilayer recursion.
W_s	TM interface factor used by the multilayer recursion.
ϑ_0	Real angle of incidence in the lossless incident medium.
ϑ_s	Complex refraction angle in layer s.
$\vartheta^{\mathrm{tra}}_{\mathrm{rea}}$	Real part of the complex transmission angle.
$\vartheta^{\mathrm{tra}}_{\mathrm{ima}}$	Imaginary part of the complex transmission angle.

Continued on next page

Table 3.1: Notation of Chapter 3 (Continued)

Notation	**Definition**
ρ	Physical refraction angle of the phase vector.
d_s	Thickness of layer s.
ω	Angular frequency.
λ	Free-space wavelength.
ε_s	Permittivity of layer s.
μ_s	Permeability of layer s.
σ_s	Conductivity of layer s.
γ_s	Complex propagation constant of layer s, $\gamma_s = \alpha_s + j\beta_s$.
α_s	Amplitude attenuation constant of layer s.
β_s	Phase constant of layer s.
A_ϑ	Real-part factor of $\cos\vartheta^{\text{tra}}$.
B_ϑ	Negative imaginary part factor of $\cos\vartheta^{\text{tra}}$.
C_ϑ	Magnitude of $\cos\vartheta^{\text{tra}}$.
ϖ	Phase parameter satisfying $\cos\vartheta^{\text{tra}} = C_\vartheta e^{-j\varpi}$.
g	Normal component of the transmitted phase vector.
c_0	Arbitrary real constant defining a plane of constant phase.
$A(x,z)$	Real attenuation factor of the transmitted field at (x,z).
$\Phi(x,z)$	Real accumulated phase of the transmitted field at (x,z).
ζ	Signed rotation angle between successive local polarisation bases.
u	Dot product of two successive TE basis vectors.
o	Signed cross product projection of two successive TE basis vectors.
k	Wavenumber magnitude.

Continued on next page

Table 3.1: Notation of Chapter 3 (Continued)

Notation	Definition
l	Propagation distance.
$\mathbf{H}$	Polarised wireless channel matrix.
$\hat{\mathbf{e}}_{\mathrm{tx}}$	Unit Jones vector of the transmitted polarisation state.
$\hat{\mathbf{e}}_{\mathrm{rx}}$	Unit Jones vector of the receive polarisation projection.
h_{ab}	Channel coefficient from transmit polarisation b to receive polarisation a.
$\bar{\mathbf{M}}$	Effective polarised channel matrix.
$\mathbf{M}_{\mathrm{C}}$	Co-polarised contribution to the effective channel matrix.
$\mathbf{M}_{\mathrm{X}}$	Cross-polarised contribution to the effective channel matrix.
H	Horizontal polarisation label.
V	Vertical polarisation label.
x	Transmitted complex baseband symbol.
y	Received complex baseband symbol.
t_p	Transmitter port indexed by p.
r_q	Receiver port indexed by q.
ϕ_{t_p}	Azimuth angle of departure at transmitter port t_p.
ϕ_{r_q}	Azimuth component of the AoA at receiver port r_q.
θ_{t_p}	Zenith angle of departure at transmitter port t_p.
θ_{r_q}	Zenith component of the AoA at receiver port r_q.
$m_{\mathrm{r}_q,\mathrm{t}_p}$	Channel coefficient from port t_p to port r_q.
$\bar{m}_{\mathrm{r}_q,\mathrm{t}_p}$	Effective channel coefficient from port t_p to port r_q.
$\alpha_{\mathrm{r}_q,\mathrm{t}_p}$	Co-polarised propagation power gain between ports t_p and r_q.
$\beta_{\mathrm{r}_q,\mathrm{t}_p}$	Cross-polarised propagation power gain between ports t_p and r_q.

Continued on next page

Table 3.1: Notation of Chapter 3 (Continued)

Notation	Definition
$\mathcal{X}$	XPD in linear power ratio form.
G	Antenna power gain.
L	Path loss in linear power ratio form.
P	Received power.
$\times$	Vector cross product operator.
$(\cdot)^{\mathrm{T}}$	Complex conjugate transpose operator.
$\|\cdot\|_2$	Euclidean norm operator for a vector.

3.2.1 Geometry of Rays and Polarisation Components

At each interaction, the electric field is decomposed into TE and TM components as [151]

$$\mathbf{E} = \mathbf{E}_{\mathrm{TE}} + \mathbf{E}_{\mathrm{TM}}, \tag{3.1}$$

where $\mathbf{E}$ is the complex electric-field vector. A ray-fixed local coordinate system (LCS) is defined at each reflection or transmission point. For nonnormal incidence, the TE unit vector is

$$\hat{\mathbf{a}}_{\mathrm{TE}}^{\mathrm{inc}} = \hat{\mathbf{a}}_{\mathrm{TE}}^{\mathrm{ref}} = \hat{\mathbf{a}}_{\mathrm{TE}}^{\mathrm{tra}} = \frac{\hat{\mathbf{k}}^{\mathrm{inc}} \times \hat{\mathbf{n}}}{\left\|\hat{\mathbf{k}}^{\mathrm{inc}} \times \hat{\mathbf{n}}\right\|_2}, \tag{3.2}$$

where $\hat{\mathbf{k}}^{\mathrm{inc}}$ is the incident propagation unit vector and $\hat{\mathbf{n}}$ is the local surface normal. The reflected and transmitted rays share the same plane of incidence, so the same oriented TE axis is retained. The corresponding TM unit vectors are

$$\hat{\mathbf{a}}_{\mathrm{TM}}^{\mathrm{inc}} = \hat{\mathbf{a}}_{\mathrm{TE}}^{\mathrm{inc}} \times \hat{\mathbf{k}}^{\mathrm{inc}}, \tag{3.3}$$

$$\hat{\mathbf{a}}_{\mathrm{TM}}^{\mathrm{ref}} = \hat{\mathbf{a}}_{\mathrm{TE}}^{\mathrm{inc}} \times \hat{\mathbf{k}}^{\mathrm{ref}}, \tag{3.4}$$

$$\hat{\mathbf{a}}_{\mathrm{TM}}^{\mathrm{tra}} = \hat{\mathbf{a}}_{\mathrm{TE}}^{\mathrm{inc}} \times \hat{\mathbf{k}}^{\mathrm{tra}}, \tag{3.5}$$

where $\hat{\mathbf{k}}^{\mathrm{ref}}$ and $\hat{\mathbf{k}}^{\mathrm{tra}}$ are the reflected and transmitted propagation unit vectors, respectively. The cross product order fixes a right-handed basis and must be used consistently throughout the path.

The local TE/TM basis is therefore defined separately at each interaction point from the incident ray direction and the local surface normal. In numerical implementation, the basis vectors must be normalised after each cross product operation. Near grazing incidence, or when the incident direction becomes nearly parallel to the selected reference normal, the norm of the cross product may become very small and the basis definition can be ill-conditioned. Such near-singular cases require a tolerance check, reorthogonalisation, or a fallback reference direction to maintain numerical stability over multiple reflections and transmissions. These checks do not change the EM formulation, but they are necessary for robust implementation of the rotation transfer matrix.

3.2.2 Reflection and Transmission Coefficients

The complex reflection and transmission coefficients of a finite multilayer slab are evaluated using the recursion in [151]:

$$A_s = \frac{e^{d_s \gamma_s \cos\vartheta_s}}{2}\left[A_{s+1}\left(1+Q_{s+1}\right)+B_{s+1}\left(1-Q_{s+1}\right)\right], \tag{3.6}$$

$$B_s = \frac{e^{-d_s \gamma_s \cos\vartheta_s}}{2}\left[A_{s+1}\left(1-Q_{s+1}\right)+B_{s+1}\left(1+Q_{s+1}\right)\right], \tag{3.7}$$

$$C_s = \frac{e^{d_s \gamma_s \cos\vartheta_s}}{2}\left[C_{s+1}\left(1+W_{s+1}\right)+D_{s+1}\left(1-W_{s+1}\right)\right], \tag{3.8}$$

$$D_s = \frac{e^{-d_s \gamma_s \cos\vartheta_s}}{2}\left[C_{s+1}\left(1-W_{s+1}\right)+D_{s+1}\left(1+W_{s+1}\right)\right], \tag{3.9}$$

with

$$Q_{s+1} = \frac{\cos\vartheta_{s+1}}{\cos\vartheta_s}\sqrt{\frac{\left(\omega\varepsilon_s - j\sigma_s\right)\mu_{s+1}}{\left(\omega\varepsilon_{s+1} - j\sigma_{s+1}\right)\mu_s}}, \tag{3.10}$$

$$W_{s+1} = \frac{\cos\vartheta_s}{\cos\vartheta_{s+1}}\sqrt{\frac{\left(\omega\varepsilon_s - j\sigma_s\right)\mu_{s+1}}{\left(\omega\varepsilon_{s+1} - j\sigma_{s+1}\right)\mu_s}}, \tag{3.11}$$

where ϑ_s is the complex refraction angle in layer s, with ϑ_0 denoting the real incidence angle in the incident medium. The quantities d_s, μ_s, ε_s, and σ_s are the thickness, permeability, permittivity, and conductivity of layer s, respectively, and ω is the angular frequency. For the passive double-positive materials considered in this thesis, the propagation constant is

$$\gamma_s = \alpha_s + j\beta_s = \sqrt{j\omega\mu_s\left(\sigma_s + j\omega\varepsilon_s\right)}, \tag{3.12}$$

where the square-root branch is selected so that $\alpha_s \geq 0$ and $\beta_s \geq 0$ under the adopted $e^{j\omega t}$ convention. Continuity of the tangential propagation constant gives $\gamma_0 \sin\vartheta_0 = \gamma_s \sin\vartheta_s$; hence,

$$\cos\vartheta_s = \sqrt{1 - \left(\frac{\gamma_0}{\gamma_s}\right)^2 \sin^2\vartheta_0}. \tag{3.13}$$

The branch of $\cos\vartheta_s$ is chosen so that the normal field satisfies the passive, outgoing wave condition. For a stack of N layers terminated by air, the recursion is initialised by $A_{N+1} = C_{N+1} = 1$ and $B_{N+1} = D_{N+1} = 0$. Equations (3.6)–(3.13) then yield $R_{\mathrm{TE}} = B_0/A_0$, $R_{\mathrm{TM}} = D_0/C_0$, $T_{\mathrm{TE}} = 1/A_0$, and $T_{\mathrm{TM}} = 1/C_0$.

It is important to note that these coefficients correspond to finite-thickness multilayer slabs rather than only to ideal single interfaces. For passive layers, the reflected, transmitted, and dissipated powers should satisfy an energy balance check after accounting for material loss. This provides a useful physical consistency test for the coefficient calculation, although the present chapter focuses on the resulting polarisation-channel prediction rather than on a separate energy audit procedure.

3.2.3 Physical Angle of Refraction in Double-Positive Materials

Equations (3.6)–(3.13) use a complex refraction angle in a lossy layer. The direction of phase propagation is real, however, and must be obtained from the phase vector rather than by interpreting the complex angle geometrically. The following derivation establishes that direction for the passive Double-Positive (DPS) materials used in the simulations.

Each wall layer is assumed to be a DPS medium with $\varepsilon > 0$, $\mu > 0$, and $\sigma \geq 0$. This assumption is consistent with the material parameters used in Section 3.4.1; the derivation is not intended for negative-index or active media.

Consider a uniform plane wave incident from lossless air onto a lossy wall, as illustrated in Fig. 3.1. The transmitted TE and TM fields share the same propagation factor. With the interface at $z = 0$, the plane of incidence in the x–z plane, and $\gamma^{\text{tra}} = \alpha^{\text{tra}} + j\beta^{\text{tra}}$, they are

$$\mathbf{E}_{\text{TE}}^{\text{tra}} = \hat{\mathbf{a}}_y T_{\text{TE}} E_{\text{TE},0}^{\text{inc}} e^{-\gamma^{\text{tra}}\left(x\sin\vartheta^{\text{tra}} + z\cos\vartheta^{\text{tra}}\right)}, \tag{3.14}$$

$$\mathbf{E}_{\text{TM}}^{\text{tra}} = \hat{\mathbf{b}} T_{\text{TM}} E_{\text{TM},0}^{\text{inc}} e^{-\gamma^{\text{tra}}\left(x\sin\vartheta^{\text{tra}} + z\cos\vartheta^{\text{tra}}\right)}, \tag{3.15}$$

where $\hat{\mathbf{b}} = \hat{\mathbf{a}}_x \cos\vartheta^{\text{tra}} - \hat{\mathbf{a}}_z \sin\vartheta^{\text{tra}}$, and $E_{\text{TE},0}^{\text{inc}}$ and $E_{\text{TM},0}^{\text{inc}}$ are the incident-field amplitudes evaluated at the interface reference point.

In accordance with Snell's law of refraction:

$$\gamma^{\text{inc}} \sin\vartheta^{\text{inc}} = \gamma^{\text{tra}} \sin\vartheta^{\text{tra}}, \tag{3.16}$$

$$\gamma = \alpha + j\beta = \sqrt{j\omega\mu\left(\sigma + j\omega\varepsilon\right)} = \sqrt{-\omega^2\mu\varepsilon + j\omega\mu\sigma}, \tag{3.17}$$

where

$$\alpha = \omega\sqrt{\mu\varepsilon}\left\{\frac{1}{2}\left[\sqrt{1+\left(\frac{\sigma}{\omega\varepsilon}\right)^2} - 1\right]\right\}^{1/2}, \tag{3.18}$$

$$\beta = \omega\sqrt{\mu\varepsilon}\left\{\frac{1}{2}\left[\sqrt{1+\left(\frac{\sigma}{\omega\varepsilon}\right)^2} + 1\right]\right\}^{1/2}. \tag{3.19}$$

After algebraic simplifications, (3.17) can be rewritten in the same form as (3.12). By substituting (3.17) into (3.16), the following relationship is obtained:

$$\sin\vartheta^{\text{tra}} = \frac{\gamma^{\text{inc}}}{\gamma^{\text{tra}}}\sin\vartheta^{\text{inc}} = \frac{\alpha^{\text{inc}} + j\beta^{\text{inc}}}{\alpha^{\text{tra}} + j\beta^{\text{tra}}}\sin\vartheta^{\text{inc}}. \tag{3.20}$$

As the ray impinges from air, the electrical conductivity of the incident medium is zero, that is, $\sigma^{\text{inc}} = \sigma_{\text{air}} = 0$. Substituting $\sigma^{\text{inc}} = 0$ into (3.18) gives $\alpha^{\text{inc}} = 0$. Consequently, (3.20) can be rewritten as:

$$\sin \vartheta^{\text{tra}} = \frac{j\beta^{\text{inc}}}{\alpha^{\text{tra}} + j\beta^{\text{tra}}} \sin \vartheta^{\text{inc}}. \tag{3.21}$$

and

$$\begin{aligned} \cos \vartheta^{\text{tra}} &= \sqrt{1 - \sin^2 \vartheta^{\text{tra}}} \\ &= \sqrt{1 - \left(\frac{j\beta^{\text{inc}}}{\alpha^{\text{tra}} + j\beta^{\text{tra}}} \sin \vartheta^{\text{inc}} \right)^2}. \end{aligned} \tag{3.22}$$

Because ϑ^{inc} is real and γ^{tra} is complex, both $\sin \vartheta^{\text{tra}}$ and $\cos \vartheta^{\text{tra}}$ are generally complex. Their standard analytic continuations are

$$\begin{aligned} \cos \vartheta^{\text{tra}} &= \sum_{n=0}^{\infty} \frac{(-1)^n}{(2n)!} \left(\vartheta^{\text{tra}} \right)^{2n} \\ &= \frac{e^{j\vartheta^{\text{tra}}} + e^{-j\vartheta^{\text{tra}}}}{2} \\ &= \cosh \left(j\vartheta^{\text{tra}} \right), \end{aligned} \tag{3.23}$$

and

$$\begin{aligned} \sin \vartheta^{\text{tra}} &= \sum_{n=0}^{\infty} \frac{(-1)^n}{(2n+1)!} \left(\vartheta^{\text{tra}} \right)^{2n+1} \\ &= \frac{e^{j\vartheta^{\text{tra}}} - e^{-j\vartheta^{\text{tra}}}}{2j} \\ &= \frac{\sinh \left(j\vartheta^{\text{tra}} \right)}{j} \\ &= -j \sinh \left(j\vartheta^{\text{tra}} \right), \end{aligned} \tag{3.24}$$

where cosh and sinh denote the hyperbolic cosine and sine functions, respectively. Let the transmission angle be expressed as $\vartheta^{\text{tra}} = \vartheta^{\text{tra}}_{\text{rea}} + j\vartheta^{\text{tra}}_{\text{ima}}$, where $\vartheta^{\text{tra}}_{\text{rea}}$ and $\vartheta^{\text{tra}}_{\text{ima}}$ are the real and imaginary components of ϑ^{tra}, both of which are real-valued quantities. By expressing the complex cosine function in terms of the real and imaginary parts of its argument, the following relation is obtained:

$$\begin{aligned}\cos\vartheta^{\mathrm{tra}} &= \cos\left(\vartheta^{\mathrm{tra}}_{\mathrm{rea}} + j\vartheta^{\mathrm{tra}}_{\mathrm{ima}}\right) \\ &= \cos\left(\vartheta^{\mathrm{tra}}_{\mathrm{rea}}\right)\cos\left(j\vartheta^{\mathrm{tra}}_{\mathrm{ima}}\right) - \sin\left(\vartheta^{\mathrm{tra}}_{\mathrm{rea}}\right)\sin\left(j\vartheta^{\mathrm{tra}}_{\mathrm{ima}}\right) \\ &= \cos\left(\vartheta^{\mathrm{tra}}_{\mathrm{rea}}\right)\cosh\left(\vartheta^{\mathrm{tra}}_{\mathrm{ima}}\right) - j\sin\left(\vartheta^{\mathrm{tra}}_{\mathrm{rea}}\right)\sinh\left(\vartheta^{\mathrm{tra}}_{\mathrm{ima}}\right). \qquad (3.25)\end{aligned}$$

Define the real quantities

$$A_{\vartheta} = \cos\left(\vartheta^{\mathrm{tra}}_{\mathrm{rea}}\right)\cosh\left(\vartheta^{\mathrm{tra}}_{\mathrm{ima}}\right), \qquad B_{\vartheta} = \sin\left(\vartheta^{\mathrm{tra}}_{\mathrm{rea}}\right)\sinh\left(\vartheta^{\mathrm{tra}}_{\mathrm{ima}}\right). \qquad (3.26)$$

Equation (3.20) then implies the polar representation

$$\cos\vartheta^{\mathrm{tra}} = A_{\vartheta} - jB_{\vartheta} = C_{\vartheta}\left(\cos\varpi - j\sin\varpi\right) = C_{\vartheta}e^{-j\varpi}, \qquad (3.27)$$

where $C_{\vartheta} = \sqrt{A^2_{\vartheta} + B^2_{\vartheta}}$ and $\varpi = \mathrm{atan2}(B_{\vartheta}, A_{\vartheta})$. Accordingly,

$$x\sin\vartheta^{\mathrm{tra}} + z\cos\vartheta^{\mathrm{tra}} = x\frac{j\beta^{\mathrm{inc}}\sin\vartheta^{\mathrm{inc}}}{\alpha^{\mathrm{tra}} + j\beta^{\mathrm{tra}}} + zC_{\vartheta}\left(\cos\varpi - j\sin\varpi\right).$$

Multiplication by γ^{tra} separates the common propagation factor into attenuation and phase terms:

$$e^{-zC_{\vartheta}\left(\alpha^{\mathrm{tra}}\cos\varpi + \beta^{\mathrm{tra}}\sin\varpi\right)}e^{-j\left[x\beta^{\mathrm{inc}}\sin\vartheta^{\mathrm{inc}} + zC_{\vartheta}\left(\beta^{\mathrm{tra}}\cos\varpi - \alpha^{\mathrm{tra}}\sin\varpi\right)\right]}. \qquad (3.28)$$

Both α^{tra} and β^{tra} are real and nonnegative for the passive DPS branch selected above.

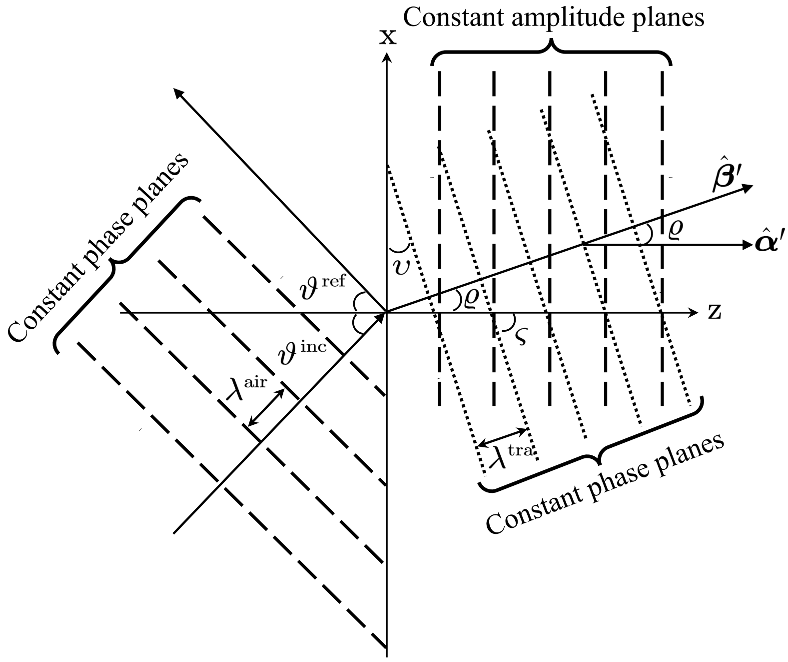

Fig. 3.1 Planes of constant phase and amplitude for the refracted wave.

By decomposing (3.28) into its real and imaginary components, the following expressions are obtained:

$$A(x,z) = e^{-zC_\vartheta\left(\alpha^{\text{tra}}\cos\varpi + \beta^{\text{tra}}\sin\varpi\right)}, \tag{3.29}$$

$$\Phi(x,z) = x\beta^{\text{inc}}\sin\vartheta^{\text{inc}} + zC_\vartheta\left(\beta^{\text{tra}}\cos\varpi - \alpha^{\text{tra}}\sin\varpi\right), \tag{3.30}$$

Equation (3.29) shows that the attenuation vector is normal to the interface for a homogeneous lossy half-space excited by a lossless incident medium. Define the normal phase constant

$$g = C_\vartheta\left(\beta^{\text{tra}}\cos\varpi - \alpha^{\text{tra}}\sin\varpi\right). \tag{3.31}$$

A plane of constant phase, $\Phi(x,z) = c_0$, is therefore described by

$$x = \frac{c_0 - gz}{\beta^{\text{inc}}\sin\vartheta^{\text{inc}}}, \tag{3.32}$$

for nonnormal incidence. The phase vector components tangent and normal to the interface are thus $\beta^{\mathrm{inc}} \sin\vartheta^{\mathrm{inc}}$ and g, respectively. The physical refraction angle ρ, measured from the positive z-axis towards the positive tangential direction, follows directly from these two components:

$$\rho = \mathrm{atan2}\left(\beta^{\mathrm{inc}} \sin\vartheta^{\mathrm{inc}}, g\right). \tag{3.33}$$

The two-argument arctangent preserves the correct quadrant and remains defined at grazing phase propagation. Because the TE and TM fields in (3.14) and (3.15) share the same propagation factor in an isotropic layer, Eq. (3.33) applies to both polarisations; their amplitudes differ through T_{TE} and T_{TM}.

3.2.4 Rotation Transfer Matrix Method for RT

Jones calculus provides a compact representation of the transformations between the global coordinate system (GCS) and the ray-fixed LCS at successive interactions [152].

In the far field, the transmit and receive antenna patterns are expressed in the spherical unit vector bases associated with azimuth ϕ and zenith θ [151]. Let $\hat{\mathbf{e}}_{\mathrm{tx}}$ and $\hat{\mathbf{e}}_{\mathrm{rx}}$ denote the corresponding Jones vectors. After separating any scalar free-space spreading and propagation phase from the polarisation transformation, the single-ray baseband relation is

$$y = (\hat{\mathbf{e}}_{\mathrm{rx}})^{\mathrm{T}} \mathbf{H} (\hat{\mathbf{e}}_{\mathrm{tx}}) x, \tag{3.34}$$

where x and y denote the transmitted and received signals, respectively, while $\hat{\mathbf{e}}_{\mathrm{tx}}$ and $\hat{\mathbf{e}}_{\mathrm{rx}}$ are the Jones vectors describing the transmitter (Tx) and receiver (Rx) polarisation states. The operator $(\cdot)^{\mathrm{T}}$ denotes matrix transpose. The matrix H captures the diattenuation, namely the unequal attenuation of $\hat{\mathrm{E}}_{\phi}$ and $\hat{\mathrm{E}}_{\theta}$, together with the channel XPR induced by reflection and transmission.

For a LOS ray, $\mathbf{H}_{\mathrm{LOS}} = \mathbf{I}_2$ only when the transmit and receive polarisation bases are aligned and the scalar path gain has been factored out. For a reflected NLOS (RNLOS) ray or an obstructed LOS (OLOS) ray, the polarisation matrix is an ordered product of basis rotations and TE/TM interaction matrices. An OLOS ray is defined here as a geometrically direct path that reaches the Rx through transmission across an intervening building element.

Let E_{TE} and E_{TM} denote the scalar field components in the current LCS, and let E'_{TE} and E'_{TM} denote the same field resolved in the next LCS. Before applying the reflection or transmission coefficients, the basis transformation is

$$\begin{bmatrix} E'_{\mathrm{TE}} \\ E'_{\mathrm{TM}} \end{bmatrix} = \begin{bmatrix} \cos(\zeta) & \sin(\zeta) \\ -\sin(\zeta) & \cos(\zeta) \end{bmatrix} \begin{bmatrix} E_{\mathrm{TE}} \\ E_{\mathrm{TM}} \end{bmatrix}, \tag{3.35}$$

where the signed angle ζ is determined from the unit TE basis vectors of the two LCSs:

$$\zeta = \mathrm{atan2}(o, u), \tag{3.36}$$

with

$$u = \hat{\mathbf{a}}_{\mathrm{TE}} \cdot \hat{\mathbf{a}}'_{\mathrm{TE}}, \tag{3.37}$$

$$o = \hat{\mathbf{k}} \cdot \left(\hat{\mathbf{a}}_{\mathrm{TE}} \times \hat{\mathbf{a}}'_{\mathrm{TE}} \right). \tag{3.38}$$

The two-argument arctangent preserves the sign and quadrant of the rotation. The same angle is obtained from the consistently oriented TM bases. For densely walled indoor propagation scenarios, such as offices or student apartments, when the first reflection occurs, the ray may have penetrated z walls during its propagation from the Tx to the wall of the first reflection. Similarly, the ray may undergo w transmissions during the propagation from the wall where it is first reflected to the Rx. For the transmission process, the complete representation of polarisation components variation can be expressed as

$$\mathbf{T} = \begin{bmatrix} T_{\mathrm{TE}} & 0 \\ 0 & T_{\mathrm{TM}} \end{bmatrix} \cdot \begin{bmatrix} \cos(\zeta^{\mathrm{tra}}) & \sin(\zeta^{\mathrm{tra}}) \\ -\sin(\zeta^{\mathrm{tra}}) & \cos(\zeta^{\mathrm{tra}}) \end{bmatrix}. \tag{3.39}$$

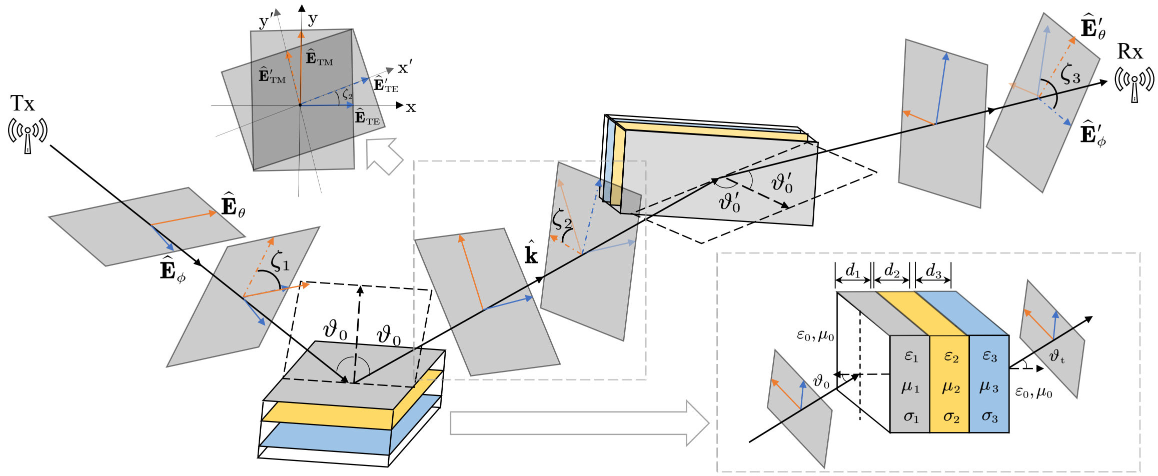

Fig. 3.2 Visualisation of reference frame transformations via rotation matrices in sequential reflections and transmissions.

For the reflection process, the complete representation of polarisation components variation can be expressed as

$$\mathbf{R} = \begin{bmatrix} R_{\mathrm{TE}} & 0 \\ 0 & R_{\mathrm{TM}} \end{bmatrix} \cdot \begin{bmatrix} \cos\left(\zeta^{\mathrm{ref}}\right) & \sin\left(\zeta^{\mathrm{ref}}\right) \\ -\sin\left(\zeta^{\mathrm{ref}}\right) & \cos\left(\zeta^{\mathrm{ref}}\right) \end{bmatrix}. \tag{3.40}$$

The polarisation-channel matrix of first-order reflection can be represented by $\mathbf{H}_{\mathrm{ref1}}$, which can be denoted as

$$\mathbf{H}_{\mathrm{ref1}} = \mathbf{T}_{z+w} \cdots \mathbf{T}_{z+1} \mathbf{R}_1 \mathbf{T}_z \cdots \mathbf{T}_1. \tag{3.41}$$

Fig. 3.2 illustrates the visualisation of rotation matrices between different reference frames during a series of reflections and transmissions, and Fig. 3.3 depicts the spherical coordinate systems for Tx and Rx.

3.3 RT Simulation

This section applies the polarimetric RT formulation to the specified indoor scenario. To isolate propagation-induced polarisation changes from receive pattern effects, the Rx is mod-

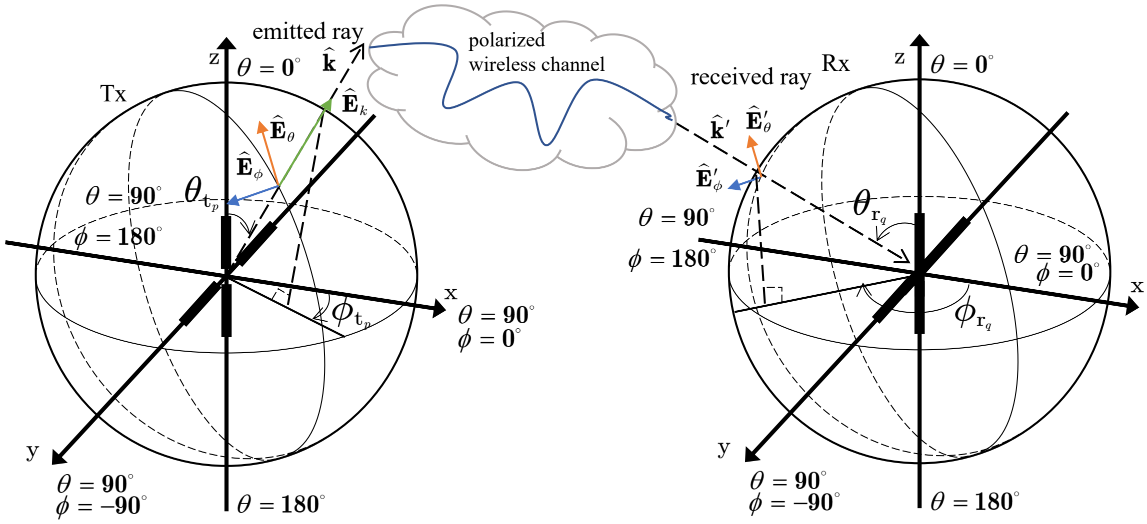

Fig. 3.3 Spherical coordinate systems for Tx and Rx.

elled as two colocated, orthogonally polarised isotropic sensors. Consequently, the receive gain is independent of AoA. This is a modelling assumption rather than a representation of a practical crossed dipole pattern.

3.3.1 System Description and Modelling Assumptions

The crossed dipole source comprises two short dipoles of length $\mathcal{L}$, with $\lambda/50 < \mathcal{L} \leq \lambda/10$. The simulations evaluate Rx locations beyond 5λ from the Tx, where the far-field approximation used for the angular field components is conservative for this electrically small source [151].

For each emitted far-field ray, the vertical and horizontal components are identified with the spherical θ- and ϕ-directed field components, respectively, as shown in Fig. 3.3 [153]. Antenna design details are outside the scope of this thesis; the source polarisation is specified by the complex ratio $E_\mathrm{V}/E_\mathrm{H}$, which includes both relative amplitude and phase.

3.3.2 Effective Channel Representation for Polarised Components

To isolate the phase difference introduced by propagation, the two transmitted polarisation components are assigned the same initial reference phase. Let $\bar{m}_{\mathrm{r}_q,\mathrm{t}_p}$ denote the effective coefficient between transmit port t_p and receive port r_q. It is written as the coherent sum of co-polarised and cross-polarised contributions [154]:

$$\begin{aligned}\bar{m}_{\mathrm{r}_q,\mathrm{t}_p} &= \sqrt{\frac{G_{\alpha_{xp},\phi_{\mathrm{t}_p},\theta_{\mathrm{t}_p}}}{L_{\mathrm{r}_q,\mathrm{t}_p}}}e^{j\Phi^{\mathrm{V}}_{\mathrm{r}_q}} + \sqrt{\frac{G_{\beta_{xp},\phi_{\mathrm{t}_p},\theta_{\mathrm{t}_p}}}{L_{\mathrm{r}_q,\mathrm{t}_{p'}}}}e^{j\Phi^{\mathrm{H}}_{\mathrm{r}_q}} \\ &= \sqrt{\alpha_{\mathrm{r}_q,\mathrm{t}_p}}m_{\mathrm{r}_q,\mathrm{t}_p} + \sqrt{\beta_{\mathrm{r}_q,\mathrm{t}_{p'}}}m_{\mathrm{r}_q,\mathrm{t}_{p'}},\end{aligned} \tag{3.42}$$

where $\Phi^{\mathrm{V}}_{\mathrm{r}_q}$ and $\Phi^{\mathrm{H}}_{\mathrm{r}_q}$ are the accumulated phases of the vertical and horizontal received components, respectively; they need not be equal. The quantities $L_{\mathrm{r}_q,\mathrm{t}_p}$ and $L_{\mathrm{r}_q,\mathrm{t}_{p'}}$ are linear path loss ratios, and G_α and G_β are the corresponding co-polarised and cross-polarised transmit antenna power gains. The alternative form defines the complex path coefficients m and the nonnegative propagation power gains α and β. The orthogonal transmit port is denoted by $\mathrm{t}_{p'}$, with $\mathrm{t}_{p'} \neq \mathrm{t}_p$. The effective matrix therefore decomposes as

$$\bar{\mathbf{M}} = \mathbf{M}_{\mathrm{C}} + \mathbf{M}_{\mathrm{X}}, \tag{3.43}$$

with

$$\mathbf{M}_{\mathrm{C}} = \begin{bmatrix} \sqrt{\alpha_{\mathrm{r}_1,\mathrm{t}_1}}m_{\mathrm{r}_1,\mathrm{t}_1} & \sqrt{\alpha_{\mathrm{r}_1,\mathrm{t}_2}}m_{\mathrm{r}_1,\mathrm{t}_2} \\ \sqrt{\alpha_{\mathrm{r}_2,\mathrm{t}_1}}m_{\mathrm{r}_2,\mathrm{t}_1} & \sqrt{\alpha_{\mathrm{r}_2,\mathrm{t}_2}}m_{\mathrm{r}_2,\mathrm{t}_2} \end{bmatrix}, \tag{3.44}$$

$$\mathbf{M}_{\mathrm{X}} = \begin{bmatrix} \sqrt{\beta_{\mathrm{r}_1,\mathrm{t}_2}}m_{\mathrm{r}_1,\mathrm{t}_2} & \sqrt{\beta_{\mathrm{r}_1,\mathrm{t}_1}}m_{\mathrm{r}_1,\mathrm{t}_1} \\ \sqrt{\beta_{\mathrm{r}_2,\mathrm{t}_2}}m_{\mathrm{r}_2,\mathrm{t}_2} & \sqrt{\beta_{\mathrm{r}_2,\mathrm{t}_1}}m_{\mathrm{r}_2,\mathrm{t}_1} \end{bmatrix}, \tag{3.45}$$

where $\mathbf{M}_{\mathrm{C}}$ and $\mathbf{M}_{\mathrm{X}}$ represent the channel of co-polarisation and cross-polarisation, respectively. Due to the assumption of isotropic Rx, antenna gains at Rx for rays with any AoA are the same. The expression for the XPD at Rx, considering the corresponding angle of

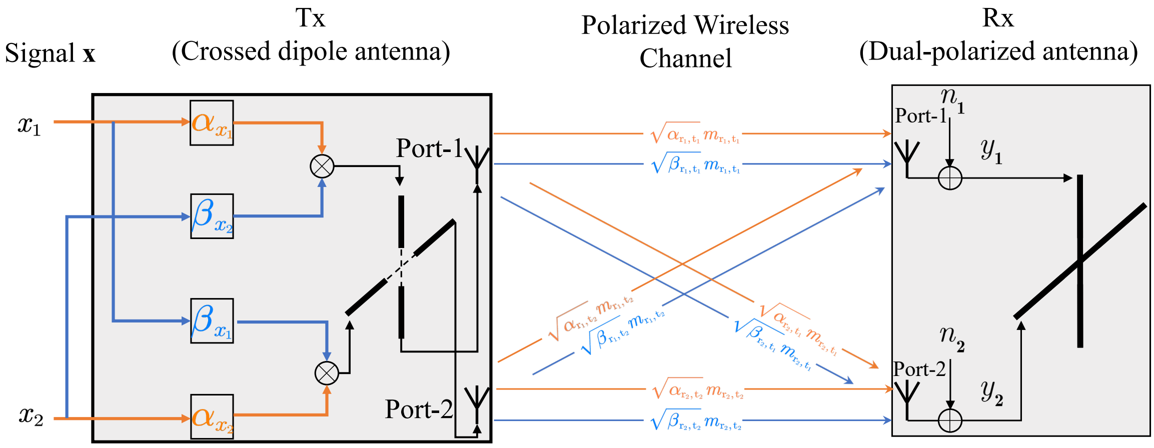

Fig. 3.4 Block diagram of a crossed dipole antenna system with co-polarisation and cross-polarisation propagation gains α and β.

departure (AoD) from t_p port of a crossed dipole antenna, can be given as

$$\mathcal{X}_{\mathrm{r}_q,\mathrm{t}_p,\phi_{\mathrm{t}_p},\theta_{\mathrm{t}_p}} = \left| \frac{\sqrt{\alpha_{\mathrm{r}_q,\mathrm{t}_p}} m_{\mathrm{r}_q,\mathrm{t}_p}}{\sqrt{\beta_{\mathrm{r}_q,\mathrm{t}_{p'}}} m_{\mathrm{r}_q,\mathrm{t}_{p'}}} \right|^2 = \frac{G_{\alpha_{x_p},\phi_{\mathrm{t}_p},\theta_{\mathrm{t}_p}} L_{\mathrm{r}_q,\mathrm{t}_{p'}}}{G_{\beta_{x_p},\phi_{\mathrm{t}_p},\theta_{\mathrm{t}_p}} L_{\mathrm{r}_q,\mathrm{t}_p}}. \tag{3.46}$$

For a given geometric path, the TE and TM components generally acquire different complex reflection or transmission coefficients. The corresponding path losses and polarisation gains therefore need not be equal: $L_{\mathrm{r}_q,\mathrm{t}_p} \neq L_{\mathrm{r}_q,\mathrm{t}_{p'}}$, $\alpha_{\mathrm{t}_p} \neq \alpha_{\mathrm{t}_{p'}}$, and $\beta_{\mathrm{t}_p} \neq \beta_{\mathrm{t}_{p'}}$. To display the mapping explicitly, the following expression considers only input x_1; the response to x_2 follows by exchanging the transmit port indices, and the complete response is obtained by linear superposition:

$$\begin{aligned} \bar{\mathbf{M}} &= \begin{bmatrix} \sqrt{\alpha_{\mathrm{r}_1,\mathrm{t}_1}} m_{\mathrm{r}_1,\mathrm{t}_1} + \sqrt{\beta_{\mathrm{r}_1,\mathrm{t}_2}} m_{\mathrm{r}_1,\mathrm{t}_2} & 0 \\ \sqrt{\alpha_{\mathrm{r}_2,\mathrm{t}_1}} m_{\mathrm{r}_2,\mathrm{t}_1} + \sqrt{\beta_{\mathrm{r}_2,\mathrm{t}_2}} m_{\mathrm{r}_2,\mathrm{t}_2} & 0 \end{bmatrix} \\ &= \begin{bmatrix} h_{\mathrm{VV}} & h_{\mathrm{VH}} \\ h_{\mathrm{HV}} & h_{\mathrm{HH}} \end{bmatrix} \begin{bmatrix} E_{x_1,\theta} & 0 \\ E_{x_1,\phi} & 0 \end{bmatrix}. \end{aligned} \tag{3.47}$$

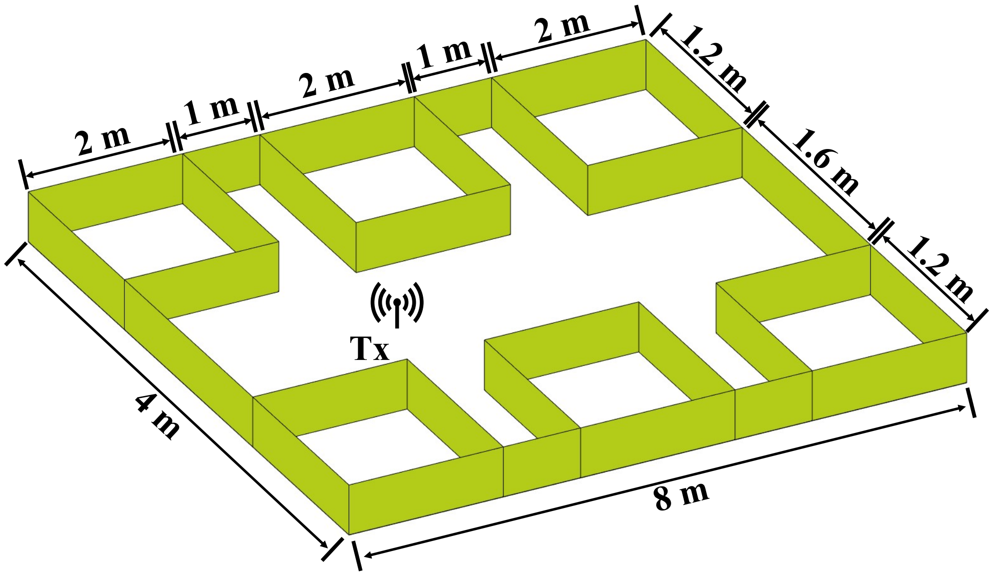

Fig. 3.5 Layout of the indoor scenario used for simulation.

For a first-order reflected path, the polarisation submatrix $\begin{bmatrix} h_{\mathrm{VV}} & h_{\mathrm{VH}} \\ h_{\mathrm{HV}} & h_{\mathrm{HH}} \end{bmatrix}$ is represented by $\mathbf{H}_{\mathrm{ref1}}$. The LOS and OLOS matrices, $\mathbf{H}_{\mathrm{LOS}}$ and $\mathbf{H}_{\mathrm{OLOS}}$, are evaluated separately because their ordered interaction products differ from that of the reflected path.

3.4 Polarised Channel Simulation and Performance Evaluation

This section presents the simulation setup, including the Tx and Rx configurations as well as the sampling parameters used in the analysis.

3.4.1 Simulation Scenario and Parameter Configuration

The considered environment is a 4 m $\times$ 8 m $\times$ 4 m rectangular hall containing six identical small rectangular rooms, as shown in Fig. 3.5. The simplified multiroom layout was selected to provide a controlled scenario containing LOS, OLOS transmission, and reflected NLOS regions. It enables multilayer wall transmission, specular reflection, and the associated

Table 3.2 Three-layer wall properties and frequency-dependent parameters.

Layer	Thickness	Permittivity		Conductivity	
	d	a	b	c	g
Concrete	30 mm	5.240	0	0.046	0.782
Brick	30 mm	3.910	0	0.024	0.160
Plasterboard	30 mm	2.730	0	0.009	0.940

polarisation transformations to be examined within a geometry that remains sufficiently simple for physical interpretation. The layout is representative of the propagation conditions investigated in this chapter, rather than of all indoor buildings. All walls, the ceiling, and the floor are modelled as three-layer composite structures stacked sequentially as concrete, brick, and plasterboard. The thickness and constitutive parameters of each layer are summarised in Table 3.2.

In terms of the conductivity and permittivity of different layers, there is typically substantial evidence indicating a frequency-dependent increase [155]. The trend is modelled and characterised using

$$\sigma(f) = c\, f_{(\mathrm{GHz})}^{g}, \qquad \varepsilon_r(f) = a\, f_{(\mathrm{GHz})}^{b}, \tag{3.48}$$

where a, b, c, and g are the layer-dependent empirical parameters listed in Table 3.2, and $f_{(\mathrm{GHz})}$ is the numerical frequency expressed in gigahertz (GHz).

The Tx operates at 5 GHz and is located at $(4.3, 4.1, 1.0)$ m in the Cartesian coordinate system of Fig. 3.5. RT simulations are performed at 250 000 Rx positions uniformly distributed across the analysis area, spanning from $x = 0$ m and $y = 0$ m to $x = 13$ m and $y = 8$ m, with grid spacings of 2.6 cm and 1.6 cm along the x- and y-axes, respectively. All Rx locations are placed at a height of 0.5 m. The present simulation includes LOS, OLOS transmission, and first-order reflected NLOS contributions. Diffraction, diffuse scattering, rough surface scattering, furniture scattering, human blockage, and higher order multipath interactions are not explicitly included in this chapter. These omitted mechanisms may modify the received power and XPR distributions, especially in cluttered rooms or at higher frequencies, where surface roughness and small objects become electrically significant. Consequently, the

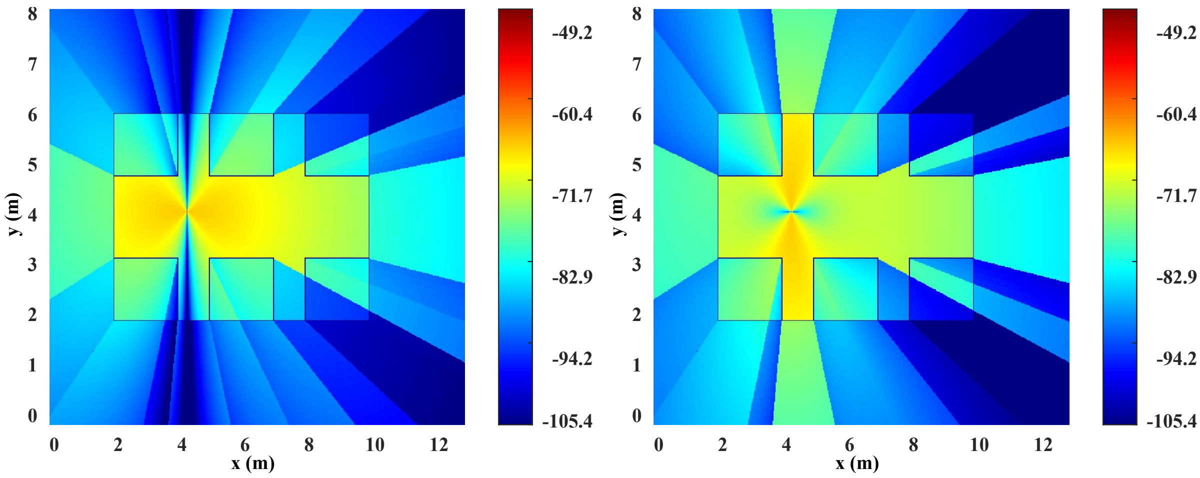

(a) P_{H}, LOS (OLOS) (b) P_{V}, LOS (OLOS)

Fig. 3.6 Received power (dBW) corresponding to LOS (OLOS) path for horizontal and vertical polarisation components.

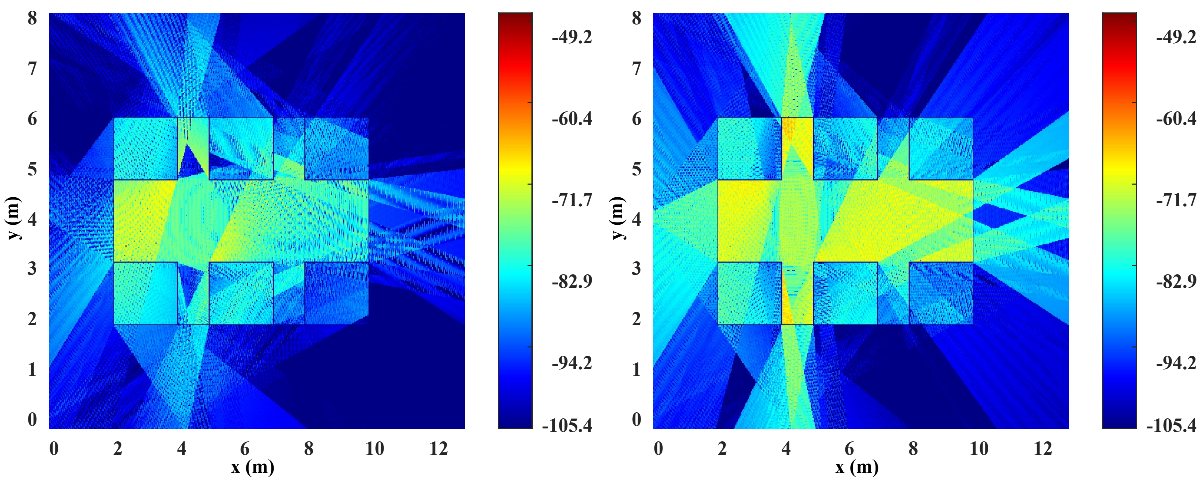

(a) P_{H}, RNLOS (b) P_{V}, RNLOS

Fig. 3.7 Received power (dBW) corresponding to RNLOS path for horizontal and vertical polarisation components.

quantitative results depend on the selected geometry and modelling assumptions and should be interpreted as a controlled, scenario-specific investigation of polarisation transformation by multilayer building materials, rather than as building-independent indoor predictions.

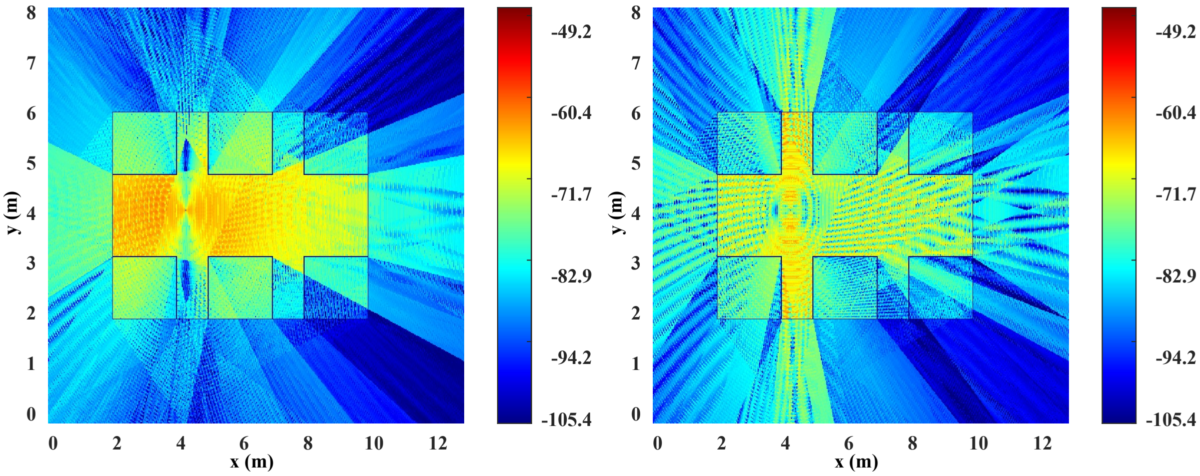

(a) P_{H}, LOS (OLOS) + RNLOS

(b) P_{V}, LOS (OLOS) + RNLOS

Fig. 3.8 Received power (dBW) corresponding to the superposition of LOS (OLOS) and RNLOS paths for horizontal and vertical polarisation components.

Excluding the antenna cross-polarisation isolation (XPI), the channel XPR is evaluated according to [61] as

$$\mathrm{XPR}_{\mathrm{V}} = \frac{|h_{\mathrm{VV}}|^2}{|h_{\mathrm{VH}}|^2}, \tag{3.49}$$

$$\mathrm{XPR}_{\mathrm{H}} = \frac{|h_{\mathrm{HH}}|^2}{|h_{\mathrm{HV}}|^2}. \tag{3.50}$$

3.4.2 Simulation Results and Discussion

Figs. 3.6 and 3.7 report the received power (dBW) of the horizontal and vertical polarisation components under LOS (OLOS) and RNLOS paths. The localised peaks and notches observed in the received-power maps align with the physical behaviour expected at multilayer interfaces, where the TM component undergoes Brewster angle transmission and both TE and TM components experience critical-angle total internal reflection. These phenomena give rise to pronounced polarisation-selective filtering. Apparent outliers in the heatmaps

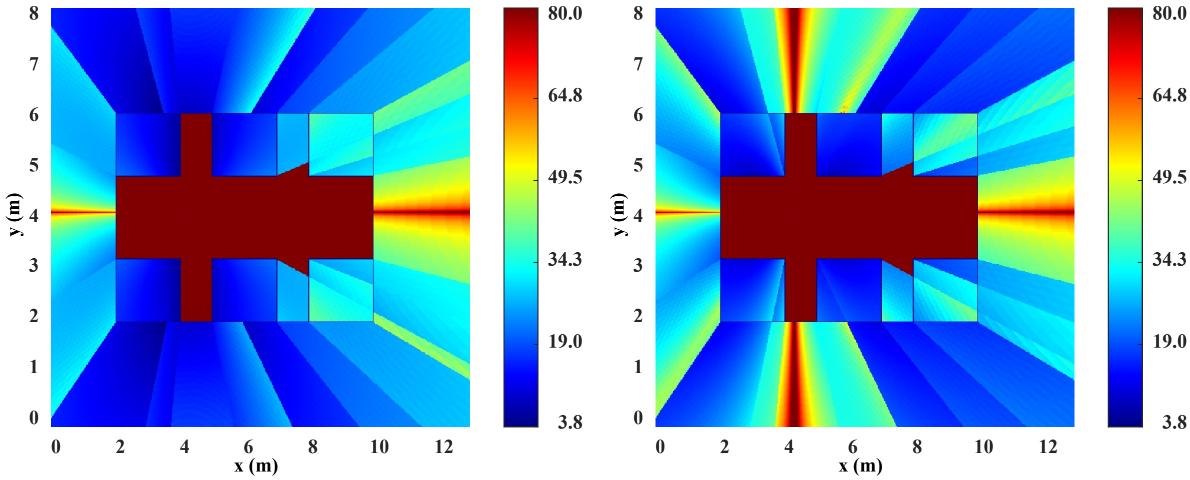

(a) XPR_H, LOS (OLOS) (b) XPR_V, LOS (OLOS)

Fig. 3.9 XPR (dB) corresponding to LOS (OLOS) path for horizontal and vertical polarisation components.

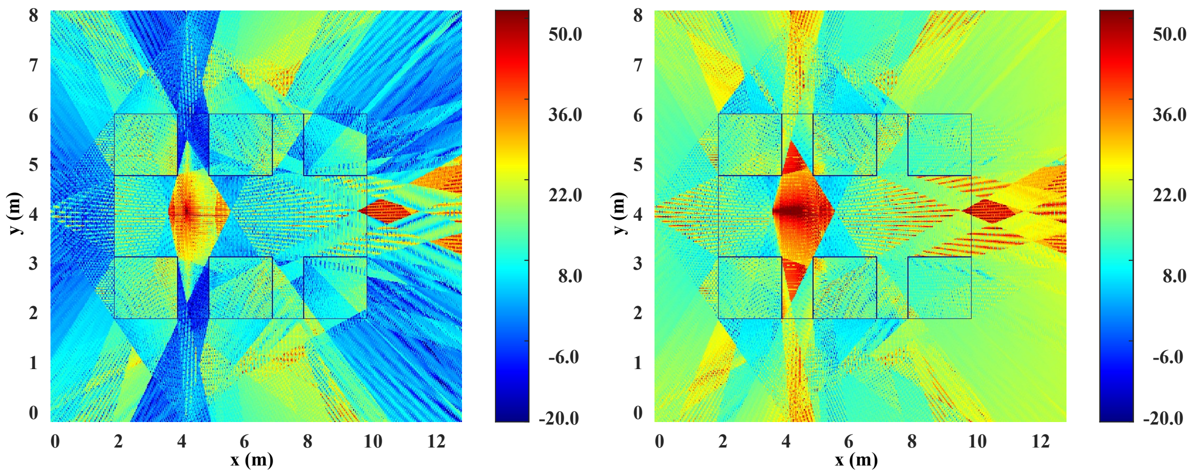

(a) XPR_H, RNLOS (b) XPR_V, RNLOS

Fig. 3.10 XPR (dB) corresponding to RNLOS path for horizontal and vertical polarisation components.

correspond to Rx locations where the incident rays approach these characteristic angles, resulting in either nearly vanishing or almost total reflection for a given polarisation.

Fig. 3.8 illustrates the total received power combining LOS (OLOS) and RNLOS paths. It is evident that the received powers of the horizontal and vertical polarisation components vary across different locations. This imbalance between the two polarisation components can

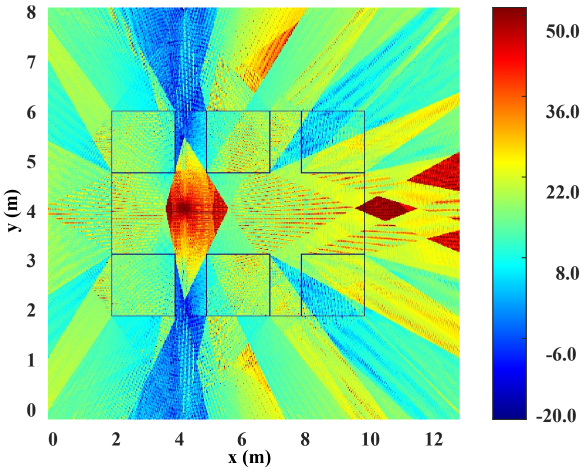

(a) XPR_H, LOS (OLOS) + RNLOS

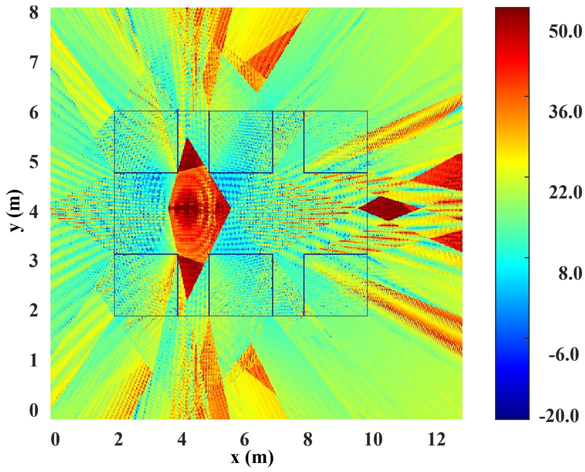

(b) XPR_V, LOS (OLOS) + RNLOS

Fig. 3.11 XPR (dB) corresponding to the superposition of LOS (OLOS) and RNLOS paths for horizontal and vertical polarisation components.

degrade the performance of modulation schemes that rely on the polarisation state for signal encoding. A detailed discussion of this effect will be presented in the next chapter.

Figs. 3.9 and 3.10 illustrate the XPR (dB) for horizontal and vertical references across LOS (OLOS) and RNLOS. In regions dominated by LOS propagation, the cross-polarised component can become numerically negligible, which causes the XPR to attain very large positive values. To maintain clarity in the plots and preserve the spatial trends, values exceeding 80 dB are truncated. It can be observed that even at identical Rx coordinates, the nature of the propagation path, whether LOS (OLOS) or RNLOS, produces substantial variations in XPR, indicating that a constant XPR value is inadequate for characterising polarised channels. In particular, reflections from multilayer walls produce TE- and TM-dependent phase and amplitude variations that perturb the balance between co-polarised and cross-polarised components, leading to spatially varying depolarisation across the environment.

3.5 Summary

This chapter developed a polarisation-aware RT formulation for frequency-dispersive multilayer partitions. The method tracks consistently oriented local TE/TM bases, applies complex multilayer reflection and transmission coefficients, and obtains the physical phase refraction direction from the real phase vector. In the specified simulation scenario, the resulting XPR varies with Rx position and path class; a single constant XPR therefore does not reproduce the spatial variation generated by the model. These results demonstrate the internal operation of the proposed formulation for LOS, OLOS, and first-order RNLOS paths within the included interaction set. They do not establish building-independent prediction accuracy.

The validation provided in this chapter is analytical and simulation-based. A direct experimental validation would require wideband polarimetric channel measurements in representative indoor environments, including the measurement of the full dual-polarised channel matrix over an Rx grid and comparison of measured co polar power, cross polar power, XPR, and phase statistics with the RT outputs. Full-wave simulations of canonical multilayer interfaces could also be used as intermediate benchmark cases. These validation steps are identified as important future work because the present chapter does not include measurement data for the polarisation-aware ray tracer.

Chapter 4

Performance Analysis and Optimisation of Indoor Polarisation Modulation via Polarisation-Aware RT

Overview

This chapter moves from the development of a polarisation-aware RT algorithm to its application in analysing indoor polarisation modulation. By employing the developed model, this chapter seeks to illuminate the interplay between depolarisation phenomena and system-level performance, thereby providing a physically grounded basis for subsequent optimisation studies.

Building upon the theoretical framework established in the preceding chapter, this chapter continues the investigation from the fundamental principles of wave propagation and the evolution of polarisation during reflection and transmission. With these foundations in place, the analysis turns to examine how depolarisation influences the behaviour of indoor wireless channels and, in particular, the performance of polarisation modulation schemes. Through comparative analysis and numerical evaluation, it is evident that conventional models of the XPR for multipath components, which often assume a constant value, fail to capture the complex variability observed in realistic propagation environments. The assumption of a constant XPR tends to either overstate or understate the degree of depolarisation, resulting in distorted estimates of cross-polarisation coupling and an incomplete characterisation of polarised propagation.

This discrepancy, together with the oversimplified handling of depolarisation in conventional channel models, results in notable performance degradation when PolarSK modulation is employed. To quantify this effect, the ABEP of various PolarSK schemes is evaluated under different system configurations and material conditions. The analysis reveals that EM interactions within unfavourable building materials inevitably give rise to an ABEP floor, which cannot be mitigated through diversity gain or constellation adjustment alone.

To overcome this limitation, an optimisation framework is developed to reduce the ABEP floor by simultaneously refining the complex permittivity and layer thickness of multilayer materials. Numerical evaluations demonstrate that this procedure substantially lowers the ABEP at high SNRs and, within the simulated scenarios and optimisation constraints considered in this chapter, suppresses or removes the observed floor effect across different constellation diagrams and MIMO systems. Finally, the physical mechanisms underlying this phenomenon are examined, offering insights into how depolarisation and multilayer material properties influence the achievable performance of indoor polarised wireless systems.

4.1 Introduction

As next-generation communication systems strive for ever greater data throughput and spectral efficiency, the use of the polarisation dimension has emerged as a promising approach to enhance transmission performance [156, 157]. In optical and satellite communication links, polarisation division multiplexing (PDM) has long been adopted to effectively expand channel capacity [156, 158]. Beyond multiplexing, the polarisation dimension also serves as a medium through which information can be directly embedded into the EM field by modulating its state of polarisation (SOP) [159]. This modulation concept, commonly referred to as PolarSK, was originally introduced in the context of optical communications [160], where the SOP remains remarkably stable and undergoes negligible distortion even across long-haul fibre propagation. With its inherent stability, PolarSK demonstrates enhanced reliability and efficiency when compared with traditional modulation schemes such as phase-shift keying (PSK) and differential phase-shift keying (DPSK) [161].

In contrast to optical fibre or satellite communication links, where the propagation medium maintains a relatively stable polarisation state, indoor wireless environments exhibit far greater variability and complexity as a consequence of their rich multipath characteristics. Within such environments, EM waves are repeatedly reflected, transmitted, diffracted, and scattered by surrounding structures, giving rise to depolarisation and distortion of the original polarised field [144]. These interactions redistribute part of the transmitted energy into orthogonal polarisation components, thereby altering the SOP of the received signal. The orientation and eccentricity of the polarisation ellipse, together with the relative amplitude and phase of the orthogonal components, may change substantially. As a result, the performance of polarisation-based modulation techniques such as PolarSK deteriorates, since signals initially transmitted with linear polarisation often arrive with elliptical characteristics [162]. This fundamental difficulty highlights the necessity of accurately modelling and predicting the behaviour of indoor polarised wireless channels.

In response to the growing need for accurate characterisation of indoor wireless propagation, early investigations sought to incorporate polarisation into geometry-based models so as to improve channel prediction fidelity [55]. Building on these efforts, geometrical theories describing depolarisation were formulated [64] and subsequently implemented in both deterministic geometry-based simulations [163] and stochastic depolarisation frameworks [164, 165]. Collectively, these early contributions provided the conceptual and analytical foundation for modelling polarised indoor MIMO channels [166–168], and they continue to inform ray-based techniques in present-day research [62, 169, 170].

Although these ray-based approaches have demonstrated considerable utility, several simplifying assumptions remain. In [62, 169, 170], reflection coefficients are typically drawn from predefined statistical distributions, without explicit consideration of their dependence on the EM properties of different building materials. Such approximations limit the physical accuracy of indoor polarised MIMO channel prediction. Furthermore, the assumption that the XPR is identical for all polarised components at the Rx imposes an additional restriction, reducing the predictive reliability of these models. Consequently, there is a clear need for a modelling framework that remains both physically consistent and computationally efficient in describing indoor polarised MIMO wireless channels.

While the aforementioned ray-based techniques have provided valuable insights into the polarised characteristics of indoor channels, their implications at the system-level remain insufficiently explored, particularly for polarisation-modulated schemes such as PolarSK. The influence of building materials on the behaviour of such systems has yet to be fully characterised. To the best of the author's knowledge, there is no unified theoretical framework that consistently links the EM and structural properties of indoor construction materials with system-level indicators such as the ABEP. Previous research has likewise tended to overlook the inherent relationship between the polarisation behaviour of wireless channels and the material composition of indoor environments. The absence of such a connection restricts the ability to predict and optimise the performance of PolarSK systems under realistic multipath conditions. To address this limitation, the present study adopts ABEP as the principal measure of performance and conducts a comprehensive analysis of how material properties govern the reliability of PolarSK transmission within indoor settings.

In this chapter, the scope of the previous investigations [146, 171–173] is extended to a unified and more comprehensive study of polarised indoor wireless channels. The work presented herein distinguishes itself through several key contributions that advance both the modelling of polarised propagation and the understanding of PolarSK system performance.

First, building upon the RT algorithm introduced in the previous chapter, this work employs the developed framework to predict the polarised characteristics of indoor wireless channels. To enhance the physical accuracy of propagation modelling, particular attention is given to the refraction process, where the exact physical angle of refraction in DPS materials is analytically derived. This refinement ensures that the ray interactions remain consistent with the underlying EM theory and improves the overall fidelity of the simulation results.

Secondly, the performance of PolarSK modulation schemes is examined under various system configurations. The simulation results indicate that, under identical conditions, PolarSK exhibits enhanced performance in NLOS environments relative to LOS settings when the SNR is below 40 dB in a 1×4 MIMO configuration. This behaviour is attributed to the increased spatial correlation present in NLOS MIMO channels. When the SNR exceeds 40 dB, however, an irreducible ABEP, which is commonly referred to as the ABEP floor, emerges in NLOS conditions, while it remains absent in LOS scenarios. Similar ABEP floor phenomena are also observed across different MIMO configurations and constellation structures.

Thirdly, to mitigate the ABEP floor, an optimisation framework is formulated that jointly adjusts the permittivity, conductivity, and thickness of each layer within a multilayer wall. This formulation provides a straightforward yet effective approach to reducing the ABEP floor of PolarSK systems and lays the foundation for further refinements in material-aware channel optimisation.

Fourthly, the underlying mechanisms responsible for the observed ABEP floor are analysed. It is found that the vertical polarisation component of the crossed dipole antenna becomes imbalanced with respect to the horizontal component. This imbalance is further accentuated by the structural layout and material composition of the indoor environment—for example, the reflection coefficient of the vertically polarised electric field approaches zero at the Brewster angle. Additionally, small-scale fading introduced by multipath propagation may cause one or both polarisation components to vanish locally, which in turn produces extreme polarisation imbalance. The disappearance of a single component ultimately manifests as the ABEP floor observed in NLOS propagation conditions.

The remainder of this chapter is organised as follows. Section 4.2 describes the transmission principles of PolarSK. Section 4.3 applies the RT framework to construct the PolarSK channel model. Section 4.4 analyses the ABEP performance of various PolarSK schemes and identifies the emergence of ABEP floors. Section 4.5 presents an iterative optimisation algorithm for mitigating the floor effect, together with numerical results and physical interpretations. The chapter concludes in Section 4.7 with a summary of the principal findings.

The notation of Chapter 4 is summarised in Table 4.1.

Table 4.1 Notation of Chapter 4

Notation	**Definition**
j	Imaginary unit, $j^2 = -1$.
$(\cdot)^{\mathrm{H}}$	Hermitian-transpose operator.
$(\cdot)^*$	Complex conjugation operator.
$\|\cdot\|_F$	Frobenius norm of a matrix.
$\|\cdot\|_2$	Euclidean norm operator for a vector.
$\lvert\cdot\rvert_{\mathrm{e}}$	Elementwise magnitude operator for a matrix.
K	Number of discrete PolarSK amplitude-angle levels.
k	Index of the transmitted PolarSK amplitude-angle level.
$\hat{k}$	Index of the competing PolarSK amplitude-angle level.
M	MPSK modulation order applied to each polarisation branch.
q_{V}	MPSK phase index of the transmitted vertical component.
q_{H}	MPSK phase index of the transmitted horizontal component.
$\hat{q}_{\mathrm{V}}$	MPSK phase index of the competing vertical component.
$\hat{q}_{\mathrm{H}}$	MPSK phase index of the competing horizontal component.
ε_k	PolarSK amplitude angle associated with level k.
P	Total number of PolarSK symbols defined by $P = KM^2$.
p	Index of the transmitted PolarSK symbol associated with $(k, q_{\mathrm{V}}, q_{\mathrm{H}})$.
$\hat{p}$	Index of the competing PolarSK symbol selected by the detector.
$\mathbf{x}_{k,q_{\mathrm{V}},q_{\mathrm{H}}} \equiv \mathbf{x}_p$	Transmitted 2×1 PolarSK Jones vector indexed by p.
$x_{p,\mathrm{V}}$	Vertical complex component of the PolarSK vector $\mathbf{x}_p$.
$x_{p,\mathrm{H}}$	Horizontal complex component of the PolarSK vector $\mathbf{x}_p$.

Continued on next page

Table 4.1: Notation of Chapter 4 (Continued)

Notation	**Definition**
T	Number of channel uses in a codeword.
t	Discrete channel-use index.
$\mathbf{c}_t$	Transmitted PolarSK vector at channel-use index t.
$\mathbf{l}_t$	Competing PolarSK vector at channel-use index t.
$\mathbf{C}$	Transmitted codeword formed by $\mathbf{c}_0,\ldots,\mathbf{c}_{T-1}$.
$\mathbf{L}$	Competing codeword formed by $\mathbf{l}_0,\ldots,\mathbf{l}_{T-1}$.
$\Delta\mathbf{x}(p,\hat{p})$	Difference vector between $\mathbf{x}_p$ and $\mathbf{x}_{\hat{p}}$.
$N[\cdot]$	Hamming distance between the binary labels of two PolarSK symbols.
$\Pr[\cdot]$	Probability of the specified event.
$\mathcal{Q}(\cdot)$	Gaussian $\mathcal{Q}$-function.
ρ	Average signal-to-noise ratio used in the error-probability analysis.
$B(a,b)$	Beta function defined by $B(a,b) = \Gamma(a)\Gamma(b)/\Gamma(a+b)$.
$\Gamma(\cdot)$	Gamma function.
$F_1(\cdot)$	Appell hypergeometric function of the first kind.
N_{T}	Number of dual-polarised transmit antenna locations.
N_{R}	Number of dual-polarised receive antenna locations.
n_{R}	Receive-location index.
m_{R}	Summation index over receive locations in the channel-normalisation factor.
$\mathbf{H}_t$	Polarised MIMO channel matrix at channel-use index t.
$\mathbf{H}$	Polarised wireless channel matrix.
h_{ab}	Channel coefficient from transmit polarisation b to receive polarisation a.
$\bar{\mathbf{h}}$	Unnormalised composite dual-polarised RT channel matrix.

Continued on next page

Table 4.1: Notation of Chapter 4 (Continued)

Notation	Definition
$\bar{\mathbf{h}}_{n_\mathrm{R}}$	Unnormalised 2×2 dual-polarised subchannel at receive location n_R.
$\tilde{\mathbf{h}}_{n_\mathrm{R}}$	Frobenius-normalised 2×2 subchannel at receive location n_R.
$\tilde{h}_{ab,n_\mathrm{R}}$	Normalised channel coefficient from transmit polarisation b to receive polarisation a at location n_R.
$\tilde{\mathbf{H}}$	Complete Frobenius-normalised polarised MIMO channel matrix.
$\tilde{\mathbf{h}}_\mathrm{V}$	Column of $\tilde{\mathbf{H}}$ associated with vertical transmission.
$\tilde{\mathbf{h}}_\mathrm{H}$	Column of $\tilde{\mathbf{H}}$ associated with horizontal transmission.
$\mathbf{H}_\mathrm{iid}$	Random channel matrix with independent $\mathcal{CN}(0,1)$ entries.
N_LOS	Number of LOS channel samples used for covariance estimation.
N_NLOS	Number of NLOS channel samples used for covariance estimation.
n_p	Channel-sample index used in the covariance estimation.
$\mathbf{H}_{\mathrm{LOS},n_p}$	LOS channel matrix of sample n_p.
$\mathbf{H}_{\mathrm{NLOS},n_p}$	NLOS channel matrix of sample n_p.
$\mathbf{R}_{0,\mathrm{RX}}$	Unnormalised receive-side sample covariance matrix.
$\mathbf{R}_{0,\mathrm{TX}}$	Unnormalised transmit-side sample covariance matrix.
$\mathbf{R}_\mathrm{RX}$	Normalised receive-side complex correlation matrix.
$\mathbf{R}_\mathrm{TX}$	Normalised transmit-side complex correlation matrix.
$\mathbf{H}_\mathrm{corr}$	Spatially correlated Rayleigh channel matrix generated by the Kronecker model.
x_a	x-coordinate of the Rx-grid point indexed by a.
y_b	y-coordinate of the Rx-grid point indexed by b.
z_c	z-coordinate of the Rx-grid point indexed by c.

Continued on next page

Table 4.1: Notation of Chapter 4 (Continued)

Notation	Definition
X	Number of Rx-grid samples along the x-direction.
Y	Number of Rx-grid samples along the y-direction.
Z	Number of Rx-grid samples along the z-direction.
$\mathrm{ABEP}_{\mathrm{avg}}$	ABEP averaged with equal weight over the specified Rx grid.
$\overline{\mathrm{ABEP}}_{\mathrm{avg}}$	Final spatially averaged ABEP produced by the coordinatewise optimisation.
s	Material layer index.
N	Number of material layers.
ε_s	Permittivity of material layer s.
$\mu_{r,s}$	Relative permeability of material layer s.
μ_s	Permeability of material layer s.
σ_s	Conductivity of material layer s.
d_s	Thickness of material layer s.
κ_s	Thermal conductivity of material layer s.
$\mathcal{A}_s$	Feasible set of absolute-permittivity values for material layer s.
$\mathcal{B}_s$	Feasible set of conductivity values for material layer s.
$\mathcal{C}_s$	Feasible set of thickness values for material layer s.
ι	Number of material parameters included in the optimisation.
i	Index of an optimisation variable.
v_i	Current value of optimisation variable i.
$v_i^{(\mathrm{i})}$	Value of optimisation variable i after coordinate sweep i.
$\bar{v}_i$	Final accepted value of optimisation variable i.

Continued on next page

Table 4.1: Notation of Chapter 4 (Continued)

Notation	**Definition**
ℓ_i	Lower bound of optimisation variable i.
u_i	Upper bound of optimisation variable i.
h_i	Grid spacing of the candidate set for optimisation variable i.
$\mathcal{S}_i$	Discrete candidate set for optimisation variable i.
G	Number of grid points in each candidate set.
$\mathfrak{i}$	Index of a complete coordinate sweep.
$\mathcal{I}$	Maximum number of complete coordinate sweeps.
$\mathcal{P}$	Fractional reduction in the spatially averaged ABEP produced by a coordinate update.
$\mathcal{P}_{\text{th}}$	Minimum fractional ABEP reduction required to accept a coordinate update.
$\mathcal{T}$	Optional lower bound on the total wall thickness.
$\mathcal{U}$	Optional upper bound on the wall thermal transmittance.
Y	Polarisation label of a transmit branch.
$\mathbf{W}_{\text{t,Y}}$	Complex Poynting vector radiated by transmit branch Y.
$P_{\text{t,Y}}$	Complex power radiated by transmit branch Y.
S_{t}	Closed spherical integration surface surrounding the transmit dipole.
$\hat{\mathbf{n}}_s$	Outward unit normal vector on S_{t}.
I_0	Complex current amplitude exciting an infinitesimal-dipole branch.
l	Length of an infinitesimal-dipole branch.
r	Radius of the spherical power-integration surface.
λ	Free-space wavelength.

Continued on next page

Table 4.1: Notation of Chapter 4 (Continued)

Notation	Definition
k_0	Free-space wavenumber defined by $k_0 = 2\pi/\lambda$.
Υ_t	Transmitted vertical-to-horizontal power ratio.
Υ_r	Received vertical-to-horizontal channel-power ratio.
$D_\mathrm{ln}(x,y,z)$	Logarithmic difference between the received and transmitted polarisation-power ratios at (x,y,z).
MAD_ln	Mean absolute logarithmic deviation over the specified Rx grid.
β_air	Phase constant in air defined by $\beta_\mathrm{air} = 2\pi/\lambda$.
E_0^+	Complex amplitude of the forward plane wave at $y = 0$.
E_0^-	Complex amplitude of the reflected plane wave at $y = 0$.
R	Complex standing-wave reflection coefficient defined by $R = E_0^-/E_0^+$.
$E_x(y)$	Resultant x-directed standing-wave electric-field component at position y.
$R_{\tilde{h}_\mathrm{HH}}$	Reflection coefficient applied to $\tilde{h}_\mathrm{HH}$ in the illustrative Channel B model.
m	Integer index of the standing-wave extrema.
L	Spatial interval used to average the standing-wave PEP or ABEP.

4.2 PolarSK Transmission Scheme

In this chapter, the polarisation states are described using Jones vectors, which are derived from the corresponding Stokes parameters in a standard orthogonal coordinate system. To clarify the basic idea of the PolarSK modulation scheme, its signal constellation is presented, offering an intuitive geometric view of how information is encoded in the polarisation domain.

The analytical formulation of the PolarSK signal is given by

$$\mathbf{x}_{k,q_\mathrm{V},q_\mathrm{H}} = \begin{bmatrix} x_{p,\mathrm{V}} \\ x_{p,\mathrm{H}} \end{bmatrix} = \begin{bmatrix} \cos\varepsilon_k e^{\left(j\frac{2\pi q_\mathrm{V}}{M}\right)} \\ \sin\varepsilon_k e^{\left(j\frac{2\pi q_\mathrm{H}}{M}\right)} \end{bmatrix}, \tag{4.1}$$

In this context, the variable $p \in \{0,1,\ldots,P-1\}$ identifies the index corresponding to each polarisation state within the system. The parameter $\varepsilon_k \in [0,\pi/2]$ represents the tilt angle of the elliptical polarisation, which determines the relative amplitudes of the vertically and horizontally polarised components. The index $k \in \{1,2,\ldots,K\}$ specifies the discrete tilt level associated with a particular polarisation state, while the phase indices q_V and q_H take values from $\{1,2,\ldots,M\}$ according to an MPSK constellation employing Gray coding. Thus, $\mathbf{x}_{k,q_\mathrm{V},q_\mathrm{H}}$ is a 2×1 Jones vector whose entries correspond to the vertical and horizontal complex field components. The subscript p used in $x_{p,\mathrm{V}}$ and $x_{p,\mathrm{H}}$ denotes the polarisation state index associated with the triplet $(k,q_\mathrm{V},q_\mathrm{H})$. The total number of available PolarSK symbols is $P = KM^2$, where K is the number of discrete tilt levels and M is the MPSK modulation order used independently on the vertical and horizontal branches. The ABEP of the PolarSK modulation scheme is then evaluated using the union bound approach, which can be expressed as:

$$\begin{aligned} ABEP \leqslant & \frac{1}{K\log_2\left(M^2K\right)} \sum_{\hat{q}_\mathrm{V}=\{1,2:2:M\}} \sum_{\hat{q}_\mathrm{H}=\{1,2:2:M\}} \\ & \times \sum_{k=1}^{K}\sum_{\hat{k}=1}^{K} N\left[(k,1,1)\to\left(\hat{k},\hat{q}_\mathrm{V},\hat{q}_\mathrm{H}\right)\right] \\ & \times \Pr\left[(k,1,1)\to\left(\hat{k},\hat{q}_\mathrm{V},\hat{q}_\mathrm{H}\right)\right], \end{aligned} \tag{4.2}$$

where $\Pr[\cdot]$ denotes the pairwise error probability (PEP), and $N[\cdot]$ refers to the Hamming distance between the transmitted and detected symbol sequences. The validity of this union bound has been thoroughly examined in [146], where its accuracy in capturing the performance characteristics of the PolarSK scheme under the considered conditions has been clearly demonstrated.

Consider the transmitted codeword $\mathbf{C} = [\mathbf{c}_0, \ldots, \mathbf{c}_{T-1}]$ corresponding to symbol vector $\mathbf{x}_p$. The PEP is the conditional probability that a maximum likelihood (ML) detector selects a competing codeword $\mathbf{L} = [\mathbf{l}_0, \ldots, \mathbf{l}_{T-1}]$ instead of $\mathbf{C}$. Conditioned on a particular set of channel realisations $\{\mathbf{H}_t\}_{t=0}^{T-1}$, the PEP is expressed as in [174].

$$\Pr\left(\mathbf{C} \to \mathbf{L} \,\middle|\, \{\mathbf{H}_t\}_{t=0}^{T-1}\right) = \mathcal{Q}\left(\sqrt{\frac{\rho}{2}\sum_{t=0}^{T-1} \|\mathbf{H}_t\left(\mathbf{c}_t - \mathbf{l}_t\right)\|_F^2}\right). \tag{4.3}$$

where t denotes the discrete time index corresponding to the sampling instant within one symbol duration, and $\|\cdot\|_F^2$ represents the squared Frobenius norm. The channel matrix $\mathbf{H}_t$ is assumed to remain constant throughout each symbol interval, and for simplicity of notation, the time index t is omitted in the subsequent expressions. Under this assumption, the conditional PEP associated with a transmitted signal $\mathbf{x}_p$ and its erroneously decoded counterpart $\mathbf{x}_{\hat{p}}$ can be formulated as

$$\begin{aligned}
\Pr(\mathbf{C} \to \mathbf{L} \,|\mathbf{H}) &= \mathcal{Q}\left(\sqrt{\frac{\rho}{2}\|\mathbf{H}(\mathbf{C}-\mathbf{L})\|_F^2}\right) \\
&= \mathcal{Q}\left(\sqrt{\frac{\rho}{2}\left\|\mathbf{H}\left(\mathbf{x}_p - \mathbf{x}_{\hat{p}}\right)\right\|_2^2}\right) \\
&= \mathcal{Q}\left(\sqrt{\frac{\rho}{2}\|\mathbf{H}\Delta\mathbf{x}(p,\hat{p})\|_2^2}\right),
\end{aligned} \tag{4.4}$$

where ρ denotes the average SNR, and the term $\Delta\mathbf{x}(p,\hat{p})$ is defined as follows:

$$\Delta\mathbf{x}(p,\hat{p}) = \begin{bmatrix} \cos\varepsilon_k e^{\left(j\frac{2\pi q_{\mathrm{V}}}{M}\right)} - \cos\varepsilon_{\hat{k}} e^{\left(j\frac{2\pi \hat{q}_{\mathrm{V}}}{M}\right)} \\ \sin\varepsilon_k e^{\left(j\frac{2\pi q_{\mathrm{H}}}{M}\right)} - \sin\varepsilon_{\hat{k}} e^{\left(j\frac{2\pi \hat{q}_{\mathrm{H}}}{M}\right)} \end{bmatrix}. \tag{4.5}$$

The function $\mathcal{Q}(\cdot)$ denotes the Gaussian $\mathcal{Q}$-function, defined as

$$\mathcal{Q}(x) \triangleq \Pr(y \geq x) = \frac{1}{\sqrt{2\pi}}\int_x^{\infty} e^{-\frac{y^2}{2}}\,\mathrm{d}y. \tag{4.6}$$

Since this integral cannot be expressed in a closed analytical form using elementary functions, several equivalent formulations have been proposed. One of the most widely used representations is Craig's formula [175], given by

$$\mathcal{Q}(x) = \frac{1}{\pi} \int_0^{\frac{\pi}{2}} e^{-\frac{x^2}{2\sin^2\psi}} \, \mathrm{d}\psi. \tag{4.7}$$

4.3 Channel Modelling of the PolarSK System Using RT

In this section, the LOS, OLOS, and RNLOS propagation rays are taken into account to characterise the impact of building materials on polarised indoor wireless channels. Each ray is modelled deterministically according to the Friis transmission relation, and the total received field is obtained by coherently summing the contributions from all propagation paths. For a given pair of transmit and receive antennas, the composite received signal can thus be written as

$$\mathbf{r}(t) = \frac{\lambda}{4\pi} \left[\left(\mathbf{G}_{\xi,\mathrm{Rx}} \mathbf{h}_{\xi} \mathbf{G}_{\xi,\mathrm{Tx}}\right) \frac{\mathbf{u}(t) e^{-\frac{j2\pi l_{\xi}}{\lambda}}}{l_{\xi}} + \sum_{i=1}^{N_{\mathfrak{r}}} \left(\mathbf{G}_{\mathfrak{r},\mathrm{Rx},i} \mathbf{h}_{\mathfrak{r},i} \mathbf{G}_{\mathfrak{r},\mathrm{Tx},i}\right) \frac{\mathbf{u}\left(t-\tau_{\mathfrak{r},i}\right) e^{-\frac{j2\pi l_{\mathfrak{r},i}}{\lambda}}}{l_{\mathfrak{r},i}} \right] e^{j2\pi f_c t} \tag{4.8}$$

where $\mathbf{u}(t) = \mathbf{x}_{k,q_\mathrm{V},q_\mathrm{H}}(t)$ denotes the complex baseband vector signal corresponding to the PolarSK modulation. The matrices $\mathbf{G}_{\xi,\mathrm{Tx}}$ and $\mathbf{G}_{\xi,\mathrm{Rx}}$ represent the field radiation patterns of the transmitting and receiving antennas, respectively, in the $\xi \in \{\mathrm{LOS}, \mathrm{OLOS}\}$ direction. The term $\mathbf{h}_{\xi}$ denotes the dual-polarised channel matrix, while l_{ξ} specifies the propagation distance. Under LOS conditions, $\mathbf{h}_{\xi}$ reduces to the identity matrix. For the OLOS case, the total propagation distance l_{OLOS} can be partitioned into two components: (i) $l_{\mathrm{OLOS,air}}$, representing the free-space propagation path, and (ii) $l_{\mathrm{OLOS,wall}}$, corresponding to the segment through the multilayer wall. The value of $l_{\mathrm{OLOS,air}}$ is determined geometrically from the spatial relationship between the propagation ray and the indoor environment, whereas $l_{\mathrm{OLOS,wall}}$ is given by

$$l_{\mathrm{OLOS,wall}} = \sum_{s=1}^{N} \frac{d_s}{\cos\rho_s}, \tag{4.9}$$

The physical phase refraction angle ρ_s is given by (3.33). For each RNLOS component indexed by i, the matrices $\mathbf{G}_{\mathfrak{r},\mathrm{Tx},i}$ and $\mathbf{G}_{\mathfrak{r},\mathrm{Rx},i}$ describe the radiation patterns of the transmitting and receiving antennas, respectively. The dual-polarised channel associated with this path is represented by $\mathbf{h}_{\mathfrak{r},i}$, while $l_{\mathfrak{r},i}$ and $\tau_{\mathfrak{r},i}$ denote its propagation distance and the relative delay with respect to the corresponding LOS or OLOS path. The subscript $\mathfrak{r}$ identifies RNLOS rays, $N_{\mathfrak{r}}$ specifies their total count, and f_c denotes the carrier frequency. The matrices $\mathbf{h}_{\mathrm{OLOS}}$ and $\mathbf{h}_{\mathfrak{r},i}$ are evaluated according to (3.41). Under the narrowband assumption adopted in this work, the approximation $\mathbf{u}(t) \approx \mathbf{u}(t-\tau_{\mathfrak{r},i})$ holds for all i. Consequently, the time variable t in (4.8) can be omitted without loss of generality, and the received signal may be equivalently written as

$$\mathbf{r} = \bar{\mathbf{h}}\mathbf{u} + \frac{\mathbf{w}}{\sqrt{\rho}}, \tag{4.10}$$

where $\bar{\mathbf{h}}$ is given by

$$\bar{\mathbf{h}} = \frac{\lambda}{4\pi}\left[\left(\mathbf{G}_{\xi,\mathrm{Rx}}\mathbf{h}_{\xi}\mathbf{G}_{\xi,\mathrm{Tx}}\right)\frac{e^{-\frac{j2\pi l_{\xi}}{\lambda}}}{l_{\xi}} + \sum_{i=1}^{N_{\mathfrak{r}}}\left(\mathbf{G}_{\mathfrak{r},\mathrm{Rx},i}\mathbf{h}_{\mathfrak{r},i}\mathbf{G}_{\mathfrak{r},\mathrm{Tx},i}\right)\frac{e^{-\frac{j2\pi l_{\mathfrak{r},i}}{\lambda}}}{l_{\mathfrak{r},i}}\right]. \tag{4.11}$$

To compare channel structures independently of their mean path gain, the RT transfer matrices are normalised so that the average squared Frobenius norm per receive location equals two. Equivalently, the average gain per transmitted polarisation is unity. Considering a representative MIMO configuration of dimension $1 \times N_{\mathrm{R}}$, comprising a single dual-polarised transmit antenna and N_{R} dual-polarised receive antennas, the subchannel associated with a given transmit–receive antenna pair can be expressed in its normalised form as

$$\tilde{\mathbf{h}}_{n_{\mathrm{R}}} = \frac{\sqrt{2}\,\bar{\mathbf{h}}_{n_{\mathrm{R}}}}{\sqrt{\frac{1}{N_{\mathrm{R}}}\sum_{m_{\mathrm{R}}=1}^{N_{\mathrm{R}}}\left\|\bar{\mathbf{h}}_{m_{\mathrm{R}}}\right\|_F^2}}, \tag{4.12}$$

where n_{R} is the receive-location index and m_{R} is the dummy index used in the normalising sum. The 2×2 subchannel $\tilde{\mathbf{h}}_{n_{\mathrm{R}}}$ is

$$\tilde{\mathbf{h}}_{n_{\mathrm{R}}} = \begin{bmatrix} \tilde{h}_{\mathrm{VV},n_{\mathrm{R}}} & \tilde{h}_{\mathrm{VH},n_{\mathrm{R}}} \\ \tilde{h}_{\mathrm{HV},n_{\mathrm{R}}} & \tilde{h}_{\mathrm{HH},n_{\mathrm{R}}} \end{bmatrix}. \tag{4.13}$$

Accordingly, the complete normalised MIMO channel matrix, denoted by $\tilde{\mathbf{H}} \in \mathbb{C}^{2N_{\mathrm{R}} \times 2}$, is formed as

$$\begin{aligned} \tilde{\mathbf{H}} &= \left[\tilde{\mathbf{h}}_1^{\mathrm{H}} \cdots \tilde{\mathbf{h}}_{n_{\mathrm{R}}}^{\mathrm{H}} \cdots \tilde{\mathbf{h}}_{N_{\mathrm{R}}}^{\mathrm{H}}\right]^{\mathrm{H}} \\ &= \left[\tilde{\mathbf{h}}_{\mathrm{V}}\ \tilde{\mathbf{h}}_{\mathrm{H}}\right], \end{aligned} \tag{4.14}$$

where $(\cdot)^{\mathrm{H}}$ denotes the complex conjugate transpose operator. The indoor environment is the scenario defined in Section 3.4.1. The walls, ceiling, and floor are represented by the three-layer material model in Table 3.2. The Tx operates at a carrier frequency of 5 GHz with a transmit power of -15 dBW (32 mW), and the RT simulations are conducted over 250,000 uniformly distributed Rx positions.

Fig. 4.1 illustrates the ABEP performance of PolarSK for unnormalised 1×1, 1×2, and 1×4 MIMO configurations employing a $K = 2$, $M = 2$ signal constellation at an SNR of 55 dB, 65dB and 75dB. The results indicate that an increase in the number of receive antennas leads to a reduction in ABEP, highlighting the effect of diversity gain. Nevertheless, to obtain a representative assessment of system performance in an indoor environment, it is more appropriate to consider the spatially averaged ABEP rather than pointwise measurements, as discussed in the subsequent sections.

4.4 ABEP Analysis

The ABEP is evaluated for three channel models: the RT channel, a dual-polarised independent and identically distributed (i.i.d.) Rayleigh channel, and a Rayleigh channel with spatial

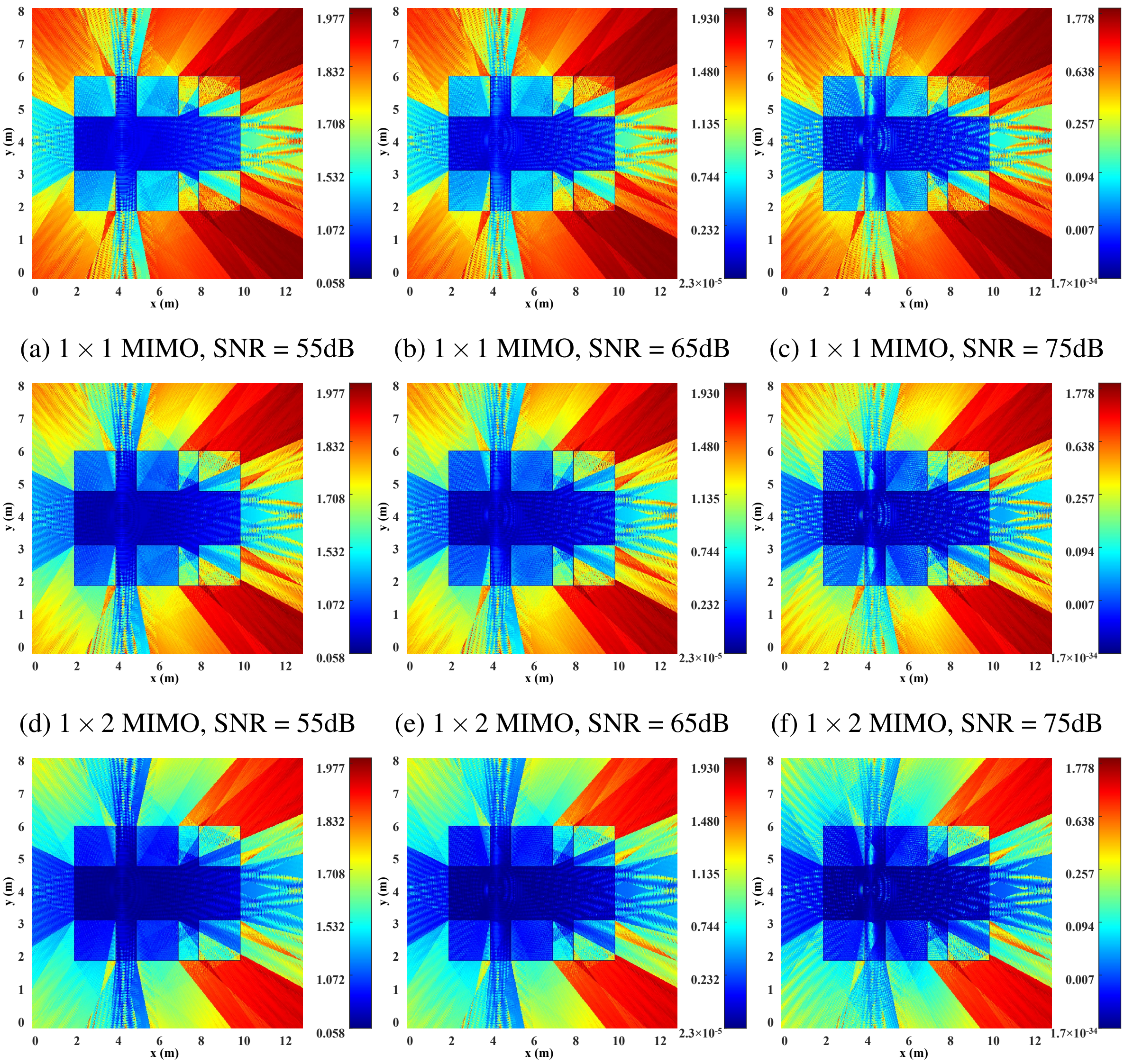

(a) 1×1 MIMO, SNR = 55dB (b) 1×1 MIMO, SNR = 65dB (c) 1×1 MIMO, SNR = 75dB

(d) 1×2 MIMO, SNR = 55dB (e) 1×2 MIMO, SNR = 65dB (f) 1×2 MIMO, SNR = 75dB

(g) 1×4 MIMO, SNR = 55dB (h) 1×4 MIMO, SNR = 65dB (i) 1×4 MIMO, SNR = 75dB

Fig. 4.1 The ABEP performance of PolarSK for unnormalised 1×1, 1×2 and 1×4 MIMO systems employing $K=2$, $M=2$ signal constellation under 55dB, 65dB and 75dB SNR.

correlation (SC). For the specified Rx grid, the spatially averaged ABEP is

$$ABEP_{\text{avg}} = \frac{1}{XYZ}\sum_{a=1}^{X}\sum_{b=1}^{Y}\sum_{c=1}^{Z} ABEP\,(x_a, y_b, z_c). \tag{4.15}$$

where x_a, y_b, and z_c are the sampling coordinates and X, Y, and Z are the corresponding numbers of grid points. This average is scenario-specific because all grid points are weighted equally.

4.4.1 Modelling of SC and i.i.d. Rayleigh Fading Channels

For a $1 \times N_\mathrm{R}$ dual-polarised MIMO configuration, the SC channel matrix has dimension $2N_\mathrm{R} \times 2$ and is generated using the Kronecker model

$$\mathbf{H}_\mathrm{corr} = \mathbf{R}_{\mathrm{R_X}}^{\frac{1}{2}} \mathbf{H}_\mathrm{iid} \mathbf{R}_{\mathrm{T_X}}^{\frac{1}{2}}, \tag{4.16}$$

where the entries of $\mathbf{H}_\mathrm{iid} \in \mathbb{C}^{2N_\mathrm{R} \times 2}$ are independent and distributed as $\mathcal{CN}(0,1)$. The Hermitian positive-semidefinite matrices $\mathbf{R}_{\mathrm{R}_X}$ and $\mathbf{R}_{\mathrm{T}_X}$ describe receive- and transmit-side second-order correlation, respectively. They are obtained by normalising the sample covariance matrices:

$$\mathbf{R}_{\mathrm{R_X}}(i,j) = \frac{\mathbf{R}_{0,\mathrm{R_X}}(i,j)}{\sqrt{\mathbf{R}_{0,\mathrm{R_X}}(i,i)\,\mathbf{R}_{0,\mathrm{R_X}}(j,j)}}, \tag{4.17}$$

$$\mathbf{R}_{\mathrm{T_X}}(n,m) = \frac{\mathbf{R}_{0,\mathrm{T_X}}(n,m)}{\sqrt{\mathbf{R}_{0,\mathrm{T_X}}(n,n)\,\mathbf{R}_{0,\mathrm{T_X}}(m,m)}}, \tag{4.18}$$

where $i,j \in \{1,\ldots,2N_\mathrm{R}\}$ and $n,m \in \{1,2\}$. The unnormalised receive and transmit sample covariance matrices are

$$\mathbf{R}_{0,\mathrm{R_X},\mathrm{LOS}} = \frac{1}{N_\mathrm{LOS}} \sum_{n_\mathrm{p}=1}^{N_\mathrm{LOS}} \mathbf{H}_{\mathrm{LOS},n_\mathrm{p}} \mathbf{H}_{\mathrm{LOS},n_\mathrm{p}}^\mathrm{H}, \tag{4.19}$$

$$\mathbf{R}_{0,\mathrm{T_X},\mathrm{LOS}} = \frac{1}{N_\mathrm{LOS}} \sum_{n_\mathrm{p}=1}^{N_\mathrm{LOS}} \mathbf{H}_{\mathrm{LOS},n_\mathrm{p}}^\mathrm{H} \mathbf{H}_{\mathrm{LOS},n_\mathrm{p}}, \tag{4.20}$$

$$\mathbf{R}_{0,\mathrm{R_X},\mathrm{NLOS}} = \frac{1}{N_\mathrm{NLOS}} \sum_{n_\mathrm{p}=1}^{N_\mathrm{NLOS}} \mathbf{H}_{\mathrm{NLOS},n_\mathrm{p}} \mathbf{H}_{\mathrm{NLOS},n_\mathrm{p}}^\mathrm{H}, \tag{4.21}$$

$$\mathbf{R}_{0,\mathrm{T_X},\mathrm{NLOS}} = \frac{1}{N_\mathrm{NLOS}} \sum_{n_\mathrm{p}=1}^{N_\mathrm{NLOS}} \mathbf{H}_{\mathrm{NLOS},n_\mathrm{p}}^\mathrm{H} \mathbf{H}_{\mathrm{NLOS},n_\mathrm{p}}. \tag{4.22}$$

Here, $N_{\text{LOS}} = 37118$ and $N_{\text{NLOS}} = 212882$ are the numbers of channel samples in the two path classes. The following matrices report the elementwise magnitudes of the resulting complex correlation coefficients, rounded to two decimal places; the full Hermitian matrices are used in the SC channel generation:

$$
\begin{aligned}
\left|\mathbf{R}_{\text{RX,LOS}}\right|_{\text{e}} &= \begin{bmatrix}
1 & 0.20 & 0.99 & 0.20 & 0.98 & 0.20 & 0.98 & 0.21 \\
0.20 & 1 & 0.20 & 0.97 & 0.20 & 0.95 & 0.20 & 0.92 \\
0.99 & 0.20 & 1 & 0.20 & 0.99 & 0.20 & 0.98 & 0.20 \\
0.20 & 0.97 & 0.20 & 1 & 0.20 & 0.97 & 0.20 & 0.95 \\
0.98 & 0.20 & 0.99 & 0.20 & 1 & 0.20 & 0.99 & 0.20 \\
0.20 & 0.95 & 0.20 & 0.97 & 0.20 & 1 & 0.20 & 0.97 \\
0.98 & 0.20 & 0.98 & 0.20 & 0.99 & 0.20 & 1 & 0.20 \\
0.20 & 0.92 & 0.20 & 0.95 & 0.20 & 0.97 & 0.20 & 1
\end{bmatrix}, \\
\left|\mathbf{R}_{\text{TX,LOS}}\right|_{\text{e}} &= \begin{bmatrix}
1 & 0.17 \\
0.17 & 1
\end{bmatrix}
\end{aligned}
\tag{4.23}
$$

$$\left|\mathbf{R}_{\mathrm{R_X,NLOS}}\right|_{\mathrm{e}} = \begin{bmatrix} 1 & 0.26 & 0.99 & 0.26 & 0.99 & 0.26 & 0.98 & 0.26 \\ 0.26 & 1 & 0.26 & 0.99 & 0.26 & 0.98 & 0.26 & 0.97 \\ 0.99 & 0.26 & 1 & 0.26 & 0.99 & 0.26 & 0.99 & 0.26 \\ 0.26 & 0.99 & 0.26 & 1 & 0.26 & 0.99 & 0.26 & 0.98 \\ 0.99 & 0.26 & 0.99 & 0.26 & 1 & 0.26 & 0.99 & 0.26 \\ 0.26 & 0.98 & 0.26 & 0.99 & 0.26 & 1 & 0.26 & 0.99 \\ 0.98 & 0.26 & 0.99 & 0.26 & 0.99 & 0.26 & 1 & 0.26 \\ 0.26 & 0.97 & 0.26 & 0.98 & 0.26 & 0.99 & 0.26 & 1 \end{bmatrix},$$

$$\left|\mathbf{R}_{\mathrm{T_X,NLOS}}\right|_{\mathrm{e}} = \begin{bmatrix} 1 & 0.24 \\ 0.24 & 1 \end{bmatrix} \tag{4.24}$$

As discussed in [146], for i.i.d. Rayleigh fading Channels, the analytical PEP can be evaluated using (4.25). In this expression, $\mathcal{B}(a,b) \triangleq \Gamma(a)\Gamma(b)/\Gamma(a+b)$ represents the Beta function, while $\Gamma(a)$ denotes the Gamma function. The term F_1 refers to the Appell hypergeometric function, and the definition is given in (4.26).

$$\begin{aligned} \Pr(p \to \hat{p}) = &\frac{\left[\left(1+\frac{\rho\Lambda_{\mathrm{V}}}{4}\right)\left(1+\frac{\rho\Lambda_{\mathrm{H}}}{4}\right)\right]^{-N_{\mathrm{R}}} \mathcal{B}\left(\frac{1}{2}, 2N_{\mathrm{R}}+\frac{1}{2}\right)}{2\pi} \\ &\times F_1\left[\frac{1}{2}, N_{\mathrm{R}}, N_{\mathrm{R}}, 2N_{\mathrm{R}}+1, \left(1+\frac{\rho\Lambda_{\mathrm{V}}}{4}\right)^{-1}, \left(1+\frac{\rho\Lambda_{\mathrm{H}}}{4}\right)^{-1}\right]. \end{aligned} \tag{4.25}$$

$$\begin{aligned} F_1(a,b_1,b_2,c;z_1,z_2) &\triangleq \sum_{d_1=0}^{\infty}\sum_{d_2=0}^{\infty} \frac{(a)_{d_1+d_2}(b_1)_{d_1}(b_2)_{d_2} z_1^{d_1} z_2^{d_2}}{(c)_{d_1+d_2} d_1! d_2!} \\ &\equiv \frac{\Gamma(c)}{\Gamma(a)\Gamma(c-a)} \int_0^1 t^{a-1}(1-t)^{c-a-1}(1-z_1 t)^{-b_1}(1-z_2 t)^{-b_2}\,\mathrm{d}t, \end{aligned} \tag{4.26}$$

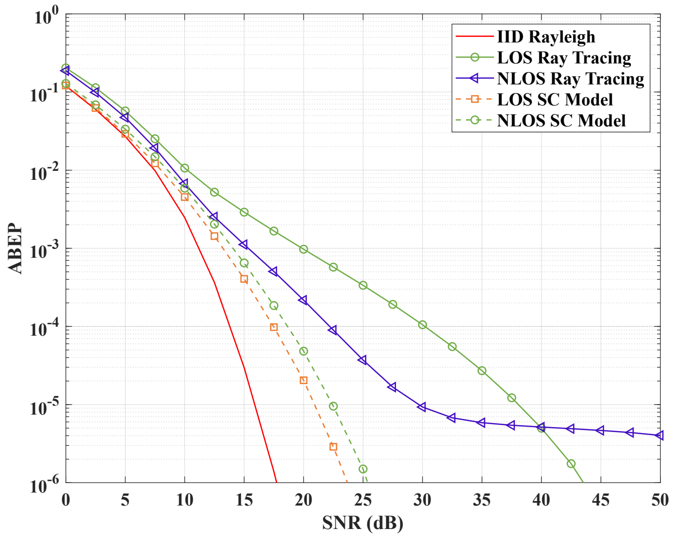

Fig. 4.2 ABEP performance of the PolarSK scheme for a normalised 1×4 MIMO system with $K = 2$ and $M = 2$ under three channel conditions: a ray-based channel, an i.i.d. Rayleigh fading channel, and an SC channel.

The integral representation is valid when the real part of c is greater than the real part of a, the real part of a is positive, and the integration path does not cross the branch cuts associated with $(1 - z_1 t)^{-b_1}$ and $(1 - z_2 t)^{-b_2}$.

4.4.2 Simulation Results under Three Channel Conditions

For the RT generated channel, each Tx–Rx position pair is identified as either LOS or NLOS according to the presence of a direct propagation path. Fig. 4.2 compares the ABEP performance of the polarised MIMO system obtained from RT generated channels with that predicted by conventional statistical channel models. For the considered geometry and normalisation, the LOS and NLOS RT curves differ from the i.i.d. Rayleigh prediction. The SC model reproduces the estimated second-order covariance but not the deterministic path phases, material-dependent TE/TM transformations, or higher-order spatial structure retained by the ray tracer; it therefore yields a different ABEP curve. These comparisons establish model sensitivity for this scenario rather than a universal ordering of the three

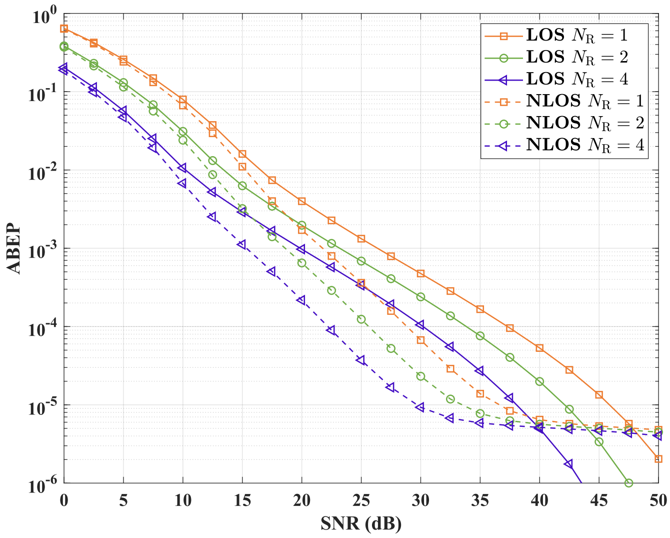

Fig. 4.3 ABEP performance of the PolarSK scheme for normalised 1×1, 1×2, and 1×4 MIMO systems with $K = 2$ and $M = 2$.

channel models. Fig. 4.3 compares 1×1, 1×2, and 1×4 configurations, while Fig. 4.4 compares $M = 2$, $M = 4$, and $M = 16$ for a 1×4 system with $K = 2$.

The comparison shows why the deterministic path structure should be retained when evaluating material-dependent polarisation effects. The present RT model includes LOS/OLOS transmission and first-order reflection; it does not include diffraction in the Chapter 4 simulations and should not be interpreted as a complete indoor channel benchmark.

As illustrated in Fig. 4.2, Fig. 4.3, and Fig. 4.4, a nonnegligible ABEP floor, also referred to as an irreducible bit error rate, can be observed in the NLOS RT scenario across various MIMO configurations and modulation constellations, especially when the SNR exceeds 40 dB. Moreover, Fig. 4.3 shows that these ABEP floors remain almost unchanged even with increasing diversity gain in polarised MIMO systems. Similarly, as seen in Fig. 4.4, although the use of lower modulation orders slightly alleviates the ABEP floor, a considerable floor still persists for all constellations, which becomes a critical constraint for high-SNR transmission.

The different behaviour of the LOS, NLOS RT, i.i.d. Rayleigh, and SC channels is caused by the degree to which deterministic polarisation and phase relationships are preserved. In the

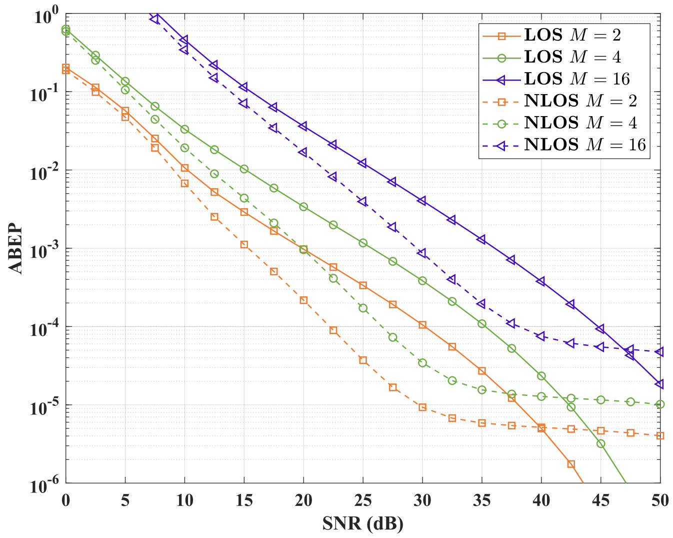

Fig. 4.4 ABEP performance of the PolarSK scheme for a normalised 1×4 MIMO system with $K = 2$ and modulation orders $M \in \{2, 4, 16\}$.

considered LOS case, the channel is dominated by the direct component and does not contain the same persistent reflected polarisation imbalance that appears in the NLOS case. In the i.i.d. Rayleigh channel, the multipath components are statistically independent with random phases, so no fixed deterministic interference structure remains as the SNR increases. The SC channel captures second-order SC, but it still averages out the deterministic phase-coherent material interactions that are retained by the RT channel. Consequently, the ABEP floor observed here is primarily a deterministic channel effect, but it also interacts with the Rx decision metric and the PolarSK constellation geometry because the effective Euclidean distances between received polarisation symbols are changed by the channel. The ABEP evaluation assumes that the Rx has the channel state information required for ML detection; imperfect channel estimation would be expected to further degrade the practical performance.

To overcome this limitation, the following section develops an optimisation framework aimed at reducing the ABEP floor by appropriately tuning the material properties and layer thicknesses of the propagation environment.

4.5 Reduction of the ABEP Floor in PolarSK Systems

In this section, I formulate a coordinatewise optimisation of the permittivity ε_s, conductivity σ_s, and thickness d_s of each wall layer. The relative permeability is fixed at unity. The objective is to reduce the scenario-averaged high-SNR ABEP metric within the prescribed material ranges; the result is a grid-dependent local solution rather than a proof of global optimality.

The ABEP floor reflects the residual error that remains even at high SNRs, which mainly arises from imperfect symbol decisions in the joint polarisation and phase domain. According to [176], such bit errors can be grouped into three main cases. The first occurs when the polarisation state is estimated correctly, but the phase is estimated incorrectly. The second appears when the phase is estimated correctly, but the polarisation state is mistaken. The third happens when both quantities are estimated wrongly at the same time.

For a fixed ML channel realisation, detector, and SNR, the conditional PEP decreases monotonically with $\|\mathbf{H}\Delta\mathbf{x}(p,\hat{p})\|_2$. The material parameters modify this distance through the complex TE and TM reflection and transmission coefficients. The proposed search therefore minimises the spatially averaged ABEP directly by modifying the received-space distances between competing PolarSK symbols.

4.5.1 Problem Formulation

As illustrated in Fig. 4.2, under the NLOS RT condition with a 1×4 MIMO configuration and a PolarSK constellation defined by $K = 2$ and $M = 2$, the ABEP floor becomes noticeable once the SNR approaches approximately 35 dB. The range from 35 to 50 dB is therefore treated as the high-SNR floor region in this simulation. Reducing the ABEP simultaneously across this entire SNR range would require repeated ABEP evaluations for many SNR samples, Rx positions, MIMO configurations, and candidate material combinations. This would substantially increase the computational burden of the nonconvex search. To obtain a tractable proxy for the high-SNR floor behaviour, the objective is therefore defined as the minimisation of the ABEP evaluated at 50 dB. This value is used as a representative

Algorithm 1: Coordinatewise optimisation of the high-SNR PolarSK ABEP metric

Input: N, ι, $\{\mathcal{A}_{1:N}\}$, $\{\mathcal{B}_{1:N}\}$, $\{\mathcal{C}_{1:N}\}$, $\{\kappa_{1:N}\}$, G, $\mathcal{I}$, $\mathcal{P}_{\text{th}}$
Output: $\overline{ABEP}_{\text{avg}}(50\text{dB})$, $\bar{v}_1, \bar{v}_2, \ldots, \bar{v}_\iota$

Order the ι variables as follows: the N permittivities of N layers, the N thickness values of N layers, and the N conductivities of N layers; label them as $v_1, v_2, \ldots, v_\iota$;

For the ith variable, $\forall i \in \{1, 2, \ldots, \iota\}$, compute the lower bound $\ell_i = \min(\cdot)$, the upper bound $u_i = \max(\cdot)$, and the grid step $h_i = \dfrac{\max(\cdot) - \min(\cdot)}{G-1}$, and define the discrete candidate set $\mathcal{S}_i = \{\ell_i, \ell_i + h_i, \ldots, u_i\}$, where "$\cdot$" can be $\mathcal{A}_s$, $\mathcal{B}_s$ or $\mathcal{C}_s$, $\forall s = 1, 2, \ldots, N$;

Initialise $v_1, v_2, \ldots, v_\iota$ and denote them by $v_1^{(0)}, v_2^{(0)}, \ldots, v_\iota^{(0)}$; set $\mathrm{i} = 0$;

Generate polarised channel matrices $\tilde{\mathbf{H}}_{\text{NLOS}}$ for NLOS scenarios using the proposed RT algorithm;

Calculate $\big(ABEP_{\text{avg}}(50\text{dB})\big)^{(0)} = ABEP_{\text{avg}}(50\text{dB})\left(v_1^{(0)}, v_2^{(0)}, \ldots, v_\iota^{(0)}\right)$ using (4.15) and set the baseline $\big(ABEP_{\text{avg}}(50\text{dB})\big)_{\text{baseline}} = \big(ABEP_{\text{avg}}(50\text{dB})\big)^{(0)}$;

while $\mathrm{i} < \mathcal{I}$ **do**
 $\mathrm{i} \leftarrow \mathrm{i} + 1$; $i \leftarrow 0$;
 while $i < \iota$ **do**
  $i \leftarrow i + 1$;
  foreach $\mathcal{J} \in \mathcal{S}_i$ **do**
   Compute $ABEP_{\text{avg}}(50\text{dB})\big(\mathcal{J}\big) = ABEP_{\text{avg}}(50\text{dB})\left(v_1^{(\mathrm{i})}, \ldots, v_{i-1}^{(\mathrm{i})}, \mathcal{J}, v_{i+1}^{(\mathrm{i}-1)}, \ldots, v_\iota^{(\mathrm{i}-1)}\right)$ using (4.15);
  end
  Let $\big(ABEP_{\text{avg}}(50\text{dB})\big)_{\min,i}^{(\mathrm{i})} = \min_{\mathcal{J} \in \mathcal{S}_i} ABEP_{\text{avg}}(50\text{dB})\big(\mathcal{J}\big)$;
  Compute the fractional reduction

$$\mathcal{P} = \frac{\big(ABEP_{\text{avg}}(50\text{dB})\big)_{\text{baseline}} - \big(ABEP_{\text{avg}}(50\text{dB})\big)_{\min,i}^{(\mathrm{i})}}{\big(ABEP_{\text{avg}}(50\text{dB})\big)_{\text{baseline}}};$$

  if $\mathcal{P} > \mathcal{P}_{\text{th}}$ **then**
   $v_i^{(\mathrm{i})} = \arg\min_{\mathcal{J} \in \mathcal{S}_i} ABEP_{\text{avg}}(50\text{dB})\big(\mathcal{J}\big)$;
   Update the baseline: $\big(ABEP_{\text{avg}}(50\text{dB})\big)_{\text{baseline}} = \big(ABEP_{\text{avg}}(50\text{dB})\big)_{\min,i}^{(\mathrm{i})}$;
  else
   $v_i^{(\mathrm{i})} = v_i^{(\mathrm{i}-1)}$;
  end
 end
end

Return the optimised ABEP at 50 dB: $\overline{ABEP}_{\text{avg}}(50\text{dB}) = \big(ABEP_{\text{avg}}(50\text{dB})\big)_{\text{baseline}}$;

Gather the final values $v_1, v_2, \ldots, v_\iota$ and denote them by $\bar{v}_1, \bar{v}_2, \ldots, \bar{v}_\iota$;

high-SNR analysis point and should not be interpreted as a typical practical operating SNR. The corresponding optimisation problem for an N-layer wall material can be written as

$$\begin{aligned}
\min_{\substack{\varepsilon_s,\sigma_s,d_s,\\ \text{for } s=1,2,\dots,N}} \quad & ABEP_{\text{avg}}(50\,\text{dB}) \\
\text{s.t.} \quad & \varepsilon_s \in \mathcal{A}_s, \qquad \text{for } s=1,2,\dots,N, \\
& \mu_{r,s} = 1, \\
& \sigma_s \in \mathcal{B}_s, \qquad \text{for } s=1,2,\dots,N, \\
& d_s \in \mathcal{C}_s, \qquad \text{for } s=1,2,\dots,N, \\
& \sum_{s=1}^{N} d_s \geq \mathcal{T}, \\
& \frac{1}{\sum_{s=1}^{N} \frac{d_s}{\kappa_s}} \leq \mathcal{U},
\end{aligned} \tag{4.27}$$

where $\mathcal{A}_s$, $\mathcal{B}_s$, and $\mathcal{C}_s$ represent the feasible ranges of permittivity, conductivity, and thickness for the sth layer of the multilayer wall, respectively. The parameter $\mathcal{T}$ defines the minimum total thickness required to maintain mechanical stability, whereas $\mathcal{U}$ specifies the maximum allowable thermal transmittance to guarantee the wall's insulation performance. The variable κ_s denotes the thermal conductivity of the sth layer.

The optimisation problem presented in (4.27) is inherently nonconvex. To address this challenge, an iterative search procedure is developed, as outlined in Algorithm 1, which systematically examines feasible combinations of the design variables to minimise $ABEP_{\text{avg}}(50\,\text{dB})$. In the case of wall structures composed of concrete, brick, and plasterboard, no unified design standards defining the minimum total thickness or the maximum thermal transmittance could be found, since such a combination is uncommon in conventional construction practice. Consequently, the constraints $\sum_{s=1}^{N} d_s \geq \mathcal{T}$ and $\left(\sum_{s=1}^{N} \frac{d_s}{\kappa_s}\right)^{-1} \leq \mathcal{U}$ are omitted, and the optimisation problem in (4.27) thus involves $3N$ independent design parameters.

Algorithm 1 requires the following input parameters: the number of wall layers N; feasible value ranges for the permittivity $\mathcal{A}_{1:N}$, conductivity $\mathcal{B}_{1:N}$, and thickness $\mathcal{C}_{1:N}$; the

Table 4.2 Optimisation search ranges and algorithm parameters.

Parameter	Configuration value	Unit
$\mathcal{A}_1$	3.542×10^{-11}–6.198×10^{-11} [173]	F/m
$\mathcal{A}_2$	3.276×10^{-11}–4.073×10^{-11} [155, 177, 178]	F/m
$\mathcal{A}_3$	1.328×10^{-11}–3.984×10^{-11} [173]	F/m
$\mathcal{B}_1$	0.0556–0.1668 [173]	S/m
$\mathcal{B}_2$	0.0308–0.1669 [155, 179]	S/m
$\mathcal{B}_3$	0.0139–0.0695 [173]	S/m
$\mathcal{C}_1$	20–65 [180]	mm
$\mathcal{C}_2$	5–50 [180]	mm
$\mathcal{C}_3$	12.5–40 [180]	mm
ι	9	–
$\mathcal{I}$	10	–
$\mathcal{P}_{\text{th}}$	0	–
G	41	–

total number of optimisation variables $\iota \leq 3N$; the number of candidate grid points G; the maximum iteration count $\mathcal{I}$; and the convergence tolerance $\mathcal{P}_{\text{th}}$.

The ι optimisation variables are denoted by $v_1,\ldots,v_\iota$ and comprise the permittivity, thickness, and conductivity of all N layers. For variable v_i, the finite candidate set is $\mathcal{S}_i = \{\ell_i, \ell_i + h_i, \ldots, u_i\}$, where $h_i = (u_i - \ell_i)/(G-1)$. A candidate is accepted only when its fractional ABEP reduction exceeds $\mathcal{P}_{\text{th}}$; otherwise, the previous value is retained. The procedure performs at most $\mathcal{I}$ complete coordinate sweeps.

4.5.2 Iterative Solution Method

The optimisation problem in (4.27) is solved using the coordinatewise iterative search procedure summarised in Algorithm 1. The procedure first evaluates the baseline $ABEP_{\text{avg}}(50\,\text{dB})$ using the initial material parameters. During each optimisation cycle, one design variable is selected while the remaining variables are kept fixed. The selected variable is swept over its feasible discrete candidate set, and the ABEP is recomputed for each candidate value. If the best candidate produces a reduction larger than the prescribed threshold, the variable is updated and the new ABEP becomes the baseline for the next step. Otherwise, the algorithm proceeds to the next variable or terminates when the maximum number of iterations is reached. This procedure is computationally simpler than exhaustive joint search over all material parameters, but it can converge to a local optimum and its result may depend on the chosen parameter ranges, grid resolution, and initial point.

The optimisation is also subject to practical interpretation limits. Although the parameter ranges are selected to be physically plausible for construction materials, practical deployment would require discrete commercially available materials, manufacturability constraints, cost constraints, fire and building regulations, mechanical strength, thermal insulation, humidity dependence, aesthetics, and tolerance to manufacturing variation. In addition, the optimum obtained for one room geometry, Tx location, Rx grid, carrier frequency, and antenna configuration may not transfer directly to another scenario. A robust design would require multiscenario optimisation and uncertainty analysis over material permittivity, conductivity, thickness, surface roughness, and frequency.

4.5.3 Simulation Results

For the non-load-bearing concrete–brick–plasterboard wall, the search ranges are given in Table 4.2. The initial objective, $\left(ABEP_{\text{avg}}(50\,\text{dB})\right)^{(0)}$, uses thicknesses $[d_1, d_2, d_3] = [30, 30, 30]\,\text{mm}$, absolute permittivities $[\varepsilon_1, \varepsilon_2, \varepsilon_3] = [4.6395, 3.4619, 2.4171] \times 10^{-11}\,\text{F/m}$, and conductivities $[\sigma_1, \sigma_2, \sigma_3] = [0.1627, 0.0308, 0.0386]\,\text{S/m}$. These values correspond to the material model defined in Table 3.2.

The results illustrated in Fig. 4.5 show that for normalised 1×1, 1×2, and 1×4 MIMO systems using a PolarSK constellation with $K = 2$ and $M = 2$, the ABEP under NLOS conditions at an SNR of 50 dB decreases markedly after 45 optimisation alternations, corresponding to five full optimisation cycles. Specifically, the ABEP reduces from 4.8007×10^{-6} to 1.5849×10^{-88}, from 4.4796×10^{-6} to 2.9496×10^{-152}, and from 4.0332×10^{-6} to 2.2251×10^{-308} for the 1×1, 1×2, and 1×4 configurations, respectively. These values correspond to very large reductions in the numerical ABEP metric for the considered simulation scenario. Because these factors are extremely large, they should be interpreted on

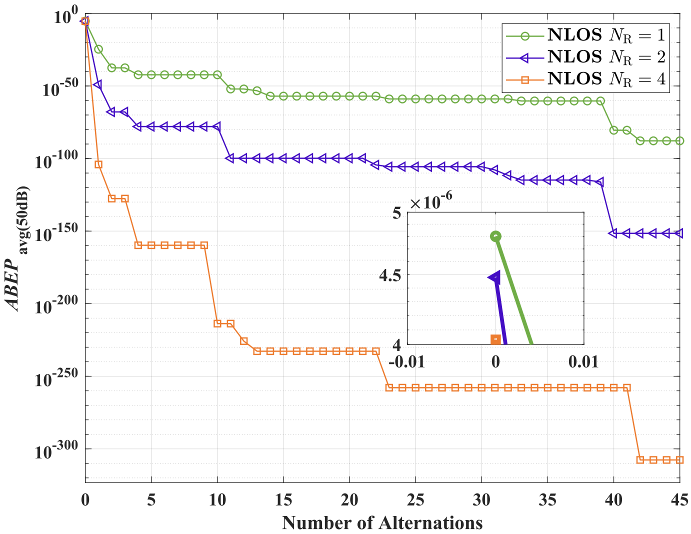

Fig. 4.5 $ABEP_{\mathrm{avg}}(50\,\mathrm{dB})$ improvement of the PolarSK scheme versus the number of iterations for normalised 1×1, 1×2, and 1×4 MIMO systems with $K = 2$ and $M = 2$ under NLOS conditions.

a logarithmic scale or as evidence of high sensitivity to deterministic polarisation imbalance, rather than as universally achievable practical gains.

The optimised parameters corresponding to each configuration are outlined as follows:

- 1×1 MIMO:
  - Thicknesses: $[27.9, 44.4, 40]\,\mathrm{mm}$
  - Permittivities: $[5.3345, 3.7939, 3.4531] \times 10^{-11}\,\mathrm{F/m}$
  - Conductivities: $[0.1668, 0.1669, 0.0695]\,\mathrm{S/m}$

- 1×2 MIMO:
  - Thicknesses: $[27.9, 10.6, 31.8]\,\mathrm{mm}$
  - Permittivities: $[4.0728, 3.515, 3.3867] \times 10^{-11}\,\mathrm{F/m}$
  - Conductivities: $[0.1668, 0.1669, 0.0695]\,\mathrm{S/m}$

- 1×4 MIMO:
  - Thicknesses: $[31.3, 19.6, 31.1]\,\mathrm{mm}$
  - Permittivities: $[4.8697, 3.7342, 3.9847] \times 10^{-11}\,\mathrm{F/m}$
  - Conductivities: $[0.1668, 0.1669, 0.0695]\,\mathrm{S/m}$

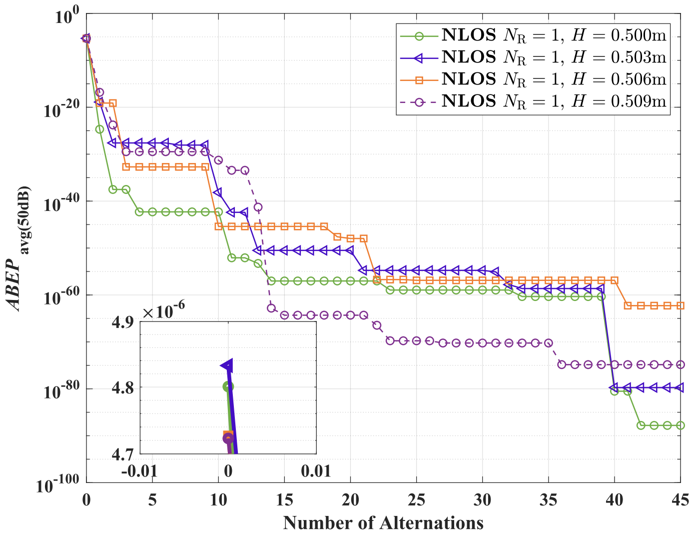

Fig. 4.6 $ABEP_{\text{avg}}(50\,\text{dB})$ improvement of the PolarSK scheme versus the number of iterations for a normalised 1×1 MIMO system with $K = 2$ and $M = 2$ under NLOS conditions, evaluated at Rx locations with different heights.

The optimised parameters differ among the MIMO configurations because each configuration weights the receive locations and polarisation subchannels differently in the ABEP objective. This observation does not by itself imply weak SC; the estimated correlation matrices in Eqs. (4.23) and (4.24) contain several large-magnitude entries.

Fig. 4.6 evaluates the normalised 1×1 system at Rx heights of 0.500, 0.503, 0.506, and 0.509 m. After 45 coordinate updates, $ABEP_{\text{avg}}(50\,\text{dB})$ decreases from 4.8007×10^{-6} to 1.5849×10^{-88}, from 4.8326×10^{-6} to 1.8583×10^{-80}, from 4.7270×10^{-6} to 5.2634×10^{-63}, and from 4.7230×10^{-6} to 1.4294×10^{-75}, respectively. These are numerical union bound values for the stated deterministic model and should be interpreted on a logarithmic scale. The corresponding local solutions are:

- Rx height $H = 0.5\,\text{m}$:
  - Thicknesses: $[27.9, 44.4, 40]\,\text{mm}$
  - Permittivities: $[5.3345, 3.7939, 3.4531] \times 10^{-11}\,\text{F/m}$
  - Conductivities: $[0.1668, 0.1669, 0.0695]\,\text{S/m}$

- Rx height $H = 0.503\,\mathrm{m}$:
  - Thicknesses: $[21.1, 10.6, 40]\,\mathrm{mm}$
  - Permittivities: $[4.6041, 3.3557, 3.2538] \times 10^{-11}\,\mathrm{F/m}$
  - Conductivities: $[0.0890, 0.1669, 0.0695]\,\mathrm{S/m}$
- Rx height $H = 0.506\,\mathrm{m}$:
  - Thicknesses: $[20, 11.7, 37.9]\,\mathrm{mm}$
  - Permittivities: $[4.4713, 3.8935, 3.9843] \times 10^{-11}\,\mathrm{F/m}$
  - Conductivities: $[0.1668, 0.0723, 0.0695]\,\mathrm{S/m}$
- Rx height $H = 0.509\,\mathrm{m}$:
  - Thicknesses: $[47, 27.5, 26.2]\,\mathrm{mm}$
  - Permittivities: $[3.5416, 3.6744, 1.3281] \times 10^{-11}\,\mathrm{F/m}$
  - Conductivities: $[0.1668, 0.1669, 0.0292]\,\mathrm{S/m}$

The different local solutions show that millimetre-scale Rx displacement changes the coherent path phases and hence the high-SNR objective. The sensitivity also reflects the finite parameter grid and the nonconvex coordinate search; it is not evidence of weak NLOS SC.

Fig. 4.7 illustrates the ABEP performance of the PolarSK scheme for normalised 1×1, 1×2, and 1×4 MIMO systems with $K = 2$ and modulation orders $M = 2$, $M = 4$, and $M = 16$, respectively, under NLOS conditions using both optimised and unoptimised multilayer wall materials. Across the SNR range from 0 to 50 dB, the observed ABEP floors are suppressed below the plotted numerical range when the optimised walls are employed for the considered MIMO configurations and constellation orders. These findings highlight the potential effectiveness of wall material optimisation in mitigating ABEP floors and enhancing system reliability in high-SNR indoor environments, while the practical realisability of the optimised wall parameters requires further material selection and experimental validation.

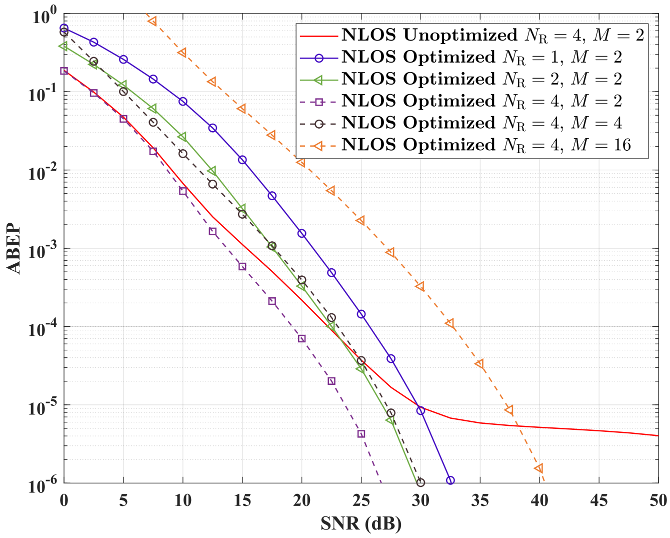

Fig. 4.7 ABEP performance under optimised and baseline wall parameters for normalised 1×1, 1×2, and 1×4 MIMO systems with $K = 2$ and $M \in \{2,4,16\}$.

4.5.4 Physical Interpretation of Simulation Results

This section provides a physical explanation of the preceding results, relating them to underlying theoretical concepts and to their practical realisation in antenna configurations.

For the ideal crossed dipole model, the vertical and horizontal branches are identical orthogonal infinitesimal dipoles. When each branch is driven by the same current amplitude and observed in its corresponding co-polarised basis, symmetry gives equal radiated power. The complex power through a spherical surface S_t for branch $\mathrm{Y} \in \{\mathrm{V},\mathrm{H}\}$ is written as [181]

$$P_{\mathrm{t,Y}} = \oiint_{S_\mathrm{t}} \mathbf{W}_{\mathrm{t,Y}} \cdot \hat{\mathbf{n}}_s \, \mathrm{d}S = \frac{377\pi}{3} \left| \frac{I_0 l}{\lambda} \right|^2 \left[1 - \frac{j}{(k_0 r)^3} \right], \tag{4.28}$$

where $\mathbf{W}_{\mathrm{t,Y}} = \frac{1}{2}\mathbf{E}_{\mathrm{t,Y}} \times \mathbf{H}^*_{\mathrm{t,Y}}$ is the complex Poynting vector, $\hat{\mathbf{n}}_s$ is the outward unit normal, r is the sphere radius, I_0 is the branch current amplitude, l is the dipole length, and $k_0 = 2\pi/\lambda$.

Hence, the transmitted vertical-to-horizontal power ratio is $\Upsilon_\mathrm{t} = \left|P_{\mathrm{t,V}}/P_{\mathrm{t,H}}\right| = 1$ under the equal excitation ideal dipole assumption.

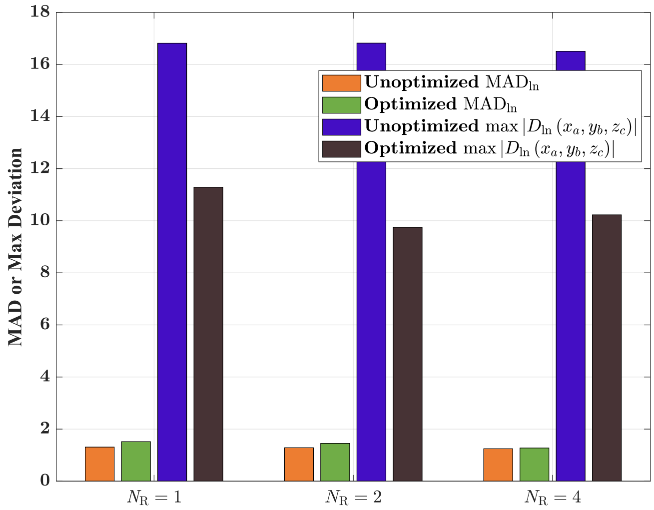

Fig. 4.8 Mean and maximum absolute logarithmic power ratio deviations for normalised 1×1, 1×2, and 1×4 MIMO systems under optimised and baseline wall parameters.

The received ratio is $\Upsilon_{\mathrm{r}} = \left\|\tilde{\mathbf{h}}_{\mathrm{V}}\right\|_2^2 / \left\|\tilde{\mathbf{h}}_{\mathrm{H}}\right\|_2^2$. Its departure from Υ_{t} is summarised by the mean absolute deviation (MAD) in the logarithmic domain

$$\mathrm{MAD_{ln}} = \frac{1}{XYZ} \sum_{a=1}^{X} \sum_{b=1}^{Y} \sum_{c=1}^{Z} \left|D_{\ln}(x_a, y_b, z_c)\right|, \tag{4.29}$$

where $D_{\ln}(x_a, y_b, z_c)$ can be expressed as

$$\begin{aligned} D_{\ln}(x_a, y_b, z_c) &= \ln\left(\Upsilon_{\mathrm{r}}(x_a, y_b, z_c)\right) - \ln\left(\Upsilon_{\mathrm{t}}(x_a, y_b, z_c)\right) \\ &= \ln\left(\Upsilon_{\mathrm{r}}(x_a, y_b, z_c)\right), \end{aligned} \tag{4.30}$$

where the second equality uses $\Upsilon_{\mathrm{t}} = 1$. The notation $\mathrm{MAD_{ln}}$ is specific to this mean absolute logarithmic metric and does not denote the conventional median absolute deviation.

Figs. 4.8 and 4.9 show that optimisation reduces $\max |D_{\ln}|$ from 16.815 to 11.288, from 16.820 to 9.749, and from 16.507 to 10.227 for the normalised 1×1, 1×2, and 1×4 systems, respectively. By contrast, $\mathrm{MAD_{ln}}$ increases slightly. The optimisation therefore contracts the extreme upper tail without reducing the average absolute deviation. The empirical CDFs in Fig. 4.9 support this interpretation; they should not be described as convergence to a mean

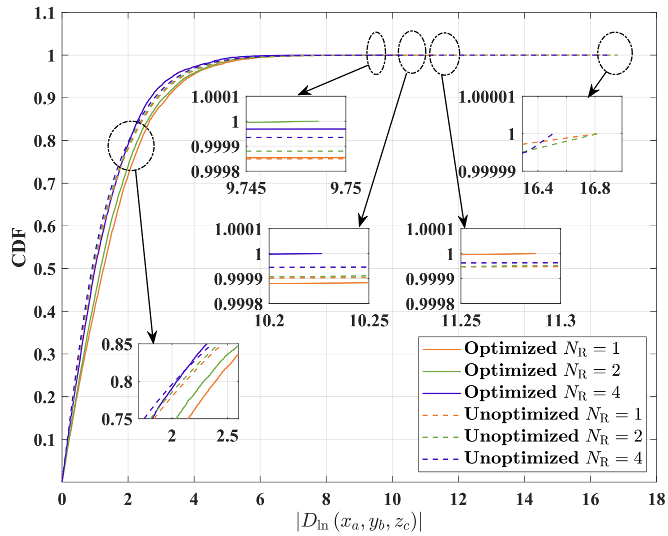

Fig. 4.9 Empirical cumulative distribution functions (CDFs) of $|D_{\mathrm{ln}}|$ for normalised 1×1, 1×2, and 1×4 MIMO systems under optimised and baseline wall parameters.

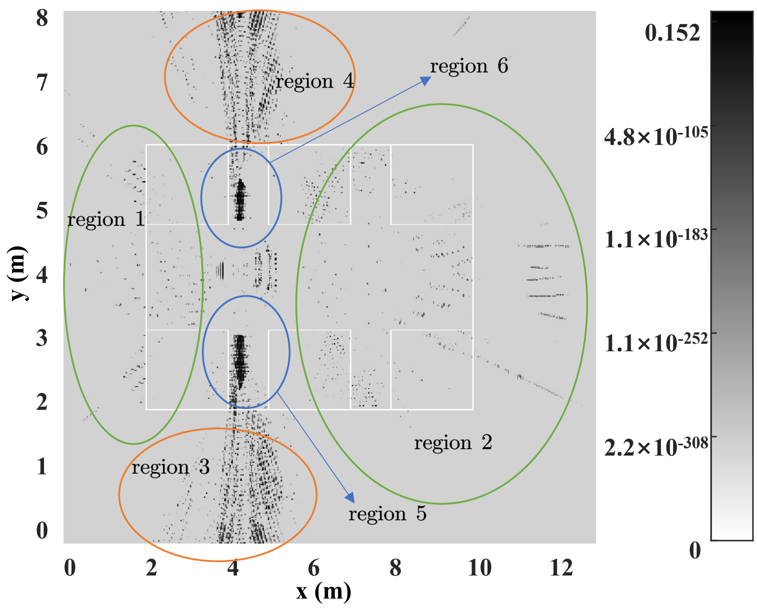

Fig. 4.10 ABEP performance of the PolarSK scheme for normalised 1×1 MIMO systems with $K = 2$ and $M = 2$ at 50 dB SNR under unoptimised building material conditions.

because a CDF characterises the complete distribution. Three mechanisms contribute to the large baseline outliers.

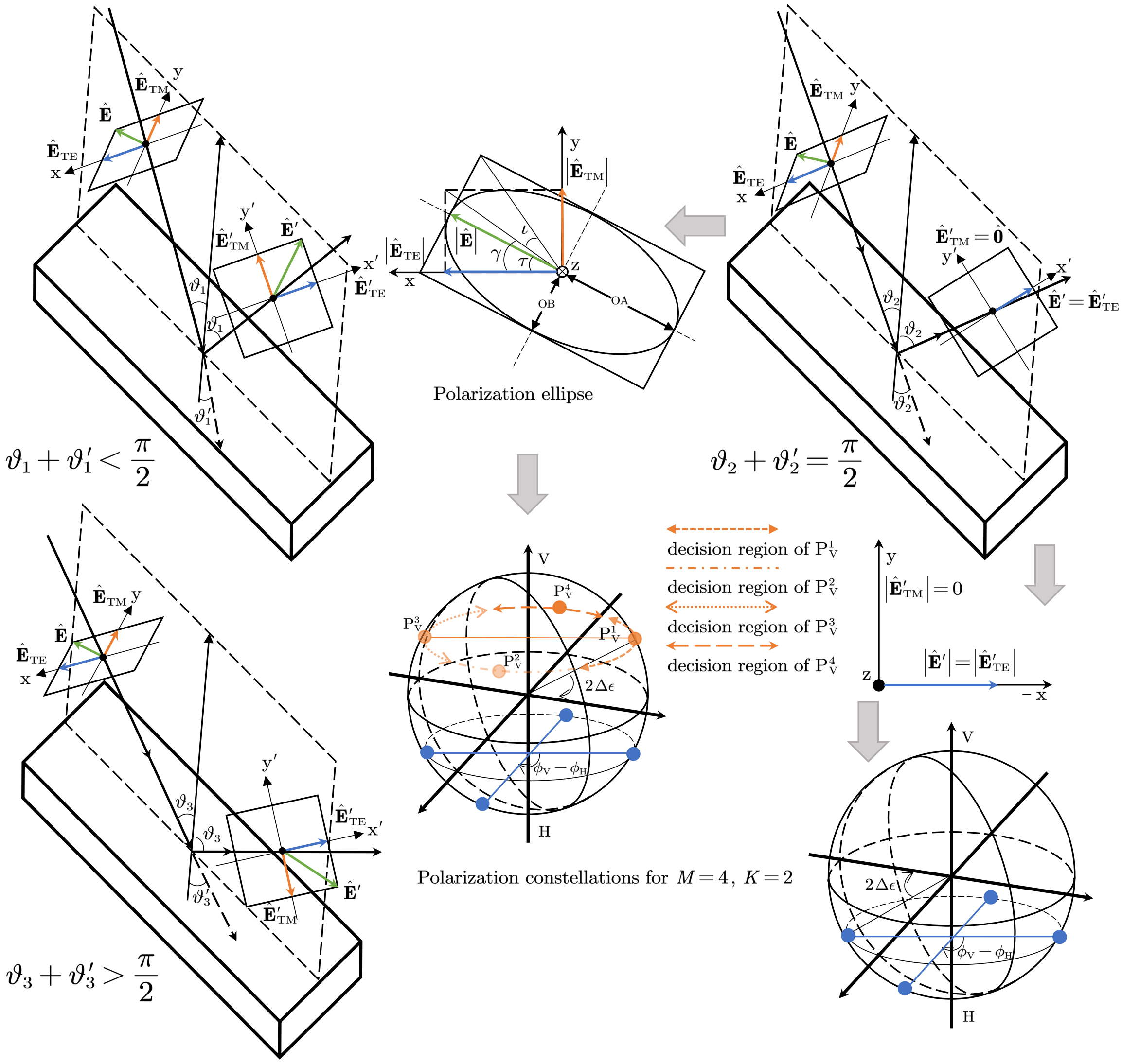

Fig. 4.11 Variation of the electric-field vector orientation upon reflection of a plane wave at different incidence angles.

1) *Power imbalance of the two polarisation components in the dominant emitted rays:* In the area illustrated in Fig. 4.10, Regions 5 and 6 exhibit pronounced disparities in power ratio, primarily due to the strong dominance of the LOS component and the negligible contribution from first-order reflections. This behaviour originates from the spatial relationship between the Tx and Rx positions together with the Tx radiation pattern, which results in a remarkably weak horizontally polarised electric field relative to the GCS. This effect can be clearly observed in Fig. 3.6a, Fig. 3.7a, Fig. 3.6b, and Fig. 3.7b.

2) *Small-scale fading:* In the region depicted in Fig. 4.10, the pronounced power ratio imbalance observed in Regions 1 and 2 is attributed to small-scale fading. The multipath interference produces standing-wave patterns in which one of the polarisation components may vanish in certain spatial locations, leading to strong polarisation asymmetry. This phenomenon is illustrated in Fig. 3.8a and Fig. 3.8b.

3) *Brewster-like reflection minimum:* In Regions 3–5 of Fig. 4.10, a dominant reflected path approaches a minimum of the TM reflection magnitude while the LOS horizontal component is weak. For a single lossless interface between isotropic nonmagnetic dielectrics, the exact Brewster condition satisfies $\vartheta_\mathrm{i} + \vartheta_\mathrm{t} = \pi/2$ and the TM reflection coefficient is zero. As illustrated in Fig. 4.11. A lossy finite multilayer wall generally exhibits a nonzero Brewster-like minimum whose angle and depth depend on the complete stack. The resulting suppression of one received polarisation branch reduces the channel-transformed distance between selected PolarSK symbols and increases their PEP; it does not remove the detector decision region mathematically.

These severe imbalances, or the near absence of one polarisation component resulting from the above mechanisms, lead to incorrect estimation of the symbol carried by the weaker polarisation branch. Consequently, ABEP floors appear in NLOS scenarios where such effects become particularly pronounced.

4.6 Discussion

Furthermore, to provide a sanity check from a theoretical perspective, two representative channel configurations are introduced to show that the ABEP metric can change by extremely large factors when one channel configuration preserves polarisation separability while another produces severe polarisation imbalance. This analysis supports the physical plausibility of strong ABEP sensitivity to deterministic channel structure. However, it should not be read as a claim that improvements of a fixed order of magnitude are guaranteed in practical buildings, since real performance depends on material availability, construction tolerances, room geometry, antenna design, and measurement uncertainty.

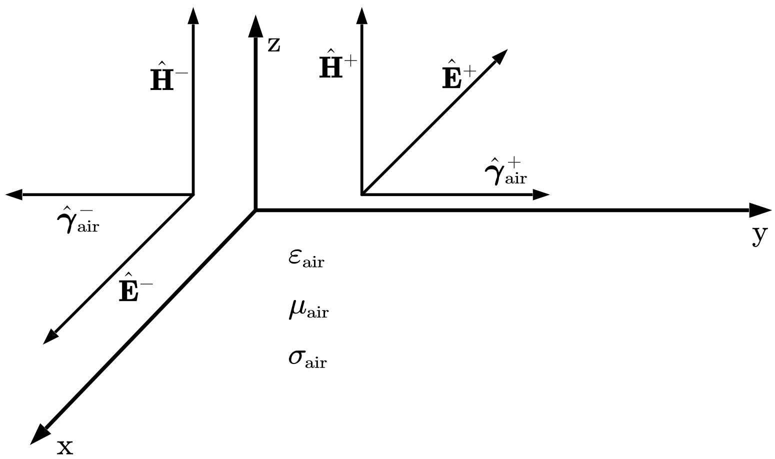

Fig. 4.12 Uniform plane-wave propagation.

The physical mechanisms behind this result are illustrated through one representative example: the standing wave in small-scale fading, which assists in completing the mathematical proof.

1. **Mathematical proof.**

   - *Standing Waves* :
     A one-dimensional standing wave provides a tractable illustration of the field extrema produced by coherent interference. Consider a time-harmonic, x-polarised plane wave and its reflection in lossless air, using the same $e^{j\omega t}$ convention as the ray tracer. With $\beta_{\mathrm{air}} = 2\pi/\lambda$, the forward and reflected phasors are

$$\mathbf{E}^+(y) = \hat{\mathbf{a}}_x E_0^+ e^{-j\beta_{\mathrm{air}} y}, \tag{4.31}$$

$$\mathbf{E}^-(y) = \hat{\mathbf{a}}_x E_0^- e^{+j\beta_{\mathrm{air}} y}. \tag{4.32}$$

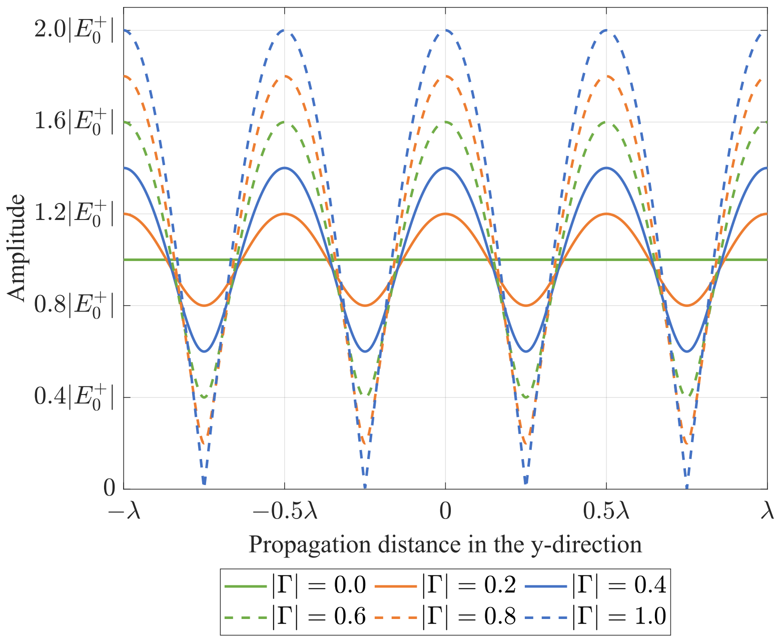

Fig. 4.13 Standing-wave patterns as functions of spatial distance for a uniform plane wave under different reflection coefficient values.

Here, E_0^+ and E_0^- are complex amplitudes referenced to $y = 0$. Their superposition is

$$\mathbf{E}(y) = \hat{\mathbf{a}}_x \left(E_0^+ e^{-j\beta_{\text{air}} y} + E_0^- e^{+j\beta_{\text{air}} y} \right). \tag{4.33}$$

Define the complex reflection coefficient at $y = 0$ by $R = E_0^- / E_0^+ = |R| e^{j\angle R}$. Factoring the forward wave from Eq. (4.33) gives

$$E_x(y) = E_0^+ e^{-j\beta_{\text{air}} y} \left[1 + R e^{j2\beta_{\text{air}} y} \right]. \tag{4.34}$$

Its magnitude is therefore

$$|E_x(y)| = |E_0^+| \sqrt{1 + |R|^2 + 2|R| \cos(2\beta_{\text{air}} y + \angle R)}. \tag{4.35}$$

Accordingly, the maximum and minimum values are, respectively, expressed as

$$
\begin{aligned}
|E_x(y)|_{\max} = |E_0^+| + |E_0^-| = |E_0^+| + |RE_0^+|, \\
\text{when } \beta_{\text{air}} y = m\pi - \frac{\angle R}{2}, \quad m \in \mathbb{Z},
\end{aligned}
\tag{4.36}
$$

and

$$
\begin{aligned}
|E_x(y)|_{\min} = \big||E_0^+| - |E_0^-|\big| = \big||E_0^+| - |RE_0^+|\big|, \\
\text{when } \beta_{\text{air}} y = \frac{(2m+1)\pi - \angle R}{2}, \quad m \in \mathbb{Z}.
\end{aligned}
\tag{4.37}
$$

Fig. 4.13 evaluates the illustrative zero phase case, $\angle R = 0$, as a function of y over $-\lambda \leq y \leq \lambda$ for $|R| \in \{0, 0.2, 0.4, 0.6, 0.8, 1\}$. A nonzero reflection phase translates the extrema but does not change their magnitudes.

By examining the union bound expression used in this chapter, which can be expressed as:

$$
\begin{aligned}
ABEP \leqslant \frac{1}{K \log_2 (M^2 K)} & \sum_{\hat{q}_{\mathrm{V}} = \{1,2:2:M\}} \sum_{\hat{q}_{\mathrm{H}} = \{1,2:2:M\}} \\
& \times \sum_{k=1}^{K} \sum_{\hat{k}=1}^{K} N \left[(k,1,1) \to \left(\hat{k}, \hat{q}_{\mathrm{V}}, \hat{q}_{\mathrm{H}} \right) \right] \\
& \times \Pr \left[(k,1,1) \to \left(\hat{k}, \hat{q}_{\mathrm{V}}, \hat{q}_{\mathrm{H}} \right) \right],
\end{aligned}
\tag{4.38}
$$

The prefactor, finite summations, and Hamming distance terms in the first two lines are fully determined once the signal constellation is specified. The remaining PEP term, $\Pr\left[(k,1,1) \to \left(\hat{k}, \hat{q}_{\mathrm{V}}, \hat{q}_{\mathrm{H}}\right)\right]$, varies with the channel response. For a normalised 1×1 MIMO system, $\Pr\left[(k,1,1)\to(\hat{k},\hat{q}_{\mathrm{V}},\hat{q}_{\mathrm{H}})\right]$ can be expressed as

$$\begin{aligned}
\Pr\left[(k,1,1)\to\left(\hat{k},\hat{q}_{\mathrm{V}},\hat{q}_{\mathrm{H}}\right)\right] &= \mathcal{Q}\left(\sqrt{\frac{\rho}{2}\left\|\tilde{\mathbf{H}}\Delta\mathbf{x}\left(p,\hat{p}\right)\right\|_2^2}\right)\\
&= \frac{1}{\pi}\int_0^{\frac{\pi}{2}} e^{\left(-\frac{\left(\sqrt{\frac{\rho}{2}\left\|\tilde{\mathbf{H}}\Delta\mathbf{x}(p,\hat{p})\right\|_2^2}\right)^2}{2\sin^2\psi}\right)}\mathrm{d}\psi\\
&= \frac{1}{\pi}\int_0^{\frac{\pi}{2}} e^{\left(-\frac{\left\{\sqrt{\frac{\rho}{2}\left\|\tilde{\mathbf{H}}\begin{bmatrix}\cos\varepsilon_k e^{\left(j\frac{2\pi q_{\mathrm{V}}}{M}\right)}-\cos\varepsilon_{\hat{k}} e^{\left(j\frac{2\pi\hat{q}_{\mathrm{V}}}{M}\right)}\\ \sin\varepsilon_k e^{\left(j\frac{2\pi q_{\mathrm{H}}}{M}\right)}-\sin\varepsilon_{\hat{k}} e^{\left(j\frac{2\pi\hat{q}_{\mathrm{H}}}{M}\right)}\end{bmatrix}\right\|_F^2}\right\}^2}{2\sin^2\psi}\right)}\mathrm{d}\psi
\end{aligned}, \quad (4.39)$$

where the normalised channel in 1×1 MIMO configuration $\tilde{\mathbf{H}}$ can be expressed as

$$\tilde{\mathbf{H}}^{N_{\mathrm{R}}=1} = \begin{bmatrix}\tilde{\mathbf{h}}_{\mathrm{V}} & \tilde{\mathbf{h}}_{\mathrm{H}}\end{bmatrix} = \begin{bmatrix}\tilde{h}_{\mathrm{VV}} & \tilde{h}_{\mathrm{VH}}\\ \tilde{h}_{\mathrm{HV}} & \tilde{h}_{\mathrm{HH}}\end{bmatrix}. \quad (4.40)$$

It can be observed from Fig. 4.13 that the amplitude of the standing-wave waveform contains fixed maxima and minima in space, and both their magnitudes and spatial positions depend on the reflection coefficient. Under three-dimensional propagation conditions, both the vertical and horizontal polarisation components of the superposed electric fields in free space may exhibit standing-wave characteristics due to the presence of reflection and interference effects.

For analytical convenience, two simplified channel conditions are considered: (A) an ideal normalised polarisation-orthogonal channel, represented by

$$\tilde{\mathbf{H}}_{|R|=0}^{N_\mathrm{R}=1} = \frac{\sqrt{2}\mathbf{H}_{|R|=0}^{N_\mathrm{R}=1}}{\left\|\mathbf{H}_{|R|=0}^{N_\mathrm{R}=1}\right\|_F} = \frac{\sqrt{2}}{\sqrt{2}}\begin{bmatrix} 1 & 0 \\ 0 & 1 \end{bmatrix} = \begin{bmatrix} 1 & 0 \\ 0 & 1 \end{bmatrix} \tag{4.41}$$

where no cross-polarisation coupling occurs and both polarisation components are fully preserved; and (B) a channel in which one polarisation component $\tilde{h}_\mathrm{HH}$ experiences standing-wave effects while the other polarisation component $\tilde{h}_\mathrm{VV}$ is transmitted without distortion, represented by

$$\tilde{\mathbf{H}}_{\left|R_{\tilde{h}_\mathrm{HH}}\right|=1}^{N_\mathrm{R}=1} = \frac{\sqrt{2}\mathbf{H}_{\left|R_{\tilde{h}_\mathrm{HH}}\right|=1}^{N_\mathrm{R}=1}}{\left\|\mathbf{H}_{\left|R_{\tilde{h}_\mathrm{HH}}\right|=1}^{N_\mathrm{R}=1}\right\|_F} = \frac{\sqrt{2}}{\sqrt{1+|E_x(y)|^2}}\begin{bmatrix} 1 & 0 \\ 0 & E_x(y) \end{bmatrix} \tag{4.42}$$

where no cross-polarisation coupling occurs, while the propagation characteristics of the two orthogonal polarisation components remain asymmetric. Similarly, for a 1×2 MIMO system,

$$\tilde{\mathbf{H}}_{|R|=0}^{N_\mathrm{R}=2} = \begin{bmatrix} 1 & 0 & 1 & 0 \\ 0 & 1 & 0 & 1 \end{bmatrix}^\mathrm{T} \tag{4.43}$$

and

$$\tilde{\mathbf{H}}_{\left|R_{\tilde{h}_\mathrm{HH}}\right|=1}^{N_\mathrm{R}=2} = \frac{\sqrt{2}}{\sqrt{1+|E_x(y)|^2}}\begin{bmatrix} 1 & 0 & 1 & 0 \\ 0 & E_x(y) & 0 & E_x(y) \end{bmatrix}^\mathrm{T}. \tag{4.44}$$

For a 1×4 MIMO system,

$$\tilde{\mathbf{H}}_{|R|=0}^{N_\mathrm{R}=4} = \begin{bmatrix} 1 & 0 & 1 & 0 & 1 & 0 & 1 & 0 \\ 0 & 1 & 0 & 1 & 0 & 1 & 0 & 1 \end{bmatrix}^\mathrm{T} \tag{4.45}$$

and

$$\tilde{\mathbf{H}}^{N_\mathrm{R}=4}_{\left|R_{\tilde{h}_\mathrm{HH}}\right|=1} = \frac{\sqrt{2}}{\sqrt{1+|E_x(y)|^2}} \begin{bmatrix} 1 & 0 & 1 & 0 & 1 & 0 & 1 & 0 \\ 0 & E_x(y) & 0 & E_x(y) & 0 & E_x(y) & 0 & E_x(y) \end{bmatrix}^\mathrm{T}. \tag{4.46}$$

In Channel A, the channel matrix $\tilde{\mathbf{H}}$ is spatially invariant, whereas in Channel B it becomes a periodic function of the spatial coordinate y, i.e., $\tilde{\mathbf{H}}(y)$. As a result, the spatially averaged ABEP can be carried out using (4.39) for Channel A. By contrast, for Channel B the spatially averaged PEP requires an explicit averaging over the spatial dimension and is therefore reformulated as follows:

$$\begin{aligned}
\Pr_\mathrm{avg}\left[(k,1,1)\to\left(\hat{k},\hat{q}_\mathrm{V},\hat{q}_\mathrm{H}\right)\right] &= \frac{1}{L}\int_0^L \frac{1}{\pi}\int_0^{\frac{\pi}{2}} e^{\left(-\frac{\left(\sqrt{\frac{\rho}{2}\left\|\tilde{\mathbf{H}}(y)\Delta\mathbf{x}(p,\hat{p})\right\|_2^2}\right)^2}{2\sin^2\psi}\right)} \mathrm{d}\psi\mathrm{d}y \\
&= \frac{1}{L}\int_0^L \frac{1}{\pi}\int_0^{\frac{\pi}{2}} e^{\left(-\frac{\left\{\sqrt{\frac{\rho}{2}\left\|\tilde{\mathbf{H}}(y)\begin{bmatrix}\cos\varepsilon_k e^{\left(j\frac{2\pi q_\mathrm{V}}{M}\right)}-\cos\varepsilon_{\hat{k}} e^{\left(j\frac{2\pi\hat{q}_\mathrm{V}}{M}\right)} \\ \sin\varepsilon_k e^{\left(j\frac{2\pi q_\mathrm{H}}{M}\right)}-\sin\varepsilon_{\hat{k}} e^{\left(j\frac{2\pi\hat{q}_\mathrm{H}}{M}\right)}\end{bmatrix}\right\|_F^2}\right\}^2}{2\sin^2\psi}\right)} \mathrm{d}\psi\mathrm{d}y, \\
&= \frac{1}{L}\int_0^L \frac{1}{\pi}\int_0^{\frac{\pi}{2}} e^{\left(-\frac{\left\{\sqrt{\frac{\rho}{2}\left\|\tilde{\mathbf{H}}_{\left|R_{\tilde{h}_\mathrm{HH}}\right|=1}\begin{bmatrix}\cos\varepsilon_k e^{\left(j\frac{2\pi q_\mathrm{V}}{M}\right)}-\cos\varepsilon_{\hat{k}} e^{\left(j\frac{2\pi\hat{q}_\mathrm{V}}{M}\right)} \\ \sin\varepsilon_k e^{\left(j\frac{2\pi q_\mathrm{H}}{M}\right)}-\sin\varepsilon_{\hat{k}} e^{\left(j\frac{2\pi\hat{q}_\mathrm{H}}{M}\right)}\end{bmatrix}\right\|_F^2}\right\}^2}{2\sin^2\psi}\right)} \mathrm{d}\psi\mathrm{d}y
\end{aligned} \tag{4.47}$$

where $L = 0.03\,\mathrm{m}$. The simulated spatially averaged ABEP results of Channel A and Channel B under different MIMO configurations are illustrated in Fig. 4.14 and Fig. 4.15, respectively (Figs. 4.14 and 4.15 present the same ABEP results using different vertical-axis ranges. Fig. 4.14 uses a restricted ABEP range to

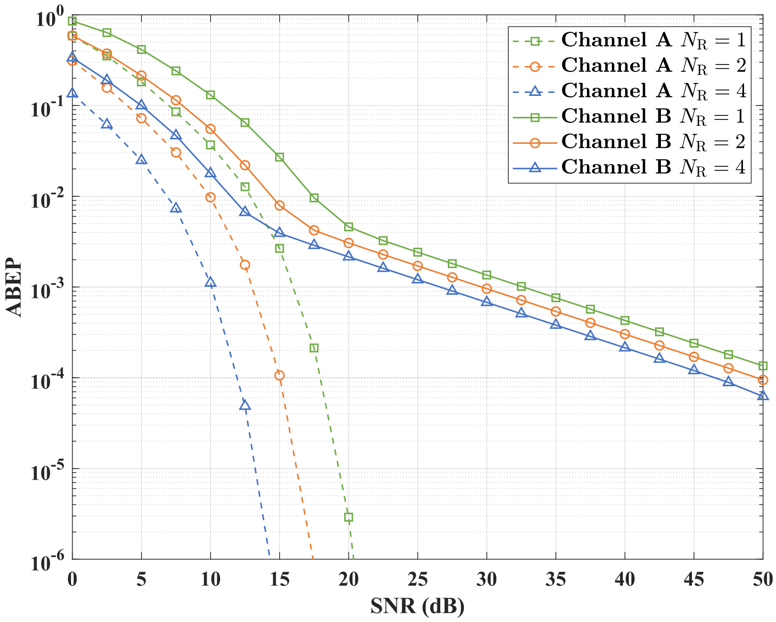

Fig. 4.14 The ABEP performance of the PolarSK scheme for normalised 1×1, 1×2, and 1×4 MIMO systems with $K = 2$ and $M = 2$, under Channel A and Channel B, respectively.

facilitate comparison in the practically relevant region, whereas Fig. 4.15 uses an extended dynamic range to reveal the complete high-SNR behaviour and the large difference between Channels A and B.). These simplified results show that Channel A can yield a substantially lower ABEP than Channel B, because the symmetric channel preserves both polarisation branches whereas Channel B introduces a severe horizontal branch standing-wave distortion. The comparison is intended as a sanity check on the physical mechanism rather than as a universal quantitative gain.

Channel B deliberately applies the standing-wave factor only to the horizontal co-polarised coefficient. In a room, both polarisation components can contain coherent multipath extrema, but their combined effect on ABEP is not necessarily monotonic because it depends on their relative amplitudes and phases. Likewise, a lossy multilayer wall can exhibit Brewster-like minima in its TM reflection magnitude rather than a universal zero at one interface angle. If a dominant-path approaches such a minimum, the resulting branch imbalance can reduce selected received symbol distances and increase the associated PEP.

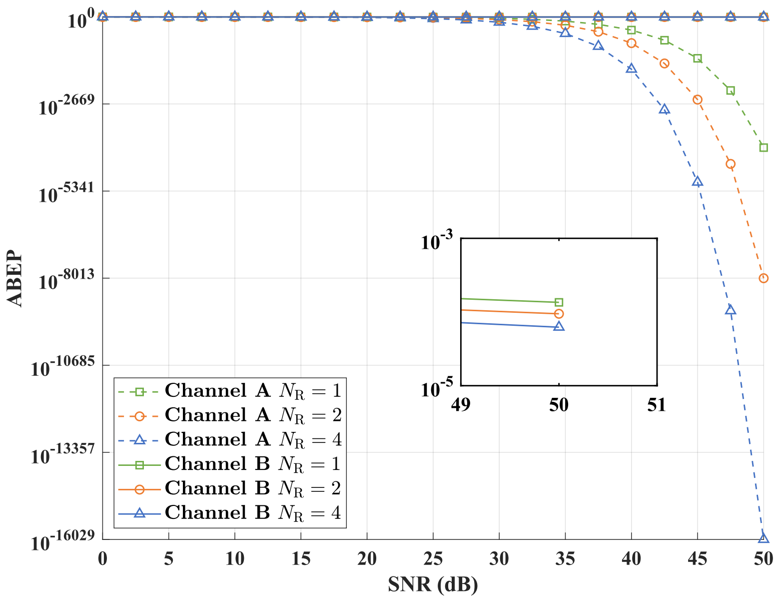

Fig. 4.15 The ABEP performance of the PolarSK scheme for normalised 1×1, 1×2, and 1×4 MIMO systems with $K = 2$ and $M = 2$, under Channel A and Channel B, respectively.

For realistic indoor channels, a complete closed-form proof remains open; nevertheless, the above heuristic argument supports the physical plausibility of the simulation results presented in this chapter.

4.7 Summary

In this chapter, the physically grounded RT algorithm introduced in the previous chapter is employed here for the prediction and evaluation of indoor polarised wireless channels. Through extensive simulation studies, the emergence of ABEP floors is observed across various MIMO configurations and signal constellations under NLOS conditions, especially when the surrounding walls are composed of materials that are unfavourable for wireless propagation. To mitigate this problem, an optimisation framework is introduced to reduce the ABEP floor of PolarSK by jointly adjusting the permittivity, conductivity, and thickness of each layer within a multilayer wall structure. Numerical evaluations confirm that the proposed optimisation effectively lowers the ABEP of PolarSK in NLOS environments at an SNR of 50 dB for the considered room geometry, Rx grid, antenna model, and material search ranges. The very large numerical reductions should be interpreted on a logarithmic scale and as scenario-specific evidence that deterministic material-induced polarisation imbalance can dominate the high-SNR performance of PolarSK. These findings demonstrate the promise of EM material optimisation in the architectural design of indoor environments, while practical deployment requires further constraints on available materials, construction feasibility, safety regulations, cost, frequency selectivity, and robustness to manufacturing tolerances.

Chapter 5

Physically Consistent RIS Macromodelling for Indoor Wireless Channel Prediction via RT

Overview

This chapter develops a self-consistent EM framework for modelling RISs in realistic indoor multipath environments and uses it to directly synthesise RIS phase distributions under multipath illumination. The approach couples deterministic RT with a circuit-based macromodel so that site-specific illumination, finite-aperture effects, and nonideal unit-cell responses are treated within a unified formulation. To preserve physical consistency, the scattered field is decomposed into coherent Floquet–Bloch channels and constrained by impedance boundary conditions together with passivity consistent modal power balance. By combining PO and diffraction grating theory, I derive incidence-aware closed-form expressions for modal reflection coefficients under arbitrary multipath excitation, while explicitly retaining multimode reradiation and parasitic/specular components. The resulting framework provides an analytically tractable and computationally efficient basis for direct multipath-aware phase synthesis and reliable prediction of RIS-assisted channel shaping in nonideal deployments.

5.1 Introduction

Indoor wireless networks for 5G/6G are expected to deliver high throughput, low latency, and reliable quality of service. In realistic site-specific environments, however, blockage, rich multipath, and irregular geometry can severely deteriorate coverage and link stability [182]. Conventional optimisation at the Tx and Rx alone cannot directly control these propagation impairments. RISs therefore attract substantial interest as a means to transform passive environments into programmable smart radio spaces [18, 183–185].

As RIS technology moves from conceptual demonstrations to deployment-oriented studies, the key bottleneck is no longer the qualitative demonstration of wavefront control, but the availability of models that are simultaneously rigorous from an EM perspective, channel-aware, and computationally tractable. On one hand, communication-level abstractions based on diagonal phase-shift matrices are attractive for optimisation but can hide important physical effects [19, 20, 186]. On the other hand, full-wave microscopic simulations can capture coupling and nonideal scattering with high fidelity, but they are often too expensive for repeated use in link-level and system-level design loops [21, 187].

Recent EM studies have clarified several essential mechanisms that any practical RIS model should preserve. The general macroscopic framework in [16] shows that RIS scattering should be decomposed into multiple coherent contributions, where desired anomalous reradiation coexists with specular, parasitic, and diffuse components, and where power balance across modes is fundamental for physical consistency. Consistent with this requirement, the impedance matrix formulation in [72] highlights that matching normal Poynting fluxes is the key feasibility condition for passive wavefront transformations. The angular response and far-field analysis in [15] further demonstrates that local reflection coefficient approximations are insufficient in many practical conditions, especially when periodicity-induced multibeam scattering and off-design illumination are present. In parallel, the Floquet–Bloch analysis in [188] provides rigorous closed-form modal insight for periodic reactive metasurfaces under arbitrary incident plane waves, highlighting why mode competition and dependence on incidence angle must be explicitly characterised rather than implicitly absorbed into idealised coefficients.

Despite these advances, an important gap remains when one attempts to translate these insights into deterministic indoor channel engineering. Existing models are often specialised to a single plane-wave excitation, to infinite or locally periodic assumptions, or to specific canonical configurations, whereas practical indoor deployments involve finite-size panels excited by superpositions of waves arriving from many directions with different amplitudes, phases, and polarisations. In addition, propagation engineering workflows require models that can be embedded into ray-based simulation pipelines and repeatedly queried during design space exploration, which imposes a strict efficiency requirement not met by brute-force full-wave solvers.

These observations make this chapter necessary for three reasons. First, without a self-consistent treatment of multimode reradiation under multipath incidence, the predicted channel-shaping capability of RIS-assisted links can be systematically biased. Second, without explicit modal characterisation that depends on incidence angle, it is difficult to explain and predict the performance degradation observed away from design illumination conditions. Third, without a computationally efficient macromodel, RIS optimisation subject to meaningful EM constraints remains hard to scale in realistic site-specific scenarios.

Motivated by the above, this chapter develops a macroscopic self-consistent EM framework for nonideal finite-size RISs under arbitrary multipath excitation. The proposed formulation combines PO and diffraction grating theory with incidence-aware Floquet–Bloch modal analysis, so that key wave physics mechanisms are preserved while retaining the efficiency required for integration into ray-based propagation simulators and iterative communication design loops. Compared with ideal single-reflection abstractions, the model explicitly retains multimode and parasitic behaviours; compared with purely microscopic solvers, it offers an analytically structured and computationally lightweight representation tailored for channel-oriented studies.

Within this context, this chapter makes four major contributions. I first formulate a unified scattering model in which the incident field is represented as a superposition of plane-wave components with arbitrary incidence angles, amplitudes, phases, and polarisations, enabling direct treatment of rich multipath excitation. I then derive closed-form Floquet–Bloch modal reflection coefficients as explicit functions of incidence angle, extending analytical characterisation beyond normal incidence design conditions and linking my derivation to established metasurface synthesis principles [73, 188, 189]. I further incorporate multimode reradiation, parasitic scattering, and finite-aperture effects into a computationally efficient macromodel suitable for channel-level evaluation in deterministic environments. Finally, I assess the framework against CST Studio Suite (CST) full-wave unit-cell simulations and indoor measurements with a 3.5 GHz varactor-tuned prototype. These two comparisons test different parts of the modelling chain and are therefore reported separately.

Overall, the proposed method narrows the gap between idealized RIS abstractions and site-specific propagation engineering by linking realistic EM scattering behaviour to communication-oriented evaluation. It therefore provides not only a modelling tool, but also a physically interpretable basis for understanding when, why, and how RIS-enabled channel shaping departs from ideal anomalous-reflection assumptions in realistic multipath conditions.

The remainder of this chapter is organised as follows. The next section presents the plane-wave expansion framework under multipath incidence. The following section introduces the multiport unit-cell model and its EM formulation. The subsequent sections discuss representative numerical results and practical implications, and the derivations and evaluations are then used to support the chapter summary.

The notation of Chapter 5 is summarised in Table 5.1.

Table 5.1 Notation of Chapter 5

Notation	**Definition**
$\mathbf{r}$	Position vector at which an electromagnetic field is evaluated.
$\Omega_i = (\theta_i, \phi_i)$	Angular direction of an incident plane wave represented by its zenith and azimuth angles.
$\theta_i^{(n)}$	Zenith angle of incident path n.

Continued on next page

Table 5.1: Notation of Chapter 5 (Continued)

Notation	Definition
$\phi_i^{(n)}$	Azimuth angle of incident path n.
n	Index of an incident RT path represented as a plane-wave component.
N	Number of incident RT paths.
$\mathbf{k}_{i,n}$	Wave vector of incident path n.
$\mathbf{E}_{i,n}$	Complex electric-field vector of incident path n.
$\|\cdot\|_F$	Frobenius norm.
$\hat{\mathbf{a}}_{\phi_i^{(n)}}$	Azimuthal unit vector of incident path n.
$\hat{\mathbf{a}}_{\theta_i^{(n)}}$	Zenithal unit vector of incident path n.
ψ_n	Polarisation orientation angle of incident path n.
k	Wavenumber magnitude of an incident plane wave.
$\mathbf{H}_{i,n}$	Complex magnetic-field vector of incident path n.
j	Imaginary unit satisfying $j^2 = -1$.
ω	Angular frequency.
f	Frequency.
λ	Free-space wavelength.
x_r	Local x-coordinate of a field evaluation point.
y_r	Local y-coordinate of a field evaluation point.
z_r	Local z-coordinate of a field evaluation point.
$\hat{\mathbf{a}}_x$	Cartesian unit vector along the local x-axis.
$\hat{\mathbf{a}}_y$	Cartesian unit vector along the local y-axis.
$\hat{\mathbf{a}}_z$	Cartesian unit vector normal to the RIS plane.
$\mathbf{E}_{i,n}^{\mathrm{TE}}$	TE-polarised incident electric field of path n.

Continued on next page

Table 5.1: Notation of Chapter 5 (Continued)

Notation	Definition
$\hat{\mathbf{a}}_{i,n}^{\mathrm{TE}}$	TE polarisation unit vector of incident path n.
$\hat{\mathbf{a}}_{i,n}^{\mathrm{TM}}$	TM polarisation unit vector of incident path n.
$\hat{\mathbf{k}}_{i,n}$	Propagation unit vector of incident path n.
l_n	Propagation length of incident path n.
$\mathbf{H}_{i,n}^{\mathrm{TM}}$	TM-polarised incident magnetic field of path n.
η_0	Intrinsic wave impedance of free space.
$\mathbf{E}_{t,i}$	Total tangential incident electric field on the RIS.
$\mathbf{H}_{t,i}$	Total tangential incident magnetic field on the RIS.
$\mathbf{r}_t$	Position vector of a source point on the RIS.
$\mathbf{E}_{t,i,n}^{\mathrm{TE}}$	Tangential TE incident electric field of path n on the RIS.
$\mathbf{E}_{t,i,n}^{\mathrm{TM}}$	Tangential TM incident electric field of path n on the RIS.
$\mathbf{H}_{t,i,n}^{\mathrm{TE}}$	Tangential TE incident magnetic field of path n on the RIS.
$\mathbf{H}_{t,i,n}^{\mathrm{TM}}$	Tangential TM incident magnetic field of path n on the RIS.
$\mathbf{J}_s$	Equivalent electric surface current density on the RIS.
$\mathbf{M}_s$	Equivalent magnetic surface current density on the RIS.
$\hat{\mathbf{n}}$	Unit normal to the RIS surface.
Γ_n	Local reflection coefficient applied to incident path n.
p	Floquet diffraction-order index along the first lattice axis.
q	Floquet diffraction-order index along the second lattice axis.
$\Gamma_{n,pq}$	Complex reflection coefficient of Floquet order (p,q) excited by incident path n.
$\Delta_{n,pq}$	Phase of Floquet order (p,q) excited by incident path n.

Continued on next page

Table 5.1: Notation of Chapter 5 (Continued)

Notation	Definition
$\mathbf{V}_{\mathrm{F}}$	Voltage vector at the external Floquet ports.
$\mathbf{V}_{\mathrm{C}}$	Voltage vector at the internal circuit ports.
$\mathbf{I}_{\mathrm{F}}$	Current vector at the external Floquet ports.
$\mathbf{I}_{\mathrm{C}}$	Current vector at the internal circuit ports.
$\mathbf{Z}_{\mathrm{FF}}$	External Floquet-port-impedance block.
$\mathbf{Z}_{\mathrm{FC}}$	Floquet-to-circuit coupling impedance block.
$\mathbf{Z}_{\mathrm{CF}}$	Circuit-to-Floquet coupling impedance block.
$\mathbf{Z}_{\mathrm{CC}}$	Internal circuit-port-impedance block.
Z_{LC}	Load impedance connected to an internal circuit port.
$\mathbf{Z}_{\mathrm{LC}}$	Diagonal matrix of internal circuit-port load impedances.
$\mathbf{Z}_{\mathrm{IN}}^{\mathrm{F}}$	Loaded input impedance matrix observed from the external Floquet ports.
Γ	Reflection coefficient matrix of the loaded unit cell.
C	Varactor capacitance.
C_m	Varactor capacitance of tuning state m.
m	Varactor tuning-state index.
M	Number of available varactor capacitance states.
σ	Polarisation label selected from $\{\mathrm{TE},\mathrm{TM}\}$.
$Z_{0,\sigma}$	Reference wave impedance for polarisation σ.
$n^{\star}$	Index of the incident path selected for the single-path RIS design.
k_0	Free-space wavenumber.
$\Phi(x,y)$	RIS phase profile at local coordinates (x,y).
Φ_{SP}	RIS phase profile produced by the single-path design.

Continued on next page

Table 5.1: Notation of Chapter 5 (Continued)

Notation	Definition
$\mathbf{k}_{r,pq}^{(n)}$	Wave vector of reflected Floquet order (p,q) generated by incident path n.
$k_{x,r,pq}^{(n)}$	Local x-component of $\mathbf{k}_{r,pq}^{(n)}$.
$k_{y,r,pq}^{(n)}$	Local y-component of $\mathbf{k}_{r,pq}^{(n)}$.
$k_{z,r,pq}^{(n)}$	Local z-component of $\mathbf{k}_{r,pq}^{(n)}$.
Φ_{MP}	RIS phase profile produced by the multipath-aware design.
$U^{(+)}$	Integrated target-polarised-field contribution independent of the controllable RIS coefficient.
$\chi^{\star}$	Common phase that aligns the controllable RIS contribution with the uncontrollable target field.
τ_U	Numerical tolerance for selecting the common phase from the uncontrollable target field.
τ_F	Numerical tolerance for identifying an undefined local controllable-field phase.
$\mathcal{C}_\Gamma$	Calibrated codebook of passive complex reflection coefficients.
$\mathcal{C}_C$	Finite set of admissible passive unit-cell load states.
N_c	Number of independently controlled RIS cells.
C_g	Hardware load state assigned to RIS cell g.
$\mathbf{C}$	Vector of hardware load states assigned to all RIS cells.
$J(\mathbf{C})$	Target-polarised received-power objective of the complete multipath macromodel.
τ_J	Relative objective-improvement tolerance for terminating coordinate descent.

Continued on next page

Table 5.1: Notation of Chapter 5 (Continued)

Notation	Definition
Ω_{ref}	Reference incidence used to visualise the implemented RIS phase map.
Δx	Sampling interval along the local x-axis.
Δy	Sampling interval along the local y-axis.
N_x	Number of RIS samples along the local x-axis.
N_y	Number of RIS samples along the local y-axis.
D_x	Sampled RIS aperture dimension along the local x-axis.
D_y	Sampled RIS aperture dimension along the local y-axis.
$k_{x,j}$	Local x-directed transverse wavenumber of spectral component j.
$k_{y,j}$	Local y-directed transverse wavenumber of spectral component j.
w_j	Weight assigned to spectral component j.
G_x	Estimated reciprocal-lattice spacing along the local x-axis.
G_y	Estimated reciprocal-lattice spacing along the local y-axis.
ε_x	Weighted reciprocal-lattice fitting residual along the local x-axis.
ε_y	Weighted reciprocal-lattice fitting residual along the local y-axis.
δk_x	Finite-aperture spectral resolution along the local x-axis.
δk_y	Finite-aperture spectral resolution along the local y-axis.
c_{tol}	Tolerance factor used in the effective-periodicity test.
$\mathbf{J}_{i,n}$	Electric incident-current template generated by path n on the RIS.
$\mathbf{M}_{i,n}$	Magnetic incident-current template generated by path n on the RIS.
$\mathbf{J}_s^{\text{SP}}$	Equivalent electric surface current produced by the single-path profile.
$\mathbf{M}_s^{\text{SP}}$	Equivalent magnetic surface current produced by the single-path profile.
$\mathbf{J}_s^{\text{MP}}$	Equivalent electric surface current produced by the multipath-aware profile.

Continued on next page

Table 5.1: Notation of Chapter 5 (Continued)

Notation	**Definition**
$\mathbf{M}_s^{\mathrm{MP}}$	Equivalent magnetic surface current produced by the multipath-aware profile.
$\mathbf{a}$	Power-normalised vector of incident RIS port or modal amplitudes.
$\mathbf{b}$	Power-normalised vector of reradiated RIS port or modal amplitudes.
Θ_{D}	Diagonal control operator of a locally controlled RIS.
Θ_{BD}	Full control operator of a beyond-diagonal RIS.
$\mathcal{G}$	Graph of the physically implemented beyond-diagonal interconnection topology.
$\mathcal{A}_{\mathrm{BD}}(\mathcal{G})$	Feasible beyond-diagonal network set associated with graph $\mathcal{G}$.
E_i	Complex incident electric-field amplitude in the canonical nonlocal-reflection analysis.
E_r	Complex desired reflected electric-field amplitude in the canonical nonlocal-reflection analysis.
θ_i	Incidence angle in the canonical nonlocal-reflection analysis.
θ_r	Desired anomalous-reflection angle in the canonical nonlocal-reflection analysis.
$\Phi_r(x)$	Spatial phase difference between the incident and desired reflected waves.
$P_n(x)$	Normal time-average power density entering the RIS at surface coordinate x.
$\mathbf{v}_0$	Coherent open-circuit excitation vector generated by all incident paths.
$\mathbf{v}_{0,n}$	Open-circuit excitation vector generated by incident path n.
$\mathbf{Z}_{\mathrm{EM}}$	EM self- and mutual-impedance matrix of the unloaded RIS.

Continued on next page

Table 5.1: Notation of Chapter 5 (Continued)

Notation	**Definition**
$\mathbf{Z}_{\mathrm{L}}(\xi)$	Tunable load-network impedance matrix of the beyond-diagonal RIS.
ξ	Vector of physically adjustable beyond-diagonal network parameters.
$\mathbf{v}$	Voltage vector at the controlled ports of the coupled RIS network.
$\mathbf{i}$	Current vector induced at the controlled ports of the coupled RIS network.
$\mathbf{G}(\mathbf{r})$	Transfer matrix from coupled RIS port currents to the electric field at $\mathbf{r}$.
$\mathbf{E}_f(\mathbf{r})$	Electric-field contribution independent of the tunable RIS loads.
$\mathbf{G}_\infty(\theta,\phi)$	Far-field limit of the RIS port-current transfer matrix.
$\mathbf{F}(\theta,\phi)$	Vector far-field radiation pattern of the complete RIS-assisted system.
$\mathbf{F}_f(\theta,\phi)$	Far-field contribution independent of the tunable RIS loads.
P_{tar}	Target-polarised far-field power-pattern metric.
$\mathbf{r}_{\mathrm{tar}}$	Target receiver or observation position.
$\mathcal{A}_{\mathrm{BD}}$	Feasible set of physically realisable beyond-diagonal networks.
$\phi_g^{(i)}$	Phase of the optimised current at controlled port g.
$\mathbf{A}(\xi)$	Coupled network matrix defined by $\mathbf{Z}_{\mathrm{L}}(\xi)-\mathbf{Z}_{\mathrm{EM}}$.
ξ_k	Continuous control parameter k of the beyond-diagonal network.
q_{tar}	Complex target-polarised field used in the beyond-diagonal objective.
$(\cdot)^{\mathrm{H}}$	Hermitian-transpose operator.
$(\cdot)^*$	Complex conjugation operator.
$\Re\{\cdot\}$	Real-part operator.
$\mathbf{h}_i$	Coherent multipath excitation vector in the abstract RIS channel model.
$\mathbf{h}_r$	Coupling vector from the RIS modes to the target.
y	Complex target field in the abstract RIS channel model.

Continued on next page

Table 5.1: Notation of Chapter 5 (Continued)

Notation	Definition
P_{tx}	Transmit power used in the RT evaluation.
θ_{d}	Desired reradiation zenith angle in the CST three-path benchmark.
ϕ_{d}	Desired reradiation azimuth angle in the CST three-path benchmark.
$E_{0,n}$	Normalised electric-field amplitude of incident path n in the CST three-path benchmark.
$\varphi_{0,n}$	Reference phase of incident path n at the local RIS origin in the CST benchmark.
$\alpha_{\mathrm{g},n}$	Grazing angle of incident path n measured from the RIS plane.
$E_{\theta}(\theta_{\mathrm{d}}, \phi_{\mathrm{d}})$	Complex θ-polarised-field component in the prescribed CST target direction.
$E_{\phi}(\theta_{\mathrm{d}}, \phi_{\mathrm{d}})$	Complex ϕ-polarised-field component in the prescribed CST target direction.
ρ_{θ}	Fraction of target-direction electric-field power in the θ-polarised component.

5.2 Plane-Wave Expansion of EM Waves Reflected by RIS under Multipath Incidence

In deterministic scenarios within infinite or semi-infinite spaces, the total incident electric field $\mathbf{E}_i(\mathbf{r})$ at a given point can be represented as a superposition of a discrete angular spectrum of incident plane waves, each contributing to the field according to ray-based models.

$$\begin{aligned}\mathbf{E}_i(\mathbf{r}) &= \iint_{\Omega_i} \mathbf{E}_i(\Omega_i) e^{(-j\mathbf{k}_i(\Omega_i)\cdot\mathbf{r})}\, \mathrm{d}\Omega_i \\ &= \int_0^{2\pi}\int_{\frac{\pi}{2}}^{\pi} \mathbf{E}_i(\theta_i,\phi_i) e^{(-j\mathbf{k}_i(\theta_i,\phi_i)\cdot\mathbf{r})} \sin\theta_i \,\mathrm{d}\theta_i\,\mathrm{d}\phi_i \\ &= \sum_{n=1}^{N} \mathbf{E}_i\left(\theta_i^{(n)},\phi_i^{(n)}\right) e^{\left(-j\mathbf{k}_i\left(\theta_i^{(n)},\phi_i^{(n)}\right)\cdot\mathbf{r}\right)}.\end{aligned} \tag{5.1}$$

The incident electric-field component vector associated with the nth plane-wave component is written as

$$\mathbf{E}_{i,n} = -\left\|\mathbf{E}_{i,n}\right\|_F \left(\hat{\mathbf{a}}_{\phi_i^{(n)}} \cos\psi_n + \hat{\mathbf{a}}_{\theta_i^{(n)}} \sin\psi_n\right). \tag{5.2}$$

Here, $\psi_n \in [0,\pi)$ denotes the polarisation orientation angle in the transverse plane of the nth incident wave. The vectors $\hat{\mathbf{a}}_{\phi_i^{(n)}}$ and $\hat{\mathbf{a}}_{\theta_i^{(n)}}$ are orthogonal unit vectors spanning the plane perpendicular to the incident wave vector $\mathbf{k}_i\left(\theta_i^{(n)},\phi_i^{(n)}\right)$, whose magnitude is k under the quasimonochromatic approximation. They form an orthonormal basis of the standard spherical coordinate system, and the angle ψ_n is measured in that transverse plane relative to $-\hat{\mathbf{a}}_{\phi_i^{(n)}}$. The angular region of interest is restricted to the lower hemisphere,

$$\Omega_i = \left\{(\theta_i,\phi_i) \,\middle|\, \theta_i \in \left[\frac{\pi}{2},\pi\right],\ \phi_i \in [0,2\pi]\right\}. \tag{5.3}$$

Each plane-wave component, defined by the triplet $(\mathbf{E}_{i,n},\mathbf{H}_{i,n},\mathbf{k}_{i,n})$, propagates towards and interacts with a planar impedance boundary according to the classical deterministic plane-wave relations, where $\mathbf{E}_{i,n} \triangleq \mathbf{E}_i\left(\theta_i^{(n)},\phi_i^{(n)}\right)$, $\mathbf{H}_{i,n} \triangleq \mathbf{H}_i\left(\theta_i^{(n)},\phi_i^{(n)}\right)$, and $\mathbf{k}_{i,n} \triangleq \mathbf{k}_i\left(\theta_i^{(n)},\phi_i^{(n)}\right)$. In particular, consider the TE component, which corresponds to a wave that is obliquely incident upon the boundary at an azimuth $\phi_i^{(n)}$ and a zenith angle $\theta_i^{(n)}$, as illustrated in Fig. 5.1. Throughout this section, all fields are represented in the frequency domain under the $e^{j\omega t}$ convention, and explicit time-domain factors are omitted. For an arbitrary incident wavevector $\mathbf{k}_{i,n}$, at position (x_r,y_r,z_r) with $\mathbf{r} = \hat{\mathbf{a}}_x x_r + \hat{\mathbf{a}}_y y_r + \hat{\mathbf{a}}_z z_r$, the incident electric field is

$$\mathbf{E}_{i,n}^{\mathrm{TE}} = -\hat{\mathbf{a}}_{i,n}^{\mathrm{TE}} \left\|\mathbf{E}_{i,n}\right\|_F \cos\psi_n e^{\left(-j\mathbf{k}_{i,n}\cdot\mathbf{r}\right)}. \tag{5.4}$$

where $\hat{\mathbf{a}}_{i,n}^{\mathrm{TE}}$ is the unit vector of TE-polarised component of the incident electric field $\mathbf{E}_{i,n}$, $\hat{\mathbf{a}}_{i,n}^{\mathrm{TE}}$ can be calculated by

$$\hat{\mathbf{a}}_{i,n}^{\mathrm{TE}} = \frac{\hat{\mathbf{a}}_z \times \hat{\mathbf{k}}_{i,n}}{\left\|\hat{\mathbf{a}}_z \times \hat{\mathbf{k}}_{i,n}\right\|_F} = \hat{\mathbf{a}}_{\phi_i^{(n)}}. \tag{5.5}$$

where $\hat{\mathbf{k}}_{i,n} = \frac{\mathbf{k}_{i,n}}{k}$ is the unit vector of incident wave,

$$\hat{\mathbf{a}}_{\phi_i^{(n)}} = -\hat{\mathbf{a}}_x \sin\phi_i^{(n)} + \hat{\mathbf{a}}_y \cos\phi_i^{(n)}. \tag{5.6}$$

Finally, using the unit vector and wavevector defined above, the TE electric field is written compactly as

$$\mathbf{E}_{i,n}^{\mathrm{TE}} = -\hat{\mathbf{a}}_{\phi_i^{(n)}} \left\|\mathbf{E}_{i,n}\right\|_F \cos\psi_n \, e^{-j\mathbf{k}_{i,n}\cdot\mathbf{r}+j2\pi l_n/\lambda}. \tag{5.7}$$

The corresponding TM magnetic field is

$$\mathbf{H}_{i,n}^{\mathrm{TM}} = -\frac{\hat{\mathbf{a}}_{\phi_i^{(n)}}}{\eta_0} \left\|\mathbf{E}_{i,n}\right\|_F \sin\psi_n \, e^{-j\mathbf{k}_{i,n}\cdot\mathbf{r}+j2\pi l_n/\lambda}. \tag{5.8}$$

Here, l_n is the propagation length of the nth path and η_0 is the free-space impedance. The common exponential retains both the spatial phase and the accumulated path phase; the minus signs follow from $\hat{\mathbf{a}}_x \sin\phi_i^{(n)} - \hat{\mathbf{a}}_y \cos\phi_i^{(n)} = -\hat{\mathbf{a}}_{\phi_i^{(n)}}$.

While this analysis is valuable for the ideal case of infinite metasurfaces, a more realistic approach for finite sized metasurfaces requires an evaluation of their scattering patterns. The PO approximation is adopted under the assumption that the RIS is electrically large relative to the wavelength and that the surface fields vary slowly over each local integration region, so that the induced equivalent currents can be approximated by their locally illuminated values.

Based on the surface equivalence principle, reciprocity, and image theory arguments, the reradiated field from an illuminated object can be represented by equivalent electric and magnetic surface current densities [190]. While canonical EM scattering problems often assume the object is either a perfect electric conductor (PEC) or a perfect magnetic conductor (PMC), a RIS presents a more complex case [16]. Consequently, for general wave transformations, the reradiated field depends on both electric and magnetic current densities.

To compute anomalous reradiation, I employ a generalised version of the method of image currents, based on Huygens' principle as proposed in [16, 190]. In this chapter, I analyse the field reradiated by an RIS in a multipath environment. I assume the incident signal is a superposition of a far-field plane wave from the primary source antenna and other reflected plane waves. The electric and magnetic fields incident on the RIS surface are obtained from the Ranplan RT software. The total incident electric field is given by (5.1), and the corresponding magnetic field is

$$\mathbf{H}_i(\mathbf{r}) = \sum_{n=1}^{N} \frac{\hat{\mathbf{k}}_{i,n} \times \mathbf{E}_{i,n}}{\eta_0} e^{\left(-j\mathbf{k}_{i,n}\cdot\mathbf{r}\right)}. \tag{5.9}$$

Only tangential field components contribute to the equivalent surface currents. For a general polarised incident wave, both tangential electric and tangential magnetic fields must retain the complete TE/TM decomposition, i.e.,

$$\mathbf{E}_{t,i}(\mathbf{r}_t) = \sum_{n=1}^{N} \left[\mathbf{E}_{t,i,n}^{\mathrm{TE}}(\mathbf{r}_t) + \mathbf{E}_{t,i,n}^{\mathrm{TM}}(\mathbf{r}_t)\right], \tag{5.10}$$

$$\mathbf{H}_{t,i}(\mathbf{r}_t) = \sum_{n=1}^{N} \left[\mathbf{H}_{t,i,n}^{\mathrm{TE}}(\mathbf{r}_t) + \mathbf{H}_{t,i,n}^{\mathrm{TM}}(\mathbf{r}_t)\right]. \tag{5.11}$$

where $\mathbf{E}_{t,i,n}(\mathbf{r}_t) = \mathbf{E}_{t,i,n}^{\mathrm{TE}}(\mathbf{r}_t) + \mathbf{E}_{t,i,n}^{\mathrm{TM}}(\mathbf{r}_t)$ and $\mathbf{H}_{t,i,n}(\mathbf{r}_t) = \mathbf{H}_{t,i,n}^{\mathrm{TE}}(\mathbf{r}_t) + \mathbf{H}_{t,i,n}^{\mathrm{TM}}(\mathbf{r}_t)$ denote the total tangential incident fields associated with the nth path. For the RIS plane $z = 0$, the above decomposition can be equivalently rewritten by expressing $\mathbf{E}_{t,i,n}^{\mathrm{TM}}(\mathbf{r}_t)$ in terms of $\mathbf{H}_{t,i,n}^{\mathrm{TM}}(\mathbf{r}_t)$ and $\mathbf{H}_{t,i,n}^{\mathrm{TE}}(\mathbf{r}_t)$ in terms of $\mathbf{E}_{t,i,n}^{\mathrm{TE}}(\mathbf{r}_t)$ as

$$\mathbf{E}_{t,i}(\mathbf{r}_t) = \sum_{n=1}^{N} \left[\mathbf{E}_{t,i,n}^{\mathrm{TE}}(\mathbf{r}_t) - \eta_0 \cos\theta_i^{(n)} \left(\hat{\mathbf{a}}_z \times \mathbf{H}_{t,i,n}^{\mathrm{TM}}(\mathbf{r}_t)\right)\right], \tag{5.12}$$

$$\mathbf{H}_{t,i}(\mathbf{r}_t) = \sum_{n=1}^{N} \left[\frac{\cos\theta_i^{(n)}}{\eta_0} \left(\hat{\mathbf{a}}_z \times \mathbf{E}_{t,i,n}^{\mathrm{TE}}(\mathbf{r}_t)\right) + \mathbf{H}_{t,i,n}^{\mathrm{TM}}(\mathbf{r}_t)\right]. \tag{5.13}$$

where $\mathbf{H}_{t,i,n}^{\mathrm{TM}}(\mathbf{r}_t) = \mathbf{H}_{i,n}^{\mathrm{TM}}$ and $\mathbf{E}_{t,i,n}^{\mathrm{TE}}(\mathbf{r}_t) = \mathbf{E}_{i,n}^{\mathrm{TE}}$. Here, the explicit expressions of $\mathbf{E}_{i,n}^{\mathrm{TE}}$ and $\mathbf{H}_{i,n}^{\mathrm{TM}}$ are given in 5.7 and 5.8, respectively.

For the analysis and design of phase-gradient metasurfaces, it is convenient to adopt the local reflection coefficient as a modelling parameter. The field reradiated by an RIS can then be modelled using equivalent electric ($\mathbf{J}_s$) and magnetic ($\mathbf{M}_s$) surface currents [16]. The RIS is assumed to lie in the plane $z = 0$ with unit normal $\hat{\mathbf{n}} = \hat{\mathbf{z}}$. These currents are obtained from the total tangential incident fields as

$$\mathbf{J}_s(\mathbf{r}_t) = \sum_{n=1}^{N} (1+\Gamma_n)\left(\mathbf{H}_{t,i,n}(\mathbf{r}_t) \times \hat{\mathbf{n}}\right), \tag{5.14a}$$

$$\mathbf{M}_s(\mathbf{r}_t) = \sum_{n=1}^{N} (1-\Gamma_n)\left(\hat{\mathbf{n}} \times \mathbf{E}_{t,i,n}(\mathbf{r}_t)\right). \tag{5.14b}$$

A pictorial representation of the above formulation is given in Fig. 5.1.

This local reflection approximation, however, is only valid under the locally periodic assumption, where the metasurface constituent elements vary adiabatically across the spatial interface compared to the wavelength. In particular, the local reflection coefficient model is equivalent to invoking a locally specular reflection assumption at each point on the interface [15]. However, the validity of this assumption is compromised for metasurfaces with abrupt phase gradients, particularly in the presence of oblique illumination. In such regimes, the local reflection approximation cannot adequately account for parasitic scattering channels, impedance mismatch between the incident and reradiated waves, and diffraction effects stemming from the inherent surface periodicity [15, 16]. To address these limitations, I employ a Floquet-based model that rigorously captures the modal spectrum of the periodic structure, thereby providing a physically consistent characterisation of the scattered field.

5.3 Macromodelling of RIS

The proposed self-consistent RIS modelling chain separates the electromagnetic characterisation from the subsequent phase synthesis. I first extract a multiport impedance representation of the unloaded unit cell from a full-wave model. The tunable loads are then reintroduced algebraically to obtain the reflection response for each admissible load state, incidence direction, and polarisation. This response is used to synthesise the far field of the finite

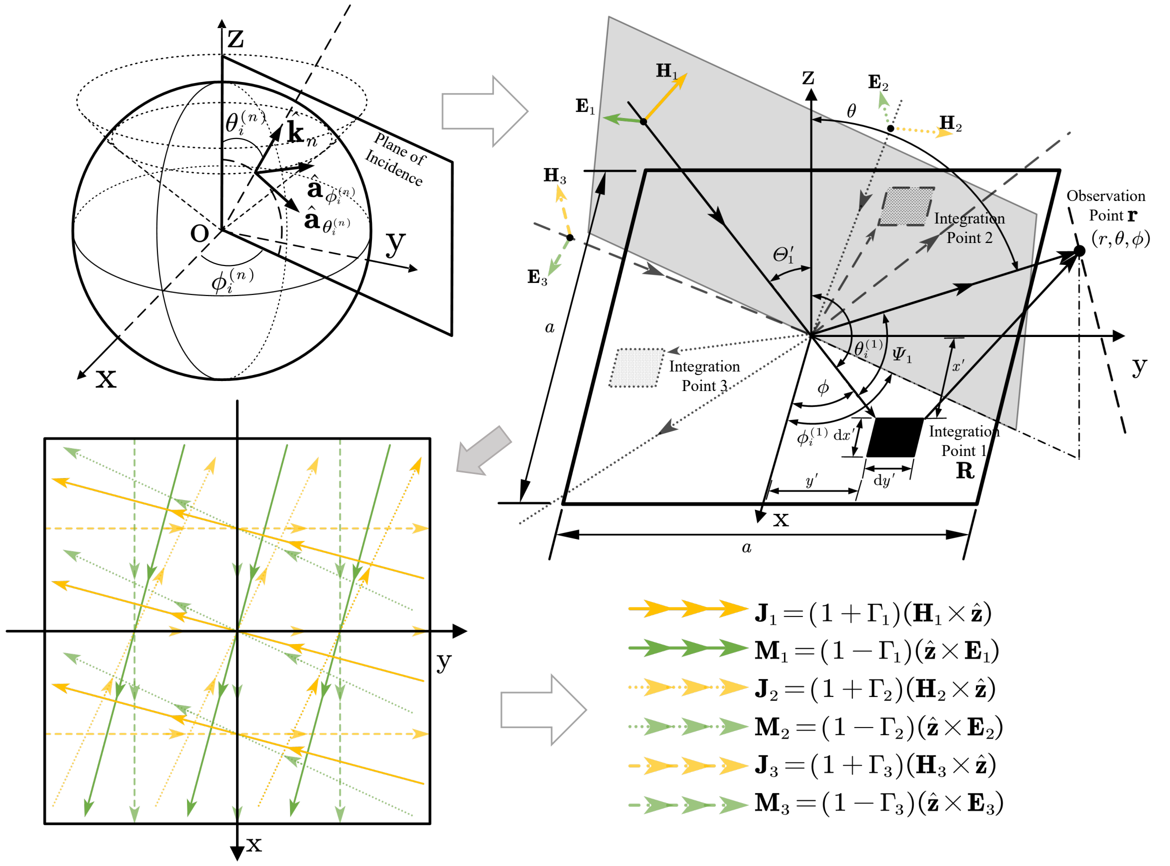

Fig. 5.1 Geometry of a rectangular conducting plate with an aperture illuminated by three uniform plane waves.

RIS aperture and is subsequently embedded in the RT model. The separation avoids a new volumetric full-wave solution for every load state while retaining the coupling represented by the extracted port-impedance matrix.

5.3.1 Derivation of the Reflection Coefficient Using a Multiport Unit-Cell Model

A direct full-wave sweep resolves the detailed geometry, material properties, and tunable loads of the RIS unit cell, but its cost grows with the number of load states and design iterations. A closed-form equivalent circuit is faster, although its fitted lumped parameters generally remain valid only over the frequency, geometry, and incidence range used for the fit. I therefore use CST to extract a multiport impedance model of the fixed unloaded

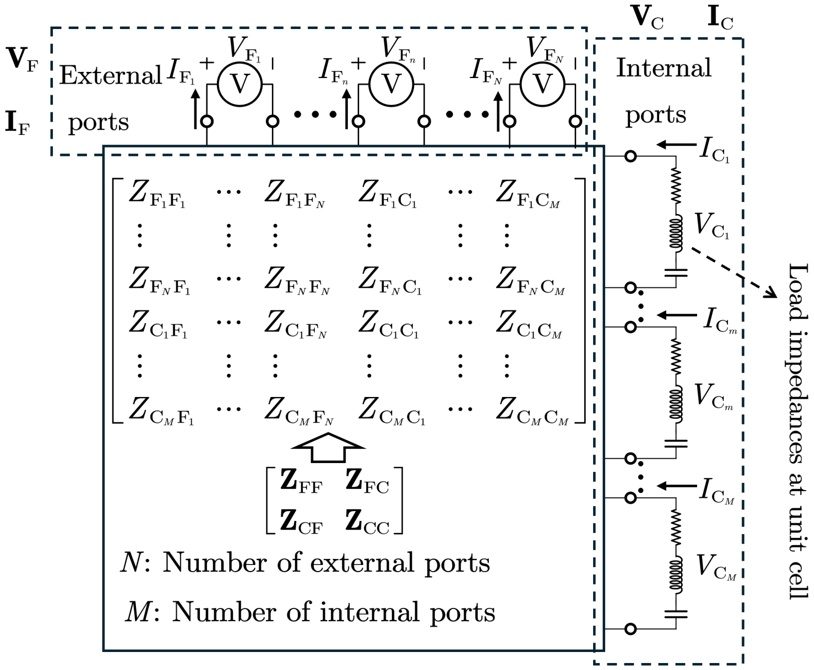

Fig. 5.2 Equivalent multiport network representation of the RIS unit cell.

geometry and vary only the circuit terminations during the subsequent load sweep. The model is accurate within the frequency and angular ranges represented by the extraction data; it is not assumed to extrapolate to a different unit-cell topology.

Let N_F and N_C denote the numbers of external Floquet ports and internal circuit ports, respectively. As illustrated in Fig. 5.2, the port voltages and currents of the unloaded unit cell satisfy

$$\begin{bmatrix} \mathbf{V}_\mathrm{F} \\ \mathbf{V}_\mathrm{C} \end{bmatrix} = \begin{bmatrix} \mathbf{Z}_\mathrm{FF} & \mathbf{Z}_\mathrm{FC} \\ \mathbf{Z}_\mathrm{CF} & \mathbf{Z}_\mathrm{CC} \end{bmatrix} \begin{bmatrix} \mathbf{I}_\mathrm{F} \\ \mathbf{I}_\mathrm{C} \end{bmatrix}. \tag{5.15}$$

Here, $\mathbf{V}_\mathrm{F} \in \mathbb{C}^{N_\mathrm{F}}$ and $\mathbf{I}_\mathrm{F} \in \mathbb{C}^{N_\mathrm{F}}$ are the external port voltage and current vectors, whereas $\mathbf{V}_\mathrm{C} \in \mathbb{C}^{N_\mathrm{C}}$ and $\mathbf{I}_\mathrm{C} \in \mathbb{C}^{N_\mathrm{C}}$ are their internal port counterparts. All currents are referenced into the unloaded multiport network. The four blocks in (5.15) therefore describe external to external, external to internal, internal to external, and internal to internal impedance coupling, respectively.

If the mth circuit port is terminated by $Z_{\mathrm{LC},m}$, the load matrix is

$$\mathbf{Z}_{\mathrm{LC}} = \mathrm{diag}\left(Z_{\mathrm{LC},1}, Z_{\mathrm{LC},2}, \ldots, Z_{\mathrm{LC},N_{\mathrm{C}}}\right). \tag{5.16}$$

Because $\mathbf{I}_{\mathrm{C}}$ is directed into the unloaded network, rather than into the loads, the termination condition is

$$\mathbf{V}_{\mathrm{C}} = -\mathbf{Z}_{\mathrm{LC}}\mathbf{I}_{\mathrm{C}}. \tag{5.17}$$

Substitution into the internal port block of (5.15) gives

$$-\mathbf{Z}_{\mathrm{LC}}\mathbf{I}_{\mathrm{C}} = \mathbf{Z}_{\mathrm{CF}}\mathbf{I}_{\mathrm{F}} + \mathbf{Z}_{\mathrm{CC}}\mathbf{I}_{\mathrm{C}}. \tag{5.18}$$

Provided that $\mathbf{Z}_{\mathrm{CC}} + \mathbf{Z}_{\mathrm{LC}}$ is nonsingular, elimination of $\mathbf{I}_{\mathrm{C}}$ yields

$$\mathbf{V}_{\mathrm{F}} = \left[\mathbf{Z}_{\mathrm{FF}} - \mathbf{Z}_{\mathrm{FC}}\left(\mathbf{Z}_{\mathrm{CC}} + \mathbf{Z}_{\mathrm{LC}}\right)^{-1}\mathbf{Z}_{\mathrm{CF}}\right]\mathbf{I}_{\mathrm{F}}. \tag{5.19}$$

Consequently, the loaded input impedance matrix observed at the external ports is the Schur complement

$$\mathbf{Z}_{\mathrm{IN}}^{\mathrm{F}} = \mathbf{Z}_{\mathrm{FF}} - \mathbf{Z}_{\mathrm{FC}}\left(\mathbf{Z}_{\mathrm{CC}} + \mathbf{Z}_{\mathrm{LC}}\right)^{-1}\mathbf{Z}_{\mathrm{CF}}. \tag{5.20}$$

When the external ports use the same real reference impedance Z_0, the corresponding reflection coefficient matrix is

$$\Gamma = \left(\mathbf{Z}_{\mathrm{IN}}^{\mathrm{F}} + Z_0\mathbf{U}\right)^{-1}\left(\mathbf{Z}_{\mathrm{IN}}^{\mathrm{F}} - Z_0\mathbf{U}\right), \tag{5.21}$$

where $\mathbf{U}$ is the $N_{\mathrm{F}} \times N_{\mathrm{F}}$ identity matrix. Equation (5.21) is used only with a consistent modal reference impedance. Modal impedances must be retained explicitly when the Floquet ports represent different modes or polarisations.

Figure 5.3 illustrates the Floquet modal circles and the corresponding modal amplitudes used to identify the propagating orders of the rectangular periodic array. For the unit cell considered in this thesis, the period is $\lambda/8$. Hence, only the fundamental Floquet order is propagating over the operating range, while the higher orders are evanescent. Each

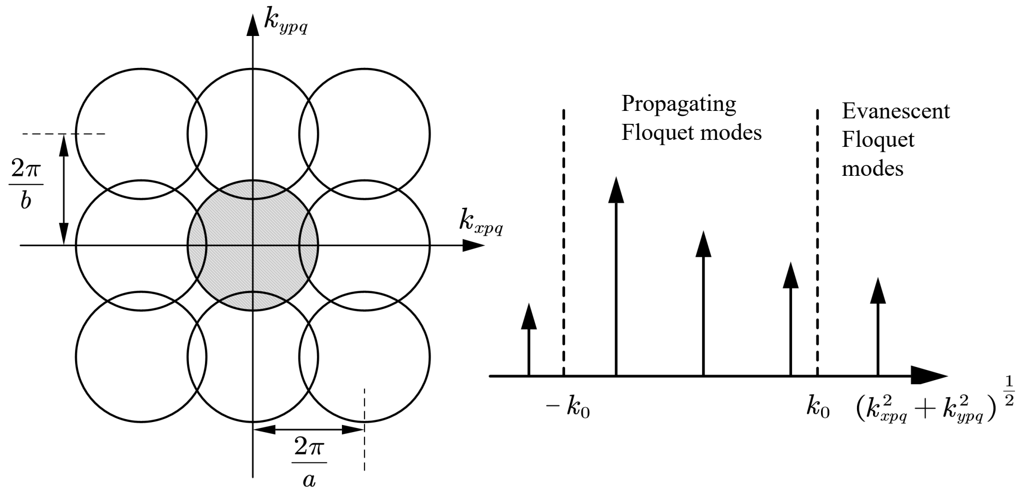

Fig. 5.3 Floquet modal circles (left) and modal amplitudes (right) for a rectangular periodic array.

polarisation-specific simulation therefore has one propagating external mode, and (5.21) reduces to a scalar co-polarised reflection coefficient. Let $\Omega_i^{(n)} \triangleq (\theta_i^{(n)}, \phi_i^{(n)})$ denote the arrival direction of the nth incident plane wave and let C_m denote the mth varactor capacitance state. For $\sigma \in \{\mathrm{TE}, \mathrm{TM}\}$,

$$\Gamma_\sigma\left(\Omega_i^{(n)}; C_m\right) = \frac{Z_{\mathrm{IN},\sigma}^{\mathrm{F}}\left(\Omega_i^{(n)}; C_m\right) - Z_{0,\sigma}\left(\theta_i^{(n)}\right)}{Z_{\mathrm{IN},\sigma}^{\mathrm{F}}\left(\Omega_i^{(n)}; C_m\right) + Z_{0,\sigma}\left(\theta_i^{(n)}\right)}, \tag{5.22}$$

where the free-space TE and TM wave impedances are

$$Z_{0,\mathrm{TE}}\left(\theta_i^{(n)}\right) = \frac{\eta_0}{\left|\cos\theta_i^{(n)}\right|}, \tag{5.23}$$

$$Z_{0,\mathrm{TM}}\left(\theta_i^{(n)}\right) = \eta_0\left|\cos\theta_i^{(n)}\right|. \tag{5.24}$$

The absolute values in (5.23) and (5.24) give positive modal reference impedances for the lower hemisphere angular convention adopted in Section 5.2. The quantities $Z_{\mathrm{IN,TE}}^{\mathrm{F}}$ and $Z_{\mathrm{IN,TM}}^{\mathrm{F}}$ are evaluated independently from (5.20) using TE and TM Floquet excitations. Thus, (5.22) preserves the dependence on incidence angle and polarisation required by the phase

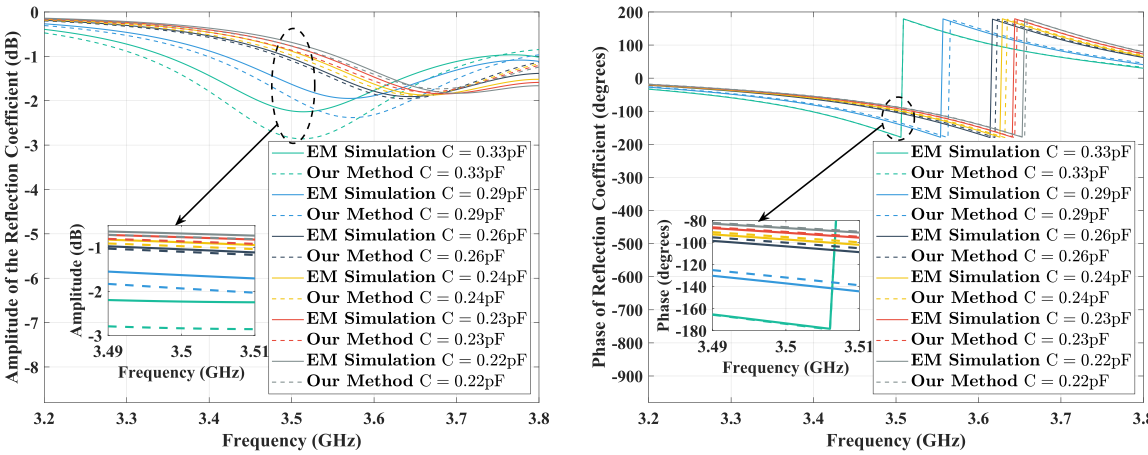

(a) Amplitude for $C = 0.22$–0.33 pF. (b) Phase for $C = 0.22$–0.33 pF.

Fig. 5.4 Reflection coefficient obtained from full-wave simulation and the multiport model for capacitances from 0.22 to 0.33 pF.

design developed in the next section. Cross-polarised conversion is outside this scalar co-polarised model and would require the corresponding full reflection dyadic.

5.3.2 Validation of the Multiport Reflection Coefficient

To construct the extracted model, I remove the two varactor diodes from the CST unit cell and place one discrete circuit port across each diode gap. Together with the external Floquet port, this produces a three port network with one external port and two internal ports. The diode loading is then restored through $\mathbf{Z}_{\mathrm{LC}}$, and the equivalent capacitance C is swept from 0.22 to 2.1 pF. For every state, I evaluate $\mathbf{Z}_{\mathrm{IN}}^{\mathrm{F}}$ using (5.20) and calculate the associated reflection coefficient using (5.21), or its scalar form in (5.22).

Figs. 5.4–5.6 compare the multiport predictions with independent full-wave simulations over 3.2–3.8 GHz. Across the complete capacitance sweep, the maximum reported amplitude and phase deviations are below 2.4 dB and 14.8°, respectively. At the 3.5 GHz operating frequency, the corresponding maxima decrease to 0.6 dB and 5.4°. These bounded discrepancies support the use of the extracted model for interpolating the considered load states within the validated frequency range; they do not establish accuracy for an untested geometry, incidence range, or polarisation channel.

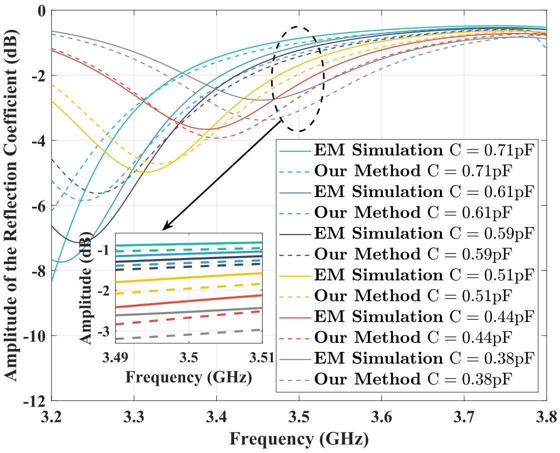

(a) Amplitude for $C = 0.38$–0.71 pF.

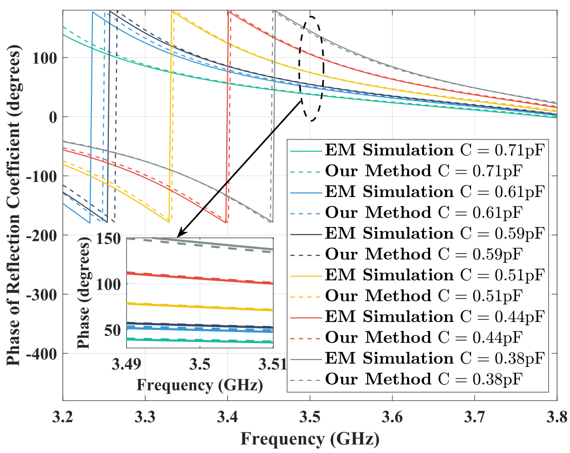

(b) Phase for $C = 0.38$–0.71 pF.

Fig. 5.5 Reflection coefficient obtained from full-wave simulation and the multiport model for capacitances from 0.38 to 0.71 pF.

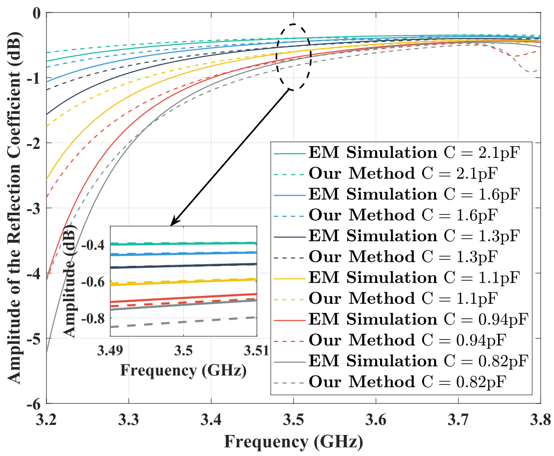

(a) Amplitude for $C = 0.82$–2.1 pF.

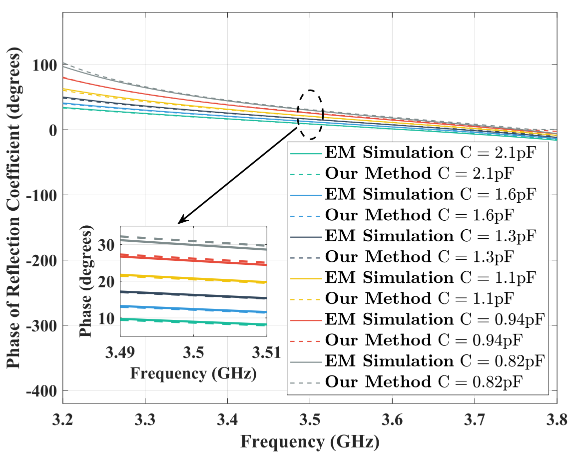

(b) Phase for $C = 0.82$–2.1 pF.

Fig. 5.6 Reflection coefficient obtained from full-wave simulation and the multiport model for capacitances from 0.82 to 2.1 pF.

Let T_{FW} be the mean runtime of one full-wave solution for one capacitance state. On the computational platform used in this study, $T_{\mathrm{FW}} = 195$ s. The initial CST extraction of the port-impedance matrix requires $T_{\mathrm{init}} = 374$ s, after which one additional multiport evaluation requires $T_{\mathrm{MP}} = 0.163$ s on average. For N_{s} capacitance states, I define the relative runtime reduction as

$$\eta_{\text{time}} = \frac{N_{\text{s}} T_{\text{FW}} - (T_{\text{init}} + N_{\text{s}} T_{\text{MP}})}{N_{\text{s}} T_{\text{FW}}}. \tag{5.25}$$

For $N_{\text{s}} = 18$, $\eta_{\text{time}} = 89.26\%$. The reduction increases with N_{s} because the fixed extraction cost is amortised over a larger load sweep.

5.3.3 Far-Field Radiation Pattern of the RIS

I next map the validated unit-cell response to the finite RIS aperture. Consider $P \times Q$ cells with spacings Δx and Δy. The centre of cell (p,q) is

$$\mathbf{r}_{pq} = \left[p - \frac{P+1}{2}\right] \Delta x \, \hat{\mathbf{a}}_x + \left[q - \frac{Q+1}{2}\right] \Delta y \, \hat{\mathbf{a}}_y, \tag{5.26}$$

where $p = 1, \ldots, P$ and $q = 1, \ldots, Q$. For polarisation σ, let the local co-polarised reflection coefficient be $\Gamma_{\sigma,pq} = A_\sigma(p,q) e^{j\psi_\sigma(p,q)}$. For a single incident plane wave with tangential wavevector $\mathbf{k}_{t,i}$, the normalised co-polarised far-field pattern under the element pattern multiplication approximation is

$$F_\sigma(\theta,\phi) = E_{\text{uc},\sigma}(\theta,\phi;\Omega_i) \sum_{p=1}^{P} \sum_{q=1}^{Q} \Gamma_{\sigma,pq} \exp\left[-j\left(\mathbf{k}_t(\theta,\phi) - \mathbf{k}_{t,i}\right) \cdot \mathbf{r}_{pq}\right], \tag{5.27}$$

where $E_{\text{uc},\sigma}$ is the embedded unit-cell pattern used by the macromodel and

$$\mathbf{k}_t(\theta,\phi) = k_0 \sin\theta \cos\phi \, \hat{\mathbf{a}}_x + k_0 \sin\theta \sin\phi \, \hat{\mathbf{a}}_y. \tag{5.28}$$

For a prescribed reradiation direction (θ_r, ϕ_r), coherent addition in (5.27) requires

$$\psi_\sigma(p,q) \equiv (\mathbf{k}_{t,r} - \mathbf{k}_{t,i}) \cdot \mathbf{r}_{pq} + \psi_0 \pmod{2\pi}, \tag{5.29}$$

where ψ_0 is an arbitrary common phase. This expression states the phase matching condition directly in terms of tangential momentum and is equivalent to a linear phase gradient for a single plane wave.

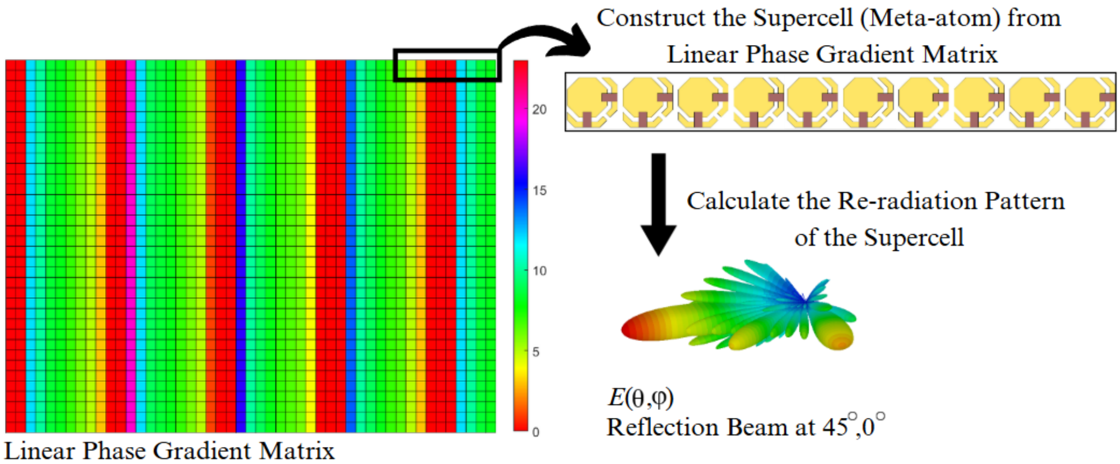

Fig. 5.7 Calculated far-field electric-field distribution $E(\theta,\phi)$ of the complete RIS aperture.

The numerical synthesis proceeds in three stages. First, (5.29) determines the continuous target phase over the aperture. Second, the target phase at each cell is mapped to an admissible capacitance state through the angle- and polarisation-dependent response in (5.22). If the resulting profile is periodic, its smallest repeating block defines the supercell used for Floquet analysis. Third, the complete aperture response is evaluated from (5.27), including the unit-cell amplitude variation associated with the selected states. Figure 5.7 shows the resulting far-field distribution for the RIS considered here.

Equation (5.27) is a finite-aperture macromodel, rather than a replacement for a full-wave solution. Its separable form is appropriate when the embedded element pattern and the extracted load response represent the relevant coupling environment. Strong nonlocal coupling, abrupt spatial variations, unmodelled cross-polarisation, or operation outside the validated angular range require the coupled formulation developed later in this chapter or a full-wave calculation.

5.3.4 Small Meeting Room RT and Measurement Validation

I validate the proposed RIS macromodel by embedding its synthesised radiation response in Ranplan Academic 7.0.0, a deterministic three-dimensional RT simulator [191]. The building model represents the measured room geometry, the Tx and Rx antenna radiation patterns, and the electromagnetic properties assigned to glass, concrete, metal, and the principal

(a) Measured environment.

(b) Corresponding RT model.

Fig. 5.8 Small meeting room and its RT reconstruction at 5G/6GIC.

furnishings [192, 193]. The validation environment is the small meeting room at the 5G/6G Innovation Centre (5G/6GIC), shown together with its corresponding RT reconstruction in Fig. 5.8.

The measurement chain comprises an Anritsu MG3692A signal generator, a 20 dBi A-INFOMW LB-229-20-C-SF horn antenna at the Tx, the RIS, an identical horn antenna at the Rx, and a Rohde & Schwarz FSH8 spectrum analyser. The source transmits a continuous wave at 3.5 GHz. The RIS comprises $37 \times 50 = 1850$ cells distributed over an aperture of 420 mm $\times$ 570 mm and is configured to reradiate towards an azimuth of 60°. The Tx is located outside the room, whereas the RIS and Rx are located inside. The Tx-to-RIS distance is 5 m, and the transmit power is 0 dBm.

The Tx and RIS positions remain fixed throughout the measurement campaign. The Rx is placed at distances of 3, 4, 5, and 6 m from the RIS and at azimuths of 60°, 70°, and 80°, subject to the available floor space. The positions at 60° and 6 m and at 80° and 3 m are physically inaccessible and are therefore omitted, leaving ten Rx positions. At each accessible position, the received power is recorded first with the RIS inactive and then with the RIS configured for 60° reradiation. The same sequence is reproduced in the RT model. The RT grid resolution is 0.1 m, and the reported three-dimensional RT runtime for this room is 2.8 s.

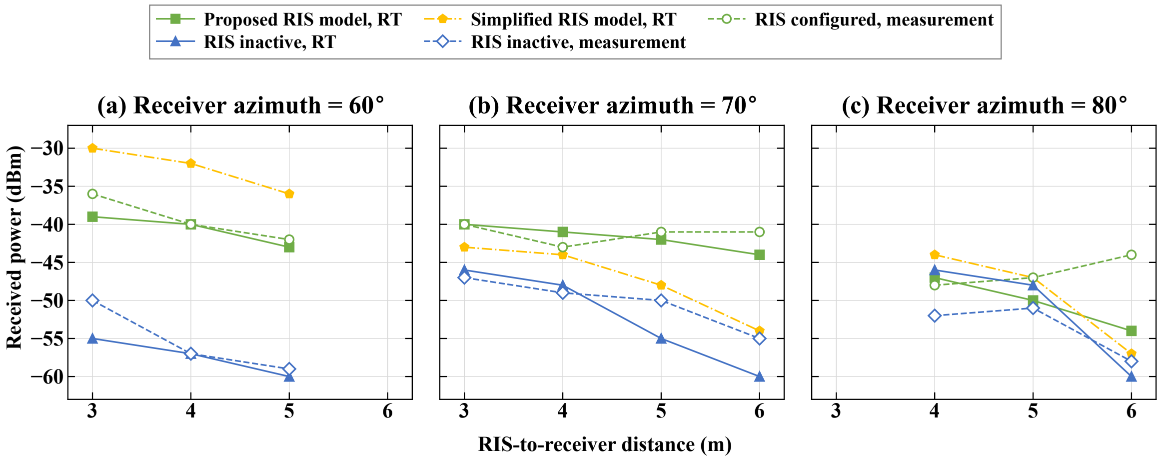

Fig. 5.9 Measured and RT-predicted received power versus distance from the RIS at Rx azimuths of (a) 60°, (b) 70°, and (c) 80°. The RIS is configured for 60° reradiation.

To determine whether a conventional simplified RIS representation can reproduce the measured received-power trend, I repeat the configured-state RT calculation using an ideal continuous phase-shift RIS model [183, 194]. The unit-modulus phase control follows the conventional communication-theoretic model in [194], while the intercepted-power and finite-aperture normalisation follow the physical-optics formulation in [183].

To embed the simplified RIS representation in the RT model, I construct an idealised main-beam-only directional pattern centred at the prescribed azimuth of 60°. Following the power-conserving finite-aperture formulation in [183], the power intercepted by the physical RIS aperture is calculated and assumed to be reradiated without loss. The imposed pattern is normalised such that its total reradiated power equals the intercepted power. Its peak gain is set to approximately 26.1 dBi for the physical RIS aperture at 3.5 GHz. As an additional abstraction adopted in this work, all intercepted power is assigned to the prescribed main beam and the radiation outside this beam is set to zero. The resulting baseline therefore contains no explicit sidelobe structure. The 26.1 dBi value therefore denotes the peak of the normalised directional pattern rather than a position-independent link gain applied at every Rx location. All room, antenna, material, and RT parameters are otherwise unchanged.

Figure 5.9 first compares the received power as a function of position. At the prescribed 60° azimuth, the proposed macromodel predicts configured-state increases of 16–17 dB relative to the RIS inactive RT result, in close correspondence with the measured increases

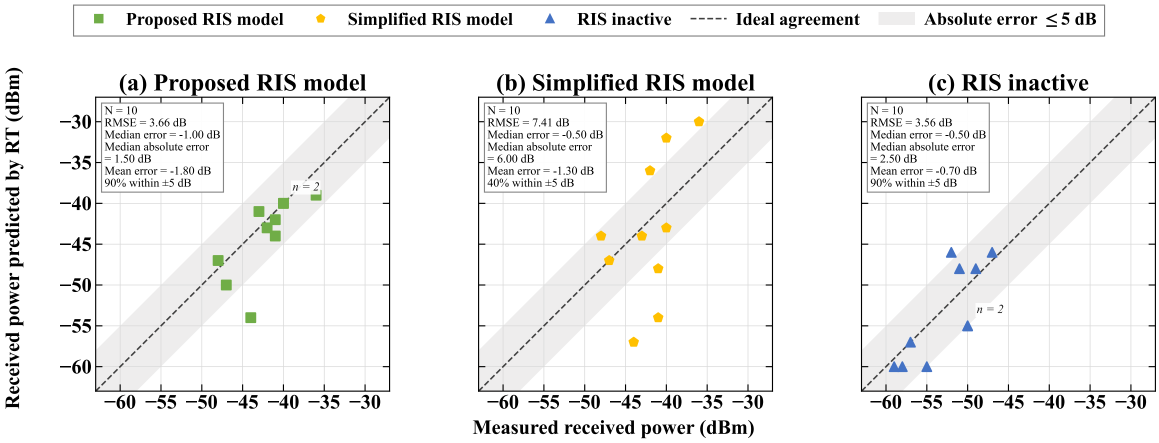

Fig. 5.10 Agreement between measured and RT-predicted received power at the ten accessible Rx positions: (a) proposed RIS model, configured state; (b) simplified RIS model, configured state; and (c) RIS inactive state.

of 14–17 dB. The simplified model predicts larger increases of 24–25 dB and consequently overestimates the configured-state received power by 6–8 dB at the three accessible target-direction positions. This systematic excess is consistent with concentrating the imposed reradiated power into the prescribed direction while omitting the sidelobe power represented by the proposed macromodel.

The results away from the prescribed direction distinguish the two RIS descriptions more clearly. At 70°, the proposed macromodel predicts increases of 6–16 dB, compared with the measured range of 6–14 dB, whereas the simplified model predicts only 3–7 dB. At 80°, the corresponding ranges are −2–6 dB for the proposed macromodel, 4–14 dB for the measurements, and 1–3 dB for the simplified model.

Although the simplified pattern contains no explicit sidelobes, a ray reradiated within the main beam can undergo subsequent interactions with the room before reaching an Rx located at another azimuth. The simplified model can therefore predict a nonzero RIS-induced received-power variation away from 60°. Such a variation arises from subsequent indoor propagation rather than from sidelobe radiation in the imposed RIS pattern. The largest local discrepancy for the proposed macromodel occurs at 80° and 6 m, where the measured configured-state increase exceeds the predicted increase by approximately 8 dB. Unmodelled diffuse scattering and fine-scale interactions associated with the furnishings and the finite

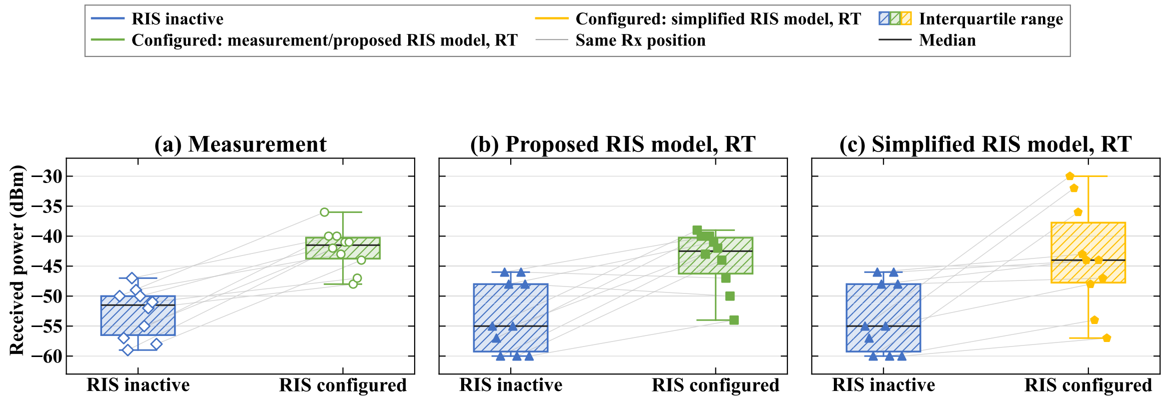

Source	Sample standard deviation (dB) (inactive, configured)	Interquartile range (dB) (inactive, configured)	Mean paired gain (dB) (configured minus inactive)
Measurement	(4.16, 3.52)	(6.50, 3.50)	10.60
Proposed RIS model, RT	(5.93, 4.90)	(11.25, 6.00)	9.50
Simplified RIS model, RT	(5.93, 8.80)	(11.25, 10.00)	10.00

Fig. 5.11 Spatial dispersion of received power across the ten accessible Rx positions in the RIS inactive and configured states: (a) measurements, (b) proposed RIS model RT results, and (c) simplified RIS model RT results.

spatial sampling of the receive antenna may contribute to this discrepancy, but the available measurements do not permit their individual contributions to be separated.

The positional trends in Fig. 5.9 are quantified in Fig. 5.10. In each panel, the dashed diagonal represents exact agreement and the shaded region represents an absolute prediction error not exceeding 5 dB. The inset statistics are evaluated over all ten Rx observations. An $n = 2$ annotation denotes two distinct observations with identical plotted coordinates. The signed error is the RT prediction minus the corresponding measurement, so a negative value denotes underprediction. For the configured proposed macromodel, the RMSE is 3.66 dB, the median absolute error is 1.50 dB, and 90% of predictions lie within ± 5 dB; the median and mean signed errors are -1.00 and -1.80 dB, respectively. For the configured simplified model, the RMSE increases to 7.41 dB, the median absolute error to 6.00 dB, and the percentage within ± 5 dB falls to 40%. Its median and mean signed errors of -0.50 and -1.30 dB are comparatively small because overprediction near 60° and underprediction away from the target direction partially cancel. For the RIS inactive state, the RMSE is 3.56 dB, the median absolute error is 2.50 dB, and 90% of predictions lie within ± 5 dB.

The agreement metrics describe prediction accuracy at corresponding positions, whereas Fig. 5.11 examines how the RIS configuration changes the dispersion of received power over the sampled geometry. Each light grey segment links the inactive and configured observations at the same Rx position, while each hatched box spans the interquartile range and its central line marks the median. The sample standard deviation and interquartile range quantify the spatial dispersion in each state. The mean paired gain is the arithmetic mean, over the ten Rx positions, of the received power in the configured state minus that in the inactive state. In the measurements, configuration reduces the sample standard deviation from 4.16 to 3.52 dB and the interquartile range from 6.50 to 3.50 dB, while providing a mean paired gain of 10.60 dB. The proposed macromodel reproduces the observed reduction in dispersion: its sample standard deviation decreases from 5.93 to 4.90 dB and its interquartile range decreases from 11.25 to 6.00 dB, with a mean paired gain of 9.50 dB. The simplified model yields a similar mean paired gain of 10.00 dB, but its sample standard deviation increases from 5.93 to 8.80 dB and its interquartile range remains comparatively large at 10.00 dB after configuration. Thus, the mean gain alone conceals the position-dependent errors identified in Fig. 5.10; the proposed macromodel more faithfully reproduces both the angular trend and the measured contraction of the configured-state power distribution.

Because the ten samples span several distances and azimuths, the statistics in Fig. 5.11 characterise dispersion over the sampled validation geometry rather than small-scale fading at a fixed location. Moreover, validation in one room cannot establish statistical validity across different buildings, RIS apertures, frequency bands, or deployment classes. Within these limits, the combined positional, agreement, and dispersion results show that retaining the synthesised angular structure improves the predictive consistency of the RT model relative to the simplified target-directed pattern.

The validation establishes two inputs required by the subsequent phase design: a computationally efficient mapping from capacitance and incidence state to the complex unit-cell response, and a finite-aperture response whose steering trend is consistent with the retained indoor measurements. It does not, by itself, determine the control profile when several incident paths illuminate the RIS simultaneously. The next section therefore combines the angle-and polarisation-dependent response in (5.22) with the plane-wave expansion of Section 5.2 to formulate the single-path reference design and then derive the multipath phase-synthesis procedure.

5.4 Simulation Framework and Settings

This section defines the two phase-synthesis procedures and the EM evaluation chain used in the numerical study. Scenario I establishes a dominant-path reference design: the incident component carrying the greatest normal power density determines the phase gradient, after which the realised RIS is illuminated by the complete multipath field. Scenario II synthesises the controllable response directly from the coherent aggregate illumination. Both procedures use the same incidence-dependent unit-cell response, finite-aperture representation, and polarimetric far-field projections, so that their comparison isolates the phase-design rule.

The numerical evidence is reported separately from the derivation. Section 5.5 first evaluates the analytical predictions against a controlled three-path CST full-wave benchmark. The analytical workflow is then applied to a room-scale deterministic multipath problem. These studies use independent incident fields; no path amplitude or phase is transferred between them.

5.4.1 Scenario I: Single-Path-Based Design

The first scenario considers a conventional single-path reference design in which the RIS phase profile is synthesised using only one incident propagation path. A custom-developed RT algorithm is first used to identify the set of plane-wave components illuminating the RIS aperture. According to the previously defined power-flow criterion, the component with the largest normal incident-power density is selected as the dominant design path.

The RIS phase profile is then synthesised to redirect this dominant incident component towards the prescribed target direction. The configured RIS is subsequently reintroduced into the original multipath environment and illuminated by the coherent aggregate field comprising all incident components. The resulting target-direction power change therefore quantifies the performance of a RIS designed for a single dominant path but operated under multipath illumination.

From a rigorous EM perspective, the selection of the primary design path should not be dictated solely by the maximum electric-field magnitude $|E_n|$. Instead, the criterion must be based on the normal incident-power density striking the RIS aperture. This distinction is critical because, for a given field amplitude, paths characterised by grazing incidence contribute significantly less power to the surface due to the obliquity factor.

To facilitate the EM analysis, a LCS is established on the RIS plane. Without loss of generality, the RIS is assumed to occupy a rectangular aperture defined in the local xy-plane. On the RIS plane $z = 0$, the tangential incident wavevector is

$$\mathbf{k}_{t,i}^{(n)} = k_0 \sin\theta_i^{(n)} \cos\phi_i^{(n)}\, \hat{\mathbf{a}}_x + k_0 \sin\theta_i^{(n)} \sin\phi_i^{(n)}\, \hat{\mathbf{a}}_y. \tag{5.30}$$

Assume that the RIS is illuminated by N incident plane-wave components. The total incident electric field is given by (5.1), and the electric field of the nth path is decomposed according to (5.2). I therefore define the TE and TM excitation amplitudes as

$$a_n^{\mathrm{TE}} = -\left\| \mathbf{E}_i\left(\theta_i^{(n)}, \phi_i^{(n)}\right) \right\|_F \cos\psi_n, \tag{5.31}$$

$$a_n^{\mathrm{TM}} = -\left\| \mathbf{E}_i\left(\theta_i^{(n)}, \phi_i^{(n)}\right) \right\|_F \sin\psi_n. \tag{5.32}$$

Hence, $\mathbf{E}_{t,i,n}^{\mathrm{TE}}(\mathbf{r}_t)$ in (5.12) and $\mathbf{H}_{t,i,n}^{\mathrm{TM}}(\mathbf{r}_t)$ in (5.13) can be expressed as

$$\mathbf{E}_{t,i,n}^{\mathrm{TE}}(\mathbf{r}_t) = a_n^{\mathrm{TE}} \hat{\mathbf{a}}_{\phi_i^{(n)}} e^{-j\mathbf{k}_{t,i}^{(n)} \cdot \mathbf{r}_t}, \tag{5.33}$$

$$\mathbf{H}_{t,i,n}^{\mathrm{TM}}(\mathbf{r}_t) = \frac{a_n^{\mathrm{TM}}}{\eta_0} \hat{\mathbf{a}}_{\phi_i^{(n)}} e^{-j\mathbf{k}_{t,i}^{(n)} \cdot \mathbf{r}_t}. \tag{5.34}$$

To synthesise the RIS phase profile from the dominant illuminating path, I select the path that maximises the normal incident-power density on the RIS. For the nth path, this density is

$$P_n^{\perp} = -\frac{\cos\theta_i^{(n)}}{2\eta_0} \left(|a_n^{\mathrm{TE}}|^2 + |a_n^{\mathrm{TM}}|^2 \right), \tag{5.35}$$

and the dominant design path is

$$n^{\star} = \arg\max_{1\leq n\leq N} P_n^{\perp}. \tag{5.36}$$

Let the desired reradiated direction be (θ_r, ϕ_r). The tangential incident and desired reflected wavevectors are

$$\mathbf{k}_{t,i}^{(n^{\star})} = k_0 \sin\theta_i^{(n^{\star})} \cos\phi_i^{(n^{\star})}\, \hat{\mathbf{a}}_x + k_0 \sin\theta_i^{(n^{\star})} \sin\phi_i^{(n^{\star})}\, \hat{\mathbf{a}}_y, \tag{5.37}$$

$$\mathbf{k}_{t,r} = k_0 \sin\theta_r \cos\phi_r\, \hat{\mathbf{a}}_x + k_0 \sin\theta_r \sin\phi_r\, \hat{\mathbf{a}}_y. \tag{5.38}$$

Therefore, the required tangential momentum increment is

$$\Delta\mathbf{k}_t = \mathbf{k}_{t,r} - \mathbf{k}_{t,i}^{(n^{\star})} = \Delta k_x \hat{\mathbf{a}}_x + \Delta k_y \hat{\mathbf{a}}_y, \tag{5.39}$$

with

$$\Delta k_x = k_0 \left(\sin\theta_r \cos\phi_r - \sin\theta_i^{(n^{\star})} \cos\phi_i^{(n^{\star})}\right), \tag{5.40}$$

$$\Delta k_y = k_0 \left(\sin\theta_r \sin\phi_r - \sin\theta_i^{(n^{\star})} \sin\phi_i^{(n^{\star})}\right). \tag{5.41}$$

Consequently, the required phase distribution is

$$\Phi(\mathbf{r}_t) = \Delta\mathbf{k}_t \cdot \mathbf{r}_t = \Delta k_x x_r + \Delta k_y y_r. \tag{5.42}$$

For the practical RIS implementation considered here, the phase profile in (5.42) is not imposed directly through an ideal local reflection coefficient. Instead, it is realised through the continuously tunable varactor capacitance of the RIS unit cell. In the state-0 diode configuration considered in the circuit model, the load connected to each internal port is represented by the series impedance

$$Z_{\mathrm{LC}}(\omega; C) = R_{\mathrm{d}} + j\omega L_{\mathrm{d}} + \frac{1}{j\omega C}, \tag{5.43}$$

where

$$R_{\mathrm{d}} = 5\ \Omega, \qquad L_{\mathrm{d}} = 0.45\times 10^{-9}\ \mathrm{H}, \tag{5.44}$$

and C denotes the continuously tunable varactor capacitance. Since the two internal circuit ports are loaded identically, the state-0 load impedance matrix is

$$\mathbf{Z}_{\mathrm{LC}}^{(0)}(\omega;C) = \mathrm{diag}\left(Z_{\mathrm{LC}}(\omega;C), Z_{\mathrm{LC}}(\omega;C)\right). \tag{5.45}$$

At the design angular frequency $\omega_0 = 2\pi f_0$, the input impedance seen from the external Floquet port for polarisation $\sigma \in \{\mathrm{TE},\mathrm{TM}\}$ and dominant incident path $\Omega_i^{(n^\star)}$ is obtained from (5.20) as

$$Z_{\mathrm{IN},\sigma}^{\mathrm{F}}(\Omega_i^{(n^\star)};C) = \mathbf{Z}_{\mathrm{FF},\sigma} - \mathbf{Z}_{\mathrm{FC},\sigma}\left(\mathbf{Z}_{\mathrm{CC},\sigma} + \mathbf{Z}_{\mathrm{LC}}^{(0)}(\omega_0;C)\right)^{-1}\mathbf{Z}_{\mathrm{CF},\sigma}. \tag{5.46}$$

The corresponding co-polarised reflection coefficient is then

$$\Gamma_\sigma\left(\Omega_i^{(n^\star)};C\right) = \frac{Z_{\mathrm{IN},\sigma}^{\mathrm{F}}\left(\Omega_i^{(n^\star)};C\right) - Z_{0,\sigma}\left(\theta_i^{(n^\star)}\right)}{Z_{\mathrm{IN},\sigma}^{\mathrm{F}}\left(\Omega_i^{(n^\star)};C\right) + Z_{0,\sigma}\left(\theta_i^{(n^\star)}\right)}, \tag{5.47}$$

where $Z_{0,\sigma}(\theta_i^{(n^\star)})$ is the free-space wave impedance of the dominant incident path for the corresponding polarisation, and $\sigma \in \{\mathrm{TE},\mathrm{TM}\}$.

I define the phase response of the loaded unit cell as

$$\phi_\sigma(C) = \arg\Gamma_\sigma\left(\Omega_i^{(n^\star)};C\right). \tag{5.48}$$

On a calibrated monotonic branch of $\phi_\sigma(C)$, and provided that the required phase is reachable, the capacitance at position $\mathbf{r}_t$ is determined from

$$\phi_\sigma\left(C_\sigma^\star(\mathbf{r}_t)\right) = \Phi(\mathbf{r}_t), \tag{5.49}$$

where the equality is understood modulo 2π. After unwrapping both phases on the selected branch, this relation is equivalently written as

$$C_\sigma^\star(\mathbf{r}_t) = \phi_\sigma^{-1}\left(\Phi(\mathbf{r}_t)\right). \tag{5.50}$$

The corresponding reflection amplitude response is then

$$\rho_\sigma(\mathbf{r}_t) = \left|\Gamma_\sigma\left(\Omega_i^{(n^\star)}; C_\sigma^\star(\mathbf{r}_t)\right)\right|. \tag{5.51}$$

Accordingly, the realised local reflection coefficient associated with the required phase profile can be written as

$$\Gamma_\sigma(\mathbf{r}_t) = \rho_\sigma(\mathbf{r}_t)\, e^{j\Phi(\mathbf{r}_t)}. \tag{5.52}$$

The corresponding synthesised scalar surface impedance is therefore

$$Z_s^\star(\mathbf{r}_t) = Z_{0,\sigma}\left(\theta_i^{(n^\star)}\right)\frac{1+\Gamma_\sigma(\mathbf{r}_t)}{1-\Gamma_\sigma(\mathbf{r}_t)}. \tag{5.53}$$

For nonzero phase-gradient components, the macroscopic superperiods of the rectangular coding lattice are

$$P_x = \frac{2\pi}{|\Delta k_x|}, \qquad P_y = \frac{2\pi}{|\Delta k_y|}. \tag{5.54}$$

If $\Delta k_x = 0$ or $\Delta k_y = 0$, the phase is invariant along the corresponding coordinate and no finite superperiod is assigned along that coordinate. In the reciprocal-lattice expressions below, I use the convention $2\pi/P_x = 0$ when $\Delta k_x = 0$ and $2\pi/P_y = 0$ when $\Delta k_y = 0$. The corresponding reciprocal-lattice vectors are

$$\mathbf{G}_{pq} = \left(\frac{2\pi p}{P_x}, \frac{2\pi q}{P_y}, 0\right), \qquad p,q \in \mathbb{Z}. \tag{5.55}$$

Once (P_x, P_y) is fixed by the dominant path, every incident path n interacts with the same periodic surface. Therefore, the tangential wavevector of the (p,q) Floquet reradiated order generated by the nth incident path is

$$\mathbf{k}_{t,r,pq}^{(n)} = \mathbf{k}_{t,i}^{(n)} + \mathbf{G}_{pq}. \tag{5.56}$$

Equivalently,

$$k_{x,r,pq}^{(n)} = k_0 \sin\theta_i^{(n)} \cos\phi_i^{(n)} + \frac{2\pi p}{P_x}, \tag{5.57}$$

$$k_{y,r,pq}^{(n)} = k_0 \sin\theta_i^{(n)} \sin\phi_i^{(n)} + \frac{2\pi q}{P_y}. \tag{5.58}$$

The longitudinal wavenumber is

$$k_{z,r,pq}^{(n)} = \begin{cases} +\sqrt{k_0^2 - \left(k_{x,r,pq}^{(n)}\right)^2 - \left(k_{y,r,pq}^{(n)}\right)^2}, & \left\|\mathbf{k}_{t,r,pq}^{(n)}\right\| \leq k_0, \\ +j\sqrt{\left(k_{x,r,pq}^{(n)}\right)^2 + \left(k_{y,r,pq}^{(n)}\right)^2 - k_0^2}, & \left\|\mathbf{k}_{t,r,pq}^{(n)}\right\| > k_0. \end{cases} \tag{5.59}$$

Hence, the (p,q) order is propagating if and only if

$$\left\|\mathbf{k}_{t,r,pq}^{(n)}\right\| \leq k_0. \tag{5.60}$$

For each propagating Floquet order, the Cartesian wavevector components in (5.57), (5.58) and (5.59) must next be converted into spherical angles, since the subsequent far-field analysis is formulated in terms of observation directions rather than Cartesian momentum components. This angular mapping is given by

$$\sin\theta_{r,pq}^{(n)} = \frac{\sqrt{\left(k_{x,r,pq}^{(n)}\right)^2 + \left(k_{y,r,pq}^{(n)}\right)^2}}{k_0}, \tag{5.61a}$$

$$\cos\theta_{r,pq}^{(n)} = \sqrt{1 - \left(\frac{k_{x,r,pq}^{(n)}}{k_0}\right)^2 - \left(\frac{k_{y,r,pq}^{(n)}}{k_0}\right)^2}, \tag{5.61b}$$

$$\cos\phi_{r,pq}^{(n)} = \frac{k_{x,r,pq}^{(n)}}{k_0 \sin\theta_{r,pq}^{(n)}}, \tag{5.61c}$$

$$\sin\phi_{r,pq}^{(n)} = \frac{k_{y,r,pq}^{(n)}}{k_0 \sin\theta_{r,pq}^{(n)}}. \tag{5.61d}$$

Equation (5.61) provides the geometric interpretation of each Floquet order wavevector in terms of observable reradiation angles. In other words, once the tangential momentum of a given order is known, its far-field propagation direction follows directly from the above relations.

The macroscopic surface impedance over one phase supercell is represented by the double Fourier expansion

$$\overline{\overline{Z}}_s(\mathbf{r}_t) = \sum_{u=-U}^{U} \sum_{v=-V}^{V} \overline{\overline{Z}}_{uv} e^{-j\left(\frac{2\pi u}{P_x} x_r + \frac{2\pi v}{P_y} y_r\right)}, \tag{5.62}$$

with Fourier coefficients

$$\overline{\overline{Z}}_{uv} = \frac{1}{P_x P_y} \int_0^{P_x} \int_0^{P_y} \overline{\overline{Z}}_s(x_r, y_r) e^{j\left(\frac{2\pi u}{P_x} x_r + \frac{2\pi v}{P_y} y_r\right)} \, \mathrm{d}y_r \, \mathrm{d}x_r. \tag{5.63}$$

To obtain a tractable analytical model while retaining the dominant co-polarised Floquet response, I henceforth approximate the RIS as a locally isotropic, polarisation-preserving periodic impedance surface, such that its dyadic surface impedance reduces to the scalar form [15]

$$\overline{\overline{Z}}_s(\mathbf{r}_t) = Z_s(\mathbf{r}_t)\,\mathbf{I}_2.$$

In this context, $Z_s(\mathbf{r}_t)$ follows (5.53), which implies that $Z_s(\mathbf{r}_t) = Z_s^{\star}(\mathbf{r}_t)$.

The modal wave admittances can be expressed as

$$Y_{pq}^{\mathrm{TE},(n)} = \frac{k_{z,r,pq}^{(n)}}{\omega \mu_0}, \tag{5.64}$$

$$Y_{pq}^{\mathrm{TM},(n)} = \frac{\omega \varepsilon_0}{k_{z,r,pq}^{(n)}}. \tag{5.65}$$

Since the Floquet expansion is formally infinite, I truncate the mode-matching problem to the finite set of retained orders

$$\mathcal{P} = \{(p,q) : -P \le p \le P,\ -Q \le q \le Q\}. \tag{5.66}$$

The number of retained Floquet harmonics is

$$M = (2P+1)(2Q+1). \tag{5.67}$$

This truncation converts the infinite-dimensional boundary-value problem into a finite matrix system. In practice, P and Q are increased until the quantities of interest satisfy the prescribed convergence tolerance.

For each retained order, I define the TE and TM tangential basis vectors as

$$\mathbf{e}_{pq}^{\mathrm{TE},(n)} = \hat{\mathbf{a}}_{\phi_{r,pq}^{(n)}} = -\sin\phi_{r,pq}^{(n)}\,\hat{\mathbf{a}}_x + \cos\phi_{r,pq}^{(n)}\,\hat{\mathbf{a}}_y, \tag{5.68}$$

$$\mathbf{e}_{pq}^{\mathrm{TM},(n)} = \cos\theta_{r,pq}^{(n)}\left(\cos\phi_{r,pq}^{(n)}\,\hat{\mathbf{a}}_x + \sin\phi_{r,pq}^{(n)}\,\hat{\mathbf{a}}_y\right). \tag{5.69}$$

Using the Cartesian tangential basis $(\hat{\mathbf{a}}_x, \hat{\mathbf{a}}_y)$, I introduce the 2×2 transformation block

$$\mathbf{T}_{n,pq} = \begin{bmatrix} -\sin\phi_{r,pq}^{(n)} & \cos\theta_{r,pq}^{(n)}\cos\phi_{r,pq}^{(n)} \\ \cos\phi_{r,pq}^{(n)} & \cos\theta_{r,pq}^{(n)}\sin\phi_{r,pq}^{(n)} \end{bmatrix}, \tag{5.70}$$

and the corresponding modal admittance block

$$\mathbf{Y}_{n,pq} = \begin{bmatrix} Y_{pq}^{\mathrm{TE},(n)} & 0 \\ 0 & Y_{pq}^{\mathrm{TM},(n)} \end{bmatrix}. \tag{5.71}$$

By stacking all retained orders in $\mathcal{P}$, I define the global block-diagonal matrices

$$\mathbf{T}_n = \mathrm{blkdiag}\{\mathbf{T}_{n,pq}\}_{(p,q)\in\mathcal{P}}, \tag{5.72}$$

$$\mathbf{Y}_n = \mathrm{blkdiag}\{\mathbf{Y}_{n,pq}\}_{(p,q)\in\mathcal{P}}, \tag{5.73}$$

where $\mathbf{T}_n, \mathbf{Y}_n \in \mathbb{C}^{2M\times 2M}$.

The Fourier coefficients of the periodic impedance generate a block-Toeplitz convolution matrix

$$\left[\mathbf{Z}_s\right]_{(p,q),(p',q')} = \overline{\overline{Z}}_{p-p',q-q'}, \tag{5.74}$$

where each entry of $\mathbf{Z}_s$ is itself a 2×2 tangential block. Thus, $\mathbf{Z}_s \in \mathbb{C}^{2M\times 2M}$.

For the nth incident path, I define the incident modal vector

$$\mathbf{a}_n \in \mathbb{C}^{2M}, \tag{5.75}$$

whose only nonzero block corresponds to the $(0,0)$ order,

$$\mathbf{a}_{n,00} = \begin{bmatrix} a_n^{\mathrm{TE}} \\ a_n^{\mathrm{TM}} \end{bmatrix}. \tag{5.76}$$

The reflected modal vector is

$$\mathbf{b}_n = \left[\cdots, \mathbf{b}_{n,pq}, \cdots\right]^T \in \mathbb{C}^{2M}, \tag{5.77}$$

with

$$\mathbf{b}_{n,pq} = \begin{bmatrix} \widetilde{A}_{n,pq}^{\mathrm{TE}} \\ \widetilde{A}_{n,pq}^{\mathrm{TM}} \end{bmatrix}. \tag{5.78}$$

By enforcing the periodic impedance boundary condition in modal form, the reflected modal vector is obtained as

$$\mathbf{b}_n = \left(\mathbf{Z}_s \mathbf{T}_n \mathbf{Y}_n + \mathbf{T}_n\right)^{-1} \left(\mathbf{Z}_s \mathbf{T}_n \mathbf{Y}_n - \mathbf{T}_n\right) \mathbf{a}_n, \tag{5.79}$$

which is the 2D multipath counterpart of the 1D mode-matching relation used in [15] and of the periodic impedance surface formulation in [195].

Therefore, the desired Floquet amplitudes are simply the two entries of the corresponding (p,q) block of $\mathbf{b}_n$, namely the TE and TM complex amplitudes of the (p,q) reradiated Floquet order, denoted by $\widetilde{A}_{n,pq}^{\mathrm{TE}}$ and $\widetilde{A}_{n,pq}^{\mathrm{TM}}$, respectively.

$$\widetilde{A}_{n,pq}^{\mathrm{TE}} = \begin{bmatrix} 1 & 0 \end{bmatrix} \mathbf{b}_{n,pq}, \tag{5.80}$$

$$\widetilde{A}_{n,pq}^{\mathrm{TM}} = \begin{bmatrix} 0 & 1 \end{bmatrix} \mathbf{b}_{n,pq}. \tag{5.81}$$

If polarisation conversion is negligible, the TE and TM systems decouple. In that case, the scalar forms reduce to

$$\mathbf{b}_n^{\mathrm{TE}} = \left(\mathbf{I} + \mathbf{Z}_s \mathbf{Y}_n^{\mathrm{TE}}\right)^{-1} \left(\mathbf{Z}_s \mathbf{Y}_n^{\mathrm{TE}} - \mathbf{I}\right) \mathbf{a}_n^{\mathrm{TE}}, \tag{5.82}$$

$$\mathbf{b}_n^{\mathrm{TM}} = \left(\mathbf{I} + \mathbf{Z}_s \mathbf{Y}_n^{\mathrm{TM}}\right)^{-1} \left(\mathbf{Z}_s \mathbf{Y}_n^{\mathrm{TM}} - \mathbf{I}\right) \mathbf{a}_n^{\mathrm{TM}}, \tag{5.83}$$

where

$$\left[\mathbf{Y}_n^{\mathrm{TE}}\right]_{(p,q),(p,q)} = Y_{pq}^{\mathrm{TE},(n)}, \tag{5.84}$$

$$\left[\mathbf{Y}_n^{\mathrm{TM}}\right]_{(p,q),(p,q)} = Y_{pq}^{\mathrm{TM},(n)}. \tag{5.85}$$

Following the evaluation of $\widetilde{A}_{n,pq}^{\mathrm{TE}}$ and $\widetilde{A}_{n,pq}^{\mathrm{TM}}$, the reflected surface field is reconstructed via the superposition of all reradiated orders generated by the complete set of incident paths. For a given (p,q) Floquet mode originating from the nth path, the associated spherical unit vectors are given by

$$\hat{\mathbf{a}}_{\phi_{r,pq}^{(n)}} = -\hat{\mathbf{a}}_x \sin\phi_{r,pq}^{(n)} + \hat{\mathbf{a}}_y \cos\phi_{r,pq}^{(n)}, \tag{5.86}$$

$$\hat{\mathbf{a}}_{\theta_{r,pq}^{(n)}} = \hat{\mathbf{a}}_x \cos\theta_{r,pq}^{(n)} \cos\phi_{r,pq}^{(n)} + \hat{\mathbf{a}}_y \cos\theta_{r,pq}^{(n)} \sin\phi_{r,pq}^{(n)} - \hat{\mathbf{a}}_z \sin\theta_{r,pq}^{(n)}. \tag{5.87}$$

The reflected electric field of this single Floquet order is

$$\mathbf{E}_{r,pq}^{(n)}(\mathbf{r}) = \left(\hat{\mathbf{a}}_{\phi_{r,pq}^{(n)}} \widetilde{A}_{n,pq}^{\mathrm{TE}} + \hat{\mathbf{a}}_{\theta_{r,pq}^{(n)}} \widetilde{A}_{n,pq}^{\mathrm{TM}}\right) e^{-j\mathbf{k}_{r,pq}^{(n)} \cdot \mathbf{r}}, \tag{5.88}$$

where $\mathbf{k}_{r,pq}^{(n)} = k_{x,r,pq}^{(n)} \hat{\mathbf{a}}_x + k_{y,r,pq}^{(n)} \hat{\mathbf{a}}_y + k_{z,r,pq}^{(n)} \hat{\mathbf{a}}_z$ is the wavevector of that reflected order. Accordingly, the total reflected electric field is

$$\mathbf{E}_r(\mathbf{r}) = \sum_{n=1}^{N} \sum_{p=-\infty}^{\infty} \sum_{q=-\infty}^{\infty} \mathbf{E}_{r,pq}^{(n)}(\mathbf{r}). \tag{5.89}$$

At the RIS interface ($z_r = 0$), the full reflected field is expanded as

$$\mathbf{E}_r(\mathbf{r}_t) = \sum_{n=1}^{N} \sum_{p=-\infty}^{\infty} \sum_{q=-\infty}^{\infty} \Big[\hat{\mathbf{a}}_{\phi_{r,pq}^{(n)}} \widetilde{A}_{n,pq}^{\mathrm{TE}} + \hat{\mathbf{a}}_{\theta_{r,pq}^{(n)}} \widetilde{A}_{n,pq}^{\mathrm{TM}} \Big] e^{-j\left(k_{x,r,pq}^{(n)} x_r + k_{y,r,pq}^{(n)} y_r\right)}. \tag{5.90}$$

Given that only the tangential components contribute to the equivalent surface currents, the tangential reflected electric field is formulated as

$$\mathbf{E}_{t,r}(\mathbf{r}_t) = \sum_{n=1}^{N} \sum_{p=-\infty}^{\infty} \sum_{q=-\infty}^{\infty} \Big[\mathbf{E}_{t,r,pq}^{\mathrm{TE},(n)}(\mathbf{r}_t) + \mathbf{E}_{t,r,pq}^{\mathrm{TM},(n)}(\mathbf{r}_t) \Big], \tag{5.91}$$

where the TE and TM modal components are respectively defined as

$$\mathbf{E}_{t,r,pq}^{\mathrm{TE},(n)}(\mathbf{r}_t) = \hat{\mathbf{a}}_{\phi_{r,pq}^{(n)}} \widetilde{A}_{n,pq}^{\mathrm{TE}} e^{-j\left(k_{x,r,pq}^{(n)} x_r + k_{y,r,pq}^{(n)} y_r\right)}, \tag{5.92}$$

$$\mathbf{E}_{t,r,pq}^{\mathrm{TM},(n)}(\mathbf{r}_t) = \Big[\hat{\mathbf{a}}_x \cos\theta_{r,pq}^{(n)} \cos\phi_{r,pq}^{(n)} + \hat{\mathbf{a}}_y \cos\theta_{r,pq}^{(n)} \sin\phi_{r,pq}^{(n)} \Big] \times \widetilde{A}_{n,pq}^{\mathrm{TM}} e^{-j\left(k_{x,r,pq}^{(n)} x_r + k_{y,r,pq}^{(n)} y_r\right)}. \tag{5.93}$$

Similarly, the corresponding tangential reflected magnetic field is given by

$$\mathbf{H}_{t,r}(\mathbf{r}_t) = \sum_{n=1}^{N} \sum_{p=-\infty}^{\infty} \sum_{q=-\infty}^{\infty} \Big[\mathbf{H}_{t,r,pq}^{\mathrm{TE},(n)}(\mathbf{r}_t) + \mathbf{H}_{t,r,pq}^{\mathrm{TM},(n)}(\mathbf{r}_t) \Big], \tag{5.94}$$

with the modal magnetic-field components expressed as

$$\mathbf{H}_{t,r,pq}^{\mathrm{TE},(n)}(\mathbf{r}_t) = -\frac{\cos\theta_{r,pq}^{(n)}}{\eta_0} \Big[\hat{\mathbf{a}}_x \cos\phi_{r,pq}^{(n)} + \hat{\mathbf{a}}_y \sin\phi_{r,pq}^{(n)} \Big] \times \widetilde{A}_{n,pq}^{\mathrm{TE}} e^{-j\left(k_{x,r,pq}^{(n)} x_r + k_{y,r,pq}^{(n)} y_r\right)}, \tag{5.95}$$

$$\mathbf{H}_{t,r,pq}^{\mathrm{TM},(n)}(\mathbf{r}_t) = \frac{1}{\eta_0} \hat{\mathbf{a}}_{\phi_{r,pq}^{(n)}} \widetilde{A}_{n,pq}^{\mathrm{TM}} e^{-j\left(k_{x,r,pq}^{(n)} x_r + k_{y,r,pq}^{(n)} y_r\right)}. \tag{5.96}$$

Within the macroscopic scattering framework, I use PO and the Huygens principle to define the aperture window as

$$W(\mathbf{r}_t) = \mathrm{rect}\left(\frac{x_r}{2L_x}\right) \mathrm{rect}\left(\frac{y_r}{2L_y}\right), \tag{5.97}$$

where $\mathrm{rect}(u)$ denotes the rectangular function

$$\mathrm{rect}(u) = \begin{cases} 1, & |u| \leq \frac{1}{2}, \\ 0, & |u| > \frac{1}{2}. \end{cases} \tag{5.98}$$

For an impenetrable RIS of negligible thickness, the total equivalent electric and magnetic surface current densities on the illuminated interface are given by

$$\mathbf{J}_s(\mathbf{r}_t) = W(\mathbf{r}_t)\hat{\mathbf{a}}_z \times [\mathbf{H}_{t,i}(\mathbf{r}_t) + \mathbf{H}_{t,r}(\mathbf{r}_t)], \tag{5.99}$$

$$\mathbf{M}_s(\mathbf{r}_t) = -W(\mathbf{r}_t)\hat{\mathbf{a}}_z \times [\mathbf{E}_{t,i}(\mathbf{r}_t) + \mathbf{E}_{t,r}(\mathbf{r}_t)]. \tag{5.100}$$

To separate the contribution associated with the truncation of the incident field from that associated with the reradiated Floquet harmonics, the total equivalent currents are decomposed as

$$\begin{aligned} \mathbf{J}_s(\mathbf{r}_t) = {} & \mathbf{J}_{\mathrm{sh}}(\mathbf{r}_t) \\ & + W(\mathbf{r}_t) \sum_{n=1}^{N} \sum_{p=-\infty}^{\infty} \sum_{q=-\infty}^{\infty} \mathbf{J}_{0,n,pq} e^{-j\mathbf{k}_{t,r,pq}^{(n)} \cdot \mathbf{r}_t}, \end{aligned} \tag{5.101}$$

$$\begin{aligned} \mathbf{M}_s(\mathbf{r}_t) = {} & \mathbf{M}_{\mathrm{sh}}(\mathbf{r}_t) \\ & + W(\mathbf{r}_t) \sum_{n=1}^{N} \sum_{p=-\infty}^{\infty} \sum_{q=-\infty}^{\infty} \mathbf{M}_{0,n,pq} e^{-j\mathbf{k}_{t,r,pq}^{(n)} \cdot \mathbf{r}_t}, \end{aligned} \tag{5.102}$$

where $\mathbf{J}_{\mathrm{sh}}(\mathbf{r}_t)$ and $\mathbf{M}_{\mathrm{sh}}(\mathbf{r}_t)$ denote the shadow current contributions generated solely by the truncation of the incident field, whereas the modal coefficients $\mathbf{J}_{0,n,pq}$ and $\mathbf{M}_{0,n,pq}$ represent the reradiated contributions of the reflected Floquet harmonics. The shadow current terms are directly determined by the incident tangential fields as

$$\mathbf{J}_{\mathrm{sh}}(\mathbf{r}_t) = W(\mathbf{r}_t)\,\hat{\mathbf{a}}_z \times \mathbf{H}_{t,i}(\mathbf{r}_t), \tag{5.103}$$

$$\mathbf{M}_{\mathrm{sh}}(\mathbf{r}_t) = -W(\mathbf{r}_t)\,\hat{\mathbf{a}}_z \times \mathbf{E}_{t,i}(\mathbf{r}_t). \tag{5.104}$$

Using the multipath decomposition of the incident tangential fields, (5.12) and (5.13), these terms may be written explicitly as

$$\begin{aligned}\mathbf{J}_{\rm sh}(\mathbf{r}_t) = W(\mathbf{r}_t)\sum_{n=1}^{N}\Big[&-\frac{\cos\theta_i^{(n)}}{\eta_0}\mathbf{E}_{t,i}^{\rm TE,(n)}(\mathbf{r}_t)\\ &+\hat{\mathbf{a}}_z\times\mathbf{H}_{t,i}^{\rm TM,(n)}(\mathbf{r}_t)\Big], \qquad (5.105)\\ \mathbf{M}_{\rm sh}(\mathbf{r}_t) = W(\mathbf{r}_t)\sum_{n=1}^{N}\Big[&-\hat{\mathbf{a}}_z\times\mathbf{E}_{t,i}^{\rm TE,(n)}(\mathbf{r}_t)\\ &-\eta_0\cos\theta_i^{(n)}\mathbf{H}_{t,i}^{\rm TM,(n)}(\mathbf{r}_t)\Big]. \qquad (5.106)\end{aligned}$$

The modal reradiated current coefficients are defined as

$$\mathbf{J}_{0,n,pq} = \hat{\mathbf{a}}_z\times\mathbf{H}_{t,r,pq}^{(n)}(\mathbf{r}_t)e^{+j\mathbf{k}_{t,r,pq}^{(n)}\cdot\mathbf{r}_t}, \qquad (5.107)$$

$$\mathbf{M}_{0,n,pq} = -\hat{\mathbf{a}}_z\times\mathbf{E}_{t,r,pq}^{(n)}(\mathbf{r}_t)e^{+j\mathbf{k}_{t,r,pq}^{(n)}\cdot\mathbf{r}_t}. \qquad (5.108)$$

Since $\mathbf{E}_{t,r,pq}^{(n)}$ and $\mathbf{H}_{t,r,pq}^{(n)}$ are single-exponential fields, $\mathbf{J}_{0,n,pq}$ and $\mathbf{M}_{0,n,pq}$ are independent of $\mathbf{r}_t$. The scattered far field radiated by these equivalent currents is evaluated via the radiation integral

$$\begin{aligned}\mathbf{E}_{\rm sc}(\hat{\mathbf{r}}) = \frac{jk_0e^{-jk_0r}}{4\pi r}\iint_{S_{\rm RIS}}\Big\{&\hat{\mathbf{r}}\times[\eta_0\mathbf{J}_s(\mathbf{r}_t)\times\hat{\mathbf{r}}]\\ &+\hat{\mathbf{r}}\times\mathbf{M}_s(\mathbf{r}_t)\Big\}e^{jk_0\hat{\mathbf{r}}\cdot\mathbf{r}_t}\,\mathrm{d}S',\end{aligned} \qquad (5.109)$$

where $\hat{\mathbf{r}}$ represents the observation direction

$$\hat{\mathbf{r}} = \hat{\mathbf{a}}_x\sin\theta\cos\phi+\hat{\mathbf{a}}_y\sin\theta\sin\phi+\hat{\mathbf{a}}_z\cos\theta. \qquad (5.110)$$

Substituting (5.101) and (5.102) into (5.109) leads to the modal decomposition of the scattered field

$$\begin{aligned}\mathbf{E}_{\text{sc}}(\theta,\phi) &= \mathbf{E}_{\text{sh}}(\theta,\phi) \\ &\quad + \frac{jk_0 e^{-jk_0 r}}{4\pi r} \sum_{n=1}^{N} \sum_{p=-\infty}^{\infty} \sum_{q=-\infty}^{\infty} \\ &\quad \mathcal{A}_{n,pq}(\theta,\phi)\, \mathbf{U}_{n,pq}(\theta,\phi),\end{aligned} \tag{5.111}$$

where the modal vector kernel $\mathbf{U}_{n,pq}(\theta,\phi)$ and the aperture factor $\mathcal{A}_{n,pq}(\theta,\phi)$ are given by

$$\mathbf{U}_{n,pq}(\theta,\phi) = \hat{\mathbf{r}} \times \left[\eta_0 \mathbf{J}_{0,n,pq} \times \hat{\mathbf{r}}\right] + \hat{\mathbf{r}} \times \mathbf{M}_{0,n,pq}, \tag{5.112}$$

$$\mathcal{A}_{n,pq}(\theta,\phi) = \iint_{S_{\text{RIS}}} W(\mathbf{r}_t) e^{-j\mathbf{k}_{t,r,pq}^{(n)}\cdot \mathbf{r}_t} e^{jk_0 \hat{\mathbf{r}}\cdot \mathbf{r}_t}\, \mathrm{d}S. \tag{5.113}$$

For the rectangular aperture defined in (5.97), the aperture factor reduces to

$$\mathcal{A}_{n,pq}(\theta,\phi) = 4L_x L_y \operatorname{sinc}\left(L_x \Delta k_{x,n,pq}\right) \operatorname{sinc}\left(L_y \Delta k_{y,n,pq}\right), \tag{5.114}$$

where the phase mismatch terms are expressed as

$$\Delta k_{x,n,pq} = k_0 \sin\theta \cos\phi - k_{x,r,pq}^{(n)}, \tag{5.115}$$

$$\Delta k_{y,n,pq} = k_0 \sin\theta \sin\phi - k_{y,r,pq}^{(n)}, \tag{5.116}$$

and $\operatorname{sinc}(u) = \sin u/u$. The unit vectors of the observation basis are defined as

$$\hat{\phi} = -\hat{\mathbf{a}}_x \sin\phi + \hat{\mathbf{a}}_y \cos\phi, \tag{5.117}$$

$$\hat{\theta} = \hat{\mathbf{a}}_x \cos\theta\cos\phi + \hat{\mathbf{a}}_y \cos\theta \sin\phi - \hat{\mathbf{a}}_z \sin\theta. \tag{5.118}$$

The TE and TM components of the scattered far field are obtained by projecting the vector field onto the local basis

$$E_{\mathrm{sc}}^{\mathrm{TE}}(\theta,\phi)=\hat{\phi}\cdot\mathbf{E}_{\mathrm{sc}}(\theta,\phi), \tag{5.119}$$

$$E_{\mathrm{sc}}^{\mathrm{TM}}(\theta,\phi)=\hat{\theta}\cdot\mathbf{E}_{\mathrm{sc}}(\theta,\phi). \tag{5.120}$$

Substituting (5.111) into (5.119) and (5.120) yields the final polarimetric components

$$\begin{aligned}E_{\mathrm{sc}}^{\mathrm{TE}}(\theta,\phi)&=E_{\mathrm{sh}}^{\mathrm{TE}}(\theta,\phi)\\&\quad+\frac{jk_0e^{-jk_0r}}{4\pi r}\sum_{n=1}^{N}\sum_{p=-\infty}^{\infty}\sum_{q=-\infty}^{\infty}\\&\qquad\mathcal{A}_{n,pq}(\theta,\phi)\,\hat{\phi}\cdot\mathbf{U}_{n,pq}(\theta,\phi),\end{aligned} \tag{5.121}$$

$$\begin{aligned}E_{\mathrm{sc}}^{\mathrm{TM}}(\theta,\phi)&=E_{\mathrm{sh}}^{\mathrm{TM}}(\theta,\phi)\\&\quad+\frac{jk_0e^{-jk_0r}}{4\pi r}\sum_{n=1}^{N}\sum_{p=-\infty}^{\infty}\sum_{q=-\infty}^{\infty}\\&\qquad\mathcal{A}_{n,pq}(\theta,\phi)\,\hat{\theta}\cdot\mathbf{U}_{n,pq}(\theta,\phi).\end{aligned} \tag{5.122}$$

5.4.2 Scenario II: Multipath-Based Design

The multipath field representation follows the same plane-wave expansion and TE/TM decomposition introduced in Scenario I. The key difference here is that all retained incident components are used jointly in the RIS synthesis stage, so that the surface profile is designed from the total multipath illumination rather than from a single reference path.

Although the local reflection coefficient approximation is not sufficiently rigorous as a final scattering model under rich multipath illumination, it provides a convenient presynthesis representation for extracting a spatially resolved phase control template from the aggregate incident field [73, 188]. Accordingly, I employ the local equivalent current model only to determine the multipath-aware phase profile, whereas the final reradiated field is evaluated using a Floquet-based mode-matching formulation if an effective superperiod exists, and using a finite-aperture Huygens radiation integral otherwise.

The incident-current templates associated with the total multipath illumination are defined as

$$\mathbf{J}_i(\mathbf{r}_t) = \mathbf{H}_{t,i}(\mathbf{r}_t) \times \hat{\mathbf{n}}, \tag{5.123}$$

$$\mathbf{M}_i(\mathbf{r}_t) = \hat{\mathbf{n}} \times \mathbf{E}_{t,i}(\mathbf{r}_t), \tag{5.124}$$

where $\hat{\mathbf{n}} = \hat{\mathbf{a}}_z$. These currents represent the unmodulated Huygens current templates on the RIS aperture prior to imposing the synthesised local phase profile.

Unlike the single-path design, the multipath-aware design derives the local coefficient $\Gamma_\sigma(\mathbf{r}_t)$ from the aggregate current templates in (5.123)–(5.124), such that the controllable reradiated contributions are coherently combined in the target direction.

As in Scenario I, the desired reradiation direction remains specified by (θ_r, ϕ_r), and the corresponding tangential reradiated wavevector is $\mathbf{k}_{t,r}$ as defined in (5.38). In the single-path design, the phase gradient in (5.42) is obtained from the difference between $\mathbf{k}_{t,r}$ and the tangential wavevector of the dominant incident path. In the multipath-aware design, however, no unique incident tangential wavevector exists from which a single momentum increment can be defined. Therefore, the phase profile is obtained by directly enforcing coherent combining of the Huygens reradiated contributions generated by the aggregate multipath-induced current templates.

For this purpose, the target-direction unit vector is obtained from (5.110) as

$$\hat{\mathbf{r}}_r = \hat{\mathbf{r}}\big|_{\theta=\theta_r, \phi=\phi_r}. \tag{5.125}$$

The target-polarisation vector is selected from the observation basis in (5.117)–(5.118) as

$$\hat{\mathbf{p}}_r = \begin{cases} \hat{\phi}\big|_{\theta=\theta_r, \phi=\phi_r}, & \text{TE target,} \\ \hat{\theta}\big|_{\theta=\theta_r, \phi=\phi_r}, & \text{TM target.} \end{cases} \tag{5.126}$$

Applying the same Huygens radiation integral as in (5.109) to the target direction $\hat{\mathbf{r}} = \hat{\mathbf{r}}_r$, and substituting the locally modulated current model into the integrand, the multipath-aware target-direction field can be written as

$$\mathbf{E}_{\mathrm{sc}}^{\mathrm{MP}}(\hat{\mathbf{r}}_r) = \frac{jk_0 e^{-jk_0 r}}{4\pi r} \iint_{S_{\mathrm{RIS}}} \left[\boldsymbol{\mathcal{F}}^{(+)}(\mathbf{r}_t) + \Gamma_\sigma(\mathbf{r}_t) \boldsymbol{\mathcal{F}}^{(-)}(\mathbf{r}_t) \right] \mathrm{d}S. \tag{5.127}$$

Here, $\boldsymbol{\mathcal{F}}^{(+)}(\mathbf{r}_t)$ denotes the Γ_σ-independent contribution density generated by the unmodulated incident-field Huygens currents and is given by

$$\boldsymbol{\mathcal{F}}^{(+)}(\mathbf{r}_t) = \{\eta_0 \hat{\mathbf{r}}_r \times [\mathbf{J}_i(\mathbf{r}_t) \times \hat{\mathbf{r}}_r] + \hat{\mathbf{r}}_r \times \mathbf{M}_i(\mathbf{r}_t)\} \, e^{jk_0 \hat{\mathbf{r}}_r \cdot \mathbf{r}_t}. \tag{5.128}$$

The term $\boldsymbol{\mathcal{F}}^{(-)}(\mathbf{r}_t)$ denotes the Γ_σ-dependent controllable contribution density and is given by

$$\boldsymbol{\mathcal{F}}^{(-)}(\mathbf{r}_t) = \{\eta_0 \hat{\mathbf{r}}_r \times [\mathbf{J}_i(\mathbf{r}_t) \times \hat{\mathbf{r}}_r] - \hat{\mathbf{r}}_r \times \mathbf{M}_i(\mathbf{r}_t)\} \, e^{jk_0 \hat{\mathbf{r}}_r \cdot \mathbf{r}_t}. \tag{5.129}$$

The scalar field component used for phase synthesis is obtained by projecting the vector field onto the desired target polarisation

$$E_{\hat{\mathbf{p}}_r}^{\mathrm{MP}}(\hat{\mathbf{r}}_r) = \hat{\mathbf{p}}_r^{\mathrm{H}} \mathbf{E}_{\mathrm{sc}}^{\mathrm{MP}}(\hat{\mathbf{r}}_r). \tag{5.130}$$

Accordingly, the projected scalar contribution densities are defined as

$$\mathcal{F}_{\hat{\mathbf{p}}_r}^{(+)}(\mathbf{r}_t) = \hat{\mathbf{p}}_r^{\mathrm{H}} \boldsymbol{\mathcal{F}}^{(+)}(\mathbf{r}_t), \tag{5.131}$$

and

$$\mathcal{F}_{\hat{\mathbf{p}}_r}^{(-)}(\mathbf{r}_t) = \hat{\mathbf{p}}_r^{\mathrm{H}} \boldsymbol{\mathcal{F}}^{(-)}(\mathbf{r}_t). \tag{5.132}$$

For an ideal continuous, lossless, polarisation-preserving local response, the synthesis objective is

$$\max_{|\Gamma_\sigma(\mathbf{r}_t)|=1} \left| U^{(+)} + \iint_{S_{\mathrm{RIS}}} \Gamma_\sigma(\mathbf{r}_t) \mathcal{F}_{\hat{\mathbf{p}}_r}^{(-)}(\mathbf{r}_t) \, \mathrm{d}S \right|^2, \tag{5.133}$$

where

$$U^{(+)} = \iint_{S_{\mathrm{RIS}}} \mathcal{F}_{\hat{\mathbf{p}}_r}^{(+)}(\mathbf{r}_t) \, \mathrm{d}S \tag{5.134}$$

is the uncontrollable projected contribution. By the triangle inequality, the controllable contributions should be mutually phase aligned and, when $U^{(+)} \neq 0$, aligned with $U^{(+)}$. The optimal common phase is therefore

$$\chi^\star = \begin{cases} \arg U^{(+)}, & |U^{(+)}| > \tau_U, \\ 0, & |U^{(+)}| \leq \tau_U, \end{cases} \tag{5.135}$$

where τ_U is a small numerical tolerance. The ideal local coefficient is

$$\Gamma_\sigma^{\text{ideal}}(\mathbf{r}_t) = \begin{cases} \exp\left\{ j \left[\chi^\star - \arg \mathcal{F}_{\hat{\mathbf{p}}_r}^{(-)}(\mathbf{r}_t) \right] \right\}, & |\mathcal{F}_{\hat{\mathbf{p}}_r}^{(-)}(\mathbf{r}_t)| > \tau_F, \\ 1, & |\mathcal{F}_{\hat{\mathbf{p}}_r}^{(-)}(\mathbf{r}_t)| \leq \tau_F, \end{cases} \tag{5.136}$$

where τ_F prevents an undefined phase at weakly illuminated or polarisation null points. The multipath-aware continuous phase profile is

$$\Phi_{\text{MP}}(\mathbf{r}_t) = \arg \Gamma_\sigma^{\text{ideal}}(\mathbf{r}_t). \tag{5.137}$$

This closed-form solution is exact only under the stated unit-modulus scalar response assumptions. A practical RIS has a finite set of passive load states and an incidence-dependent response, so I use the continuous solution only to initialise the hardware design. For cell g centred at $\mathbf{r}_g$, the initial passive state is

$$\Gamma_{\sigma,g}^{(0)} = \underset{\Gamma_c \in \mathcal{C}_\Gamma}{\arg\min} \left| \Gamma_\sigma^{\text{ideal}}(\mathbf{r}_g) - \Gamma_c \right|, \tag{5.138}$$

where $\mathcal{C}_\Gamma$ is the calibrated complex coefficient codebook, including amplitude loss. If the state is parameterised by capacitance, every candidate is evaluated using (5.43)–(5.52). In the final forward model, path n uses its own response $\Gamma_\sigma(\Omega_i^{(n)}; C_g)$; a single angle-independent coefficient is not applied to all incident paths.

Quantisation and incidence dependence generally remove the global optimality of the closed-form phase alignment. I therefore refine the cell states with the local response multipath macromodel. For $\mathbf{C} = [C_1, \ldots, C_{N_c}]^{\mathrm{T}}$, I define

$$J(\mathbf{C}) = \left|\hat{\mathbf{p}}_r^{\mathrm{H}} \mathbf{E}_{\mathrm{tot}}(\mathbf{r}_{\mathrm{tar}}; \mathbf{C})\right|^2, \tag{5.139}$$

where $\mathbf{E}_{\mathrm{tot}}$ contains all retained incident paths, their incidence-dependent loaded unit-cell responses, finite-aperture reradiation, and the non-RIS background field. This model remains diagonal at the control level because the state of cell g acts through its own local coefficient. Starting from (5.138), coordinate descent updates cell g according to

$$C_g \leftarrow \arg\max_{C \in \mathcal{C}_C} J(C_1, \ldots, C_{g-1}, C, C_{g+1}, \ldots, C_{N_c}), \tag{5.140}$$

where $\mathcal{C}_C$ is the finite set of admissible passive load states. Sweeps stop when no state changes or when the relative improvement in J is below τ_J. Each accepted update is nondecreasing in J, and the finite state space guarantees termination at a coordinatewise local optimum. Several initial common phase offsets may be tested to reduce sensitivity to quantisation.

The implemented reference incidence phase map is

$$\Phi_{\mathrm{MP}}^{\mathrm{HW}}(\mathbf{r}_g) = \arg \Gamma_\sigma(\Omega_{\mathrm{ref}}; C_g). \tag{5.141}$$

This map is used only for visualisation; performance is evaluated from the per-path responses. For a target in the radiative near field, the exact source-to-target distance and dyadic Green function replace the fixed-direction far-field kernel in (5.127). The far-field expression is used only when the target satisfies the corresponding Fraunhofer distance condition.

Unlike the single-path phase profile in (5.42), the multipath-aware phase profile in (5.141) is not necessarily a linear phase ramp. Therefore, its effective superperiod cannot be obtained directly from (5.54). I instead test its periodicity from the complex phase field

$$Q_\sigma(x_r, y_r) = e^{j\Phi_{\mathrm{MP}}^{\mathrm{HW}}(x_r, y_r)}. \tag{5.142}$$

For a sampled RIS aperture with

$$x_m = x_0 + m\Delta x, \tag{5.143}$$

$$y_n = y_0 + n\Delta y, \tag{5.144}$$

the two-dimensional discrete Fourier transform is

$$\widetilde{Q}_\sigma[\mu,\nu] = \sum_{m=0}^{N_x-1}\sum_{n=0}^{N_y-1} Q_\sigma(x_m,y_n)w(x_m,y_n)e^{-j2\pi\left(\frac{\mu m}{N_x}+\frac{\nu n}{N_y}\right)}, \tag{5.145}$$

where $w(x_m,y_n)$ is an optional window function. After applying a fast Fourier transform (FFT) shift, the associated spatial frequencies are

$$k_x[\mu] = \frac{2\pi}{N_x\Delta x}\left(\mu - \frac{N_x}{2}\right), \tag{5.146}$$

$$k_y[\nu] = \frac{2\pi}{N_y\Delta y}\left(\nu - \frac{N_y}{2}\right). \tag{5.147}$$

The spectral energy is defined as

$$\mathcal{E}[\mu,\nu] = \left|\widetilde{Q}_\sigma[\mu,\nu]\right|^2. \tag{5.148}$$

After excluding the direct current (DC) component unless the phase profile is nearly uniform, the non-DC samples are sorted in descending order of $\mathcal{E}[\mu,\nu]$. The dominant harmonic set $\mathcal{K}_\alpha$ is selected as the smallest set satisfying

$$\frac{\sum_{j=1}^{S}\mathcal{E}_{s_j}}{\sum_{j=1}^{N_f}\mathcal{E}_{s_j}} \geq \alpha, \tag{5.149}$$

where

$$0.8 \leq \alpha \leq 0.9, \tag{5.150}$$

and $s_j = (\mu_j, \nu_j)$ denotes the index of the jth strongest non-DC Fourier sample. The corresponding dominant spatial harmonics are

$$\mathcal{K}_\alpha = \left\{ \mathbf{q}_j = (k_{x,j}, k_{y,j}) = \big(k_x[\mu_j], k_y[\nu_j]\big) : j = 1, \ldots, S \right\}. \tag{5.151}$$

To remain consistent with the rectangular supercell formulation in Scenario I, the selected harmonics are tested against an axis-aligned reciprocal lattice:

$$k_{x,j} \approx m_j G_x^{\mathrm{MP}}, \tag{5.152}$$

$$k_{y,j} \approx n_j G_y^{\mathrm{MP}}, \tag{5.153}$$

$$m_j, n_j \in \mathbb{Z}. \tag{5.154}$$

With weights $w_j = \mathcal{E}_{s_j}$, the least-squares estimate along each coordinate that has at least one nonzero assigned lattice index is

$$G_x^{\mathrm{MP}} = \frac{\sum_{j=1}^{S} w_j m_j k_{x,j}}{\sum_{j=1}^{S} w_j m_j^2}, \tag{5.155}$$

$$G_y^{\mathrm{MP}} = \frac{\sum_{j=1}^{S} w_j n_j k_{y,j}}{\sum_{j=1}^{S} w_j n_j^2}. \tag{5.156}$$

The estimate for a coordinate is undefined if its denominator in (5.155) or (5.156) is zero. In that case, the phase is treated as invariant along that coordinate, and no finite superperiod is assigned. For coordinates with defined estimates, the corresponding fitting residuals are

$$\varepsilon_x = \sqrt{\frac{\sum_{j=1}^{S} w_j \left(k_{x,j} - m_j G_x^{\mathrm{MP}}\right)^2}{\sum_{j=1}^{S} w_j}}, \tag{5.157}$$

$$\varepsilon_y = \sqrt{\frac{\sum_{j=1}^{S} w_j \left(k_{y,j} - n_j G_y^{\mathrm{MP}}\right)^2}{\sum_{j=1}^{S} w_j}}. \tag{5.158}$$

Let

$$D_x = N_x \Delta x, \tag{5.159}$$

$$D_y = N_y \Delta y. \tag{5.160}$$

The finite-aperture spectral resolutions are

$$\delta k_x = \frac{2\pi}{D_x}, \tag{5.161}$$

$$\delta k_y = \frac{2\pi}{D_y}. \tag{5.162}$$

The multipath phase profile is regarded as effectively periodic along each coordinate with a defined lattice estimate if

$$\varepsilon_x \le c_{\mathrm{tol}} \delta k_x, \tag{5.163}$$

$$\varepsilon_y \le c_{\mathrm{tol}} \delta k_y, \tag{5.164}$$

where c_{tol} is a tolerance factor of order unity. If the applicable conditions in (5.163) and (5.164) are satisfied and the corresponding fitted spacings are nonzero, the finite effective multipath superperiods are

$$P_x^{\mathrm{MP}} = \frac{2\pi}{|G_x^{\mathrm{MP}}|}, \tag{5.165}$$

$$P_y^{\mathrm{MP}} = \frac{2\pi}{|G_y^{\mathrm{MP}}|}. \tag{5.166}$$

When the effective superperiods in (5.165) and (5.166) exist, the Floquet formulation derived in Scenario I is reused by replacing

$$P_x \to P_x^{\mathrm{MP}}, \tag{5.167}$$

$$P_y \to P_y^{\mathrm{MP}}. \tag{5.168}$$

Accordingly, the reciprocal-lattice vector in (5.55) becomes

$$\mathbf{G}_{pq}^{\mathrm{MP}} = pG_x^{\mathrm{MP}}\hat{\mathbf{a}}_x + qG_y^{\mathrm{MP}}\hat{\mathbf{a}}_y, \tag{5.169}$$

and the Floquet tangential wavevector follows from (5.56) as

$$\mathbf{k}_{t,r,pq}^{(n),\mathrm{MP}} = \mathbf{k}_{t,i}^{(n)} + \mathbf{G}_{pq}^{\mathrm{MP}}. \tag{5.170}$$

All subsequent quantities, including $k_{x,r,pq}^{(n)}$, $k_{y,r,pq}^{(n)}$, $k_{z,r,pq}^{(n)}$, the propagation condition, the angular mapping, the surface impedance Fourier coefficients, the mode-matching matrix equation, and the far-field projections, are then obtained from (5.57)–(5.122) with the replacements in (5.167)–(5.170).

If either applicable condition in (5.163) or (5.164) is not satisfied, no physically meaningful Floquet supercell is assigned to the multipath phase profile. In that case, I define the path-resolved incident-current templates as $\mathbf{J}_{i,n} = \mathbf{H}_{t,i,n} \times \hat{\mathbf{n}}$ and $\mathbf{M}_{i,n} = \hat{\mathbf{n}} \times \mathbf{E}_{t,i,n}$. The hardware response is then applied separately to every incident path at each cell as

$$\mathbf{J}_s^{\mathrm{MP}}(\mathbf{r}_g) = \sum_{n=1}^{N} \left[1 + \Gamma_\sigma(\Omega_i^{(n)}; C_g)\right] \mathbf{J}_{i,n}(\mathbf{r}_g), \tag{5.171}$$

$$\mathbf{M}_s^{\mathrm{MP}}(\mathbf{r}_g) = \sum_{n=1}^{N} \left[1 - \Gamma_\sigma(\Omega_i^{(n)}; C_g)\right] \mathbf{M}_{i,n}(\mathbf{r}_g). \tag{5.172}$$

The scattered field is then evaluated by the finite-aperture Huygens radiation integral in (5.109), with $(\mathbf{J}_s, \mathbf{M}_s)$ replaced by $(\mathbf{J}_s^{\mathrm{MP}}, \mathbf{M}_s^{\mathrm{MP}})$. The TE and TM components are obtained using the same projections in (5.119)–(5.120).

The numerical phase maps reported in the following section were generated from the aggregate multipath illumination and demonstrate the continuous multipath-aware synthesis principle. The hardware codebook coordinate refinement in (5.139)–(5.140) completes the deployment-oriented implementation procedure, but the existing figures have not been regenerated with this additional refinement. Consequently, I do not attribute any further numerical gain to the refinement in the present thesis; such a claim requires rerunning the simulations with the calibrated per-angle codebook.

5.4.3 Multipath Illumination of a Nonlocal Beyond-Diagonal RIS

The preceding synthesis treats the RIS as a collection of locally controlled cells. In an abstract power wave representation, its control operator is diagonal,

$$\mathbf{b} = \Theta_{\mathrm{D}}\mathbf{a}, \qquad \Theta_{\mathrm{D}} = \mathrm{diag}\left(e^{j\phi_1}, \ldots, e^{j\phi_{N_c}}\right), \tag{5.173}$$

where $\mathbf{a}$ and $\mathbf{b}$ contain power-normalised incident and reradiated modal amplitudes. This representation assumes that each controlled degree of freedom changes only its corresponding local channel. It does not represent lateral power transport, load-to-load coupling, or conversion between different surface and radiation modes.

A nonlocal or beyond-diagonal RIS is instead described by a full operator

$$\mathbf{b} = \Theta_{\mathrm{BD}}\mathbf{a}, \tag{5.174}$$

whose off-diagonal entries transfer power between controlled ports or modes. This distinction is physical rather than merely algebraic. For anomalous reflection from θ_i to θ_r with unchanged polarisation in a homogeneous medium, the reflected amplitude required by global power conservation is [72]

$$|E_r| = |E_i|\sqrt{\frac{\cos\theta_i}{\cos\theta_r}}. \tag{5.175}$$

For TE fields, the time average of the normal power density at the surface is

$$P_n(x) = \frac{1}{2\eta_0}\left[-|E_i|^2\cos\theta_i + |E_r|^2\cos\theta_r + |E_i||E_r|(\cos\theta_r - \cos\theta_i)\cos\Phi_r(x)\right], \tag{5.176}$$

where $\Phi_r(x) = k_0(\sin\theta_i - \sin\theta_r)x + \phi_0$. Substitution of (5.175) into (5.176) cancels the spatially averaged term, but leaves an oscillatory component whenever $\cos\theta_i \neq \cos\theta_r$. Therefore, perfect anomalous reflection with unchanged polarisation cannot, in general, satisfy $P_n(x) = 0$ pointwise with a passive local lossless sheet. A passive nonlocal surface resolves this conflict by accepting power where $P_n(x) < 0$, transporting it laterally through guided, evanescent, or coupled network channels, and reradiating it where $P_n(x) > 0$. The net normal power exchange over one superperiod remains zero.

The attainable off-diagonal coupling is determined by the implemented network architecture. A fully connected network permits pairwise coupling between all controlled ports, whereas group-, tree-, and band-connected networks impose progressively sparser connection graphs. The admissible set must therefore be written as $\mathcal{A}_{\mathrm{BD}}(\mathcal{G})$ for a specified hardware graph $\mathcal{G}$; optimising an unrestricted dense matrix and then deleting unavailable couplings is not physically equivalent to optimising the implemented topology. A sparse architecture preserves the required channel-shaping subspace only when its coupling graph connects the relevant incident and target modal subspaces. This condition is channel- and architecture-dependent and cannot be assumed a priori [186].

Full Coupled Network Forward Model

Let $\mathbf{v}_0 = \sum_{n=1}^{N} \mathbf{v}_{0,n}$ denote the coherent open-circuit excitation produced at the N_c controlled ports by all RT incident paths. Let $\mathbf{Z}_{\mathrm{EM}}$ be the full EM self- and mutual-impedance matrix of the unloaded RIS, and let $\mathbf{Z}_{\mathrm{L}}(\xi)$ be the tunable load-network matrix controlled by the hardware variables ξ. With the voltage convention

$$\mathbf{v} = \mathbf{v}_0 + \mathbf{Z}_{\mathrm{EM}}\mathbf{i} = \mathbf{Z}_{\mathrm{L}}(\xi)\mathbf{i}, \tag{5.177}$$

the induced current vector is

$$\mathbf{i}(\xi) = \left[\mathbf{Z}_{\mathrm{L}}(\xi) - \mathbf{Z}_{\mathrm{EM}}\right]^{-1}\mathbf{v}_0. \tag{5.178}$$

The inverse exists only away from an uncontrolled singular resonance. Equation (5.178) shows why a beyond-diagonal RIS cannot be designed by assigning independent phases: changing one network parameter generally changes every component of $\mathbf{i}$.

This forward model retains two effects that must not be absorbed into an abstract phase matrix. First, the off-diagonal entries of $\mathbf{Z}_{\mathrm{EM}}$ represent EM mutual coupling even when the tunable loads are diagonal. Second, the fixed field $\mathbf{E}_f$ in (5.179) contains structural scattering from the unloaded support and conductors. A unilateral approximation may neglect feedback from the RIS towards the Tx when that reverse interaction is demonstrably weak, but it does not justify neglecting coupling among RIS ports. The approximation must be checked by comparing the reduced and full network solutions over the intended frequency band and illumination set.

Let $\mathbf{G}(\mathbf{r})$ map the port currents to the electric field at $\mathbf{r}$, including finite-aperture effects, element patterns, polarisation, and propagation from the RIS. The complete field is

$$\mathbf{E}_{\mathrm{tot}}(\mathbf{r};\xi) = \mathbf{E}_f(\mathbf{r}) + \mathbf{G}(\mathbf{r})\left[\mathbf{Z}_{\mathrm{L}}(\xi) - \mathbf{Z}_{\mathrm{EM}}\right]^{-1}\mathbf{v}_0, \tag{5.179}$$

where $\mathbf{E}_f$ contains the Tx, environment, and unloaded structure contributions. In the far field, I define $\mathbf{G}_\infty(\theta,\phi) = \lim_{r\to\infty} re^{jk_0 r}\mathbf{G}(r,\theta,\phi)$. The vector radiation pattern is then

$$\mathbf{F}(\theta,\phi;\xi) = \mathbf{F}_f(\theta,\phi) + \mathbf{G}_\infty(\theta,\phi)\left[\mathbf{Z}_{\mathrm{L}}(\xi) - \mathbf{Z}_{\mathrm{EM}}\right]^{-1}\mathbf{v}_0. \tag{5.180}$$

The target-polarised power pattern is proportional to

$$P_{\mathrm{tar}}(\theta,\phi;\xi) = \frac{1}{2\eta_0}\left|\hat{\mathbf{p}}(\theta,\phi)^{\mathrm{H}}\mathbf{F}(\theta,\phi;\xi)\right|^2. \tag{5.181}$$

For a target in the near field, (5.179), rather than (5.180), is used with the exact dyadic Green function.

Determination of the Beyond-Diagonal Control Pattern

The design variable is ξ, or equivalently the admissible matrix $\mathbf{Z}_{\mathrm{L}}(\xi)$; an independent phase vector is not the primary design variable. For a target position $\mathbf{r}_{\mathrm{tar}}$ and polarisation $\hat{\mathbf{p}}_r$, the physically constrained problem is

$$\xi^{\star} = \arg\max_{\xi \in \mathcal{A}_{\mathrm{BD}}} \left| \hat{\mathbf{p}}_r^{\mathrm{H}} \mathbf{E}_{\mathrm{tot}}(\mathbf{r}_{\mathrm{tar}}; \xi) \right|^2, \tag{5.182}$$

where $\mathcal{A}_{\mathrm{BD}} = \mathcal{A}_{\mathrm{BD}}(\mathcal{G})$ contains only physically realisable networks having the selected connection graph. After solving (5.182), the displayed control or "phase" pattern is derived from the solution, for example

$$\phi_g^{(i)} = \arg i_g(\xi^{\star}), \tag{5.183}$$

or from the phase of the corresponding equivalent aperture field. This derived pattern must not be interpreted as a set of independent local reflection phases.

For continuous tuning, the objective gradient can be evaluated without finite differences. Let $\mathbf{A}(\xi) = \mathbf{Z}_{\mathrm{L}}(\xi) - \mathbf{Z}_{\mathrm{EM}}$, $q = \hat{\mathbf{p}}_r^{\mathrm{H}} \mathbf{E}_{\mathrm{tot}}$, and $J = |q|^2$. Differentiation of (5.178) gives

$$\frac{\partial \mathbf{i}}{\partial \xi_k} = -\mathbf{A}^{-1} \frac{\partial \mathbf{Z}_{\mathrm{L}}}{\partial \xi_k} \mathbf{i}, \tag{5.184}$$

and hence

$$\frac{\partial J}{\partial \xi_k} = 2\Re \left\{ q^* \hat{\mathbf{p}}_r^{\mathrm{H}} \mathbf{G}(\mathbf{r}_{\mathrm{tar}}) \frac{\partial \mathbf{i}}{\partial \xi_k} \right\}. \tag{5.185}$$

Equations (5.184) and (5.185) support projected gradient or sequential quadratic programming over continuous passive network parameters. For quantised states, the same forward model is used in coordinate descent or branch-and-bound. A diagonal physical load matrix can still produce a beyond-diagonal effective response through the full $\mathbf{Z}_{\mathrm{EM}}$; an interconnected tuning network makes $\mathbf{Z}_{\mathrm{L}}$ itself nondiagonal.

The potential target-direction improvement can be bounded in an ideal power wave model. Let $\mathbf{h}_i$ be the coherent multipath excitation vector at the RIS and $\mathbf{h}_r$ the coupling vector from the RIS modes to the target. Ignoring the fixed background term for this bound, the target field is

$$y = \mathbf{h}_r^{\mathrm{H}} \Theta \mathbf{h}_i. \tag{5.186}$$

For an ideal diagonal phase-only RIS, the optimum is

$$|y_{\mathrm{D}}^{\star}| = \sum_{g=1}^{N_c} |h_{r,g}||h_{i,g}|, \tag{5.187}$$

obtained with $\phi_g = \chi + \arg h_{r,g} - \arg h_{i,g}$. For any lossless full operator satisfying $\Theta^{\mathrm{H}}\Theta = \mathbf{I}$, the Cauchy–Schwarz inequality gives

$$|y_{\mathrm{BD}}| \leq \|\mathbf{h}_r\|_2 \|\mathbf{h}_i\|_2. \tag{5.188}$$

Consequently, if the beyond-diagonal architecture contains the diagonal designs as a subset and the global optimum is found, its target power gain satisfies

$$1 \leq \frac{|y_{\mathrm{BD}}^{\star}|^2}{|y_{\mathrm{D}}^{\star}|^2} \leq \frac{\|\mathbf{h}_r\|_2^2 \|\mathbf{h}_i\|_2^2}{\left(\sum_{g=1}^{N_c} |h_{r,g}||h_{i,g}|\right)^2}. \tag{5.189}$$

The upper bound is attainable only if the admissible reciprocal network can realise the required modal mapping. Equality at the lower bound occurs when diagonal control already aligns all useful modal power; therefore, a beyond-diagonal RIS does not guarantee a strict gain in every channel. Its potential benefit is greatest when the incident and target coupling magnitudes are poorly matched, when lateral power redistribution is required, or when parasitic or specular modes must be suppressed. Equation (5.189) is consequently a theoretical feasibility bound, rather than a performance prediction for a particular unit cell, network topology, or indoor channel.

Physical Feasibility Conditions

The following conditions are imposed during, rather than after, optimisation:

1. **Passivity:** with $\mathbf{v}_{\mathrm{L}} = \mathbf{Z}_{\mathrm{L}}\mathbf{i}$, the absorbed power must be nonnegative for every $\mathbf{i}$, which requires
$$\frac{\mathbf{Z}_{\mathrm{L}} + \mathbf{Z}_{\mathrm{L}}^{\mathrm{H}}}{2} \succeq \mathbf{0}. \tag{5.190}$$

For an ideal lossless network the Hermitian part is zero. In a power-normalised scattering representation, the equivalent conditions are $\Theta^{\mathrm{H}}\Theta \preceq \mathbf{I}$ and $\Theta^{\mathrm{H}}\Theta = \mathbf{I}$, respectively.

2. **Reciprocity:** a passive reciprocal interconnection requires $\mathbf{Z}_{\mathrm{L}} = \mathbf{Z}_{\mathrm{L}}^{\mathrm{T}}$, or equivalently $\Theta = \Theta^{\mathrm{T}}$ when identical power wave references are used. A desired transformation that violates this symmetry requires nonreciprocal or time-varying hardware.

3. **Global power balance:** the power entering the nonlocal surface over a superperiod or the complete finite-aperture must equal reradiated plus dissipated power. Local regions may exhibit apparent absorption or generation, but a passive lossless design must satisfy zero net absorbed power; the apparent gain regions are supplied by lateral power transport.

4. **Causality and stability:** $\mathbf{Z}_{\mathrm{L}}(s)$ must be a positive-real matrix over frequency, and $\mathbf{Z}_{\mathrm{L}} - \mathbf{Z}_{\mathrm{EM}}$ must remain nonsingular with an adequate stability margin over the operating band and component tolerances.

5. **Hardware topology:** the sparsity, coupling range, tuning interval, quantisation, conductor/dielectric loss, bias network, voltage limits, and thermal limits must be included in $\mathcal{A}_{\mathrm{BD}}$. An arbitrary dense unitary matrix is not automatically realisable by a finite passive circuit.

6. **Polarisation and modal completeness:** if cross-polarisation conversion is retained, all TE/TM blocks must be included in the coupled operator. The propagating mode power balance must use power-normalised modes, while sufficiently many evanescent modes must be retained to converge the near-surface coupling.

Equations (5.178)–(5.182) define the calculation chain required for a physically constrained implementation: obtain each $\mathbf{v}_{0,n}$ from RT, extract $\mathbf{Z}_{\mathrm{EM}}$ and $\mathbf{G}$ from a full-wave or validated reduced-order model, optimise only the admissible network parameters, and then recompute the complete radiation pattern and power balance. This formulation is consistent with the channel-informed nondiagonal approach in [196] and with the spatial-dispersion requirements in [72]. Although this procedure is more computationally demanding than diagonal phase synthesis, it avoids interpreting a locally assigned phase profile as a complete nonlocal EM design.

Scope and Future Work

The preceding formulation establishes the theoretical requirements for extending the multipath synthesis framework from a local diagonal RIS to a nonlocal beyond-diagonal RIS. It deliberately stops short of a numerical performance comparison. In particular, (5.178)–(5.182) do not define a physically realisable device until the connection graph $\mathcal{G}$, the frequency-dependent component models, and the associated admissible set $\mathcal{A}_{\mathrm{BD}}(\mathcal{G})$ have been specified. The matrices $\mathbf{Z}_{\mathrm{EM}}$ and $\mathbf{G}$ must also be extracted for the same finite aperture and reference planes used by the network model. Consequently, no target-direction gain, radiation-pattern improvement, or efficiency advantage is claimed for a nonlocal RIS in this thesis.

Numerical and full-wave assessment of the nonlocal extension is therefore reserved for future work. A topology-specific study should first construct $\mathbf{Z}_{\mathrm{L}}(\xi)$ for a selected reciprocal interconnection and calibrate $\mathbf{Z}_{\mathrm{EM}}$ and $\mathbf{G}$ over the intended frequency band. For each coherent multipath field supplied by the RT model, the constrained problem in (5.182) should then be solved subject to the passivity, reciprocity, stability, tuning, and sparsity conditions stated above. The resulting network should subsequently be evaluated using circuit and full-wave co-simulation of the finite RIS, including conductor and dielectric losses, component tolerances, bias-network parasitics, mutual coupling, edge diffraction, and polarisation conversion.

Any future comparison with a diagonal RIS should retain identical incident fields, aperture, target, materials, bandwidth, and power normalisation, leaving the control architecture as the only independent variable. It should report the target-polarised and total reradiated powers, aperture efficiency, integrated power, sidelobe and specular-mode levels, cross-polarisation, bandwidth, and uncertainty sensitivity, together with the global power balance and residuals of the passivity, reciprocity, and stability tests. Only after these checks can the conditions under which nonlocal coupling improves upon diagonal control be quantified reliably. The subsequent CST benchmark and PEC T-shaped room studies therefore evaluate only the local diagonal RIS framework and do not validate the nonlocal extension.

5.5 Performance Evaluation of Single-Path and Multipath RIS Designs

This section evaluates the phase-synthesis framework in two sequential stages. First, a canonical three-path benchmark compares the analytical model with CST full-wave simulation under matched aperture, excitation, and target-direction conditions. This comparison establishes the scope within which the analytical model reproduces the full-wave response. Second, the resulting analytical workflow is applied to a site-specific PEC T-shaped room to compare the single-path and multipath-aware phase designs in a controlled indoor multipath environment. The ordering is deliberate: the model-level evidence is established before the room-scale field redistribution is interpreted. The CST benchmark and the PEC room study use independent incident fields, and no path amplitude or phase is transferred between the two data sets.

5.5.1 CST Full-Wave Validation

The first validation stage isolates the phase synthesis from the additional propagation complexity of a complete room. Both models are evaluated at 3.5 GHz using identical incident directions, centre-referenced phases, electric-field amplitudes, and $\hat{\phi}$-polarised plane-wave definitions. Three incident waves illuminate the RIS with the parameters in Table 5.2, and the prescribed reradiation direction is $(\theta_\mathrm{d}, \phi_\mathrm{d}) = (26^\circ, 34^\circ)$. All reported electric-field amplitudes are asymptotic far-field quantities scaled according to $1/r$ and referenced to 1 m; they must not be interpreted as physical near-field values evaluated at a distance of 1 m.

Table 5.2 Three incident paths used in the CST full-wave benchmark.

Path	$\theta_i^{(n)}$	$\phi_i^{(n)}$	$E_{0,n}$	$\varphi_{0,n}$	**Polarisation**
Ray 1	56.000°	−128.000°	1.000	0.000°	ϕ-polarised
Ray 2	55.753°	54.964°	0.720	−179.910°	ϕ-polarised
Ray 3	64.401°	7.026°	0.480	−101.617°	ϕ-polarised

The angles in Table 5.2 are expressed in the local RIS spherical coordinate system. The angle $\theta_i^{(n)}$ is measured from the RIS surface normal, and $\phi_i^{(n)}$ is the corresponding azimuth. The phasor $E_{0,n}e^{j\varphi_{0,n}}$ specifies the normalised electric-field excitation of path n at the local RIS origin, such that $\mathbf{E}_{i,n}(\mathbf{0}) = E_{0,n}e^{j\varphi_{0,n}}\hat{\mathbf{a}}_{\phi_i^{(n)}}$ under the CST ϕ-polarisation convention. The associated grazing angles, $\alpha_{\mathrm{g},n} = 90^\circ - \theta_i^{(n)}$, are 34.000°, 34.247°, and 25.599° for Rays 1–3, respectively.

Ray 1 defines the single-path reference profile because it carries the greatest normal incident power. After removal of the common factor $1/(2\eta_0)$, the normal power weights $E_{0,n}^2 \cos\theta_i^{(n)}$ are 0.559193, 0.291736, and 0.099549 for Rays 1–3, respectively. The tangential momentum difference between Ray 1 and the desired outgoing wave gives the phase-gradient periods

$$a = \frac{\lambda}{\left|\sin\theta_{\mathrm{d}}\sin\phi_{\mathrm{d}} - \sin\theta_i^{(1)}\sin\phi_i^{(1)}\right|}, \qquad b = \frac{\lambda}{\left|\sin\theta_{\mathrm{d}}\cos\phi_{\mathrm{d}} - \sin\theta_i^{(1)}\cos\phi_i^{(1)}\right|}. \tag{5.191}$$

These periods are well defined for the single-path reference because one incident tangential wavevector is selected. Under multipath illumination, the coherent aperture field generally has neither a unique incidence angle nor a globally linear phase. The multipath-aware profile is therefore obtained from the coherent target-field objective in (5.133)–(5.135), followed by hardware-state mapping and the path-resolved evaluation in (5.171)–(5.172); the single-path periods are not reapplied to the aggregate field.

Three controlled scenarios, denoted S1–S3, are evaluated. In S1, the phase profile designed for Ray 1 is illuminated only by Ray 1. In S2, the same profile is illuminated coherently by all three paths. In S3, the multipath-aware profile is synthesised for, and illuminated by, the same three-path field. Because S2 and S3 have identical incident fields, their comparison isolates the effect of redesigning the RIS phase profile. In contrast, S1 contains less incident aperture power and therefore provides a single-wave reference rather than an equal-input baseline for S3.

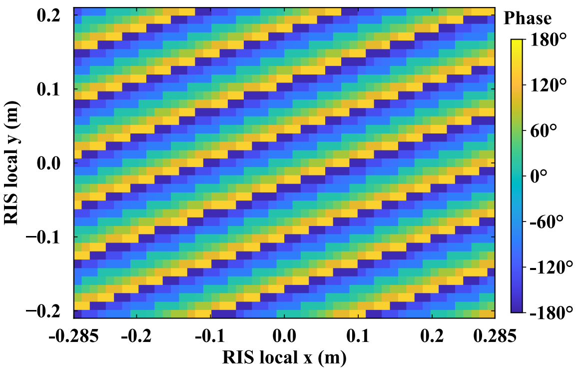

(a) Single-path phase distribution.

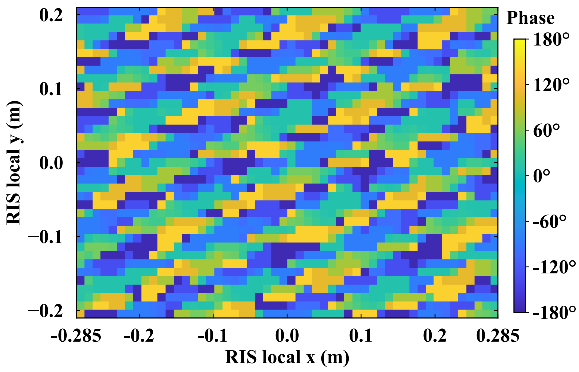

(b) Multipath-aware phase distribution.

Fig. 5.12 Comparison of the designed RIS phase distributions under single-path and multipath illumination.

Figure 5.12 shows the corresponding control profiles. The single-path profile is approximately a linear phase ramp because it compensates one tangential momentum difference. The multipath-aware profile is spatially nonuniform because it compensates the phase of the coherent three-wave aperture excitation before aligning the controllable $\hat{\theta}$-polarised contribution in the target direction. This distinction follows directly from the two synthesis objectives.

The analytical implementation represents the RIS as a locally responding Huygens aperture. Each element is assigned an angle- and polarisation-independent scalar reflection coefficient $\Gamma(C) = A(C)e^{j\phi(C)}$ selected from an 18-state discrete capacitance codebook, and the same coefficient is applied to every incident path and tangential field component. The analytical aperture and the CST aperture contain 50×37 elements over approximately 0.565×0.4181 m, with an 11.3×11.3 mm period. CST resolves the finite three-dimensional unit-cell geometry, lumped-element branches, material losses, inter-element coupling, edge diffraction, polarisation conversion, and parasitic scattering modes. The two models are therefore suitable for comparing the beam direction and angular response trends, but equality of their absolute polarisation-resolved amplitudes is not expected without a common angle-dependent unit-cell calibration.

Table 5.3 Target-direction asymptotic far-field amplitudes referenced to 1 m for the CST three-path benchmark.

Method	Case	$\lvert E_\theta \rvert$ (V/m)	$\lvert E_\phi \rvert$ (V/m)	$\lvert E \rvert_{\mathrm{RSS}}$ (V/m)
Analytical model	S1	0.517172	1.544437	1.628728
Analytical model	S2	0.515714	1.544517	1.628341
Analytical model	S3	0.689662	1.296814	1.468795
CST full-wave model	S1	0.140564	0.754065	0.767055
CST full-wave model	S2	0.145818	0.749157	0.763216
CST full-wave model	S3	0.235529	0.645876	0.687480

Table 5.3 reports the two spherical field components and their root-sum-square magnitude, $|E|_{\mathrm{RSS}} = \sqrt{|E_\theta|^2 + |E_\phi|^2}$, at the target direction. The S3 phase profile is designed to maximise the desired E_θ component rather than $|E|_{\mathrm{RSS}}$. Relative to S2, S3 increases $|E_\theta|$ by 2.525 dB in the analytical model and by 4.165 dB in CST. Over the same comparison, $|E_\phi|$ decreases by 1.518 and 1.289 dB, respectively, and $|E|_{\mathrm{RSS}}$ decreases by 0.896 and 0.908 dB. The improvement is therefore polarisation-selective and must not be interpreted as an enhancement of the total vector-field magnitude.

The distinction between S1 and the two three-path cases is also relevant when interpreting unnormalised amplitudes. Direct integration of the normal incident Poynting flux over the analytical aperture gives $P_{\mathrm{inc,S1}} \approx 1.77675 \times 10^{-4}$ W and $P_{\mathrm{inc,S2/S3}} \approx 3.02762 \times 10^{-4}$ W. The latter is greater by a factor of 1.7040, or 2.315 dB. Hence, an S3/S1 comparison combines the additional incident multipath power with the change in phase profile, whereas S3/S2 is the appropriate equal-illumination comparison of the two design rules.

Figures 5.13 and 5.14 compare orthogonal angular cuts through the prescribed direction. For a quantitative comparison of the vector-field envelopes, the analytical 0.1° samples were linearly interpolated onto the CST 1° grids. The Pearson correlation coefficients for the θ-cuts are 0.964, 0.969, and 0.953 for S1–S3, respectively. The corresponding coefficients for the ϕ-cuts are 0.970, 0.933, and 0.785. The θ-cut envelopes therefore exhibit strong

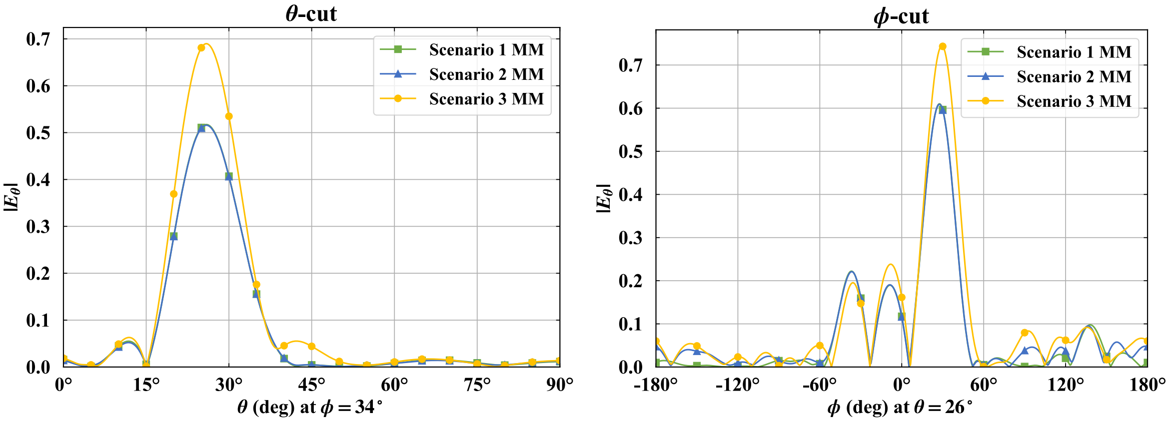

(a) Proposed method, θ-cut at $\phi = 34°$. (b) Proposed method, ϕ-cut at $\theta = 26°$.

Fig. 5.13 Radiation-pattern cuts obtained using the proposed analytical method.

agreement, whereas the lower S3 ϕ-cut correlation identifies a substantive difference in angular shape. Both models nevertheless place a directive response in the vicinity of $(\theta_\mathrm{d}, \phi_\mathrm{d})$, supporting the phase-gradient orientation and predicted beam direction.

At the target direction, the CST-to-analytical ratios of $|E|_\mathrm{RSS}$ are 0.470953, 0.468708, and 0.468057 for S1–S3, respectively. These values correspond to amplitude offsets of -6.540, -6.582, and -6.594 dB and remain close to an average ratio of 0.469. This repeatable offset indicates a systematic difference in the unit-cell and aperture representations, but it is not a universal normalisation factor. In particular, the CST-to-analytical ratios of $|E_\theta|$ are 0.272, 0.283, and 0.342, and the S3 ϕ-cut has a lower shape correlation. A single amplitude scale factor therefore cannot reproduce the polarisation-resolved response.

Let $E_\theta(\theta_\mathrm{d}, \phi_\mathrm{d})$ and $E_\phi(\theta_\mathrm{d}, \phi_\mathrm{d})$ denote the complex spherical components of the reported far field in the target direction. The fraction of target-direction electric-field power in the θ-polarised component is

$$\rho_\theta = \frac{|E_\theta(\theta_\mathrm{d}, \phi_\mathrm{d})|^2}{|E_\theta(\theta_\mathrm{d}, \phi_\mathrm{d})|^2 + |E_\phi(\theta_\mathrm{d}, \phi_\mathrm{d})|^2}. \tag{5.192}$$

The CST results give $100\rho_\theta = 3.36\%$, 3.65%, and 11.74% for S1, S2, and S3, respectively. The reradiated field at the target direction is therefore predominantly ϕ-polarised in all three

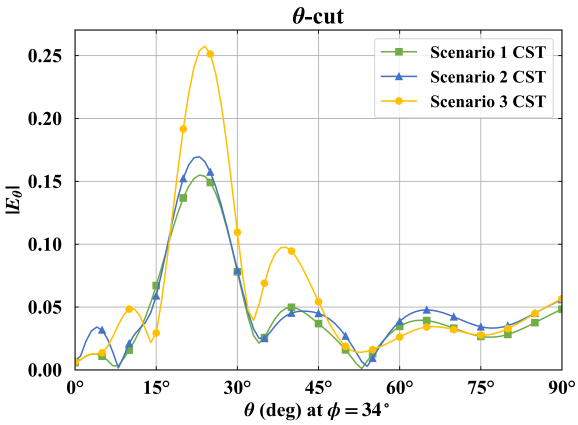

(a) Full-wave simulation, θ-cut at $\phi = 34°$.

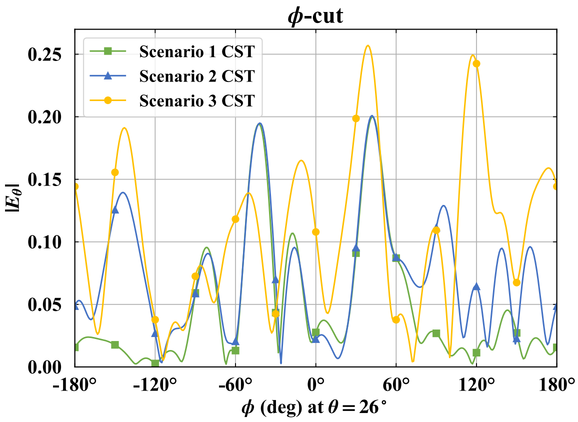

(b) Full-wave simulation, ϕ-cut at $\theta = 26°$.

Fig. 5.14 Radiation-pattern cuts obtained from full-wave simulations.

cases, although the multipath-aware design increases the relative contribution of the desired θ-polarised component.

The remaining discrepancies follow from both constitutive and implementation differences. CST inherently includes oblique-incidence spatial dispersion, co-polarised and cross-polarised channels, mutual coupling, finite-aperture edge effects, conductor and dielectric losses, and parasitic or specular scattering. The residual difference must therefore be interpreted as a combined unit-cell calibration, aperture efficiency, loss, coupling, discretisation, and polarisation-channel error rather than an incorrect spatial phase-gradient orientation.

The full-wave benchmark therefore provides a qualified validation of the analytical framework. It supports the predicted beam direction, the multipath phase-synthesis mechanism, and the normalised θ-cut trends. It does not establish quantitative equivalence of the absolute or polarisation-resolved fields. Such equivalence would require an angle-dependent reflection dyadic, a coupling-aware finite-array model, and a capacitance codebook calibrated to the implemented CST unit cell and lattice. With this validation scope established, the analytical framework is subsequently applied to the PEC room without treating the room-scale results as an additional full-wave validation.

5.5.2 Application to the PEC T-Shaped Room

The second stage applies the phase-synthesis framework to a T-shaped room bounded by PEC walls. The PEC boundaries eliminate wall transmission and material absorption while retaining deterministic reflection-induced multipath. This controlled enclosure isolates the RIS-induced spatial field redistribution from uncertainty associated with frequency-dependent wall parameters. The transmit power is $P_{\text{tx}} = -15$ dBW.

The room study retains the coherent target-field phase-synthesis principle used in the preceding CST full-wave validation while selecting a different target polarisation. Specifically, the target-polarisation vector is set to $\hat{\mathbf{p}}_r = \hat{\phi}|_{\theta=\theta_r,\phi=\phi_r}$. The RIS phase profiles are therefore synthesised to coherently align the controllable ϕ-polarised reradiated-field contributions at the prescribed target direction (θ_r, ϕ_r). Equivalently, the synthesis seeks to maximise $\left|E_\phi(\theta_r, \phi_r)\right|^2$, rather than the total vector-field magnitude. This target-polarisation objective is retained in both room-scale numerical realisations.

Within each realisation, the room geometry, source, target region, propagation assumptions, retained incident field, target polarisation, and normalisation reference are fixed; only the RIS phase-design rule is changed. Two independent numerical realisations are considered. The first uses incident fields generated by the deterministic RT algorithm developed in this thesis, whereas the second uses incident fields generated independently with Sionna. For each realisation, the results are presented in the same order: the phase profiles, the polarisation-resolved background fields, the ϕ- and θ-polarised RIS-only fields, and the polarisation-resolved reradiation patterns. Because the two RT implementations retain different path sets and produce different complex incident fields, their results are evaluated separately and are not combined or interpreted as a direct comparison of absolute field levels.

The first realisation uses the RT algorithm developed in this thesis. Its incident paths are transformed into the local RIS coordinate system and are independent of the three paths used in the CST benchmark in Table 5.2. Table 5.4 lists the four retained components, including their local directions, magnitudes, phases, and complex ϕ- and θ-polarised electric-field components.

Table 5.4 Incident paths generated by the RT algorithm developed in this thesis for the first evaluation in the PEC T-shaped room.

Index	θ **(Incident)**	ϕ_{local} **(Azimuth)**	ψ_{local} **(Elevation)**	$\lvert E \rvert$	E_ϕ	E_θ
1	27.06°	-21.92°	-62.94°	6.169×10^{-4}	$2.434\times10^{-4}\angle-3.20^\circ$	$5.668\times10^{-4}\angle-3.20^\circ$
2	63.51°	-11.95°	-26.49°	8.248×10^{-4}	$5.529\times10^{-4}\angle-78.73^\circ$	$6.120\times10^{-4}\angle-78.73^\circ$
3	52.23°	-14.89°	-37.77°	8.556×10^{-4}	$5.305\times10^{-4}\angle-27.88^\circ$	$6.713\times10^{-4}\angle-27.88^\circ$
4	68.42°	-9.47°	-21.58°	6.945×10^{-4}	$4.750\times10^{-4}\angle121.7^\circ$	$5.067\times10^{-4}\angle121.7^\circ$

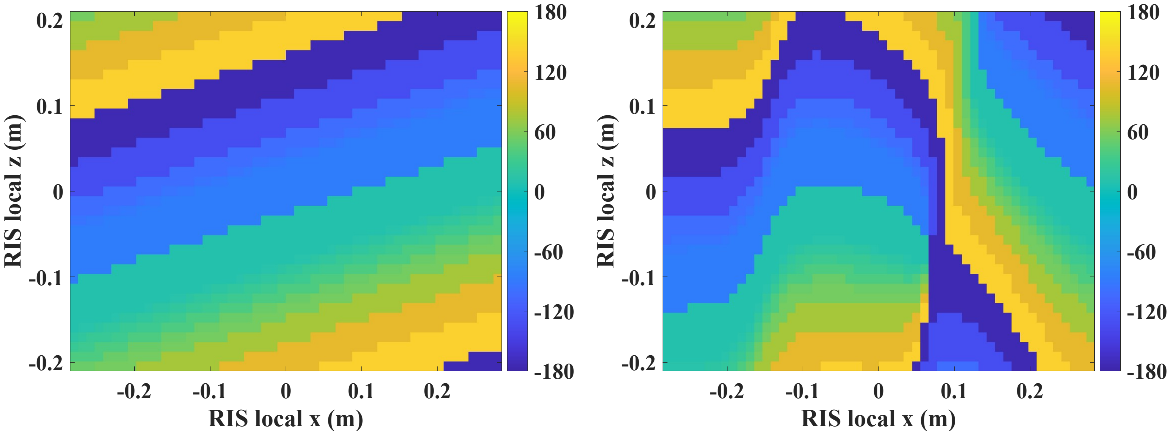

(a) Single-path phase distribution. (b) Multipath-aware phase distribution.

Fig. 5.15 RIS phase distributions synthesised from the incident fields predicted by the RT algorithm developed in this thesis.

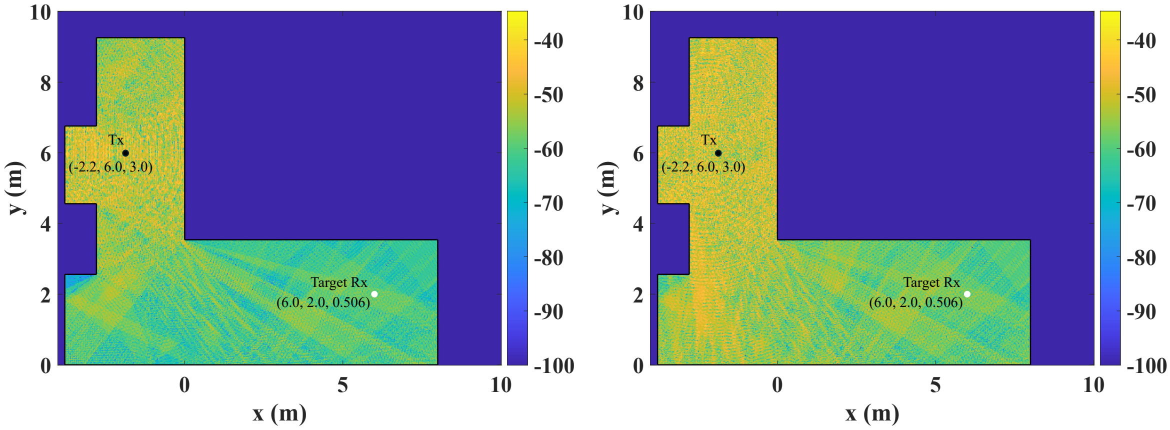

(a) ϕ-polarised background field. (b) θ-polarised background field.

Fig. 5.16 Polarisation-resolved background field distributions predicted by the RT algorithm developed in this thesis for the PEC T-shaped room at $P_{\text{tx}} = -15$ dBW.

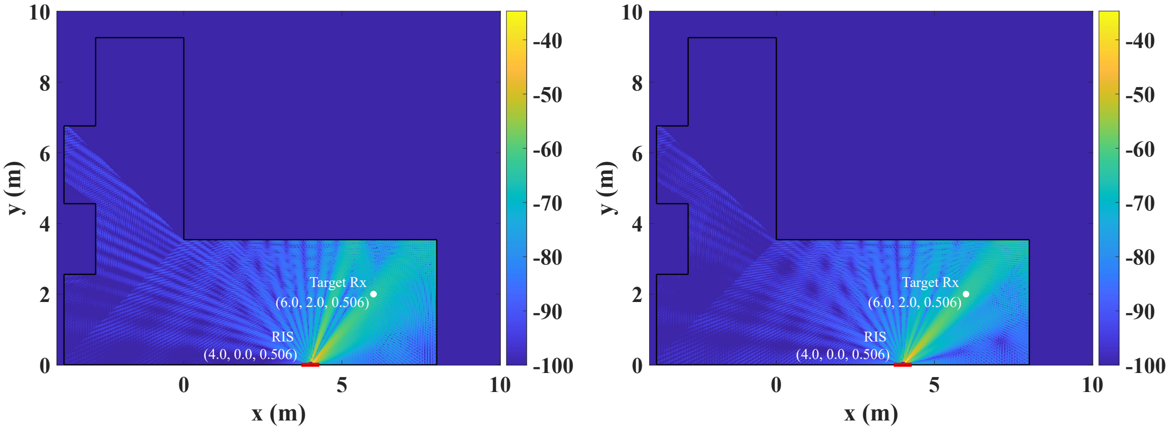

(a) ϕ-polarised RIS-only field for the single-path phase profile.

(b) ϕ-polarised RIS-only field for the multipath-aware phase profile.

Fig. 5.17 ϕ-polarised RIS-only field distributions predicted by the RT algorithm developed in this thesis under multipath illumination at $P_{\text{tx}} = -15$ dBW.

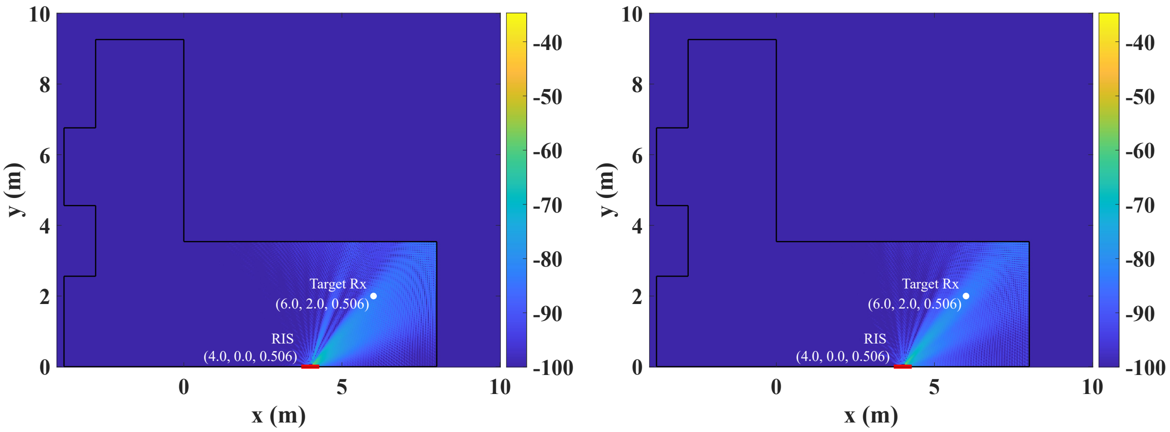

(a) θ-polarised RIS-only field for the single-path phase profile.

(b) θ-polarised RIS-only field for the multipath-aware phase profile.

Fig. 5.18 θ-polarised RIS-only field distributions predicted by the RT algorithm developed in this thesis under multipath illumination at $P_{\text{tx}} = -15$ dBW.

Fig. 5.15 presents the single-path and multipath-aware phase profiles. The single-path profile follows the phase progression associated with the retained component selected using the normal incident-power criterion. In contrast, the multipath-aware profile is derived from the coherent aggregate incident field and compensates its spatial phase so that the controllable ϕ-polarised contributions combine coherently in the prescribed target direction.

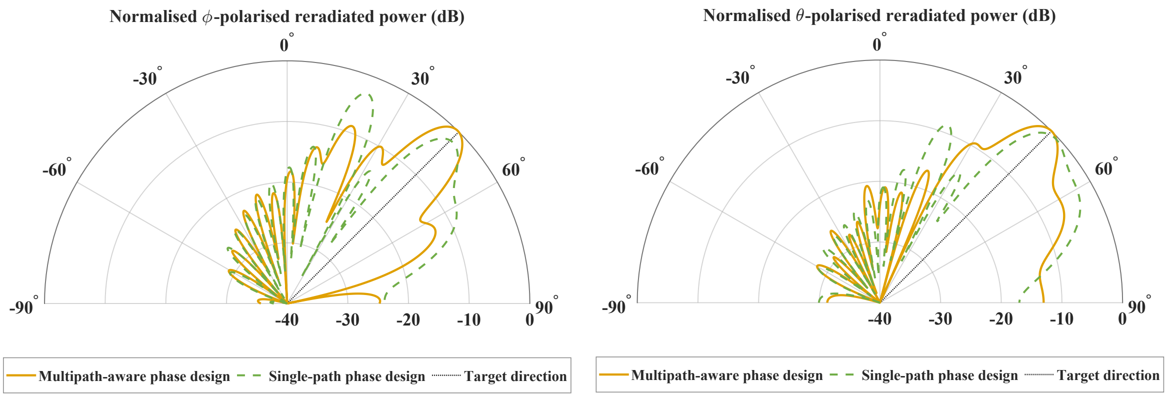

(a) Normalised ϕ-polarised reradiated power. (b) Normalised θ-polarised reradiated power.

Fig. 5.19 Normalised polarisation-resolved RIS reradiation patterns predicted by the RT algorithm developed in this thesis.

Fig. 5.16 establishes the fixed ϕ- and θ-polarised background fields before RIS reradiation is added, thereby preventing room-induced field maxima from being attributed to the RIS. Figs. 5.17 and 5.18 then compare the corresponding ϕ- and θ-polarised RIS-only fields under the same complete four-path illumination. The differences between each pair therefore isolate the effect of the phase-design rule. The ϕ-polarised maps represent the primary designed response, whereas the θ-polarised maps document the accompanying polarisation-resolved response. Finally, Fig. 5.19 compares the normalised angular responses of the two phase profiles for both polarisations. The common target-direction marker permits their main-lobe locations to be assessed against the prescribed direction.

The corresponding normalised RIS-only target-direction reradiation gain comparison is quantified in Table 5.5. Within each polarisation, the multipath-aware result is used as the 0 dB reference. Relative to this reference, the single-path profile is lower by 1.978 dB for the ϕ-polarised component and by 0.690 dB for the θ-polarised component. Equivalently, the multipath-aware design provides target-direction reradiation gains of 1.978 and 0.690 dB, respectively. Because both profiles are evaluated under the same four-path illumination, these values quantify the within-data-set effect of the phase redesign and must not be interpreted as absolute link gains.

Table 5.5 Normalised RIS-only target-direction reradiation gain comparison obtained using the RT algorithm developed in this thesis.

Scenario	**ϕ-polarised gain**	**θ-polarised gain**
Single-path phase under multipath illumination	-1.978 dB	-0.690 dB
Multipath-aware phase under multipath illumination	0.000 dB	0.000 dB
Improvement	$+1.978$ dB	$+0.690$ dB

The second realisation uses an independent incident field generated with Sionna. Table 5.6 lists the fifteen retained components. Their amplitudes and phases differ from those of the four-path data set in Table 5.4. The Sionna results therefore constitute a separate numerical realisation rather than an additional excitation combined with the first data set, and no field quantities are combined across the two realisations.

Table 5.6 Incident paths generated in the Sionna-based evaluation of the PEC T-shaped room.

Index	**θ (Incident)**	**ϕ_{local} (Azimuth)**	**ψ_{local} (Elevation)**	$\lvert E\rvert$	E_ϕ	E_θ
1	52.23°	−14.89°	−37.77°	7.853×10^{-4}	$6.569\times10^{-4}\angle-124.27°$	$4.303\times10^{-4}\angle-124.27°$
2	63.51°	−11.95°	−26.49°	7.850×10^{-4}	$6.069\times10^{-4}\angle-22.55°$	$4.979\times10^{-4}\angle-22.55°$
3	68.42°	−9.46°	−21.58°	6.726×10^{-4}	$5.046\times10^{-4}\angle29.84°$	$4.447\times10^{-4}\angle29.84°$
4	63.63°	−9.46°	−26.37°	6.331×10^{-4}	$4.861\times10^{-4}\angle131.30°$	$4.055\times10^{-4}\angle131.30°$
5	27.06°	−21.91°	−62.94°	5.317×10^{-4}	$5.271\times10^{-4}\angle-173.63°$	$6.968\times10^{-5}\angle-173.63°$
6	46.95°	−10.26°	−43.05°	5.039×10^{-4}	$4.284\times10^{-4}\angle102.47°$	$2.653\times10^{-4}\angle102.47°$
7	75.44°	−173.80°	−14.56°	4.785×10^{-4}	$3.475\times10^{-4}\angle-28.65°$	$3.289\times10^{-4}\angle151.35°$
8	56.73°	−172.81°	−33.27°	4.388×10^{-4}	$3.471\times10^{-4}\angle-135.80°$	$2.685\times10^{-4}\angle44.20°$
9	50.26°	−171.83°	−39.74°	4.383×10^{-4}	$3.616\times10^{-4}\angle145.92°$	$2.477\times10^{-4}\angle-34.08°$
10	29.04°	−14.89°	−60.96°	4.176×10^{-4}	$4.032\times10^{-4}\angle27.56°$	$1.088\times10^{-4}\angle27.56°$
11	31.56°	−11.95°	−58.44°	3.764×10^{-4}	$3.548\times10^{-4}\angle-20.48°$	$1.258\times10^{-4}\angle-20.48°$
12	21.13°	−18.67°	−68.87°	3.664×10^{-4}	$3.656\times10^{-4}\angle63.66°$	$2.385\times10^{-5}\angle63.66°$
13	18.34°	−21.91°	−71.66°	3.647×10^{-4}	$3.644\times10^{-4}\angle15.34°$	$1.555\times10^{-5}\angle-164.66°$
14	35.57°	−170.04°	−54.43°	3.632×10^{-4}	$3.315\times10^{-4}\angle-128.21°$	$1.484\times10^{-4}\angle51.79°$
15	14.06°	−21.91°	−75.94°	2.836×10^{-4}	$2.813\times10^{-4}\angle142.23°$	$3.610\times10^{-5}\angle-37.77°$

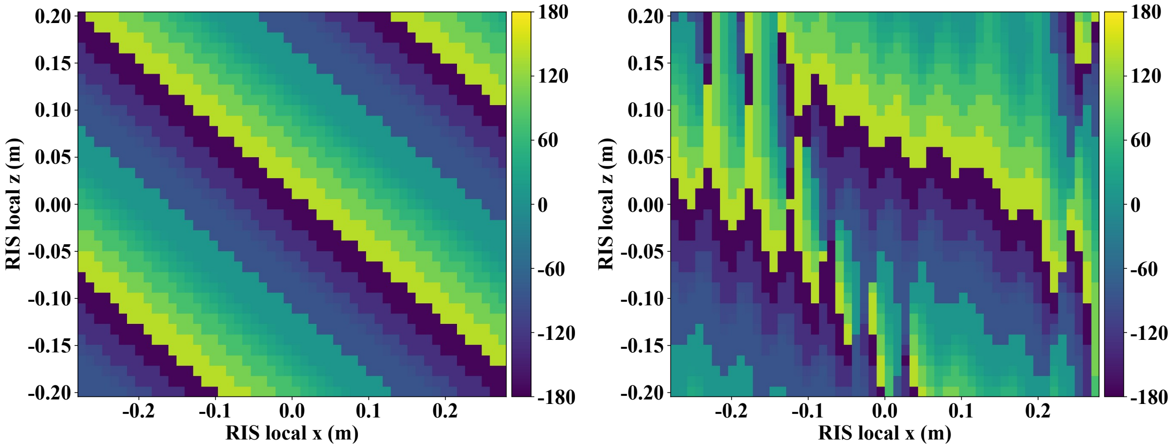

(a) Single-path phase distribution. (b) Multipath-aware phase distribution.

Fig. 5.20 RIS phase distributions synthesised from the Sionna-derived incident fields.

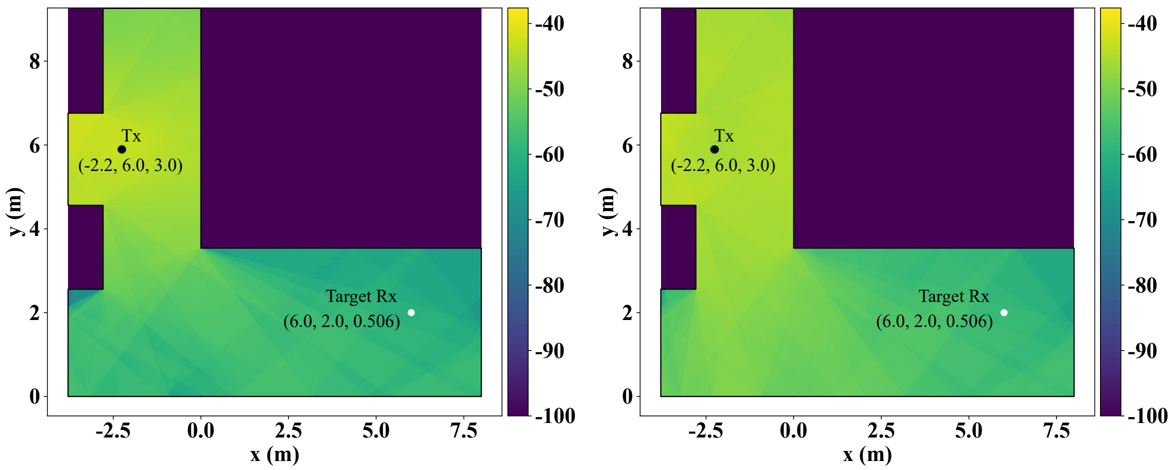

(a) ϕ-polarised background field. (b) θ-polarised background field.

Fig. 5.21 Polarisation-resolved background field distributions predicted using Sionna for the PEC T-shaped room at $P_{\text{tx}} = -15$ dBW.

Fig. 5.20 presents the single-path and multipath-aware phase profiles using the same left-to-right convention as Fig. 5.15. Their regular and spatially varying structures reflect synthesis from a single reference component and from the coherent aggregate illumination, respectively. Fig. 5.21 then establishes the fixed Sionna-derived background fields for the ϕ- and θ-polarised components.

Figs. 5.22 and 5.23 compare the ϕ- and θ-polarised RIS-only fields, respectively, for the two phase profiles. Both profiles are evaluated under the same complete Sionna-generated

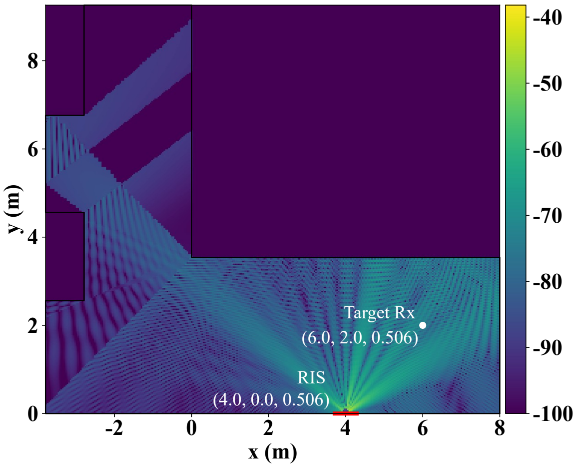

(a) ϕ-polarised RIS-only field for the single-path phase profile.

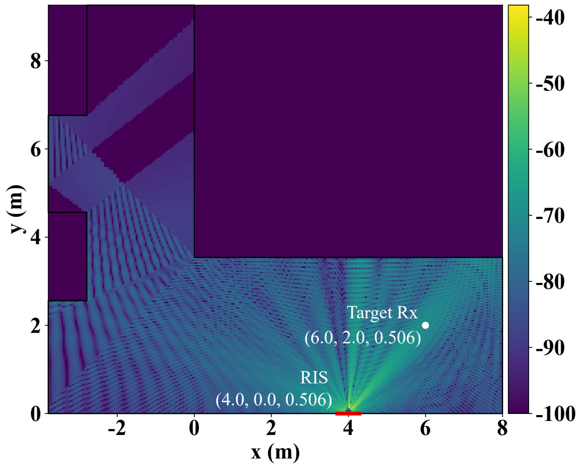

(b) ϕ-polarised RIS-only field for the multipath-aware phase profile.

Fig. 5.22 Sionna-based ϕ-polarised RIS-only field distributions under multipath illumination at $P_{\text{tx}} = -15$ dBW.

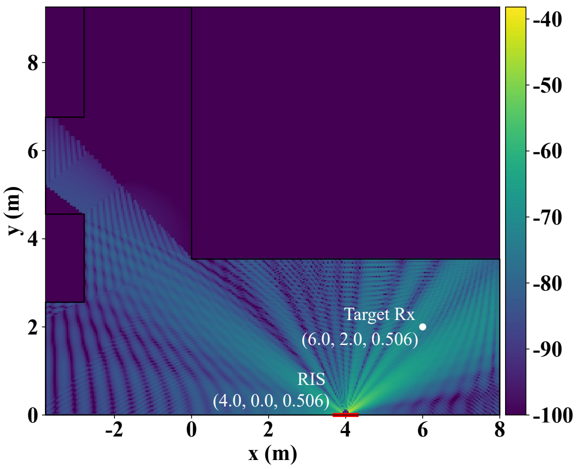

(a) θ-polarised RIS-only field for the single-path phase profile.

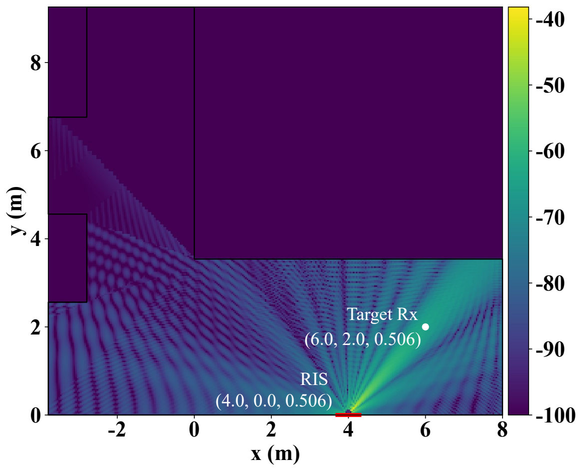

(b) θ-polarised RIS-only field for the multipath-aware phase profile.

Fig. 5.23 Sionna-based θ-polarised RIS-only field distributions under multipath illumination at $P_{\text{tx}} = -15$ dBW.

incident field; hence, the differences within each figure arise from the phase-design rule rather than from a change in illumination. The ϕ-polarised maps represent the primary designed response, while the θ-polarised maps report the accompanying polarisation-resolved response. Finally, Fig. 5.24 compares the corresponding polarisation-resolved angular responses against the common prescribed target direction.

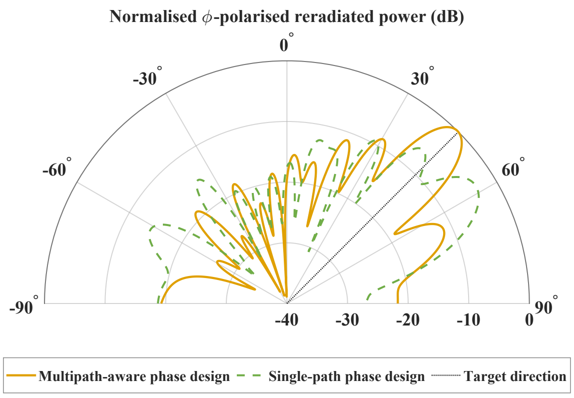

(a) Normalised ϕ-polarised reradiated power.

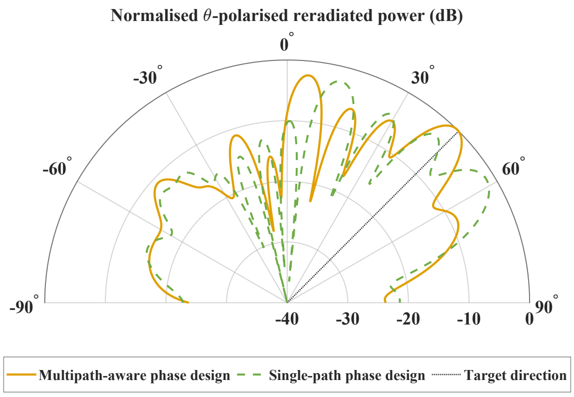

(b) Normalised θ-polarised reradiated power.

Fig. 5.24 Normalised polarisation-resolved RIS reradiation patterns obtained using Sionna-derived incident fields.

Although the Sionna field maps and the maps obtained using the RT algorithm developed in this thesis both show RIS-only contributions, they are based on independent incident-field realisations and different retained path sets. They therefore support separate within-data-set comparisons and must not be used for a direct comparison of absolute field levels between the two RT implementations.

The corresponding normalised RIS-only target-direction reradiation gain comparison for the Sionna realisation is quantified in Table 5.7. Within each polarisation, the multipath-aware result is used as the 0 dB reference. Relative to this reference, the single-path profile is lower by 8.420 dB for the ϕ-polarised component and by 5.948 dB for the θ-polarised component. Equivalently, the multipath-aware design provides target-direction reradiation gains of 8.420 and 5.948 dB, respectively. Because both profiles are evaluated under the same fifteen-path Sionna illumination, these values quantify the within-data-set effect of the phase redesign and must not be interpreted as absolute link gains.

Table 5.7 Normalised Sionna-based RIS-only target-direction reradiation gain comparison.

Scenario	**ϕ-polarised gain**	**θ-polarised gain**
Single-path phase under multipath illumination	-8.420 dB	-5.948 dB
Multipath-aware phase under multipath illumination	0.000 dB	0.000 dB
Improvement	$+8.420$ dB	$+5.948$ dB

The PEC room study extends the phase-synthesis framework from the preceding model-level full-wave benchmark to a room-scale propagation problem; it does not constitute an additional full-wave validation. The two stages employ the same coherent target-field synthesis principle but use different target polarisations: the CST benchmark is designed for the θ-polarised reradiated-field component, whereas the PEC room study is designed for the ϕ-polarised component. Within each room-scale realisation, the controlled comparison isolates the effect of replacing the single-path phase profile with the multipath-aware profile.

For both the realisation generated using the RT algorithm developed in this thesis and the independent Sionna realisation, the multipath-aware profile produces the stronger normalised ϕ-polarised RIS-only reradiation response in the prescribed target direction. Changes in the θ-polarised component are reported as polarisation-resolved consequences of the phase redesign rather than as the primary optimisation objective. Tables 5.5 and 5.7 both quantify normalised RIS-only target-direction reradiation gains. Their numerical values must nevertheless not be cross-compared because the two realisations retain different path sets and complex incident fields and use independent within-data-set normalisation references. In addition, the lossless PEC enclosure excludes material absorption and transmission. The results consequently support controlled comparisons of the two phase-design rules within each data set, rather than a universal performance prediction for arbitrary indoor materials, geometries, or deployments.

5.6 Summary

This chapter presented and evaluated a physically consistent RIS macromodelling framework for indoor RT. The formulation connects deterministic RT inputs and a coherent multipath plane-wave expansion to a load-dependent multiport unit-cell response and finite-aperture reradiation based on equivalent Huygens sources and Floquet–Bloch modal information. It also provides the field quantities required for single-path and multipath-aware phase synthesis while preserving the phase, direction, and polarisation of each retained incident component. The resulting framework therefore provides an electromagnetically interpretable RIS processing layer without requiring a full-wave solution of the complete indoor environment.

The component- and room-level evaluations support complementary aspects of the framework. Over 3.2–3.8 GHz, the multiport model remained within 2.4 dB in amplitude and 14.8° in phase of the full-wave unit-cell results; at 3.5 GHz, the corresponding deviations were 0.6 dB and 5.4°. Reusing the extracted port-impedance matrix reduced the runtime of the 18-state sweep by 89.26%. In the measured small meeting room, the proposed model achieved an RMSE of 3.66 dB over ten Rx positions, compared with 7.41 dB for the simplified main-beam-only model, with 90% and 40% of their respective predictions lying within ±5 dB of the measurements. The proposed model also reproduced the measured reduction in spatial received-power dispersion. These results show that retaining the synthesised angular response improves predictive consistency relative to a target-directed main-beam approximation in the tested setting.

The phase-design evaluations further demonstrate the importance of coherent multipath illumination. In the three-path CST benchmark, the multipath-aware design increased the target E_θ component by 2.525 dB analytically and 4.165 dB in CST relative to the strongest-path design, although the total-field magnitude decreased by approximately 0.9 dB. The improvement is therefore polarisation-selective rather than a total-field enhancement. In the two PEC room realisations, the corresponding normalised target-direction gains in the optimised E_ϕ component were 1.978 dB and 8.420 dB within their separate data sets and normalisations. These results support the coherent target-field synthesis mechanism but do not establish a universal link gain. The summary remain limited by the local diagonal response, the continuous profiles not being regenerated after finite-codebook refinement, and measurements in only one room at one frequency. The beyond-diagonal formulation specifies the relevant physical network constraints, but no numerical or experimental gain is claimed for it. Within these limits, the framework provides a traceable route from multipath RT fields and circuit-level unit-cell data to finite-aperture RIS prediction and polarisation-selective phase design.

Chapter 6

Conclusion and Future Work

6.1 Conclusion

This thesis has addressed the problem of connecting EM interactions with materials and engineered surfaces to polarised indoor channel and system predictions without requiring a full-wave solution of an entire room. I have developed a physically consistent modelling framework in which field bases, complex phases, material responses, path transformations, RIS circuit responses, and finite-aperture reradiation are defined compatibly from one stage to the next. The framework is an EM processing layer for deterministic RT rather than a replacement for the geometry and path-search capabilities of an established RT platform. Within this scope, the thesis makes three principal contributions.

1. Chapter 3 establishes a three-dimensional polarisation-aware RT formulation for frequency-dispersive multilayer materials. Consistent local TE and TM bases, complex multilayer reflection and transmission coefficients, and coherent field accumulation are retained along each modelled path. The resulting simulations show that XPR varies with Rx position and propagation mechanism; consequently, neither a scalar penetration loss nor a spatially constant XPR can reproduce the modelled polarisation transformation in the investigated environment. This contribution provides the field-level foundation for the subsequent system and RIS studies, although its building-

scale XPR predictions have not yet been validated through a dedicated polarimetric measurement campaign.

2. Chapter 4 connects the polarisation-aware channel model to PolarSK performance and to BWP optimisation. The results identify high-SNR ABEP floors produced by coherent multipath interference and material-dependent polarisation imbalance in the investigated NLOS cases. Coordinatewise searches over permittivity, conductivity, and layer thickness reduce the stated ABEP objective for the prescribed room, antenna configurations, Rx grid, and candidate ranges. These results demonstrate a mechanism by which passive material properties can influence a communication metric, but they do not establish a global optimum, a building-independent gain, or a directly manufacturable wall design.

3. Chapter 5 presents the principal and most experimentally mature contribution: a circuit-informed RIS macromodel integrated with three-dimensional RT. The model links coherent multipath illumination, a load-dependent multiport unit-cell response, and finite-aperture reradiation to polarisation-selective phase synthesis. The multiport representation agrees with the evaluated unit-cell full-wave data within 0.6 dB in amplitude and 5.4° in phase at 3.5 GHz, while reducing the runtime of the 18-state sweep by 89.26%. In the measured small meeting room, the configured proposed model attains an RMSE of 3.66 dB, compared with 7.41 dB for a simplified main-beam-only RIS model, and reproduces the measured contraction in spatial received-power dispersion. The CST comparison and two controlled PEC room realisations further support the target-field synthesis mechanism under their stated normalisations. They also show that a gain in the optimised polarisation component need not imply a gain in total-field magnitude. The beyond-diagonal extension is formulated subject to physical network constraints, but its numerical and experimental evaluation remains future work.

These conclusions must be interpreted in relation to five limitations. First, experimental support is uneven across the thesis: the RT formulation in Chapter 3 and the PolarSK and BWP results in Chapter 4 are supported primarily by analytical checks and simulations, and no end-to-end experimental validation of the predicted PolarSK performance has been performed. The Chapter 5 evidence is stronger but remains confined to controlled full-wave cases and measurements at ten accessible Rx positions in one room at one frequency. Second, the deliberately simplified geometries and retained path sets do not exhaustively represent diffraction, diffuse and rough-surface scattering, detailed furniture, human blockage, motion, or higher-order interactions. Third, material parameters are treated as known model inputs; construction variability, parameter uncertainty, and frequency-dependent measurement error are not propagated to the reported channel and ABEP results. Fourth, the BWP search does not impose the complete manufacturability, cost, fire-safety, thermal, mechanical, environmental, and architectural constraints required in a real building. Fifth, the reported RIS phase-design results retain local scalar-control approximations and do not fully resolve angle-dependent polarisation conversion, finite-array mutual coupling, hardware tolerances, or a realised beyond-diagonal network. The numerical improvements are therefore conditional on the specified frequencies, geometries, antennas, materials, path sets, and RIS models.

Subject to these limitations, the thesis establishes a traceable route from material and circuit descriptions to polarised paths, coherent channel quantities, communication performance, and RIS-assisted reradiation. Its contribution is not a universal accuracy guarantee or a substitute for full-wave and measurement-based validation. Rather, it is a computationally tractable and physically interpretable framework in which the assumptions responsible for each prediction can be identified, tested, and progressively refined.

6.2 Future Work

The limitations identified above define a prioritised programme for extending and validating the framework.

1. **End-to-end wideband polarimetric validation:** The highest priority is a measurement campaign that evaluates the complete chain from multilayer material characterisation to the dual-polarised channel matrix and PolarSK error performance. Measurements should cover multiple rooms, wall constructions, frequencies, antenna orientations, and spatially dense Rx grids. Controlled material samples would permit independent estimation of complex constitutive parameters, while a PolarSK hardware link would test the predicted ABEP trends and high-SNR floors directly. Reporting position-resolved errors, uncertainty intervals, XPR distributions, and repeatability would distinguish model-form error from measurement and material uncertainty.

2. **Wideband and dynamic propagation modelling with additional interaction mechanisms:** The present frequency-domain treatment should be extended with causal wideband material and RIS responses, path delays, Doppler shifts, and time-varying geometry. Human blockage and body scattering should be calibrated from measurements, and the path engine should incorporate validated diffraction, diffuse and rough-surface scattering, furniture interactions, and higher-order paths where they materially affect the selected metric. Model-order control and acceleration strategies will be required so that each added mechanism delivers a quantified accuracy benefit commensurate with its computational cost.

3. **Robust joint optimisation of passive materials and programmable RISs:** BWP and RIS control should be formulated as a joint, multiobjective design problem across positions, frequencies, polarisations, and user states. Passive materials can provide persistent coarse spatial shaping, while programmable RISs can adapt the residual field to changing users and traffic. Suitable objectives include coverage, ABEP, capacity, interference, sidelobe level, and energy consumption. The feasible set must include measured material uncertainty, discrete hardware states, construction tolerances, manufacturability, thickness, cost, safety, thermal and mechanical limits, and architectural constraints. Robust or stochastic optimisation would then replace gains obtained

for one nominal room by performance bounds over explicitly defined deployment uncertainties.

4. **Coupling-aware and beyond-diagonal RIS validation:** Quantitative polarised-field prediction requires an angle- and polarisation-dependent reflection dyadic, calibrated load-state data, finite-array mutual coupling, edge diffraction, loss, and hardware tolerances. The finite-codebook optimisation formulated in Chapter 5 should be applied to regenerated field results and compared against continuous-profile upper bounds. For a beyond-diagonal RIS, a specific interconnection topology and physically realisable impedance or admittance network should be designed under passivity, reciprocity, power-balance, stability, bandwidth, and component constraints. Full-wave simulations followed by hardware measurements are then required before any gain over a local diagonal RIS can be claimed. This programme can subsequently be extended to wideband, multi-RIS, and multiuser operation.

5. **Standardisation and industrial integration:** Reproducible benchmark rooms, open material and unit-cell response databases, and common reporting metrics are needed to compare polarisation-aware and RIS-assisted RT methods. A benchmark should specify geometry, material uncertainty, antennas, retained interactions, field normalisation, computational cost, and measurement uncertainty rather than reporting received-power error alone. The EM processing layer developed in this thesis could then be exposed through a modular interface to commercial and open RT platforms, enabling industrial users to exchange calibrated material and RIS models without replacing their established geometry and path-search workflows. Standardised measurement protocols and validation thresholds would support eventual use in building design, network planning, and deployment assessment.

References

[1] W. Saad *et al.*, “A vision of 6G wireless systems: applications, trends, technologies, and open research problems,” *IEEE Network*, vol. 34, no. 3, pp. 134–142, May/Jun. 2020.

[2] Y. J. Guo *et al.*, “Quasi-optical multi-beam antenna technologies for B5G and 6G mmWave and THz networks: A review,” *IEEE Open J. Antennas Propag.*, vol. 2, pp. 807–830, Jun. 2021.

[3] W. Jiang *et al.*, “The road towards 6G: A comprehensive survey,” *IEEE Open J. Commun. Soc.*, vol. 2, pp. 334–366, Feb. 2021.

[4] M. Z. Chowdhury *et al.*, “6G wireless communication systems: Applications, requirements, technologies, challenges, and research directions,” *IEEE Open J. Commun. Soc.*, vol. 1, pp. 957–975, Jul. 2020.

[5] C.-X. Wang *et al.*, “On the road to 6G: visions, requirements, key technologies, and testbeds,” *IEEE Commun. Surveys Tuts.*, vol. 25, no. 2, pp. 905–974, 2nd Quart., 2023.

[6] A. Goldsmith, *Wireless Communications*. Cambridge, U.K.: Cambridge Univ. Press, 2005.

[7] H. Obeidat *et al.*, “Indoor environment propagation review,” *Comput. Sci. Rev.*, vol. 37, Aug. 2020, Art. no. 100272.

[8] Y. Zhang *et al.*, “How friendly are building materials as reflectors to indoor LOS MIMO communications?” *IEEE Internet Things J.*, vol. 7, no. 9, pp. 9116–9127, Sep. 2020.

[9] Cisco, "Cisco vision: 5G-thriving indoors," Feb. 2017. [Online]. Available: https://www.cisco.com/c/dam/en/us/solutions/collateral/service-provider/ultra-services-platform/5g-ran-indoor.pdf

[10] S. Zvanovec *et al.*, "Wireless LAN networks design: Site survey or propagation modeling?" *Radioengineering*, vol. 12, no. 4, pp. 42–49, Dec. 2003.

[11] A. A. M. Saleh *et al.*, "A statistical model for indoor multipath propagation," *IEEE J. Sel. Areas Commun.*, vol. SAC-5, no. 2, pp. 128–137, Feb. 1987.

[12] Q. H. Spencer *et al.*, "Modeling the statistical time and angle of arrival characteristics of an indoor multipath channel," *IEEE J. Sel. Areas Commun.*, vol. 18, no. 3, pp. 347–360, Mar. 2000.

[13] C. Guo *et al.*, "Advances on exploiting polarization in wireless communications: Channels, technologies, and applications," *IEEE Commun. Surveys Tuts.*, vol. 19, no. 1, pp. 125–166, 1st Quart., 2017.

[14] Y. Liu *et al.*, "Reconfigurable Intelligent Surfaces: Principles and Opportunities," *IEEE Commun. Surveys Tuts.*, vol. 23, no. 3, pp. 1546–1577, 3rd Quart., 2021.

[15] A. Diaz-Rubio *et al.*, "Macroscopic modeling of anomalously reflecting metasurfaces: Angular response and far-field scattering," *IEEE Trans. Antennas Propag.*, vol. 69, no. 10, pp. 6560–6571, Oct. 2021.

[16] V. Degli-Esposti *et al.*, "Reradiation and scattering from a reconfigurable intelligent surface: A general macroscopic model," *IEEE Trans. Antennas Propag.*, vol. 70, no. 10, pp. 8691–8706, Oct. 2022.

[17] F. H. Danufane *et al.*, "On the path-loss of reconfigurable intelligent surfaces: An approach based on Green's theorem applied to vector fields," *IEEE Trans. Commun.*, vol. 69, no. 8, pp. 5573–5592, Aug. 2021.

[18] M. Di Renzo *et al.*, “Smart radio environments empowered by reconfigurable intelligent surfaces: How it works, state of research, and the road ahead,” *IEEE J. Sel. Areas Commun.*, vol. 38, no. 11, pp. 2450–2525, Nov. 2020.

[19] C. Huang *et al.*, “Reconfigurable intelligent surfaces for energy efficiency in wireless communication,” *IEEE Trans. Wireless Commun.*, vol. 18, no. 8, pp. 4157–4170, Aug. 2019.

[20] Q. Wu *et al.*, “Intelligent reflecting surface enhanced wireless network via joint active and passive beamforming,” *IEEE Trans. Wireless Commun.*, vol. 18, no. 11, pp. 5394–5409, Nov. 2019.

[21] B. Sihlbom *et al.*, “Reconfigurable intelligent surfaces: Performance assessment through a system-level simulator,” *IEEE Wireless Commun.*, vol. 30, no. 4, pp. 98–106, Aug. 2023.

[22] J. Poutanen *et al.*, “Angular and shadowing characteristics of dense multipath components in indoor radio channels,” *IEEE Trans. Antennas Propag.*, vol. 59, no. 1, pp. 1–9, Jan. 2011.

[23] K. Haneda *et al.*, “A statistical spatio-temporal radio channel model for large indoor environments at 60 and 70 GHz,” *IEEE Trans. Antennas Propag.*, vol. 63, no. 6, pp. 2694–2704, Jun. 2015.

[24] J. Tan *et al.*, “A full 3-D GPU-based beam-tracing method for complex indoor environments propagation modeling,” *IEEE Trans. Antennas Propag.*, vol. 63, no. 6, pp. 2705–2718, Jun. 2015.

[25] A. Schiavoni *et al.*, “Ray tracing simulations at millimeter waves in different indoor and outdoor scenarios,” in *Proc. Eur. Conf. Antennas Propag. (EuCAP)*, Davos, Switzerland, Apr. 2016, pp. 1–5.

[26] S. Loredo *et al.*, “Indoor MIMO channel modeling by rigorous GO/UTD-based ray tracing,” *IEEE Trans. Veh. Technol.*, vol. 57, no. 2, pp. 680–692, Mar. 2008.

[27] G. R. Maccartney *et al.*, "Indoor office wideband millimeter-wave propagation measurements and channel models at 28 and 73 GHz for ultra-dense 5G wireless networks," *IEEE Access*, vol. 3, pp. 2388–2424, Oct. 2015.

[28] Y. Yu *et al.*, "Measurement and empirical modeling of massive MIMO channel matrix in real indoor environment," in *Proc. 8th Int. Conf. Wireless Commun. Signal Process. (WCSP)*, Yangzhou, China, Oct. 2016, pp. 1–5.

[29] X. Wu *et al.*, "60-GHz millimeter-wave channel measurements and modeling for indoor office environments," *IEEE Trans. Antennas Propag.*, vol. 65, no. 4, pp. 1912–1924, Apr. 2017.

[30] L. Zhou *et al.*, "Path loss model based on cluster at 28 GHz in the indoor and outdoor environments," *Sci. China Inf. Sci.*, vol. 60, no. 8, Art. no. 080302, Aug. 2017.

[31] L. Zhang *et al.*, "Multifrequency wireless channel measurements and characterization in large indoor office environments," *IEEE Trans. Antennas Propag.*, vol. 71, no. 6, pp. 5221–5234, Jun. 2023.

[32] D. M. J. Devasirvathan, "Multi-frequency propagation measurements and models in a large metropolitan commercial building for personal communications," in *Proc. IEEE Int. Symp. Pers., Indoor Mobile Radio Commun. (PIMRC)*, London, U.K., Sep. 1991, pp. 98–103.

[33] G. F. Pedersen, *COST 231-Digital Mobile Radio Towards Future Generation Systems*. Brussels, Belgium: European Commission, 1999.

[34] P. Kyösti *et al.*, "WINNER II channel models—Part I: Channel models," IST-4-027756 WINNER II, Deliverable D1.1.2, ver. 1.2, Sep. 2007, updated Feb. 2008.

[35] H. Hashemi, "The indoor radio propagation channel," *Proc. IEEE*, vol. 81, no. 7, pp. 943–968, Jul. 1993.

[36] P. Series, *Propagation Data and Prediction Methods for the Planning of Indoor Radiocommunication Systems and Radio Local Area Networks in the Frequency Range 900 MHz to 100 GHz*, document Rec. ITU-R 1238-7, 2012.

[37] I. Dey *et al.*, "Joint fading and shadowing model for large office indoor WLAN environments," *IEEE Trans. Antennas Propag.*, vol. 62, no. 4, pp. 2209–2222, Apr. 2014.

[38] N. R. Diaz *et al.*, "Wideband channel characterization for wireless communications inside a short haul aircraft," in *Proc. IEEE 59th Veh. Technol. Conf. (VTC Spring)*, Milan, Italy, May 2004, pp. 223–228.

[39] Y. Wang *et al.*, "A hybrid technique based on combining ray tracing and FDTD methods for site-specific modeling of indoor radio wave propagation," *IEEE Trans. Antennas Propag.*, vol. 48, no. 5, pp. 743–754, May. 2000.

[40] K. L. Virga *et al.*, "Efficient wide-band evaluation of mobile communications antennas using $[Z]$ or $[Y]$ matrix interpolation with the method of moments.," *IEEE Trans. Antennas Propag.*, vol. 47, no. 1, pp. 65–76, Jan. 1999.

[41] J.Song *et al.*, "Multilevel fast multipole algorithm for electromagnetic scattering by large complex objects.," *IEEE Trans. Antennas Propag.*, vol. 45, no. 10, pp. 1488–1493, Oct. 1997.

[42] K. Ito *et al.*, "Signal path loss simulation of human arm for galvanic coupling intra-body communication using circuit and finite element method models," in *Proc. IEEE 12th Int. Symp. Auton. Decentralized Syst. (ISADS)*, Taichung, Taiwan, Mar. 2015, pp. 230–235.

[43] K. S. Kunz *et al.*, *The Finite Difference Time Domain Method for Electromagnetics*. Boca Raton, FL, USA: CRC Press, 1993.

[44] B. Gschwendtner *et al.*, "Ray tracing vs. ray launching in 3-D microcell modelling," in *Proc. 1st Eur. Pers. Mobile Commun. Conf. (EPMCC)*, Sep. 1995, pp. 74–79.

[45] T. Imai, "A survey of efficient ray-tracing techniques for mobile radio propagation analysis," *IEICE Trans. Commun.*, vol. E100-B, no. 5, pp. 666–679, May. 2017.

[46] M. C. Lawton *et al.*, "The application of a deterministic ray launching algorithm for the prediction of radio channel characteristics in small-cell environments," *IEEE Trans. Veh. Technol.*, vol. 43, pp. 955–969, Nov. 1994.

[47] G. E. Athanasiadou *et al.*, "A ray tracing algorithm for microcellular and indoor propagation modelling," in *Proc. 9th Int. Conf. Antennas Propag. (ICAP)*, Eindhoven, The Netherlands, Apr. 1995, pp. 231–235.

[48] B. S. Lee *et al.*, "Indoor space-time propagation modelling using a ray launching technique," in *Proc. 11th Int. Conf. Antennas Propag. (ICAP)*, Manchester, U.K., Apr. 2001, vol. 1, pp. 279–283.

[49] Y.-K. Yoon *et al.*, "Intelligent ray tracing for the propagaiton prediction," in *Proc. 2012 IEEE Int. Symp. Antennas Propag. (APSURSI)*, Chicago, IL, USA, Jul. 2012, pp. 1–2.

[50] G. de la Roche *et al.*, Eds., *LTE-Advanced and Next Generation Wireless Networks: Channel Modelling and Propagation*. Chichester, U.K.: John Wiley & Sons, 2013.

[51] Z. Lai *et al.*, "Intelligent ray launching algorithm for indoor scenarios," *Radioengineering*, vol. 20, no. 2, pp. 398–408, Jun. 2011.

[52] S. Loredo *et al.*, "Accuracy analysis of GO/UTD radio-channel modeling in indoor scenarios at 1.8 and 2.5 GHz," *IEEE Antennas and Propag. Mag.*, vol. 43, pp. 37–51, Oct. 2001.

[53] G. de la Roche *et al.*, "Combination of geometric and finite difference models for radio wave propagation in outdoor to indoor scenarios," in *Proc. Eur. Conf. Antennas Propag. (EuCAP)*, Barcelona, Spain, Apr. 2010, pp. 1–5.

[54] T. Imai *et al.*, "Proposal on novel ray-launching method with quasi-uniform spatial resolution, and its effect on calculation amount reduction," *IEICE Tech. Rep.*, vol. 115, no. 450, AP2015-203, pp. 71–76, Feb. 2016.

[55] G. E. Athanasiadou *et al.*, “A novel 3-D indoor ray-tracing propagation model: The path generator and evaluation of narrow-band and wide-band predictions,” *IEEE Trans. Veh. Technol.*, vol. 49, no. 4, pp. 1152–1168, Jul. 2000.

[56] F. Mani *et al.*, “Parameterization of a polarimetric diffuse scattering model in indoor environments,” *IEEE Trans. Antennas Propag.*, vol. 62, no. 8, pp. 4361–4364, Aug. 2014.

[57] F. Mani *et al.*, “A ray based indoor propagation model including depolarizing penetration,” in *Proc. 3rd Eur. Conf. Antennas Propag. (EuCAP)*, Berlin, Germany, Mar. 2009, pp. 3835–3838.

[58] F. Mani *et al.*, “Accuracy of depolarization and delay spread predictions using advanced ray-based modeling in indoor scenarios,” *EURASIP J. Wireless Commun. Netw.*, vol. 2011, Art. no. 11, Jun. 2011.

[59] D. Wei *et al.*, “An energy efficient polarization modulation scheme for nonlinear power amplifier,” in *Proc. 2012 IEEE GLOBECOM Workshops (GC Wkshps)*, Anaheim, CA, USA, Dec. 2012, pp. 69–74.

[60] D. Wei *et al.*, “A power amplifier energy efficient polarization modulation scheme based on the optimal pre-compensation,” *IEEE Commun. Lett.*, vol. 17, no. 3, pp. 513–516, Mar. 2013.

[61] C. Oestges *et al.*, “Dual-polarized wireless communications: From propagation models to system performance evaluation,” *IEEE Trans. Wireless Commun.*, vol. 7, no. 10, pp. 4019–4031, Oct. 2008.

[62] C. Oestges *et al.*, “Propagation modeling of MIMO multipolarized fixed wireless channels,” *IEEE Trans. Veh. Technol.*, vol. 53, no. 3, pp. 644–654, May. 2004.

[63] M. Shafi *et al.*, “Polarized MIMO channels in 3-D: Models, measurements and mutual information,” *IEEE J. Sel. Areas Commun.*, vol. 24, no. 3, pp. 514–527, Mar. 2006.

[64] S.-C. Kwon *et al.*, "Geometrical theory of channel depolarization," *IEEE Trans. Veh. Technol.*, vol. 60, no. 8, pp. 3542–3556, Oct. 2011.

[65] X. Wu *et al.*, "Theoretical polarized channel model and analysis of XPD and polarization correlation under narrowband macrocell environment," in *Proc. 15th Int. Symp. Wireless Pers. Multimedia Commun. (WPMC)*, Taipei, Taiwan, Sep. 2012, pp. 468–472.

[66] F. Quitin *et al.*, "Analytical model and experimental validation of cross polar ratio in polarized MIMO channels," in *Proc. IEEE PIMRC*, Cannes, France, Sep. 2008, pp. 1–5.

[67] M. Li *et al.*, "Correlation and capacity evaluation for dual polarized MIMO system based on an extended 3-D geometry-based stochastic channel model," in *Proc. 8th Int. Conf. Commun. Netw. China (CHINACOM)*, Guilin, China, Aug. 2013, pp. 235–240.

[68] S. K. Yong *et al.*, "Three-dimensional spatial fading correlation models for compact MIMO receivers," *IEEE Trans. Wireless Commun.*, vol. 4, no. 6, pp. 2856–2869, Nov. 2005.

[69] T. Svantesson *et al.*, "Analysis of electromagnetic field polarizations in multiantenna systems," *IEEE Trans. Wireless Commun.*, vol. 3, no. 2, pp. 641–646, Mar. 2004.

[70] F. Quitin *et al.*, "Multipolarized MIMO channel characteristics: Analytical study and experimental results," *IEEE Trans. Antennas Propag.*, vol. 57, no. 9, pp. 2739–2745, Sep. 2009.

[71] M. Di Renzo *et al.*, "Smart radio environments empowered by reconfigurable intelligent surfaces: How it works, state of research, and the road ahead," *IEEE J. Sel. Areas Commun.*, vol. 38, no. 11, pp. 2450–2525, Nov. 2020.

[72] V. S. Asadchy *et al.*, "Perfect control of reflection and refraction using spatially dispersive metasurfaces," *Phys. Rev. B*, vol. 94, no. 7, Art. no. 075142, Aug. 2016.

[73] N. M. Estakhri *et al.*, "Wave-front transformation with gradient metasurfaces," *Phys. Rev. X*, vol. 6, no. 4, Art. no. 041008, Oct. 2016.

[74] D. He *et al.*, “The design and applications of high-performance ray-tracing simulation platform for 5G and beyond wireless communications: A tutorial,” *IEEE Commun. Surveys Tuts.*, vol. 21, no. 1, pp. 10–27, 1st Quart., 2019.

[75] J. Hoydis *et al.*, “Sionna RT: Differentiable ray tracing for radio propagation modeling,” in *Proc. 2023 IEEE Globecom Workshops (GC Wkshps)*, Kuala Lumpur, Malaysia, pp. 317–321, Dec. 2023.

[76] F. Aït Aoudia *et al.*, “Sionna RT: Technical report,” arXiv:2504.21719v2, Nov. 2025.

[77] NVIDIA Corporation, “Sionna RT documentation,” [Online]. Available: https://nvlabs.github.io/sionna/rt/. Accessed: Jul. 25, 2026.

[78] J. Hoydis *et al.*, “Learning radio environments by differentiable ray tracing,” *IEEE Trans. Mach. Learn. Commun. Netw.*, vol. 2, pp. 1527–1539, Oct. 2024.

[79] D. Dupleich *et al.*, “Measurement-based validation of ray-tracing model at sub-THz for ISAC applications of blockage in industrial scenario,” in *Proc. 2024 4th URSI Atlantic Radio Science Meeting (AT-RASC)*, Gran Canaria, Spain, pp. 1–4, May. 2024.

[80] L. Zhang *et al.*, “WiSegRT: Dataset for site-specific indoor radio propagation modeling with 3D segmentation and differentiable ray-tracing,” in *Proc. 2024 Int. Conf. Comput., Netw. Commun. (ICNC)*, Big Island, HI, USA, pp. 744–748, Feb. 2024.

[81] S. Bastos *et al.*, “Generation of 5G/6G wireless channels using Raymobtime with Sionna’s ray-tracing,” in *Proc. XLI Brazilian Symp. Telecommun. Signal Process. (SBrT)*, São José dos Campos, Brazil, Oct. 2023.

[82] A. Zubow *et al.*, “Ns3 meets Sionna: Using realistic channels in network simulation,” arXiv:2412.20524, Dec. 2024.

[83] S. Amatare *et al.*, “DT-RaDaR: Digital twin assisted robot navigation using differential ray-tracing,” arXiv:2411.12284, Nov. 2024.

[84] A. E. Güneşer *et al.*, “RIS optimization algorithms for urban wireless scenarios in Sionna RT,” in *Proc. 2025 IEEE 101st Veh. Technol. Conf. (VTC2025-Spring)*, Oslo, Norway, pp. 1–6, Jun. 2025.

[85] K. Guan *et al.*, “CloudRT: A Chinese example of open science infrastructure and services,” *Cultures of Science*, vol. 4, no. 4, pp. 217–226, Dec. 2021.

[86] C. Han *et al.*, “Terahertz wireless channels: A holistic survey on measurement, modeling, and analysis,” *IEEE Commun. Surveys Tuts.*, vol. 24, no. 3, pp. 1670–1707, 3rd Quart., 2022.

[87] H. Qiu *et al.*, “Emulation of radio technologies for railways: A tapped-delay-line channel model for tunnels,” *IEEE Access*, vol. 9, pp. 1512–1523, Jan. 2021.

[88] L. Ma *et al.*, “Satellite-terrestrial channel characterization in high-speed railway environment at 22.6 GHz,” *Radio Sci.*, vol. 55, no. 3, Art. no. e2019RS006995, Mar. 2020.

[89] X. Ou, X. Guo, K. Guan, Z. Ma, and J. Liao, “Propagation characterization for intraship scenario towards 5G-enabled smart maritime,” in *Proc. 2022 3rd URSI Atlantic and Asia Pacific Radio Science Meeting (AT-AP-RASC)*, Gran Canaria, Spain, May. 29–Jun. 3, 2022, pp. 1–4.

[90] A. Habib *et al.*, “Integration of RIS into CloudRT simulator for railway tunnel scenarios,” in *Proc. 2025 19th Eur. Conf. Antennas Propag. (EuCAP)*, Stockholm, Sweden, Mar. 30–Apr. 4, 2025, pp. 1–5.

[91] Altair Engineering, Inc., “Altair WinProp documentation,” [Online]. Available: https://help.altair.com/winprop/. Accessed: Jul. 25, 2026.

[92] U. Jakobus *et al.*, “Recent advances of FEKO and WinProp,” in *Proc. 2018 IEEE Int. Symp. Antennas Propag. & USNC/URSI Nat. Radio Sci. Meeting*, Boston, MA, USA, Jul. 2018, pp. 409–410.

[93] O. Appelman, “Ray tracing simulation accuracy for predicting indoor wireless signal reception,” M.S. thesis, Eindhoven Univ. Technol., Eindhoven, The Netherlands, 2023.

[94] A. S. Haron *et al.*, “The performance of 2.4 GHz and 5 GHz Wi-Fi router placement for signal strength optimization using Altair WinProp,” in *Proc. 2021 IEEE 7th Int. Conf. Smart Instrum., Meas. Appl. (ICSIMA)*, Bandung, Indonesia, Aug. 2021, pp. 25–29.

[95] A. Elfrgani *et al.*, “Virtual drive test for vehicle antenna evaluation,” in *Proc. 2018 IEEE Int. Symp. Antennas Propag. & USNC/URSI Nat. Radio Sci. Meeting*, Boston, MA, USA, Jul. 2018, pp. 1665–1666.

[96] B. Colo *et al.*, “Ray tracing simulations in millimeter-wave vehicular communications,” in *Proc. 2019 IEEE 30th Annu. Int. Symp. Pers., Indoor Mobile Radio Commun. (PIMRC)*, Istanbul, Turkey, Sep. 2019, pp. 1039–1042.

[97] J. Elizalde *et al.*, “Parametric study of radio propagation in railways based on ray-tracing simulations,” in *Proc. 2023 17th Eur. Conf. Antennas Propag. (EuCAP)*, Florence, Italy, Mar. 2023, pp. 1–5.

[98] A. Perez *et al.*, “Ray tracing analysis for UAV-assisted integrated access and backhaul millimeter wave networks,” in *Proc. 2019 IEEE 20th Int. Symp. A World of Wireless, Mobile and Multimedia Netw. (WoWMoM)*, Washington, DC, USA, Jun. 2019, pp. 1–5.

[99] R. Wang *et al.*, “Indoor wireless signal modeling with smooth surface diffraction effects,” in *Proc. 2024 18th Eur. Conf. Antennas Propag. (EuCAP)*, Glasgow, U.K., Mar. 2024, pp. 1–5.

[100] Ranplan Wireless, “Ranplan Professional,” [Online]. Available: https://www.ranplanwireless.com/products/professional. Accessed: Jul. 25, 2026.

[101] Ranplan Wireless, “Ranplan Professional datasheet,” ver. 7.2, Oct. 2025. [Online]. Available: https://www.ranplanwireless.com/hubfs/Datasheets/Ranplan-Professional-Datasheet-28Oct2025.pdf. Accessed: Jul. 25, 2026.

[102] Ranplan Wireless, “Advanced 5G network modelling showcased by Ranplan at 5G North America,” May 2018. [Online]. Available: https://www.ranplanwireless.com/news/ranplan-features-advanced-indooroutdoor-5g-network. Accessed: Jul. 25, 2026.

[103] W. Yang *et al.*, “Verification of an intelligent ray launching algorithm in indoor environments in the Ka-band,” *Radio Sci.*, vol. 56, no. 9, Art. no. e2020RS007252, Sep. 2021.

[104] C. Qin *et al.*, “Simulation-based investigation on spatial channel hardening of massive MIMO in different indoor scenarios and with different array topologies,” in *Proc. 2020 XXXIIIrd Gen. Assem. Sci. Symp. Int. Union Radio Sci. (URSI GASS)*, Rome, Italy, Aug. 29–Sep. 5, 2020, pp. 1–4.

[105] S. Bakirtzis *et al.*, “EM DeepRay: An expedient, generalizable, and realistic data-driven indoor propagation model,” *IEEE Trans. Antennas Propag.*, vol. 70, no. 6, pp. 4140–4154, Jun. 2022.

[106] K. Qiu *et al.*, “IRDM: A generative diffusion model for indoor radio map interpolation,” in *Proc. 2023 IEEE Global Commun. Conf. (GLOBECOM)*, Kuala Lumpur, Malaysia, Dec. 2023, pp. 1–6.

[107] S. Bakirtzis *et al.*, “Stochastic evaluation of indoor wireless network performance with data-driven propagation models,” in *Proc. 2022 IEEE Global Commun. Conf. (GLOBECOM)*, Rio de Janeiro, Brazil, Dec. 2022, pp. 3587–3592.

[108] L. Zhou *et al.*, “An environment-adaptive radio propagation path loss model with ray-based validation,” *IEEE Antennas Wireless Propag. Lett.*, vol. 23, no. 10, pp. 3217–3221, Oct. 2024.

[109] Ranplan Wireless, “Designed an indoor network for a private hospital in Ireland,” Jun. 2022. [Online]. Available: https://www.ranplanwireless.com/resources/indoor-network-for-private-hospital. Accessed: Jul. 25, 2026.

[110] Ranplan Wireless, “5G private wireless network design for a smart factory,” Oct. 2024. [Online]. Available: https://www.ranplanwireless.com/resources/smart-factory-japan. Accessed: Jul. 25, 2026.

[111] EDX Wireless, “EDX SignalPro,” [Online]. Available: https://edx.com/products/signalpro. Accessed: Jul. 25, 2026.

[112] EDX Wireless, “Ray tracing,” Apr. 2022. [Online]. Available: https://edx.com/ray-tracing/. Accessed: Jul. 25, 2026.

[113] EDX Wireless, “Propagation model tuning in SignalPro,” Mar. 2022. [Online]. Available: https://edx.com/blogs/propagation-model-tuning-in-signalpro. Accessed: Jul. 25, 2026.

[114] M. Al-Safwani *et al.*, “Signal strength measurements at VHF in the eastern region of Saudi Arabia,” *Arab. J. Sci. Eng.*, vol. 28, no. 2C, pp. 3–18, Dec. 2003.

[115] A. A. Omorinoye *et al.*, “On the optimisation of practical wireless indoor and outdoor microcells subject to QoS constraints,” *Appl. Sci.*, vol. 7, no. 9, Art. no. 948, Sep. 2017.

[116] EDX Wireless, “Smart city wireless network planning,” [Online]. Available: https://edx.com/industries/iot-smart-cities. Accessed: Jul. 25, 2026.

[117] EDX Wireless, “P25/TETRA network planning using EDX SignalPro,” Jan. 2013. [Online]. Available: https://edx.com/wp-content/uploads/2024/06/P25-TETRA-Network-Planning-using-EDX-SignalPro.pdf. Accessed: Jul. 25, 2026.

[118] EDX Wireless, “Satellite connectivity,” Sep. 2025. [Online]. Available: https://edx.com/satellite-rf-planning/. Accessed: Jul. 25, 2026.

[119] Siradel, “Siradel Web Services: A cloud native network planning API,” [Online]. Available: https://www.siradel.com/telecom/network-planning-api/. Accessed: Jul. 25, 2026.

[120] Siradel, "Siradel Web Services: Simulation API," [Online]. Available: https://www.siradel.com/siradel-web-services-simulation-api/. Accessed: Jul. 25, 2026.

[121] Siradel, "Volcano 5G: Siradel announces enhanced version of its Volcano propagation model," Oct. 2019. [Online]. Available: https://www.siradel.com/volcano-5g-siradel-announces-enhanced-version-of-its-volcano-propagation-model/. Accessed: Jul. 25, 2026.

[122] R. Charbonnier *et al.*, "Calibration of ray-tracing with diffuse scattering against 28-GHz directional urban channel measurements," *IEEE Trans. Veh. Technol.*, vol. 69, no. 12, pp. 14264–14276, Dec. 2020.

[123] M. Z. Aslam *et al.*, "Analysis of 60-GHz in-street backhaul channel measurements and LiDAR ray-based simulations," in *Proc. 2020 14th Eur. Conf. Antennas Propag. (EuCAP)*, Copenhagen, Denmark, Mar. 2020, pp. 1–5.

[124] G. S. Bhatia *et al.*, "Efficient ray-tracing channel emulation in industrial environments: An analysis of propagation model impact," in *Proc. 2023 Joint Eur. Conf. Netw. Commun. & 6G Summit (EuCNC/6G Summit)*, Gothenburg, Sweden, Jun. 2023, pp. 180–185.

[125] G. S. Bhatia *et al.*, "Tuning of ray-based channel model for 5G indoor industrial scenarios," in *Proc. 2023 IEEE Int. Mediterranean Conf. Commun. Netw. (MeditCom)*, Dubrovnik, Croatia, Sep. 2023, pp. 311–316.

[126] G. Gougeon *et al.*, "Ray-tracing calibration from channel sounding measurements in a millimeter-wave industrial scenario," in *Proc. 2024 18th Eur. Conf. Antennas Propag. (EuCAP)*, Glasgow, U.K., Mar. 2024, pp. 1–5.

[127] G. S. Bhatia *et al.*, "Exploring RIS coverage enhancement in factories: From ray-based modeling to use-case analysis," in *Proc. 2024 18th Eur. Conf. Antennas Propag. (EuCAP)*, Glasgow, U.K., Mar. 2024, pp. 1–5.

[128] Remcom, “Wireless InSite 3D wireless prediction software,” [Online]. Available: https://www.remcom.com/wireless-insite-propagation-software. Accessed: Jul. 25, 2026.

[129] Remcom, “Wireless InSite indoor propagation analysis tutorial,” [Online]. Available: https://www.remcom.com/resources/video/wireless-insite-indoor-propagation-analysis-tutorial. Accessed: Jul. 25, 2026.

[130] H. A. Obeidat *et al.*, “Verifying received power predictions of Wireless InSite software in indoor environments at WLAN frequencies,” *Appl. Comput. Electromagn. Soc. J.*, vol. 35, no. 10, pp. 1118–1125, Oct. 2020.

[131] R. Verdecia-Peña *et al.*, “Propagation characterization based on ray-tracing at 60 GHz band: A typical indoor office scenario and validation measurements,” in *Proc. 2023 IEEE 24th Int. Workshop Signal Process. Adv. Wireless Commun. (SPAWC)*, Shanghai, China, Sep. 2023, pp. 346–350.

[132] Remcom, “Millimetre wave ray tracing simulation with diffuse scattering in an office environment,” [Online]. Available: https://www.remcom.com/resources/articles-and-papers/mmwave-ray-tracing-simulation-with-diffuse-scattering-in-an-office-environment. Accessed: Jul. 25, 2026.

[133] H. A. N. Obeidat *et al.*, “Indoor propagation channel simulations for 6G wireless networks,” *IEEE Access*, vol. 12, pp. 133863–133876, Aug. 2024.

[134] X. Cheng *et al.*, “M^{3}SC: A generic dataset for mixed multi-modal sensing and communication integration,” *China Commun.*, vol. 20, no. 11, pp. 13–29, Nov. 2023.

[135] Forsk, “CrossWave propagation model,” [Online]. Available: https://www.forsk.com/crosswave-propagation-model. Accessed: Jul. 25, 2026.

[136] Forsk, “Atoll radio frequency planning and optimisation software,” [Online]. Available: https://www.forsk.com/atoll-overview. Accessed: Jul. 25, 2026.

[137] T. Curry *et al.*, “5G coverage, prediction, and trial measurements,” arXiv:2003.09574, Mar. 2020.

[138] Commission for Communications Regulation, “Mobile wireless and broadband licences: Annual compliance report, Jul. 2024–Jun. 2025,” ComReg 26/02, Jan. 2026. [Online].
Available: https://www.comreg.ie/publication/mobile-wireless-and-broadband-licences-annual-compliance-report-jul-2024-jun-2025/. Accessed: Jul. 25, 2026.

[139] FarrPoint, “Recommendations on a new reporting standard for mobile coverage,” Canadian Radio-television and Telecommunications Commission, Catalogue no. BC92-141/2025E-PDF, Apr. 2025. [Online].
Available: https://crtc.gc.ca/eng/publications/reports/farrpoint2025.htm. Accessed: Jul. 25, 2026.

[140] S. Ju *et al.*, “Millimeter wave and sub-terahertz spatial statistical channel model for an indoor office building," *IEEE J. Sel. Areas Commun.*, vol. 39, no. 6, pp. 1561-1575, Jun. 2021.

[141] C.-X. Wang *et al.*, “A survey of 5G channel measurements and models,” *IEEE Commun. Surveys Tuts.*, vol. 20, no. 4, pp. 3142–3168, 4th Quart., 2018.

[142] D. He *et al.*, “Physics and AI-based Digital Twin of Multi-spectrum Propagation Characteristics for Communication and Sensing in 6G and Beyond,” *IEEE J. Sel. Areas Commun.*, vol. 41, no. 11, pp. 3461–3473, Nov. 2023.

[143] K. Haneda *et al.*, “Measurement-Based Analysis of Spatial Degrees of Freedom in Multipath Propagation Channels,” *IEEE Trans. Antennas. Propag.*, vol. 61, no. 2, pp. 890–900, Feb. 2013.

[144] Y. He *et al.*, “On polarization channel modeling,” *IEEE Wireless Commun.*, vol. 23, no. 1, pp. 80-86, Feb. 2016.

[145] J. Zhang *et al.*, “Generalized polarization-space modulation,” *IEEE Trans. Commun.*, vol. 68, no. 1, pp. 258-273, Jan. 2020.

[146] J. Zhang *et al.*, “Polarization shift keying (PolarSK): system scheme and performance analysis,” *IEEE Trans. Veh. Technol.*, vol. 66, no. 11, pp. 10139-10155, Nov. 2017.

[147] Q. Li *et al.*, “Polarized spatial scattering modulation,” *IEEE Commun. Lett.*, vol. 23, no. 12, pp. 2252-2256, Dec. 2019.

[148] K. Guan *et al.*, “Channel Characterization for Intra-Wagon Communication at 60 GHz and 300 GHz Bands,” *IEEE Trans. Veh. Technol.*, vol. 68, no. 6, pp. 5193-5207, Jun. 2019.

[149] Y. Zhang *et al.*, “Lower-bound capacity based wireless friendliness evaluation for walls as reflectors,” *IEEE Trans. Broadcast.*, vol. 67, no. 4, pp. 917-924, Dec. 2021.

[150] J. Zhang *et al.*, “Two-ray reflection resolution algorithm for planar material electromagnetic property measurement at the millimeter-wave bands,” *Radio Sci.*, vol. 55, no. 3, pp. 1-3, Mar. 2020.

[151] C. A. Balanis, *Advanced Engineering Electromagnetics.* Hoboken, NJ, USA: Wiley, 2012.

[152] R. C. Jones, “A new calculus for the treatment of optical systems. I. Description and discussion of the calculus,” *J. Opt. Soc. Amer.*, vol. 31, no. 7, pp. 488–493, Jul. 1941.

[153] M. Landmann *et al.*, “Polarization behavior of discrete multipath and diffuse scattering in urban environments at 4.5 GHz,” *EURASIP J. Wireless Commun. Netw.*, vol. 2007, Art. no. 57980, Jan. 2007.

[154] Y. Lim *et al.*, “Relationship between cross-polarization discrimination (XPD) and spatial correlation in indoor small-cell MIMO systems,” *IEEE Wirel. Commun. Lett.*, vol. 7, no. 4, pp. 654–657, Aug. 2018.

[155] *Effects of Building Materials and Structures on Radiowave Propagation Above About 100 MHz*, document Recommendation ITU-R 2040-3, P Series, 2023.

[156] H. Chen *et al.*, “Robust symbol detection based on quaternion neural networks in wireless polarization-shift-keying communications,” *IEEE Trans. Neural Netw. Learn. Syst.*, vol. 35, no. 11, pp. 16064–16075, Nov. 2024.

[157] C. Y. Kataria *et al.*, “Secure antenna polarization modulation line-of-sight analysis and demonstration,” *IEEE Trans. Antennas Propag.*, vol. 69, no. 7, pp. 4100–4108, Feb. 2021.

[158] W. Zhai *et al.*, “An ultraefficient broadband photonic channelizer based on polarization-division multiplexing and integrated dual-polarization coherent detection receiver,” *IEEE Trans. Microw. Theory Techn.*, vol. 70, no. 3, pp. 1821–1831, Mar. 2022.

[159] S. Benedetto *et al.*, “Theory of polarization shift keying modulation,” *IEEE Trans. Commun.*, vol. 40, no. 4, pp. 708–721, Apr. 1992.

[160] S. Benedetto *et al.*, “Direct detection of optical digital transmission based on polarization shift keying modulation,” *IEEE J. Sel. Areas Commun.*, vol. 13, no. 3, pp. 531–542, Apr. 1995.

[161] X. Wu *et al.*, “Polarization shift keying for wireless communication,” *IEEE Trans. Wireless Commun.*, vol. 18, no. 10, pp. 4927–4941, Oct. 2019.

[162] A. Kattunen *et al.*, “Modeling the multipath cross-polarization ratio for 5–80-GHz radio links,” *IEEE Trans. Wireless Commun.*, vol. 18, no. 10, pp. 4768–4778, Oct. 2019.

[163] S. C. Kwon *et al.*, “Geometrically based statistical model for polarized body-area-network channels,” *IEEE Trans. Veh. Technol.*, vol. 62, no.8, pp. 3518–3530, Oct. 2013.

[164] S. Jaeckel *et al.*, “A geometric polarization rotation model for the 3-D spatial channel model,” *IEEE Trans. Antennas Propag.*, vol. 60, no.12, pp. 5966–5977, Dec. 2012.

[165] X. Yin *et al.*, "Empirical stochastic modeling of multipath polarizations in indoor propagation scenarios," *IEEE Trans. Antennas Propag.*, vol. 63, no.12, pp. 5799–5811, Dec. 2015.

[166] F. F. Fan *et al.*, "A wideband compact printed dipole antenna array with SICL feeding network for 5G application," *IEEE Antennas Wireless Propag. Lett.*, vol. 22, no. 2, pp. 283–287, Feb. 2023.

[167] P. F. Hu *et al.*, "A tri-band dual-polarized omnidirectional dielectric resonator antenna with a planar feed for indoor applications," *IEEE Trans. Antennas Propag.*, vol. 72, no. 1, pp. 401–411, Jan. 2024.

[168] I. A. Hemadeh *et al.*, "Polarization modulation design for reduced RF chain wireless," *IEEE Trans. Commun.*, vol. 68, no. 6, pp. 3890–3907, Jun. 2020.

[169] T. Svantesson, "A double-bounce channel model for multi-polarized MIMO systems," in *Proc. IEEE 56th Veh. Technol. Conf. (VTC 2002-Fall)*, vol. 2, Vancouver, BC, Canada, Sep. 2002, pp. 691–695.

[170] Q. Li *et al.* "A correlation-based electromagnetic time reversal technique to locate indoor transient radiation sources," *IEEE Trans. Microw. Theory Techn.*, vol. 69, no. 9, pp. 3945–3957, Sep. 2021.

[171] J. Zhang *et al.*, "Bit error probability of spatial modulation over measured indoor channels," *IEEE Trans. Wireless Commun.*, vol. 13, no. 3, pp. 1380–1387, Mar. 2014.

[172] G. Yu *et al.*, "A ray-launching algorithm for polarized wireless channel prediction," in *Proc. 2023 IEEE GLOBECOM Workshops (GC Wkshps)*, Kuala Lumpur, Malaysia, Dec. 2023, pp. 1928–1933.

[173] Y. Zhang *et al.*, "Wireless friendliness evaluation and optimization for sandwich building materials as reflectors," *IEEE Trans. Antennas Propag.*, vol. 72, no. 3, pp. 2697–2711, Mar. 2024.

[174] B. Clerckx *et al.*, *MIMO Wireless Networks: Channels, Techniques and Standards for Multi-Antenna, Multi-User and Multi-Cell Systems,* 2nd ed. Oxford, UK: Academic Press, 2013.

[175] M. K. Simon, "Evaluation of average bit error probability for space-time coding based on a simpler exact evaluation of pairwise error probability," *J. Commun. Netw.*, vol. 3, no. 3, pp. 257–264, Sep. 2001.

[176] P. Henarejos *et al.*, "3-D polarized modulation: System analysis and performance," *IEEE Trans. Commun.*, vol. 66, no. 11, pp. 5305–5316, Nov. 2018.

[177] S. Stefanov *et al.*, "Dielectric properties of common building materials for UWB propagation studies,," *IEEE Antennas Propag. Mag.*, vol. 62, no. 1, pp. 72–78, Jan. 2020.

[178] C. A. Grosvenor *et al.*, "Time-domain free-field measurements of the relative permittivity of building materials," *IEEE Trans. Instrum. Meas.*, vol. 58, no. 7, pp. 2275–2282, Jul. 2009.

[179] S. Pisa *et al.*, "Permittivity measurement on construction materials through free space method," in *Proc. 2017 IEEE Int. Instrum. Meas. Technol. Conf. (I2MTC)*, Turin, Italy, May. 2017, pp. 1–4.

[180] G. H. Söffker, *Constructing Architecture: Materials, Processes, Structures.* Basel, Switzerland: Birkhäuser Verlag AG, 2005.

[181] C. A. Balanis, *Antenna Theory: Analysis and Design.* Hoboken, NJ, USA: Wiley, 2016.

[182] Q. Wu *et al.*, "Towards smart and reconfigurable environment: Intelligent reflecting surface aided wireless network," *IEEE Commun.Mag.*, vol. 58, no. 1, pp. 106–112, Jan. 2020.

[183] Ö. Özdogan *et al.*, "Intelligent reflecting surfaces: Physics, propagation, and pathloss modeling," *IEEE Wireless Commun. Lett.*, vol. 9, no. 5, pp. 581–585, May. 2020.

[184] E. Basar *et al.*, “Wireless communications through reconfigurable intelligent surfaces,” *IEEE Access*, vol. 7, pp. 116753–116773, Aug. 2019.

[185] M. Di Renzo *et al.*, “Smart radio environments empowered by reconfigurable AI meta-surfaces: An idea whose time has come,” *EURASIP J. Wireless Commun. Netw.*, vol. 2019, no. 1, pp. 1–20, May. 2019.

[186] Q. Li *et al.*, “Reconfigurable intelligent surfaces relying on non-diagonal phase shift matrices,” *IEEE Trans. Veh. Technol.*, vol. 71, no. 6, pp. 6367–6383, Jun. 2022.

[187] Y. Liu *et al.*, “An equivalence principle-based hybrid method for propagation modeling in radio environments with reconfigurable intelligent surfaces,” *IEEE Trans. Antennas Propag.*, vol. 72, no. 7, pp. 5961–5973, Jul. 2024.

[188] A. Epstein *et al.*, “Floquet-Bloch analysis of refracting Huygens metasurfaces,” *Phys. Rev. B*, vol. 90, no. 23, Art. no. 235127, Dec. 2014.

[189] N. Yu *et al.*, “Light propagation with phase discontinuities: Generalized laws of reflection and refraction,” *Science*, vol. 334, no. 6054, pp. 333–337, Oct. 2011.

[190] C. A. Balanis, *Advanced Engineering Electromagnetics*, 2nd ed. Hoboken, NJ, USA: Wiley, 2012.

[191] W. Yang *et al.*, “Indoor measurement based verification of ray launching algorithm at the Ka-band,” in *Proc. 2020 XXXIIIrd Gen. Assem. Sci. Symp. Int. Union Radio Sci. (URSI GASS)*, Rome, Italy, 2020, pp. 1–4.

[192] J. Zhang *et al.*, “Fundamental wireless performance of a building,” *IEEE Wireless Commun.*, vol. 29, no. 1, pp. 186-193, Feb. 2022.

[193] J. M. Rigelsford *et al.*, “Wireless/energy efficiency of typical building components and architecture,” WiFEEB Project, Deliverable D1.2, Jan. 2013.

[194] Q. Wu *et al.*, "Intelligent reflecting surface enhanced wireless network via joint active and passive beamforming," *IEEE Trans. Wireless Commun.*, vol. 18, no. 11, pp. 5394–5409, Nov. 2019.

[195] R.-B. Hwang, *Periodic Structures: Mode-Matching Approach and Applications in Electromagnetic Engineering*. Singapore: John Wiley & Sons, 2013.

[196] Z. Liu *et al.*, "Channel-informed RIS analysis and optimization using hybrid ray-tracing and full-wave simulation framework," *IEEE Trans. Antennas Propag.*, vol. 74, no. 1, pp. 909–921, Jan. 2026.